DEVELOPING CRYOGENIC ION VIBRATIONAL SPECTROSCOPY METHODS FOR THE CHARACTERIZATION OF MOLECULAR INTERACTIONS

By

Jonathan M. Voss

A dissertation submitted in partial fulfillment of the requirements for the degree of

Doctor of Philosophy

(Chemistry)

at the

UNIVERSITY OF WISCONSIN-MADISON

2018

Date of final oral examination: 7/20/2018

The dissertation is approved by the following members of the Final Oral Committee:
Etienne Garand, Professor, Chemistry
John C. Wright, Professor, Chemistry
Tim Bertram, Professor, Chemistry
Thomas Brunold, Professor, Chemistry

DEVELOPING CRYOGENIC ION VIBRATIONAL SPECTROSCOPY METHODS FOR THE CHARACTERIZATION OF MOLECULAR INTERACTIONS

Jonathan M. Voss

Under the supervision of Professor Etienne Garand

at the

UNIVERSITY OF WISCONSIN-MADISON

Molecular interactions play subtle roles in regulating reactivity and three-dimensional molecular structure in catalytic and biological processes. By more fully understanding these weak interactions, they can be used to help finely tune chemical reactivity and structure. However, an in-depth analysis of these effects is often difficult to obtain, due to the simultaneous combination of various forces (dispersion, electrostatic, H-bonding, charge transfer, etc.) between multiple species (solute, solvent, surface). Furthermore, the transient nature of the species involved in such molecular embraces further complicates the study of these interactions. This body of work presents gas-phase vibrational spectroscopy techniques that were developed in order to isolate and characterize the weak molecular interactions present in a variety of systems.

First, the prototypical $[Ru(bpy)(tpy)(H_2O)]^{2+}$ (bpy=2,2′-bipyridine, tpy=2,2′:6′,2“-terpyridine) water oxidation catalyst is used to demonstrate the ability to form short-lived species. The resting catalyst and two of its intermediates, $[Ru(bpy)(tpy)(OH)]^{2+}$ and $[Ru(bpy)(tpy)(O)]^{2+}$

are accessed via an electrochemical flow cell and are confirmed via mass spectrometry. The $[Ru(bpy)(tpy)(H_2O)]^{2+}$ and $[Ru(bpy)(tpy)(OH)]^{2+}$ complexes are additionally probed with IR predissociation spectroscopy and the vibrational frequencies are used to help rationalize the e^-/H^+ loss. These results demonstrate that upon oxidation, the electron loss is mostly shared between the Ru^{3+} center and the OH^- ligand.

Second, the Na^+(glucose) system is used to develop and test a conformation-specific experimental IR-IR approach. The conformational landscape of the Na^+(glucose) complex is rationalized with IR-IR spectroscopy via ion-dip or isomer-burning schemes. By collecting numerous double resonance spectra, the presence of eight unique Na^+(glucose) structures is confirmed. The data suggest the overall gas-phase α/β-glucose ratio closely matches that of the solution-phase value. Probing the structural landscape in such a manner demonstrates the ability to understand conformationally complex systems with many species present at a single mass-to-charge ratio.

Third, the double resonance approach is extended to the simple protonated peptide, triglycine, which serves to model intramolecular interactions present in protein backbones. The results reveal the presence of two Gly_3H^+ structures in our experiment, protonated at either the terminal amine or amide oxygen. The conformer-specific spectra allow H-bonding strengths of individual N-H and O-H groups to be experimentally estimated, which is in turn used to rationalize the stabilities of the two structures.

Fourth, a scheme for forming solvated complexes inside a cryogenic ion trap is presented to highlight the delicate interplay of solute-solvent and solvent-solvent interactions in $[bmim]^+\cdot(H_2O)_n$ clusters. Predissociation spectra show that the water molecules solvate the C2-H moiety of the imidazolium ring for the small n = 1 and 2 clusters. This solvation motif is attributed

to electrostatic and dispersion forces between the water and C2-H. For larger cluster complexes, the cooperative water-water interactions are found to drive the formation of solvent networks on top of the imidazolium ring.

Finally, a new experimental scheme for solvating ions is presented. In these experiments, D_2O was clustered around the prototypical glycine ion, $GlyH^+$. When the D_2O cluster spectra are compared with their H_2O counterparts, it is easy to distinguish the vibrational features related to the ion core and the solvation network. Trends relating to the completion of solvation shells and solvent-solute and solvent-solvent interaction strengths are highlighted with this technique.

Table of Contents

List of Figures

List of Tables

Acknowledgements

There are many people who have contributed to various stages of my academic pursuits whom I wish to thank. By no means is the following list of individuals exhaustive, as I have been fortunate to have the support of numerous mentors, family members, and friends. I am deeply grateful for all of the help along the way.

I should first thank a few influential undergraduate mentors. At the outset of college, Professor Peter Massey encouraged me to tread the most academically rigorous available paths, of which I am still exploring. Professor Fred Smith exposed me to undergraduate research and played a large role in my transition to graduate school. He continues to challenge me to reach my fullest professional potentials. I must also thank Professor Michael Saliby for his wonderful instruction as an advisor and educator. He taught many of my undergraduate courses and made chemistry a joy to study.

I am of course very grateful to Etienne for all he has done as a graduate advisor and feel very fortunate to have been part of his group. He has always made himself available to give instruction in the lab or to discuss projects, even during the busyness of pursuing tenure. I'm thankful for the freedom he gave me in lab to explore a variety of experimental systems, as well as the diverse set of skills I acquired along the way. He consistently invested in me professionally, allowing me to travel to conferences to speak. He even sent me abroad for a collaboration.

I wish to thank past and current members of the Garand Group for their help during graduate school. I was trained by and worked closely with Brett Marsh and Erin Duffy, for which I am very thankful. I also owe a great deal to Kaitlyn Fischer, who assisted (and suffered with) me in lab with some tricky experiments; she was a great help. I must also credit Jia Zhou for her invaluable contributions to many projects through scientific insight, data analysis, and manuscript

preparation. She is an integral part of the group. Finally, I thoroughly enjoyed the friendships and memories I have shared with all the other members of the Garand Group. Remember: It's about the experience, not the numbers.

I must also thank my family for their support and encouragement throughout my life. I credit my successes to my mother, Jacki, who has sacrificed much to support me and taught me how to be successful. I also wish to thank Faith for sharing these very special years in Madison with me. She always celebrated with me in the good times and made the strenuous times more palatable. I look forward to continuing our adventure together.

On a final note, I eagerly await the work that will emerge from the lab in the coming years. I'm confident that Etienne and his students will continue to push the limit of possibility and accomplish remarkable things.

CHAPTER 1

Introduction

1.1 Overview

Molecular interactions play subtle yet important roles that help dictate reactivity and three-dimensional structure in catalytic and biological systems. For example, charge transfer, ion-mediated, electrostatic, and hydrogen-bonding forces are known to help facilitate catalysis[1-3] and govern biological function.[4-6] The potential to finely tune chemical reactivity as well as higher order structure has, not surprisingly, led to a great effort to understand these types of interactions at the molecular level. However, a detailed characterization of these effects is often difficult to obtain, due to the complex combination of various forces between multiple species (solute, solvent, and surface).

Computational chemistry has been used extensively to model molecular forces, but its application to study such effects in many systems is still limited. For example, reliable interaction energies may be found for very simple systems using a coupled-cluster technique, but such an approach is computationally expensive and often impractical when considering < 30 atoms.[7] On the other hand, sufficiently complex systems necessitate the use of less expensive theoretical methods, which routinely fail to accurately characterize non-covalent interactions.[8] Furthermore, catalytic systems can be difficult to address computationally due to the open shell nature of metal atoms, which can cause significant errors through spin contamination. As such, theoretical predictions are often not enough on their own and there is a need to experimentally probe non-covalent effects.

Experimental efforts to understand non-bonding effects include UV/VIS,[9,10] infrared (IR)/ Raman,[11-14] and electron paramagnetic resonance (EPR)/ nuclear magnetic resonance (NMR).[15-18] The drawback of these techniques is that they lack selectivity, yielding measurements which are representative of an ensemble of aqueous species experiencing unique chemical environments. For

example, multiple three-dimensional structures may simultaneously exist for a biological molecule in solution. Similarly, a reaction mixture may contain a multitude of transient intermediate complexes at any given time. Additionally, important information involving the nature of molecular interactions may be masked by the solution itself. There is a clear challenge in gaining direct insights about specific non-covalent forces with conventional experimental techniques. Thus, another method capable of selectively preparing, preserving, and probing molecular species must be used.

Mass spectrometry has been widely used to selectively prepare and isolate catalytic and biological ions directly from solution. In addition to providing information about the overall molecular weight of a complex, it is capable of describing the direct connectivity of molecular ions via collision-induced dissociation (CID),[19,20] surface-induced dissociation (SID),[21,22] electron transfer dissociation (ETD),[23,24] or ultra-violet photodissociation (UVPD).[25,26] Due to the high vacuum environment inside mass spectrometers, these instruments are very well suited to preserve highly reactive aqueous complexes and delicate molecular embraces. While mass spectrometry has been used to provide information about reactivity, non-covalent interactions, and higher order structures when coupled to methods such as hydrogen/deuterium exchange (HDX),[27,28] ion mobility spectrometry,[29,30] chemical cross linking,[31,32] such studies do not provide sufficiently rich details about non-bonding forces.

While the isolated environment afforded by mass spectrometers make these instruments an ideal platform in which to study non-covalent interactions, the low number density of ions inside them prevents the use of direct absorption spectroscopy in such systems. While the intensity of light absorbed cannot be used to collect a spectrum, a number of schemes involving photodissociation of molecular ions have been employed to gather UV/VIS[33,34] and IR[35,36] spectra

in the gas-phase. During photodissociation, chemical bonds or molecular clusters are decomposed as the result of resonant absorption of photons. Since a change in molecular weight upon photoexcitation is easily detectable with mass spectrometry, spectral information can be gathered by monitoring changes of mass as the energy of the incident light is varied.

Since the frequency of infrared light absorbed is highly dependent on bonding type and local environment, this spectroscopic method is a very attractive option to study non-covalent interactions of isolated ions inside a mass spectrometer. However, the energy of a single infrared photon is typically insufficient to induce bond fragmentation. For example, breaking a water O-H bond (bond dissociation energy = 41,550 cm^{-1})[37] would take 11 photons resonant with the asymmetric water stretching mode (ν_3 = 3755 cm^{-1}) or 26 photons at the energy of the fundamental water bending mode (ν_1 = 1595 cm^{-1}).[38] Such experiments require the extremely high photon fluxes of free-electron lasers or synchrotron light sources, which are very expensive and are not readily accessible. Additionally, multiple photon absorption yields inherently non-linear spectra, which are difficult to compare with harmonic vibrational spectra.[39]

Another method used recently couples absorption of a single IR photon with ionizing or photodissociating UV/VIS photons.[40-42] Such experimental techniques provide a more straightforward approach to obtain a linear photofragmentation spectra. Additionally, the "pump-probe" laser approach provides the ability to distinguish between molecular conformers, which are common for large and floppy biomolecules. The drawback of this approach requires that an appropriate chromophore be embedded in the molecule being studied and is therefore not applicable to many systems.

Another approach that can be widely applied to overcome these experimental difficulties is predissociation spectroscopy. In this spectroscopic scheme, a weakly bound "messenger" adduct

is lost from the species being probed when even just a single photon is absorbed. Ar and CO_2 have been used to "tag" molecules that experience rapid cooling in a supersonic expansion.[43,44] However, many systems of interest are generated via electrospray ionization and cannot be tagged through supersonic expansion. To solve this, ions can be trapped and cooled at cryogenic temperatures in order to form adduct species for predissociation spectroscopy.[45,46] The low binding energy of these tags (~100's of cm^{-1}) allows molecular ions to be probed as low as the "IR fingerprint" region. Such spectra can be compared directly to theoretical calculations.

Although cryogenic ion vibrational spectroscopy is capable of routinely collecting high resolution IR spectra of isolated molecular ions, it still suffers from a number of technological setbacks. For example, it is necessary to develop suitable methods for generating transient reaction species, selectively probing conformational populations, reliably forming solvated complexes, and disentangling solute-solvent spectral features in order to more fully realize the power of predissociation spectroscopy. Such methodology improvements are the subject of this thesis and are presented in detail in Chapters 3-7.

Chapter 3 presents an electrochemical technique for generating short-lived catalytic reaction intermediates. The experimental technique was optimized using the prototypical $[Ru(bpy)(tpy)(H_2O)]^{2+}$ (bpy=2,2′-bipyridine, tpy=2,2′:6′,2"-terpyridine) water oxidation catalyst.[47,48] The resting catalyst and two of its intermediates, $[Ru(bpy)(tpy)(OH)]^{2+}$ and $[Ru(bpy)(tpy)(O)]^{2+}$ are accessed by varying the potential of an in-line electrochemical cell and are confirmed via mass spectrometry. The $[Ru(bpy)(tpy)(H_2O)]^{2+}$ and $[Ru(bpy)(tpy)(OH)]^{2+}$ complexes are probed with IR predissociation spectroscopy and the vibrational frequencies are used to help rationalize the e^-/H^+ loss. The IR spectra demonstrate that upon oxidation, the electron loss is mostly shared between the Ru^{3+} center and the OH^- ligand. This study represents the ability

to generate and selectively probe transient aqueous reaction intermediates, which should be applicable to other systems.

In Chapter 4, the Na^+(glucose) system is used to develop an IR-IR double resonance technique capable of exploring diverse conformational landscapes. This approach involves only minimal modifications to the traditional IR predissociation setup, which allows conformation-specific experiments to be carried out via ion-dip or isomer-burning schemes. By collecting numerous double resonance spectra, the presence of eight unique Na^+(glucose) structures (three α- and five β-conformers) are confirmed. The overall gas-phase α/β ratio of glucose closely matches that of the solution-phase value. The ability to dissect conformational complexities in such a manner can be widely applied to complexes such as glycans, which decorate the surfaces of biomolecules and are difficult to understand with MS alone.

In Chapter 5, the double resonance technique is extended to the simple protonated peptide, triglycine, in order to understand the delicate balance of intramolecular interactions that lead to peptide stabilization. The results reveal the presence of two Gly_3H^+ structures, protonated at either the terminal amine or amide oxygen. Conformer specific spectra allow H-bonding strengths of individual N-H and O-H groups to be experimentally estimated, which is in turn used to rationalize the stabilities of the two structures.

Chapter 6 presents a robust method for forming relatively large solvated complexes using the ionic liquid cation butyl methyl imidazolium ($BMIM^+$). The technique relies on a liquid nitrogen cooled octopole ion trap to generate $[BMIM]^+\cdot(H_2O)_n$, n = 1–8, species which are probed with predissociation spectroscopy. The spectra show that the water molecules solvate the C2-H moiety of the imidazolium ring for the small n = 1 and 2 clusters. This solvation motif is attributed to electrostatic and dispersion forces between the water and C2-H. For larger cluster complexes,

the cooperative water-water interactions is found to drive the formation of solvent networks on top of the imidazolium ring.

In Chapter 7, a new experimental scheme for separating solute-solvent spectral features is presented. In these experiments, D_2O was clustered around the prototypical glycine ion, $GlyH^+$. When the D_2O cluster spectra are compared with their H_2O counterparts, it is easy to distinguish the vibrational features related to the ion core and the solvation network. Trends relating to the completion of solvation shells and solvent-solute and solvent-solvent interaction strengths are highlighted by this technique.

In Chapter 8, preliminary data is presented that demonstrates the ability to extract insights about H/D exchange reaction barriers and mechanisms. These carefully executed CIVS experiments perhaps foreshadow the types of gas-phase methods that may be employed in the near future to obtain an even deeper understanding of the role of molecular interactions in reactions.

1.2 Mass Spectrometry

Mass spectrometry is an extremely powerful analytical technique that uses mass-to-charge ratio (m/z) as well as isotopic patterns to ascertain molecular mass and composition. Mass spectrometry operates under high vacuum conditions, where mean free paths are significantly increased as compared to ambient pressures. Due to the decreased number of collisions with background gas, ionized complexes are easily manipulated with electric fields. A mass spectrometer thus serves as an ideal environment to isolate and study molecular ions as well as charged clusters that exhibit weakly interacting moieties.

1.2.1 Electrospray Ionization

In the 1980's, the Nobel laureate John Fenn showed that solution phase species could be easily introduced into a mass spectrometer via electrospray ionization (ESI).[49-51] This "soft" ionization technique quickly became the preferred method to gently transfer biological molecules to the gas phase without bond fragmentation occurring. In ESI, a dilute solution is flowed through a small (μm) metal or glass capillary and is directed towards a mass spectrometer entrance. The large electrical potential difference between the ESI capillary (kV) and the mass spectrometer inlet (V) creates a large electric field around the solution emerging from the ESI tip. This field induces charges on the solution surface, and with sufficiently high capillary potentials, the surface tension can be overcome by repulsive forces. With the breakdown of surface tension, a Taylor cone is formed. Small droplets are created on the tip of the Taylor cone, which subsequently undergo Coulombic explosion.[52]

As droplets in the ESI plume explode and evaporate, solute species are transferred to the gas phase. Several mechanisms, such as the ion ejection model (IEM),[53,54] the charged residue

model (CRM),[55,56] and the chain ejection model (CEM),[57,58] have been proposed to explain the formation of isolated gaseous ions. In the IEM, small ions are displaced from the droplet surface by the repulsive forces present due to other like charges on the droplet exterior. The CRM is used to describe how globular species, such as proteins embedded within a droplet, are ionized during ESI. In the CRM, evaporation of solvent occurs from the droplet surface until only a single analyte is contained in the droplet, until the remaining solvent is removed and a bare ion remains. Finally, the CEM explains how long chains, like unfolded proteins or polymers, are sequentially expelled through the surface of the droplet.

1.2.2 Time-of-Flight Mass Spectrometry

Linear time-of-flight (TOF) mass spectrometry was first used by Wiley and McLaren[59] to determine mass-to-charge ratio by measuring the time it takes an ion to travel a known distance. This setup relies on the principle that ions of different masses *(m)* will travel at different velocities *(v)* when given the same initial kinetic energy *(E_K).* This relationship is expressed as

$$E_K = \frac{1}{2}mv^2 \qquad \text{(eq. 1.2.1)}$$

Since velocity is defined as distance traveled per unit time, this equation is rewritten as

$$E_K = \frac{1}{2}m\left(\frac{L}{t}\right)^2 \qquad \text{(eq. 1.2.2)}$$

where *L* is the flight path length and *t* is time. Potential energy *(E_P)* is given to an ion with an electric charge *(q)* by the application of an electric field (*U)*. The potential energy is converted to kinetic energy as ion acceleration occurs, which is written as

$$E_P = qU = E_K \qquad \text{(eq. 1.2.3)}$$

The electric charge *(q)* of an ion is the product of the charge number *(z)* and the elementary charge constant *(e)* by

$$q = ze \qquad \text{(eq. 1.2.4)}$$

and mass, time-of-flight, and charge are related by

$$\frac{1}{2}m\left(\frac{L}{t}\right)^2 = zeU \qquad \text{(eq. 1.2.5)}$$

Rearrangement of this equation shows that the mass-to-charge ratio of an ion is proportional to the square of the time-of-flight multiplied by a constant, given by

$$\frac{m}{z} = \left(\frac{2eU}{L^2}\right)t^2 \qquad \text{(eq. 1.2.6)}$$

Since *e, U,* and *L* are constant during an experiment, *m/z* is determined by measuring ion flight time. Eq. 1.2.6 shows that flight time is directly proportional to ion mass and inversely related to charge. Thus, it is possible for ions of different mass and charge to have the same mass-to-charge

ratio. In such a case, the spacing of isotopic peaks can be used in order to determine the overall molecular weights of the individual species.

Due to slight variations of initial ion energies, differences in ion positions in the acceleration region, as well as subtle fluctuations in *U*, ions of the same *m/z* will arrive at the detector at different times, causing decreased mass resolution. To alleviate the spread of kinetic energies, a reflectron[60] can be used to apply an electric field *(E_R)* to slow, stop, and turn ions in a focused packet towards the detector. The reflectron electric field is equivalent to the applied electric potential *(U_R)* divided by the length of the reflectron *(D)*. The depth *(d)* that ions travel into the reflectron before being stopped depends on their kinetic energy, and can be described by

$$d = \frac{E_K}{qE_R} = \frac{qU}{qU_R/D} = \frac{UD}{U_R} \qquad \text{(eq. 1.2.7)}$$

At this depth, ions are redirected and have stopped moving. Thus, their average velocity is half their initial velocity *(v_i)* and the time *(t_0)* taken to reach *d* is given by

$$t_o = \frac{d}{v_i/2} = \frac{2d}{v_i} \qquad \text{(eq. 1.2.8)}$$

Since the path of ions through the reflectron is symmetric, the total time ions spend being reflected *(t_R)* is twice t_0 or

$$t_R = 2\left(\frac{d}{v_i/2}\right) = \frac{4d}{v_i} \qquad \text{(eq. 1.2.9)}$$

The distances traveled by the ions before *(L_1)* and after *(L_2)* the reflectron allow the time spent in the time of flight tube *(t_{tube})* to be found by

$$t_{tube} = \frac{L_1+L_2}{v_i} \quad \text{(eq. 1.2.10)}$$

The total time *(t_{tot})* it takes ions to reach the detector is then given by

$$t_{tot} = t_{tube} + t_R = \frac{L_1+L_2+4d}{v_i} \quad \text{(eq. 1.2.11)}$$

By rearranging eq. 1.2.6, v_i is found by

$$v_i = \sqrt{\frac{2zeU}{m}} \quad \text{(eq. 1.2.12)}$$

By substitution of eq. 1.2.12 into eq. 1.2.11, it can be shown that *m/z* in a reflectron TOF mass spectrometer is determined by

$$\frac{m}{z} = \left[\frac{2eU}{(L_1+L_2+4d)^2}\right] t_{tot}^2 \quad \text{(eq. 1.2.13)}$$

1.3 Infrared Spectroscopy

Infrared spectroscopy is routinely used to study molecular structure through vibrational motion of atoms within a molecule. Molecular vibrations occur when an oscillating electromagnetic field of appropriate energy interacts with the transition dipole of vibrating atoms. That is, absorption occurs when the frequency of an IR photon is resonant with a molecular vibration. Since vibrational transitions occur at discrete energies, the frequency of the absorbed photon gives information about the bond type as well as the local chemical environment around the vibrating atoms. The unique set of photon energies necessary to induce vibrational motions therefore serves as a basis to distinguish different molecular groups present in a system and can be thought of as a "fingerprint" used to identify a molecule.

In conventional IR spectroscopy, the absorbance *(a)* is found by measuring the intensity of light before *(I_o)* and after *(I)* a sample

$$A = log\left(\frac{I}{I_o}\right) \qquad \text{(eq. 1.3.1)}$$

Absorbance is also proportional to the product of the sample's extinction coefficient *(ε)*, the pathlength of the sample *(l)*, and the sample concentration *(C)*, summarized by the Beer-Lambert Law,

$$A = \varepsilon lC \qquad \text{(eq. 1.3.2)}$$

The extinction coefficient is related to the vibrational absorption cross section *($\sigma(v)$)* as well as the number density *(ρ)* of molecules in the sample. Thus, the Beer-Lambert Law can be written as

$$A = log\left(\frac{I(v)}{I_o}\right) = \sigma(v)l\rho \quad \text{(eq. 1.3.3)}$$

In a concentrated solution, this product is typically sufficiently large to cause a measurable difference between the incident and transmitted light.

Obtaining an infrared spectrum directly by traditional methods is not feasible for gas-phase ions, which have drastically lower number densities in a mass spectrometer. Due to electrostatic repulsion, an ion trap is capable of storing only 10^4 – 10^8 ions at a time. However, a single laser pulse may contain 10^{14} – 10^{16} photons. The large contrast in magnitudes results in an immeasurable difference between the incident and transmitted light. Therefore a different approach is needed to acquire an IR spectrum of molecular ions inside a mass spectrometer.

1.3.1 Principles of Infrared Predissociation Spectroscopy

In order to overcome the low density of ions in a mass spectrometer, action spectroscopy is used. In action spectroscopy, the mass change of molecules affected by incident light *($N(v)/N_o$)* is used to obtain infrared spectra. Instead of using the typical form of Beer's Law, given by

$$I(v) = I_o e^{-\sigma(v)l\rho} \quad \text{(eq 1.3.4)}$$

we use

$$N(v) = N_o e^{-\sigma(v)\Phi(v)} \quad \text{(eq. 1.3.5)}$$

where $\Phi(\nu)$ is the photon fluence on the sample. For experiments with pulsed lasers, the photon fluence is sufficiently large to cause the exponential product to approach 1, which leads to a measureable number of affected molecules.[61] In such experiments, ions are cooled to cryogenic temperatures and "tagged" with a weakly bound and minimally perturbative D_2 molecule. When an IR photon is absorbed by a tagged complex, the energy dissipates via intramolecular vibrational redistribution (IVR), resulting in the loss of the D_2 molecule.[62] Figure 1.1 shows a schematic depiction of the IVR process upon absorption of an IR photon. The loss of the tag occurs on the order of picoseconds to nanoseconds, which occurs long before the photofragment reaches the reflectron, where it is separated from the tag.

Figure 1.1 Schematic of internal vibrational redistribution (IVR) process.

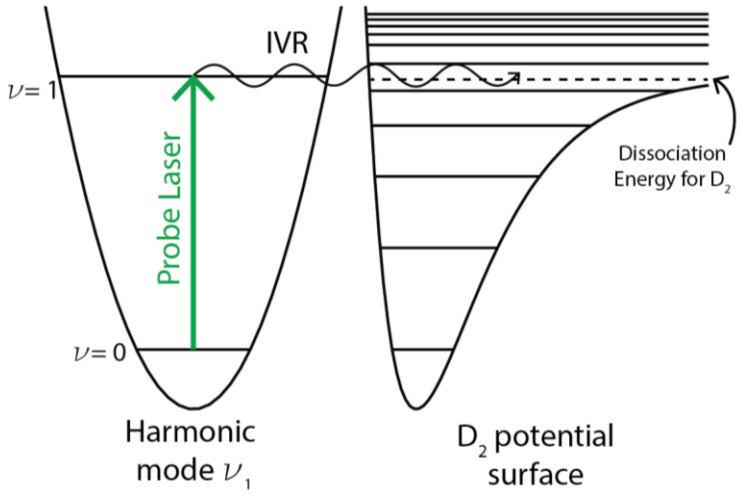

The loss of D_2 in such a case can be modeled by Ramsberger-Rice-Kassel-Marcus (RRKM) theory,[62] where the energy dependent rate constant for unimolecular dissociation *(k(E*))* is given by

$$k(E^*) = \frac{\sigma W^*(E-E_o)}{h\rho(E)} \qquad \text{(eq. 1.3.6)}$$

where σ is the reaction path degeneracy, $W^*(E - E_o)$ is the density of states between energy E and E_o (i.e. the barrier height of the reaction), h is Planck's constant, and $\rho(E)$ is the density of states at energy E. If the vibrational energy levels of the system are known, the $W^*(E - E_o)$ and $\rho(E)$ terms can be found using the Beyer and Swinehart algorithm.[63] For the present case, the barrier height for reaction is assumed to be the binding energy of the D_2 tag.

Calculated unimolecular reaction rates for the protonated triglycine complex, $Gly_3H^+ \cdot D_2$, were obtained using RRKM theory and are shown in Figure 1.1. The reaction rates are represented as half-lives of $Gly_3H^+ \cdot D_2$ upon excitation and are dependent on the internal energy of the ion upon vibration i.e. the energy of the photon absorbed. The harmonic vibrational frequencies of the tagged triglycine structure, optimized at the cam-B3LYP/def2tzvpp level of theory, were used to estimate the densities of states alone the reaction path coordinate. This level of theory was also used to find the binding energy of D_2 in this complex, which is found to be only ~150 cm^{-1}. The rate of photodissociation corresponding to this binding energy is shown in green in Figure 1.1. It's apparent that even with photons of modest energy (500 cm^{-1}), the excited complex dissociates on a timescale that is much faster (< ns) than the ion flight time (~10's of μs). Furthermore, even tags with higher binding energies are predicted to photodissociate at a rate that is compatible with the

TOF experiment. This is crucial for considering experiments that monitor direct loss of H_2O, which has a much higher binding energy, from a clustered complex.

Figure 1.2 Results of RRKM calculations for the lifetimes of $Gly_3H^+ \cdot D_2$ as a function of internal ion energy and different binding energies of the D_2 tag. The two dotted lines correspond to the typical range ion times-of-flight in the present work.

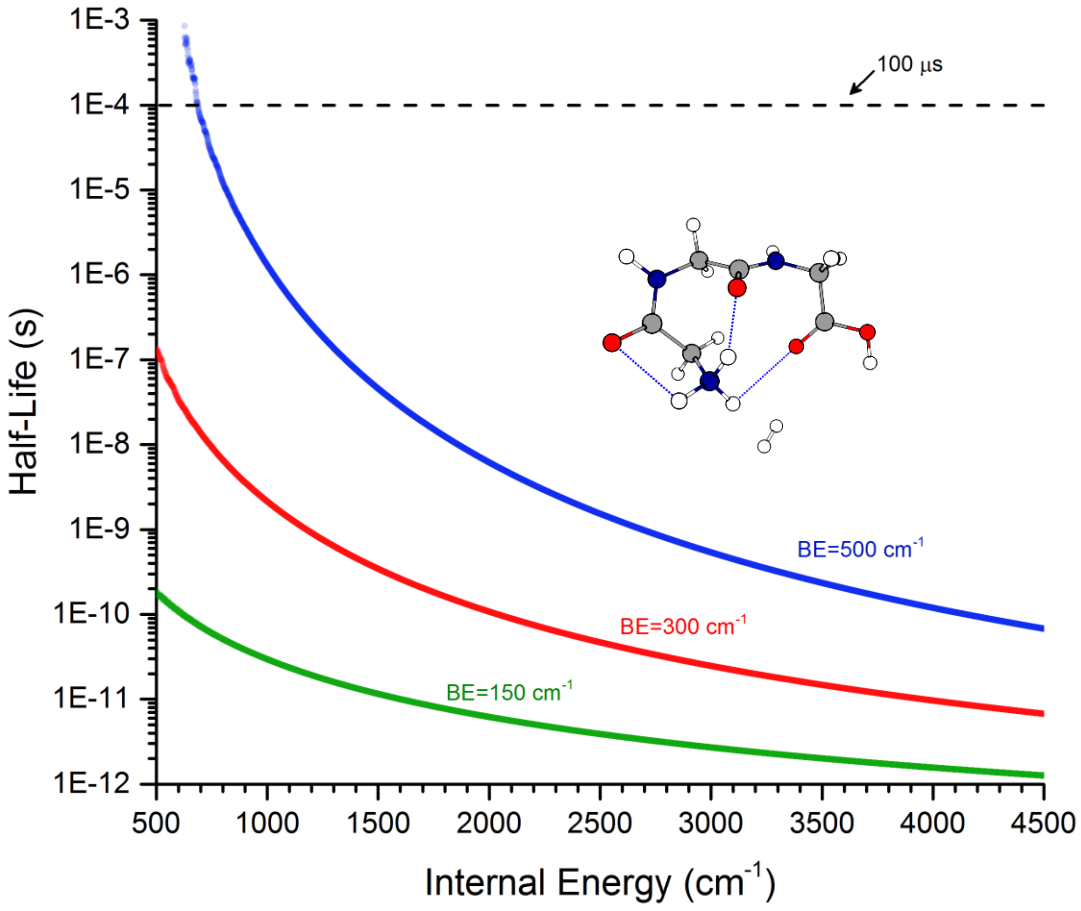

1.3.2 The Harmonic Oscillator Model and Vibrational Selection Rules

To help interpret experimental spectra, energies of molecular vibrations can be calculated. To simplify this process, atoms bonded together are viewed as masses connected by a spring. The internuclear potential energy therefore has the form

$$V(r) = \frac{1}{2}k(r - r_e)^2 + \frac{1}{6}\gamma(r - r_e)^3 + \cdots \quad \text{(eq. 1.3.4)}$$

where k and γ are force constants and $(r\text{-}r_e)$ is the change in bond length from the equilibrium bond length (r_e). If the vibrations under consideration have small nuclear displacements, i.e. are fundamental modes, then the higher order terms become negligible. Thus, the potential energy depends on only the quadratic (harmonic) term and can be written as

$$V(r) = \frac{1}{2}k(r - r_e)^2 \quad \text{(eq. 1.3.5)}$$

This potential term can be substituted into the Schrödinger equation,

$$\left(-\frac{\hbar^2}{2\mu}\frac{\partial^2}{\partial r^2} + \frac{1}{2}k(r - r_e)^2\right)\Psi(r) = E\Psi(r) \quad \text{(eq. 1.3.6)}$$

Where $\hbar$ is Planck's constant divided by 2π and μ is the reduced mass of the bonded atoms given by

$$\mu = \frac{m_1 m_2}{m_1 + m_2} \quad \text{(eq. 1.3.7)}$$

Rearrangement of eq 1.3.6 gives

$$\frac{\partial^2}{\partial r^2}\Psi(r) + \frac{2\mu}{\hbar^2}\left(E - \frac{1}{2}k(r - r_e)^2\right)\Psi(r) = 0 \qquad \text{(eq. 1.3.8)}$$

Solving this second order differential equation works only for quantized values and gives vibrational energy levels described by

$$E_v = \frac{h}{2\pi}\left(\frac{k}{\mu}\right)^{1/2}\left(v + \frac{1}{2}\right) \qquad v = 0, 1, 2, \cdots \qquad \text{(eq. 1.3.9)}$$

Where *v* is the vibrational quantum number. This equation is written more simply as

$$E_v = hv\left(v + \frac{1}{2}\right) \qquad \text{(eq. 1.3.10)}$$

where ν is the oscillator frequency. The energy associated with a transition from a fundamental vibrational levels corresponds to the absorbed photon by

$$\Delta E_{0\to1} = \hbar\left(\frac{k}{\mu}\right)^{1/2} = h\upsilon_{photon} \qquad \text{(eq. 1.3.11)}$$

Therefore the frequency (in wavenumbers!) of the observed photon is

$$\tilde{\upsilon}_{photon} = \frac{1}{2\pi c}\left(\frac{k}{\mu}\right)^{1/2} \qquad \text{(eq. 1.3.12)}$$

Within the framework of the harmonic oscillator, selection rules required for a vibrational transition can be derived. The intensity of absorption is related to the transition dipole moment *(μ_v)* by

$$\mu_v = \langle \Psi_v | \vec{\mu} | \Psi_v' \rangle \qquad \text{(eq. 1.3.13)}$$

Where $\vec{\mu}$ is the molecular dipole moment, which can be expanded in terms of the *(r-r_e)* coordinates as

$$\mu_r = \mu_{r_e} + \left(\frac{\partial \mu_r}{\partial r}\right)(r - r_e) + \left(\frac{\partial^2 \mu_r}{\partial r^2}\right)(r - r_e)^2 + \cdots \qquad \text{(eq. 1.3.14)}$$

The vibrational wavefunctions have the form

$$\psi_v = N_v H_v e^{\frac{-\sqrt{\mu k}(r-r_e)^2}{2\hbar}} \qquad \text{(eq. 1.3.15)}$$

Where N_v is a normalization constant and H_v is a Hermite polynomial. By substituting these wavefunctions into eq. 1.3.13, it can be shown that the transition dipole moment, μ_v, is non-zero only when $\Delta v = \pm 1$. Furthermore, as a result of the $(\delta\mu/\delta r)_{re}$ term in eq. 1.3.14, absorptions only occur for vibrations which change the molecular dipole moment.

Since the harmonic oscillator has been used to model vibrations, any anharmonic modes such as overtones or combinations bands, are not predicted.[64,65] This is especially prevelant in strongly H-bonded systems, such as water clusters.[66] The deviation of the harmonic and Morse

potentials at high vibrational quanta or large internuclear separations are demonstrated in Figure 1.3.

Figure 1.3 The harmonic and Morse potentials with selected vibrational levels.

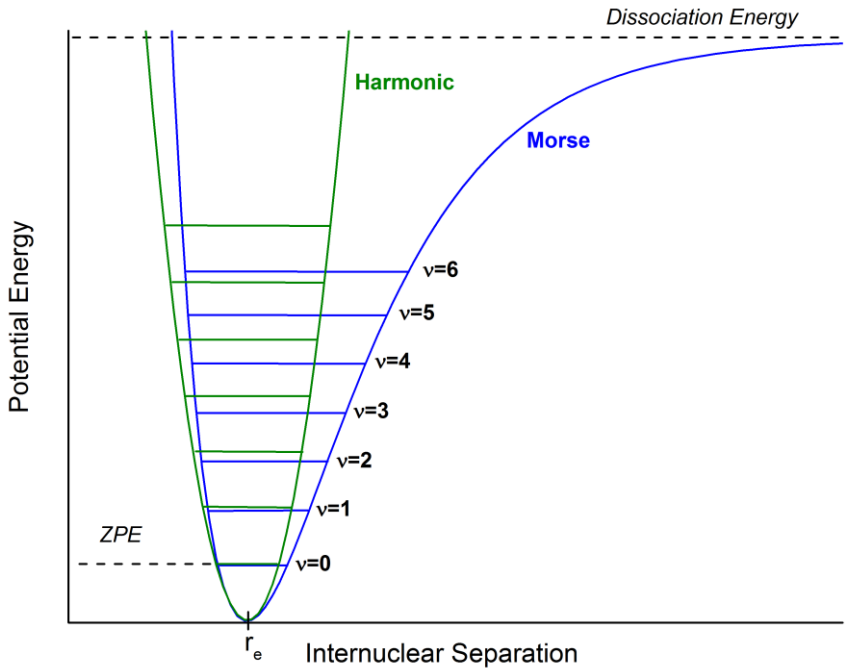

1.4 References

1. G. Carbone, J. Burnley, J.E. Moses . *Chem. Comm.* 2013, 49, 2759-2761. (A catalytic and *tert*-butoxide ion-mediated amidation of aldehydes with *para*-nitro azides)

2. Y. Wang, T.Y. Yu, H.B. Zhang, Y.C. Luo, P.F. Xu. *Angew. Chem. Int. Ed.* **2012**, 51, 12339-12342. (Hydrogen-Bond-Mediated Supramolecular Iminium Ion Catalysis)

3. H. Mandai, K. Fujii, H. Yasuhara, N. Abe, K. Mitsudo, T. Korenaga, S. Suga. *Nature Comm.* **2016**, 7, 11297. (Enantioselective acyl transfer catalysis by a combination of common catalytic motifs and electrostatic interactions.)

4. K.A. Dill. *Biochemistry*. **1990**, 29, 7133-7155.

5. D.A. Doyle, C.J. Morais, R.A. Pfuetzner, A. Kuo, J.M. Gulbis, S.L. Cohen, B.T. Chait, R. MacKinnon. *Science*. **1998**, 280, 69–77 (The structure of the potassium channel: molecular basis of K+ conduction and selectivity)

6. M. Fujitsuka, T. Majima. *Chem. Sci.* 2017, 8, 1752-1762. (Charge transfer dynamics in DNA revealed by time-resolved spectroscopy.)

7. P. Hobza. *Acc. Chem. Res.* **2012**, 45, 663-672. (Calculations on noncovalent interactions and databases of benchmark interaction energies.)

8. J.G. Brandenburg, M. Hochheim, T. Bredow, S. Grimme. *J. Phys. Chem. Lett.* **2014**, 5, 4275-4284.

9. O.F. Mohammed, O.H. Kwon, C.M. Othon, A.H. Zewail. *Angew. Chem. Int. Ed.* **2009**, 48, 6251-6256. (Charge transfer assisted by collective h-bonding dynamics)

10. C.A. Fuller, C.E. Finlayson. *Phys. Chem. Chem. Phys.* **2017**, 19, 31781-31787. (Solvatochromism in perylene diimides, exp and theory)

11. M. Rozenberg, A. Loewenschuss, Y. Marcus. *Phys. Chem. Chem. Phys.* **2002**, 2, 2699-2702. (An empirical correlation between stretching vibration redshift and hydrogen bond length.)

12. D. DianaNanova, S. Beck, A. Fuchs, T. Glaser, C. Lennartz, W. Kowalsky, A. Pucci, M. Kroeger. *Organic Electronics*. **2012**, 13, 1237-1244. (charge transfer in thin films of donor-acceptor complexes studied by IR)

13. K. Munroe, D.H. Magers, N.J. Hammer. *J. Chem. Phys. B.* **2011**, 115, 7699-7707. (Raman Spect. Signatures of noncovalent interactions between trimethylamine n-oxide and water)

14. M.B. Fitzpatrick, Y. Obara, K. Fujita, D.E. Brown, D.M. Dooley, T. Kohzuma, R.S. Czernuszewicz. *J. Inorg. Biochem*. **2010**, 104, 250-260. (Non-cov int. in blue copper protein pie-pie)

15. A. Sandip, S.A. Shelke, B. Gunnar, G.B. Sandholt, S.T. Sigurdsson. *Org. Biomol. Chem.* **2014**, 12, 7366-7374. (non covalent spin labeling dna rna by epr)

16. H.H. Lo, N.O. Gopal, S.C. Sheu, S.C. Ke. *J. Phys. Chem. C*, **2014**, 118, 2877–2884. (TiO2 epr charge transfer)

17. M.A. Nanny, J.M. Bortiatynski, P.G. Hatcher. *Environ. Sci. Technol*. **1997**, 31, 530-534 (non colvalent int between this and this C13 NMR)

18. D. Donghi, R.K. Sigel. *Methods Mol. Biol*. **2012**, 848, 253-273. (Metal ion rna interactions with NMR)

19. A.R. Johnson, E.E. Carlson. *Anal. Chem*. **2015**, 87, 10668-10678. (CID for natural products)

20. J.M. Wells, S.A. McLuckey. *Meth. Enzym.* **2005**, 402, 148-185. (CID of proteins)

21. M. Zhou, V.H. Wysocki. *Acc. Chem. Res.* **2014**, 47, 1010-1018. (Dissecting noncovalent interactions through SID)

22. S.R. Harvey, Y. Lie, W. Liu, V.H. Wysocki, A. Laganowski. *Chem. Commun.* **2017**, 53, 3106-3109.

23. M.S. Kim, A. Pandey. *Proteomics*. **2012**, 12, 530-542. (ETD MS in proteomics).

24. N.M. Riley, J.J. Coon. *Anal. Chem.* **2018**, 90, 40-64. (ETD in proteomics).

25. M.R. Robinson, J.M. Taliaferro, K.N. Dalby, J.S. Brodbelt. *J. Proteome Res.* **2016**, 15, 2739-2748. (UVPD)

26. J.P. O'Brien, W. Li, Y. Zhang, J.S. Brodbelt. *JACS*. **2014**, 136, 12920-12928. (UVPD)

27. H.S. Beeston, J.R. Ault, S.D. Pringle, J.M. Brown, A.E. Ashcroft. *Proteomics*. **2015**, 15, 2842-2850. (Protein structure HDX)

28. H.A. Cox, R.R. Julian, S.W. Lee, J. L. Beauchamp. *JACS*. **2004**, 126, 6485-6490. (HDX peptides)

29. B.C. Bohrer, S.I. Merenbloom, S.L. Koeniger, A.E. Hilderbrand, D.E. Clemmer. *Annual Rev. Anal. Chem*. **2008**, 1, 293-327. (Biomolecule Ion mobility.)

30. J.M. Dilger, S.J. Valentine, M.S. Glover, D.E. Clemmer. *Am. Soc. Mass Spectr.* **2013**, 24, 768-779. (IMS-MS)

31. A.N. Holding. *Methods*. **2015**, 89, 54-63. (XL-MS).

32. A.J. Sinz. *Mass Spectrom.* **2003**, 38, 1225-1237. (XL-MS)

33. B.F. Milne, Y. Toker, A. Rubio, S.B. Nielsen. *Angew. Chem. Int. Ed.* **2015**, 54, 2170-2173. (UV/VIS of chlorophyll)

34. S. Xu, J.E.T. Smith, M.J. Weber. *J. Chem. Phys.* **2016,** 145, 024304. (Rubpy UV/VIS)

35. N. C. Polfer, N.C.; Oomens, J. *Mass Spectrometry Reviews*, **2009**, 28, 468-494.

36. B. Chiavarino, M. E. Crestoni, S. Fornarini, D. Scuderi and J.-Y. Salpin, *Journal of the American Chemical Society*, **2013**, 135, 1445-1455.

37. Y.R. Luo. Comprehensive Handbook of Chemical Bond Energies, CRC Press, Boca Raton, FL, 2007

38. Y. Bouteiller, J.P. Perchard. *Chem. Phys.* **2004**, 305, 1-12.

39. J.P. Schermann. *Spectroscopy and Modeling of Biomolecular Building Blocks.* **2008**, 59-128.

40. E.G. Buchanan, W.H. James III, S.H. Choi, L. Guo, S.H. Gellman, C.W. Müller, T.S. Zwier. *J. Chem. Phys*. **2012**, 137, 09430

41. J.C. Dean, E.G. Buchanan, T.S. Zwier. *J. Am. Chem. Soc*. **2012**, 134, 17186-17201,

42. N.S. Nagornova, T.R. Rizzo, O.V. Boyarkin. *Angew. Chem., Int. Ed.* **2013**, 52, 6002-6005

43. T.D. Vaden, J.M. Lisy, P.D. Carnegie, E. Dinesh Pillai and M.A. Duncan. *Physical Chemistry Chemical Physics.* **2006**, 8, 3078-3082.

44. M.C. Thompson, J. Ramsay, J.M. Weber, *Angew. Chem. Int. Ed.*, **2016,** 55, 15171-15174

45. M. Z. Kamrath, E. Garand, P. A. Jordan, C. M. Leavitt, A. B. Wolk, M. J. Van Stipdonk, S. J. Miller and M. A. Johnson, *Journal of the American Chemical Society*, **2011**, 133, 6440- 6448.

46. C.J. Johnson, A.B. Wolk, J.A. Fournier, E.N. Sullivan, G.H. Weddle and M.A. Johnson, *The Journal of Chemical Physics*, **2014**, 140, 221101.

47. D.J. Wasylenko, C. Ganesamoorthy, B.D. Koivisto, M.A. Henderson, C.P. Berlinguette. *Inorg. Chem.* **2010**, 49, 2202-2209

48. K.J. Takeuchi, M.S. Thompson, D.W. Pipes, T.J. Meyer. *Inorg. Chem*. **1984**, 23, 1845-1851

49. M. Yamashita, J.B. Fenn,, *J. Phys. Chem.*, **1984,** 88, 4451-4459.

50. M. Yamashita, J.B. Fenn, *J. Phys. Chem.*, **1984,** 88, 4671-4675.

51. J.B. Fenn, M. Mann, C.K. Meng, S.F. Wong, C.M. Whitehouse, *Science*, **1989,** 246, 64-71.

52. A. Gomez, K.Q. Tang, *Physics of Fluids*, **1994,** 6, 404-414

53. S. Nguyen, J.B. Fenn, *Proceedings of the National Academy of Sciences of the United States of America*, **2007,** 104, 1111-1117.

54. J.V. Iribarne, B.A. Thomson, *J. Chem. Phys.*, **1976,** 64, 2287-2294.

55. M. Dole, L.L. Mack, R.L. Hines, R.C. Mobley, L.D. Ferguson, M.B. Alice, *J. Chem. Phys.*, **1968,** 49, 2240-2249.

56. L.L. Mack, P. Kralik, A. Rheude, M. Dole, *J. Chem. Phys.* **1970,** 52, 4977-4986.

57. L. Konermann, A.D Rodriguez, Liu, *J. Anal. Chem.*, **2012,** 84, 6798-6804.

58. M.T. Donor, S.A. Ewing, M.A. Zenaidee, W.A. Donald, J.S. Prell, *Anal. Chem.*,**2017,** 89, 9, 5107-5114

59. W.C. Wiley, I.H. McLaren, *Rev. Sci. Instrum.*, **1955,** 26, 1150-1157

60. B.A. Mamyrin, V.I. Karataev, D.V. Shmikk, V.A. *Zagulin, Zhurnal Eksperimentalnoi I Teoreticheskoi Fiziki*, **1973,** 64, 82-89

61. A.M. Rijs, J. Oomens, ijs, *J., Eds.*, **2015**, 364, V-VII.

62. A.B. Wolk, C.M. Leavitt, E. Garand, M.A. Johnson, *Acc. Chem. Res.*, **2014,** 47, 202- 210.

63. T. Beyer, D.F. Swinehart, *Commun. ACM*, **1973,** 16, 379

64. D.P. Tabor, R. Kusaka, P.S. Walsh, E.L. Sibert, T.S. Zwier, *The Journal of Physical Chemistry Letters*, **2015,** 6, 1989-1995.

65. P.D. Carnegie, A.B. McCoy, M.A. Duncan, *The Journal of Physical Chemistry A*, **2009,** 113, 4849-4854.

66. A.B. McCoy, *The Journal of Physical Chemistry B,* **2014,** 118, 8286-8294.

CHAPTER 2

Experimental Details

2.1 Overview

The experimental apparatus, which is shown in Figure 2.1, was built in the spring of 2013 and is based on the design of the photofragment spectrometer in the lab of Mark Johnson.[1,2] Since being built, the apparatus has undergone several modifications, which have increased the quality of data and have enabled more sophisticated experiments to be performed. First, the instrument was upgraded with a longer time-of-flight tube, which increased the resolution of the mass spectrometer. Second, an additional variable temperature ion trap was incorporated before the primary 10 K cold trap.[3] This additional trap is capable of forming solvated clusters and mediating gas-phase reactions. Finally, isomer-specific spectroscopy has been enabled through introduction of a second laser through the center ring electrode of the primary ion trap.[4]

All molecular ions discussed in later chapters were generated through electrospray ionization[5-7] of dilute solutions containing relevant precursor species. Ions were transferred into the instrument through a ~0.3 mm ID stainless steel capillary and were guided through three differentially pumped stages. In the third stage, ions were stored in an octopole trap mounted on the cold head of a liquid nitrogen cryostat. The ions were then extracted to into a 3D quadrupole (Paul) ion trap, which was held at 10 K by a closed-cycle helium cryocooler. A buffer gas consisting of helium and D_2 was pulsed into the trap in a short burst, which collisionally cooled ions and formed $M^+(D_2)_n$ adducts. Ions were extracted from this trap at 10 Hz into the time-of-flight region, where $M^+(D_2)_n$ species were mass-selected with a gated deflector. After mass gating, the ions were intersected with the output of a tunable OPO/OPA infrared laser, which induced photofragmentation and loss of D_2. The photofragment ions were separated in a two-stage reflectron and were directed to a multi-channel plate (MCP) detector. Monitoring the photofragment intensity as a function of laser wavelength yielded linear IR spectra.

Figure 2.1 Diagram of the homebuilt cryogenic ion infrared photofragment spectrometer. (A) Overhead view of the apparatus, with key components of the time-of-flight region labeled. (B) A close-up side view of the region outlined in green from panel A. Panel B shows the reaction and main trap regions in greater detail and also gives typical experimental operating pressures.

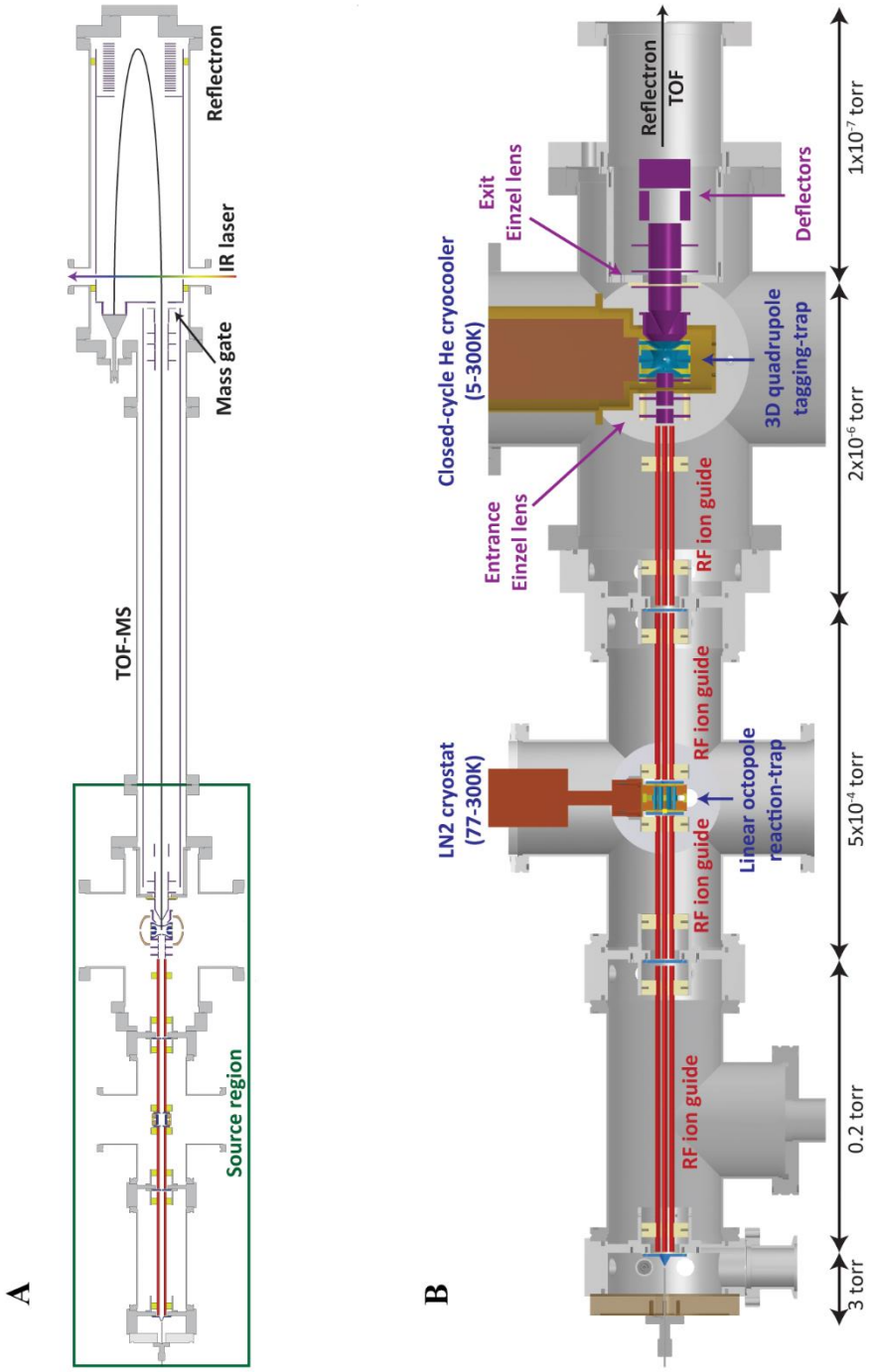

2.2 Ion Source

The ions studied in this thesis were generated by electrospray ionization of dilute solutions containing the relevant molecular precursors. The solutions were made with solvents including HPLC grade water, methanol, ethanol, or acetonitrile. The solutions were placed in a syringe (Hamilton) and were pushed through a 30 μm fused silica capillary (New Objective) at a rate of ~1-4 μL/min. The ions enter the instrument through a 10 cm stainless steel capillary (inner diameter of 0.3 mm), which is held in place by a compression fitting. This allows the entrance capillary to be easily removed and cleaned without venting the instrument. In the first vacuum region, the ions arrive at and pass through a 0.75 mm biased skimmer. Once through the skimmer, ions enter a second chamber and travel through hexapole ion guides powered by radio frequency (RF) supplies based on the design of O'Connor and coworkers.[8,9] The first and second chambers are pumped by 15 L/s mechanical pumps and have operating pressures of ~3 Torr and ~200 mTorr.

2.3 Reaction Trap Region

After passing through a floated aperture, the ions arrive in the reaction trap region. This stage is pumped by a 300 L/s turbomolecular pump and has a typical operating pressure of $2x10^{-4}$ Torr. In this region, ions are transferred through another hexapole guide and are collected and stored in a 2 cm long linear octopole ion trap powered by the same type of RF oscillator used for the other ion guides. Two 3.8 mm copper apertures provide entrance and exit potentials for the trap. A static DC voltage is applied to the entrance aperture while the exit aperture switches between high and low potentials to either stop or extract ions. The entire trap assembly is mounted to a liquid nitrogen cryostat (VPF-100, Janis Research Company) and is capable of reaching temperatures from 77-300 K. The trap is electrically isolated by a 1 mm thick piece of thermally

conductive ceramic (Precision Ceramics). The trap temperature is controlled with a 50 W cartridge heater and is monitored with a silicon diode.

A solenoid pulsed valve is connected to the reaction trap by a short polytetrafluoroethylene (PTFE) tube and introduces short bursts of buffer gas (helium or nitrogen), which helps to slow down and collisionally cool ions. When a few drops of solvent are seeded into the gas line, sufficient solvent vapor is introduced to the trap to cause clustering around trapped ions as they thermalize. Experimental parameters such as applied electric potentials, reaction trap timings, buffer gas pressure, and buffer gas pulse duration can be adjusted to control the extent clustering. Care must be taken when introducing solvent in this manner as the trap is prone to icing. An example of solvation of protonated diglycine by water is shown in Figure 2.2.

2.4 Tagging Trap Region

When released from the reaction trap, ions travel through a set of hexapole guides and are focused by a set of cylindrical einzel lenses into a 3D quadrupole "tagging" trap (Jordan TOF). The trap design is based upon the work of Kamrath[2] and Wang.[10] This region of the instrument has an operating pressure of $1x10^{-6}$ Torr and is pumped by an 800 L/s turbomolecular pump. The trap is mounted to the second stage of a closed-cycle helium cryocooler (Janis Research Company) and has 1.5 W of cooling power at 4.2 K. The trap is capable of being heated from 4-300 K by a 50 W cartridge and the temperature is monitored by a silicon diode. The cryocooler is attached to the vacuum chamber by a linear translation stage (McAllister Technical Services), which allows the trap height to be changed as thermal expansion occurs. The entire trap assembly is housed within an aluminum radiation shield to ensure maximum cooling is achieved. A solenoid pulsed valve is attached to the trap by PTFE tubing, which introduces short bursts of 10% D_2 in helium

Figure 2.2 Mass spectra of $GlyGlyH^+$ with water seeded in a He buffer gas with the reaction trap at 300 K (A) and 80 K (B-E). As the pressure of the buffer gas increases, the number of water adducts formed also increases.

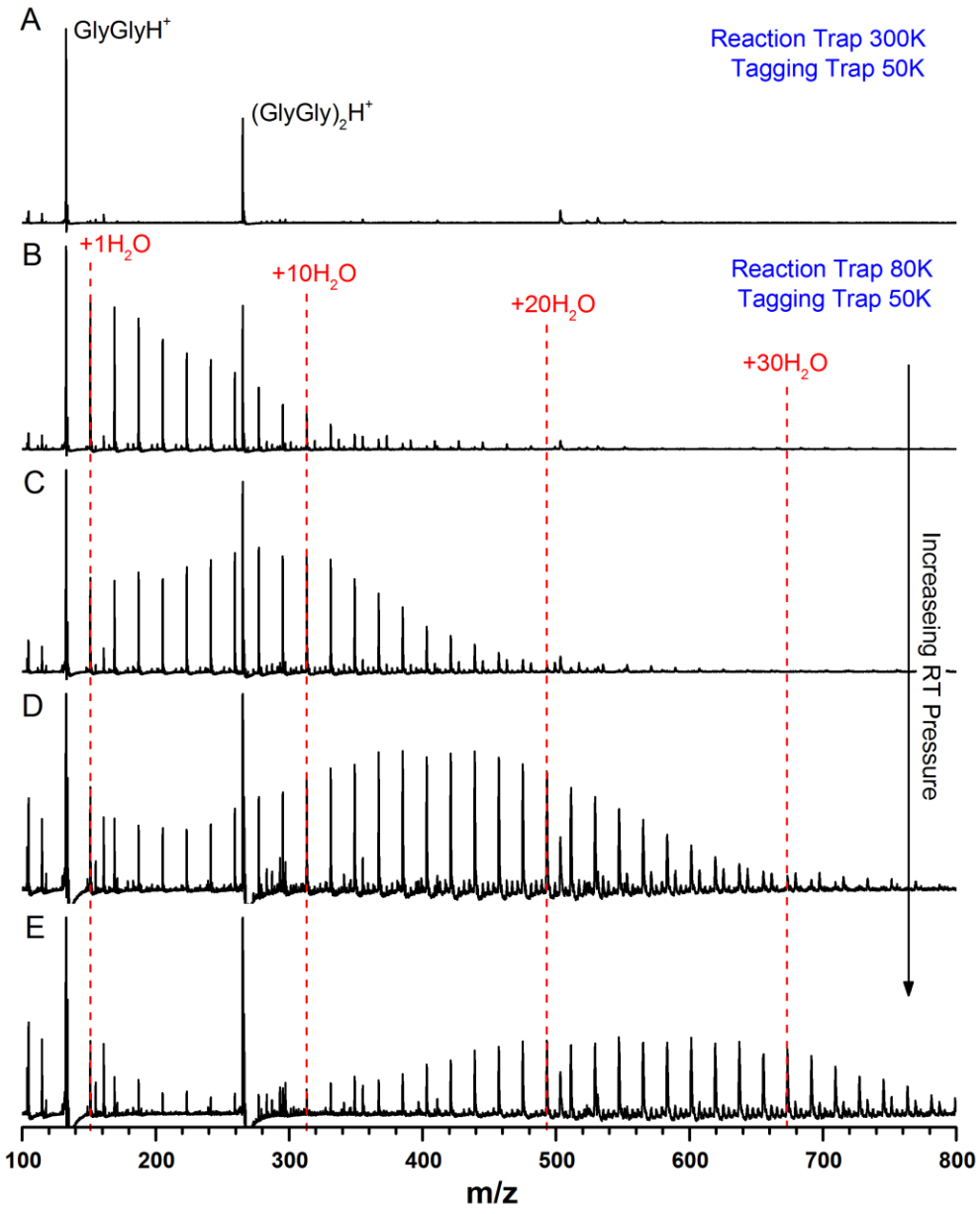

to the trap. When the trap is held at 10 K, ions are sufficiently and quickly cooled and form weakly bound D_2-tagged complexes, which serve as the parent species for predissociation spectroscopy. Figure 2.3 shows a mass spectrum that demonstrates D_2 tagging of protonated glycine.

The 3D quadrupole trap is chosen since it can be simply coupled to a time-of-flight mass spectrometer. After tagging has occurred, the trap RF voltages are turned off and the two trap end cap voltages are pulsed, acting as Wiley-McLaren type plates.[11] This quickly and effectively extracts ions from the trap and accelerates them into the TOF region.

2.5 Time-of-Flight Region

After leaving the trap, the ions move through a grid electrode held at the TOF liner voltage (~1950 V) as well as a 3 mm aperture. This stage of the instrument is pumped by a 300 L/s turbomolecular pump and has an operating pressure of $1x10^{-7}$ Torr. The first section of the TOF region is ~1m long and contains einzel lenses and deflectors at both ends. The deflectors at the back end are pulsed and act to mass select D_2-tagged ions at specific m/z for vibrational predissociation spectroscopy. Shortly after being mass selected, tagged ions are intersected with the output from a tunable OPO/OPA laser system pumped by 1064 nm light from a Nd:YAG laser. Vibrational energy is transferred to the D_2 molecule on a short enough timescale that photofragmentation occurs prior to the dual-stage reflectron (Jordan TOF). In the reflectron,[12] photofragments are separated from any remaining tagged complexes and are directed to a pair of microchannel plates (MCPs). Monitoring the photofragment peak intensity as a function of laser wavelength yields a linear IR spectrum. Figure 2.4 shows mass-selected tagged ions with and without resonant IR absorption. Figure 2.5 illustrates the type of spectrum that is gathered by monitoring the amount of photofragmentation as the laser frequency is varied.

Figure 2.3 Mass spectra of protonated glycine ions, $GlyH^+$, at 10 K in the absence (top) and presence (bottom) of D_2 gas.

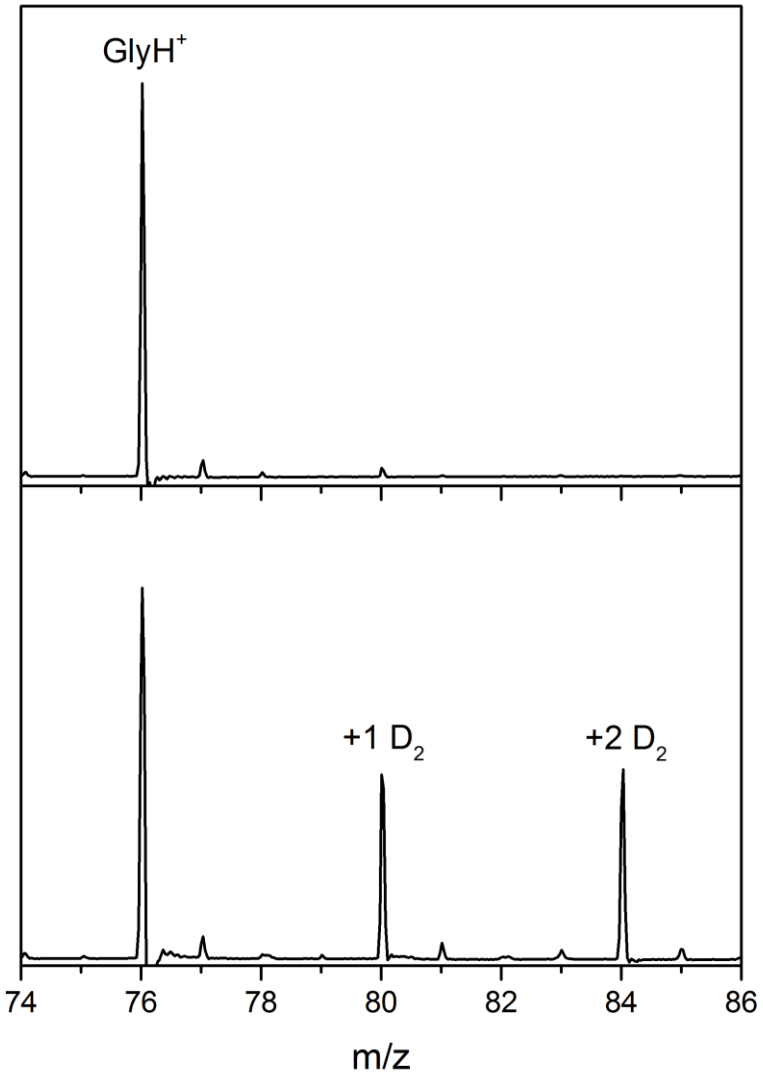

Figure 2.4 Mass spectra of $GlyH^+ \cdot (D_2)$ without resonant IR absorption (top) and with IR resonance (bottom) showing formation of the $GlyH^+$ photofragment.

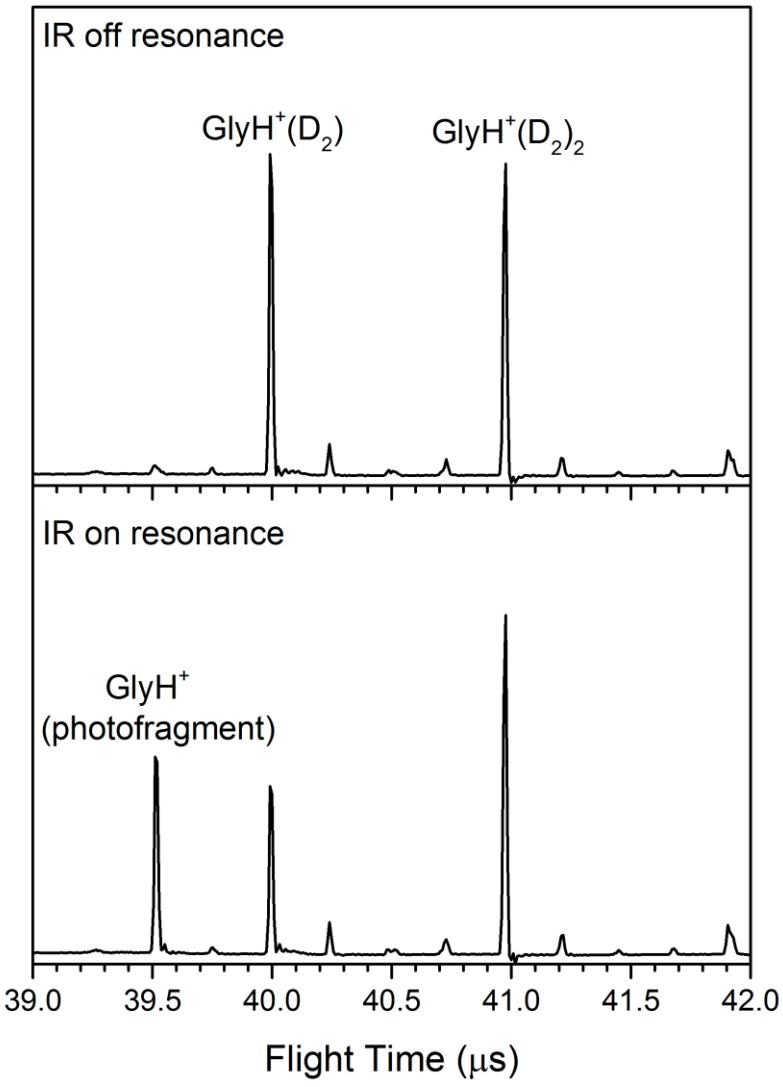

Figure 2.5 IR predissociation spectrum of $GlyH^+\cdot(D_2)$ obtained by monitoring $GlyH^+$ photofragment as laser is scanned between 1400 – 2000 cm^{-1} and 2800 – 3800 cm^{-1}.

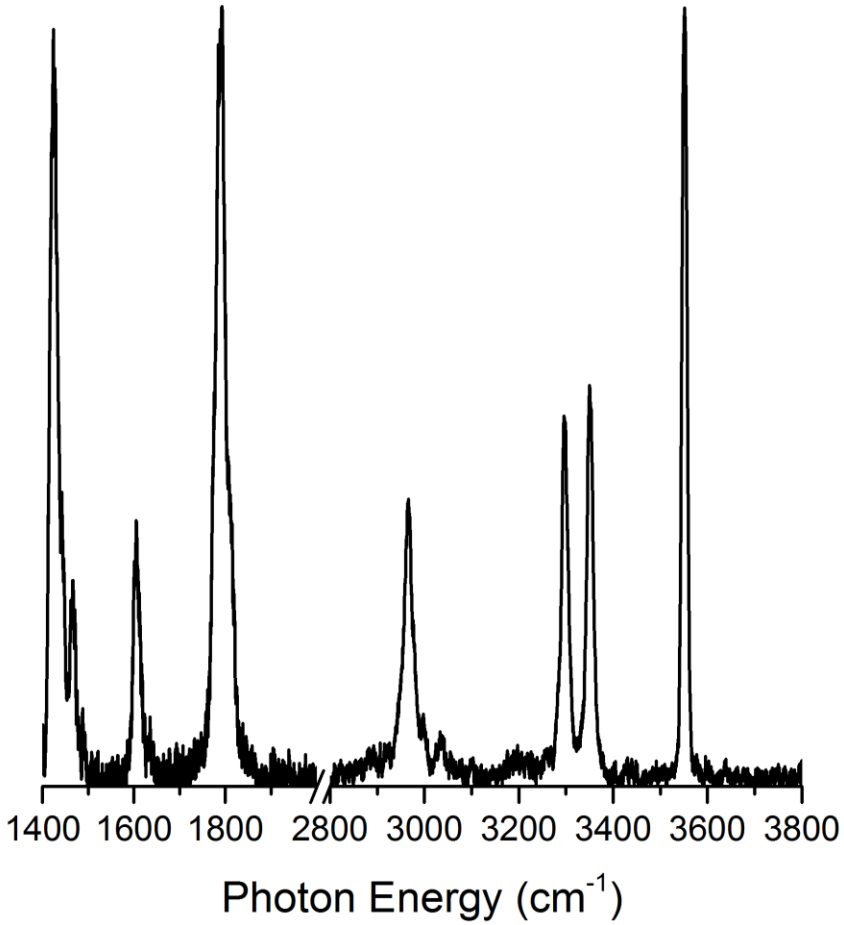

Figure 2.6 (A) Harmonic potentials for molecular oscillators, ν_1 and ν_2. Absorbed energy is transferred to the tag via internal vibrational redistribution. The dashed line designates the minimum amount of energy necessary for D_2 loss to occur. (B) Double resonance IR-IR spectrum. (C) Mass spectra showing photofragment enhancement from resonant probe laser (black trace) and dipped signal from resonant pump laser (grey). It's apparent the photofragment intensity from only the probe laser corresponds to the baseline of the IR-IR spectrum.

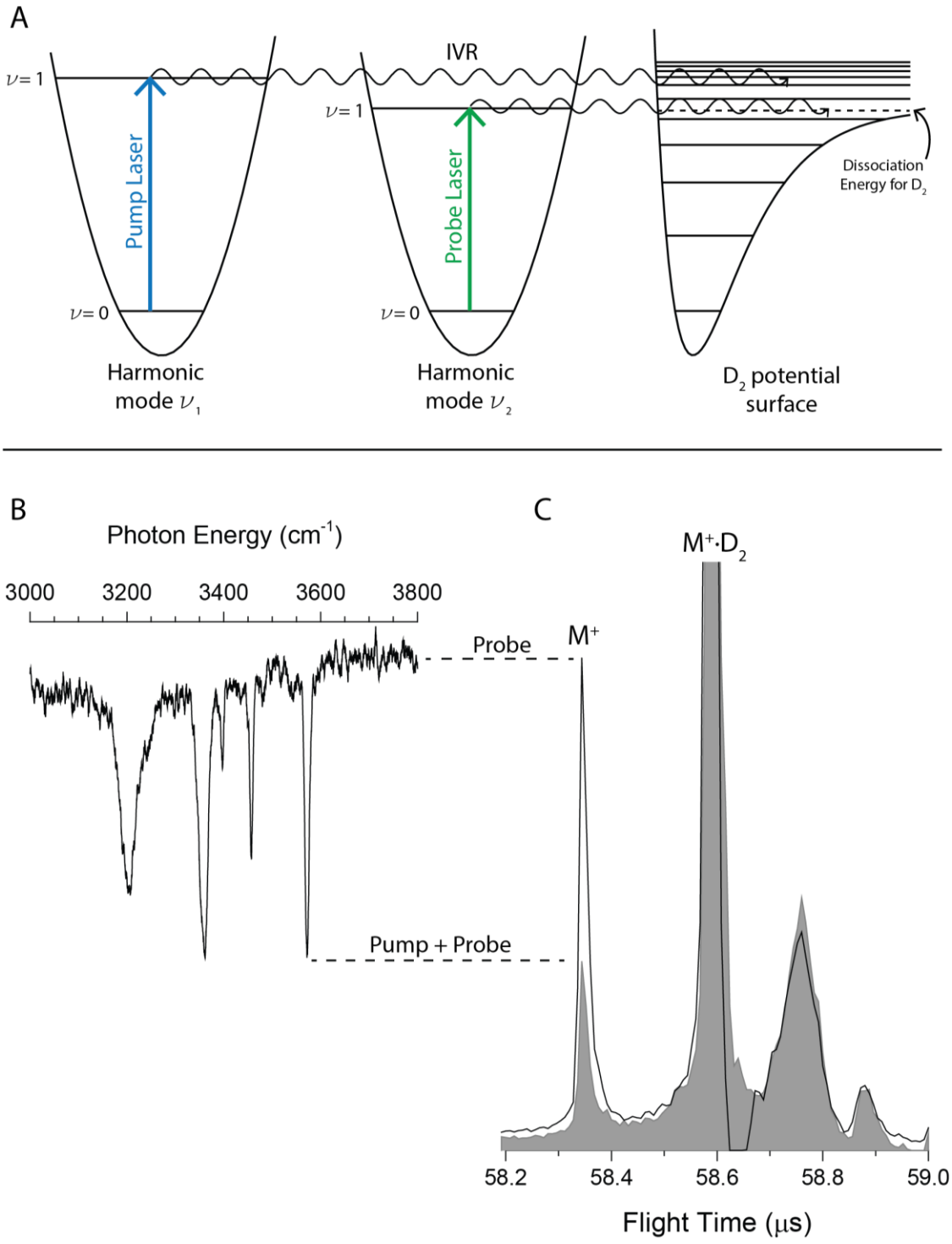

2.6 IR-IR Double-Resonance

Double-resonance depletion spectroscopy is used to obtain conformation specific IR spectra.[4,13-16] A schematic for this spectroscopic process is given in Figure 2.6. The TOF probe laser is fixed to a specific IR transition and the energy absorbed is redistributed such that the complex exceeds the minimum threshold for D_2 dissociation. The pump laser is pulsed into the main trap before the ions are released into the TOF region. When the pump laser is resonant with a transition belonging to the same structure as the probed transition, internal vibrational redistribution occurs within the trap and the D_2 tag is lost prior to ion ejection. The loss of tagged species causes a depletion in the monitored TOF photofragment signal. The resulting dip spectrum directly yields the IR transitions of the structure(s) giving rise to the probed transition.

2.7 Laser System

The IR light used to photodissociate ions in the tagging trap and TOF region is generated by two identical laser systems. Each is comprised of a Continuum Powerlite neodymium:yttrium aluminum garnet (Nd:YAG) laser and a LaserVision optical parametric oscillator and optical parametric amplifier (OPO/OPA). The Nd:YAG laser pumps 1064 nm light at 10 Hz into the OPO/OPA, which generates IR light tunable from 600 cm^{-1} to 4500 cm^{-1}.

The output of each laser system is guided through an N_2-purged enclosure, which minimizes power losses due to ambient CO_2 and H_2O absorption. The output from the “probe” laser system is focused by a set of spherical mirrors and is directed towards the TOF region by a periscope. Just before entering the instrument through a KBr window, it is reflected by a third spherical mirror that focuses the beam for maximum overlap with the ion beam path. The output from the “pump” laser system is guided through a periscope towards the tagging trap chamber. It

is carefully focused into a KBr window and passes through the middle RF electrode of the 3D quadrupole trap to intersect tagged ions. The OPO/OPA generates light by splitting the 1064 nm (ω_o) light from the Nd:YAG laser into two beams. One of the beams passes through a $\lambda/4$ waveplate into a β-barium borate (BBO) crystal where second harmonic generation (SHG) occurs, producing 532 nm ($2\omega_o$) light. The 532 nm light is directed into an OPO stage comprised of two potassium titanyl phosphate (KTP) crystals in an optical cavity. In the OPO, the 532 nm functions as the pump frequency (ω_p) and by second-order nonlinear optical processes is converted into two lower energy waves described by

$$\omega_p = \omega_s + \omega_i \qquad \text{(eq. 2.1)}$$

where ω_s and ω_i are the signal and idler frequencies, respectively. The signal, which is higher in frequency, ranges anywhere from 710 – 880 nm, while the idler ranges from 1350 – 2120 nm. The signal frequency is recombined with the remaining 1064 nm light in the OPA stage, which consists of four KTP crystals. Here, the signal ω_s and the 1064 nm light undergo a difference-frequency generation (DFG) process described by

$$\omega_{mid} = \omega_s - \omega_o \qquad \text{(eq. 2.2)}$$

where ω_{mid} is 2000 – 4500 cm^{-1}. When only mid IR light is desired, the residual 1064 nm light is dumped from the beam and the idler frequency is removed by a polarized filter. Power in this region is measured at 3900 cm^{-1} and is typically around 30 mJ/pulse.

Figure 2.7 Pump laser and OPO/OPA setup

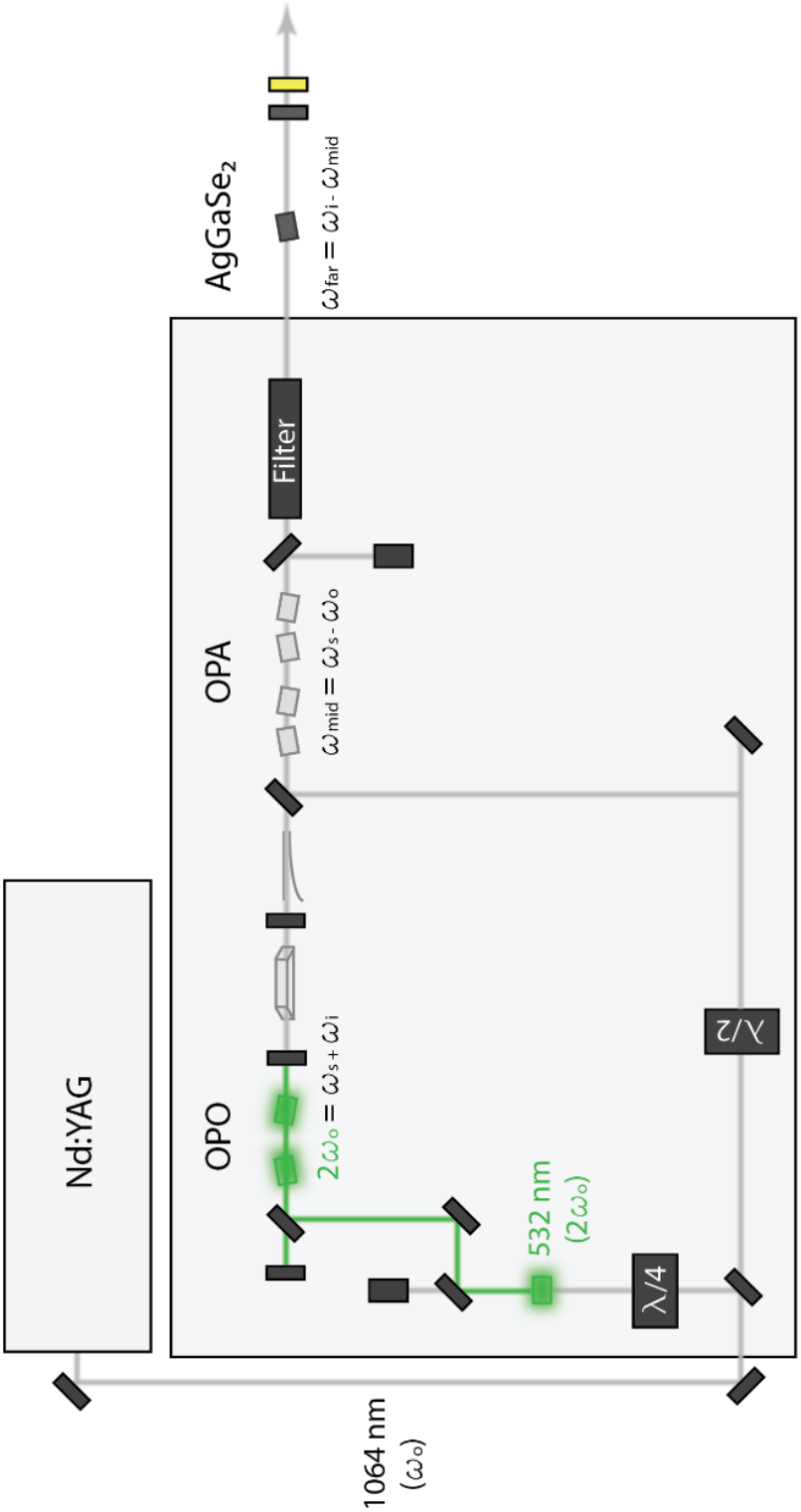

In order to access the far IR region, from 600 cm^{-1} to 2400 cm^{-1}, removal of the polarized filter just after the OPA stage is required. With this filter removed, the idler light is mixed with the ω_{mid} in an additional $AgGaSe_2$ crystal to create far IR light by the DFG process

$$\omega_{far} = \omega_i - \omega_{mid} \quad \text{(eq. 2.3)}$$

Unwanted residual light from this mixing process is removed directly after the $AgGaSe_2$ crystal with either a ZnSe filter for the 1400 cm^{-1} to 2400 cm^{-1} range or a 5.5 micron filter for the 600 cm^{-1} to 1800 cm^{-1} range. Power for these spectral regions is significantly lower than that of the mid IR range, with typical powers at 1594 cm^{-1} of 2.0 mJ/pulse and 1.5 mJ/pulse for the ZnSe or 5.5 micron filter, respectively. It should be noted that since there is no compensator crystal after the $AgGaSe_2$ crystal, the beam moves substantially in space at the highest and lowest wavelengths of this region.

2.8 Data Acquisition

The signal (photofragment intensity versus time-of-flight) from the MCP detector is amplified and measured by a 100 MHz digital oscilloscope (PicoScope), which is capable of recording mass spectra at the 10 Hz experimental timescale. From the oscilloscope, the signal is routed to a computer where it is displayed and recorded by a homemade LabView (National Instruments) data acquisition (DAQ) program, which was written by Brett M. Marsh (PhD 2015) and later modified by Steven J. Kregel. This program allows the incoming signal from the digital oscilloscope to be adjusted to reflect the data displayed on the stand-alone oscilloscope (Tetronix) and is capable of recording MS or IR data.

For recording mass spectral data, a file path must first be designated with the MS mode enabled. After an integer value is chosen for the number of MS traces to be recorded, the program is then run. Once running, the trigger delay (μs), sample window width (μs), and range (V) can be adjusted. Once the desired settings are achieved, the data is collected by clicking the acquire button. Once all of the MS traces are recorded, the program automatically stops running.

For recording infrared predissociation spectra, a file path must be designated, the IR mode must be enabled, and the number of desired scans should be set. In order to communicate correctly with the OPO/OPA software, the IR range to be collected must be designated (mid or far). It is also necessary to specify the starting and ending wavelengths (in near-IR wavenumbers). Conversion from the near IR to mid and far IR is found by

$$\tilde{\nu}_{mid} = \tilde{\nu}_{near} - 9394\ cm^{-1} \qquad \text{(eq. 2.4)}$$

$$\tilde{\nu}_{far} = 28182\ cm^{-1} + 2\tilde{\nu}_{near} \qquad \text{(eq. 2.5)}$$

It is also necessary to specify the scan rate for the laser system. Typical scan rates for the mid and far regions are 3 cm^{-1}/sec and 0.75 cm^{-1}/sec, respectively. When all of this information is entered, the program can be run. Once running, the trigger delay, sample window, and range can be adjusted as desired. Once the acquire button is pressed, the DAQ program communicates with the OPO/OPA computer system, which automatically scans the specified frequency range. During the scan, the DAQ program records mass spectra as a function of laser wavelength. Additionally, an on-the-fly spectrum is generated by monitoring the photofragment intensity associated with vibrational excitation. At the end of a scan, the OPO/OPA computer brings the laser system back

to the starting position. If the number of scans collected is less than that initially requested, a new file is created and another scan begins.

2.9 Data Processing

The files generated by the DAQ program can be processed with a separate LabView processing program (also written by Brett M. Marsh). For MS data, the program combines the designated amount of scans and creates an averaged mass spectrum (ion intensity versus time-of-flight). The data processing program saves the composite spectrum as a ".dat" file.

In order to generate an IR spectrum, a few additional settings in the processing program must be specified. The start and end wavelengths (near IR), an interpolation value (usually 1/10 the laser scan rate), a value for shots-per-point, the integration range corresponding to the photofragment, and the display frequency (near, mid, far) are selected. Once the program is run, a plot of photofragment intensity versus laser frequency is generated.

Some spectral features are not adequately resolved given the signal-to-noise ratio of a single IR scan. Therefore, it is often appropriate to average multiple scans together using the data processing program. The program interpolates scans on an individual basis, prompting the user to select files to be analyzed and averaged together. Anywhere from 10-30 scans are typically necessary to achieve satisfactory signal-to-noise ratios in the mid and far-IR regions.

2.10 Experimental Timings

In order to carry out successful predissociation experiments, which occur at 10 Hz, it is necessary to coordinate precise pulse valve, ion extraction, and laser timings. The experimental timing scheme is outlined below in Figure 2.8. The sequence begins when the pulse valve of the

main tagging trap is triggered by the T_0 output of a delay generator (DG1). All other experimental timings are referenced to T_0 from DG1, and the following triggering scheme is discussed in an order that corresponds to the ion path through the instrument.

The reaction trap timings are controlled by a second delay generator (DG2), which sets the timings for the pulse valve and trap exit apertures (high and low voltages). The duration of time ions spend in the main trap (typically around 95 ms) is determined by channel A of DG1. At this time, the RF voltages in the main trap are turned off, which causes the RF power supply to send a TTL signal to a third delay generator (DG3). DG3 controls the timings of the main trap end caps (Wiley McLaren 1 and 2), the mass gate, and the TOF laser Q-switch. The mass gate timings are adjusted to select the desired tagged species. The Q-switch timing is set to give the best temporal overlap with tagged complexes, which typically occurs 0.4-1.5 μs after the mass gate trigger. Furthermore, it is important to note that the flashlamps' timing is adjusted to ensure no more than 6 W of power is output from the YAG pump laser.

In an IR-IR double resonance experiment, another laser is focused into the tagging trap. The triggers for the flashlamps and Q-switch occur ~5 ms before the main trap RF voltages are turned off and ions are extracted. The ~90 ms before the laser pulse allows ample time for removal of the buffer gas from the trap volume prior to ion–laser interactions, ensuring no additional cooling and formation of D_2-adducts is possible afterwards.

Figure 2.8 Schematic of experimental times for an IR-IR double resonance experiment in positive ion mode.

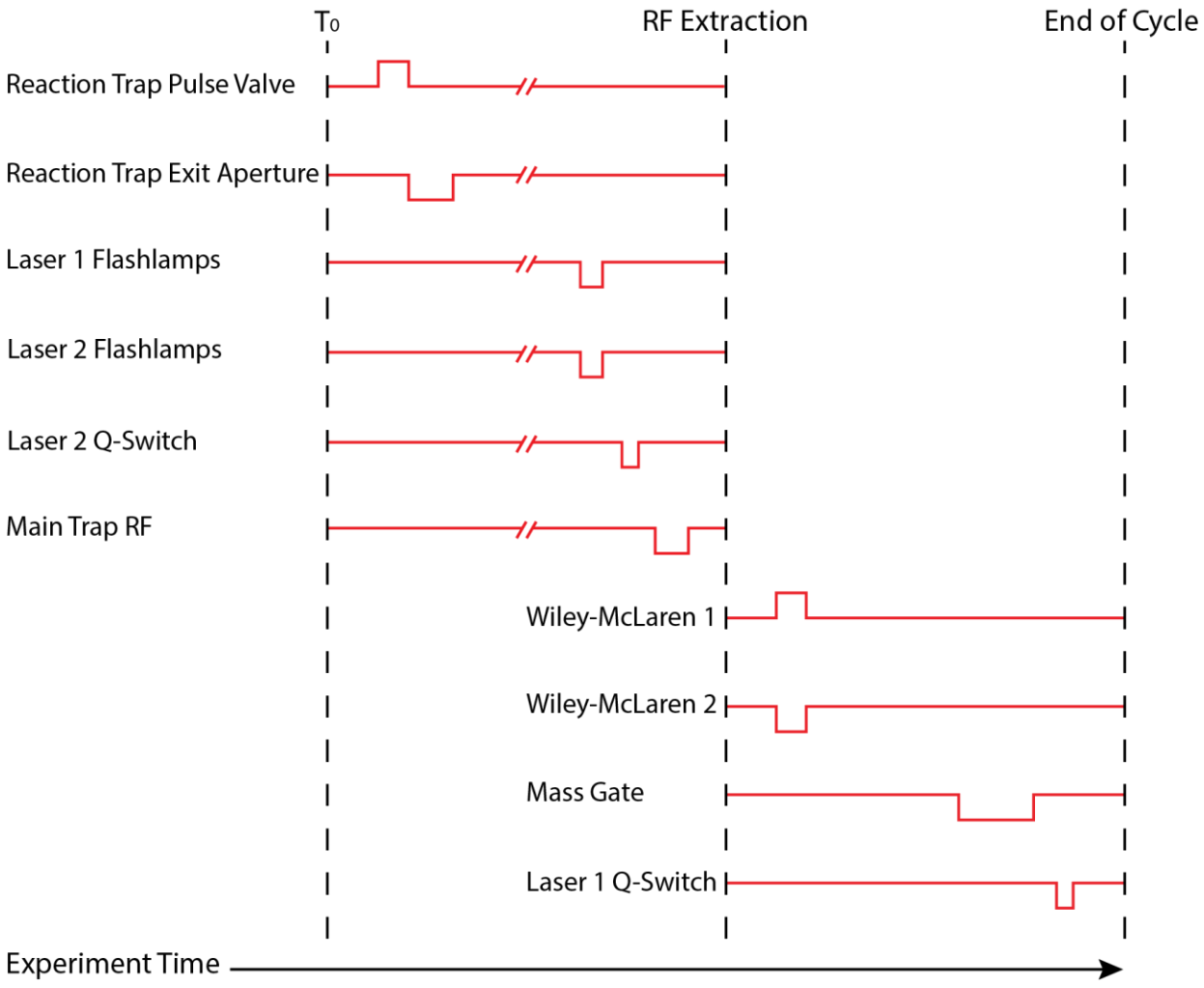

Table 2.1 Sample timings for IR-IR double resonance / dual trap experiment.

Delay Generator 1 (DG1)	**Channel**	**Timing**
Main Trap Pulse Valve	T_0	-
Main Trap RF	A	T_0 + 95 ms
Laser 1 Flash Lamps Delay	C	A – 263 μs
Laser 1 Flash Lamps Width	D	C + 10 μs
DG2 (Triggered by T_0)	**Channel**	**Timing**
Reaction Trap High	A	7.0 ms
Reaction Trap Low	B	A + 0.900 ms
Reaction Trap Pulse Valve	C	25.0 ms
DG3 (Triggered by Main Trap RF)	**Channel**	**Timing**
Wiley-McLaren (WMC) 1 (Low)	A	0 + 500 ns
WMC 1 (High)	B	A + 500 ns
WMC 2 (Low)	C	0 + 500 ns
WMC 2 (High)	D	C + 500 ns
Mass Gate (High)	E	0 + 29.24 μs
Mass Gate (Low)	F	E + 200 μs
Laser 1 Q-Switch (Delay)	G	0 + 29.77 μs
Laser 1 Q-Switch (Width)	H	G + 10 μs
DG4 (Triggered by T_0)	**Channel**	**Timing**
Laser 2 Q-Switch Delay	A	T_0 + 94 ms
Laser 2 Q-Switch Width	B	A + 10 μs
Laser 2 Flashlamp Delay	C	A – 284 μs
Laser 2 Flashlamp Width	D	C + 10 μs

2.11 Voltage Settings

The voltages applied to the various stages of the instrument generally decrease in magnitude from the capillary entrance to the main tagging trap. The voltages in various regions are used to achieve different experimental techniques. For example, the RF1 bias voltage can be increased to induced ion fragmentation in the early high-pressure stages of the instrument. On the other hand, reaction trap biases can be lowered to "soften" trapping conditions for the formation of large solvated clusters. Likewise, the main trap voltages can be used to vary the amount of tagging. These experimental voltages change subtly on a daily basis, and may change considerably depending on the species being studied. Typical voltages used are show in Table 2.2.

Table 2.2 Table of adjustable voltages supplied to the instrument during operation for positive ions. Items in ***bold italics*** correspond to voltages in the TOF region.

Power Supply	Applied Voltage	Power Supply	Applied Voltage
ESI	+ 2.5 kV	RF 3 Amplitude	+ 3.88 V
Capillary	+ 111.7 V	RF 4 Amplitude	+ 3.98 V
Skimmer	+ 111.8 V	RT RF Amplitude	+ 4.02 V
RF1	+ 73.6 V	Main Trap Amplitude	+ 0.60 V
Aperture 1	+ 67.1 V		
RF2	+ 66.5 V	***MCP***	***- 4.5 kV***
RT Entrance	+ 65.3 V	***WMC 1***	***+ 56 V***
RT Bias	+ 58.5 V	***WMC 2***	***- 351 V***
RT Exit High	+ 72.8 V	***Liner***	***- 1900 V***
RT Exit Low	+ 37.5 V	***Focus 1***	***0 V***
RF3 Bias	+ 50.1 V	***Deflector L/R 1***	***- 1950 V***
Aperture 2	+ 150.0 V	***Deflector U/D 1***	***-1570 V***
RF 4 Bias	+ 37.5 V	***Focus 2***	***- 492 V***
Einzel 1&3	- 22.9 V	***Deflector L/R 2***	***- 1900 V***
Einzel 2	+ 40.8 V	***Mass Gate 1***	***- 2000 V***
Main Trap Bias	+ 39.6 V	***Mass Gate 2***	***- 580 V***
RF 1 Amplitude	+ 4.57 V	***Reflectron 1***	***- 1181 V***
RF 2 Amplitute	+ 4.48 V	***Reflectron 2***	***+ 140 V***

2.12 References

1. M.Z. Kamrath, E. Garand, P.A. Jordan, C.M. Leavitt, A.B. Wolk, M.J. Van Stipdonk, S.J. Miller and M.A. Johnson, *Journal of the American Chemical Society,* **2011,** 133, 6440-6448.

2. M.Z. Kamrath, R.A. Relph, T.L. Guasco, C.M. Leavitt and M.A. Johnson *International Journal of Mass Spectrometry,* **2011,** 300, 91-98.

3. B.M. Marsh, J.M. Voss, E. Garand, *J. Chem. Phys.,* **2015,** 143, 204201.

4. J.M. Voss, S.J. Kregel, K.C. Fischer, E. Garand, *Journal of The American Society for Mass Spectrometry,* **2018,** 29, 42-50.

5. M. Yamashita, J.B. Fenn, *J. Phys. Chem.,* **1984,** 88, 4451-4459.

6. M. Yamashita, J.B. Fenn, *J. Phys. Chem.,* **1984,** 88, 4671-4675.

7. J.B. Fenn, N. Mann, C.K. Meng, S.F. Wong, C.M. Whitehouse, *Science,* **1989,** 246, 64-71.

8. P.O'Connor, C. Costello, W. Earle, *J. Am. Soc. Spectrom.,* **2002,** 13, 1370-1375.

9. R. Mathur, P.B. O'Connor, *Review of Scientific Instruments,* **2006,** 77.

10. X.-B. Wang, L.-S. Wang, *Review of Scientific Instruments,* **2008,** 79.

11. W.C. Wiley, I.H. McLaren, *Rev. Sci. Instrum.,* **1955,** 26, 1150-1157.

12. B.A. Mamyrin, V.I. Karataev, D.V. Shmikk, V.A. *Zagulin, Zhurnal Eksperimentalnoi I Teoreticheskoi Fiziki,* **1973,** 64, 82-89

13. E.G. Buchanan, W.H. James III, S.H. Choi, L. Guo, S.H. Gellman, C.W. Müller, T.S. Zwier. *J. Chem. Phys*. **2012**, 137, 09430

14. J.C. Dean, E.G. Buchanan, T.S. Zwier. *J. Am. Chem. Soc*. **2012**, 134, 17186-17201,

15. N.S. Nagornova, T.R. Rizzo, O.V. Boyarkin. *Angew. Chem., Int. Ed.* **2013**, 52, 6002-6005

16. J.M. Voss, K.C. Fischer, E. Garand, *Journal of Molecular Spectroscopy*, **2018,** 347, 28 - 34 (2018).

CHAPTER 3

Mass Spectrometric and Vibrational Characterization of Reaction Intermediates in $[Ru(bpy)(tpy)(H_2O)]^{2+}$ Catalyzed Water Oxidation

Published: J.M. Voss, E.M. Duffy, B.M. Marsh, and E. Garand. *ChemPlusChem*, 82, 691–694 (2017)

Abstract

Mass spectrometry coupled with an in-line electrochemical electrospray ionization source is used to capture some of the reaction intermediates formed in the $[Ru(bpy)(tpy)(H_2O)]^{2+}$ (bpy=2,2'-bipyridine, tpy=2,2':6',2"-terpyridine) catalyzed water oxidation reaction. By controlling the applied electrochemical potential, we identified the parent complex, as well as the first two oxidation complexes, identified as $[Ru(bpy)(tpy)(OH)]^{2+}$ and $[Ru(bpy)(tpy)(O)]^{2+}$. The structures of the parent and first oxidation complexes are probed directly in the mass spectrometer by using infrared predissociation spectroscopy of D_2-tagged ions. Comparisons between experimental vibrational spectra and density functional theory calculations confirmed the identity and structure of these two complexes. Moreover, the frequency of the O–H stretching mode in $[Ru(bpy)(tpy)(OH)]^{2+}$ shows that this complex features a Ru–OH interaction that is more covalent than ionic.

Author Contributions

JMV optimized the flow cell source; EMD synthesized the catalyst; JMV, EMD, and BMM acquired experimental spectra; EMD and EG performed theoretical calculations; JMV and EG performed data analyses; JMV, EMD, and EG wrote the manuscript.

3.1 Introduction

Studying reaction intermediates can provide fundamental insight into the mechanism of a chemical reaction. However, such key reaction species are typically present in only minor concentrations, necessitating a sensitive and selective probe, such as electrospray ionization mass spectrometry (ESI-MS).[1–8] MS identifies ions by their mass-to-charge (m/z) ratio, and with additional characterization tools such as collision-induced dissociation, can also provide some structural information. Coupling spectroscopic characterization with MS, by schemes such as infrared multiple photon dissociation (IRMPD),[9] UV+IR resonant photodissociation,[10] and cryogenic ion vibrational predissociation (CIVP),[11] can further provide rich and detailed structural information as well as benchmarks for theoretical methods used to characterize reaction processes. ESI can be easily adapted to directly probe different types of analytes.[12–17] Particularly, an in-line electrochemical (EC) cell can be coupled to an ESI source, such that intermediates and products formed under specific EC potentials can be sampled. Several examples of such EC-ESI experiments have been previously demonstrated.[18–21]

Herein, we present the application of an EC-ESI source to study the intermediates present in the electrochemical water oxidation reaction catalyzed by the mononuclear ruthenium complex[22–24] $[Ru(bpy)(tpy)(H_2O)]^{2+}$ (hereafter denoted as $[Ru(H_2O)]^{2+}$; bpy=2,2'-bipyridine, tpy=2,2':6',2"-terpyridine). This family of ruthenium complexes serves as a prototypical single-metal-center homogeneous water oxidation catalyst, and has been the subject of numerous studies.[4, 5, 22, 25–30] We show that we can selectively detect the first two oxidized complexes in the proposed catalytic cycle, shown in Figure 3.1, by controlling the applied EC potential. We further probed the structures of these mass-selected species directly in the mass spectrometer by CIVP. This combination of approaches allows us to directly capture and characterize complexes formed

Figure 3.1 (Top) Water oxidation involving the $[Ru(bpy)(tpy)(H_2O)]^{2+}$ complex. (Bottom) The structure of the $[Ru(bpy)(tpy)(H_2O)]^{2+}$ species. The hydrogen atoms on the bipyridine and terpyridine ligands have been omitted.

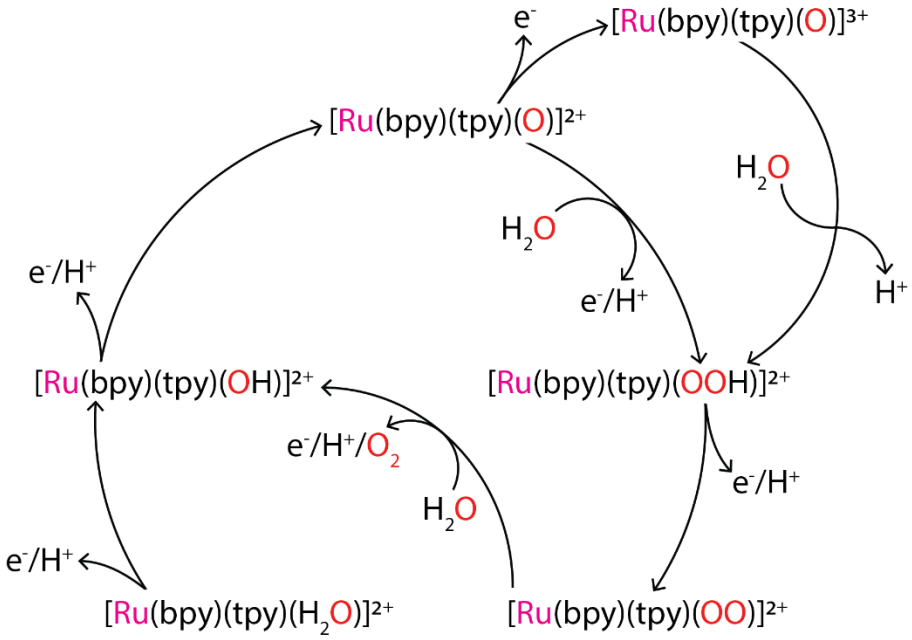

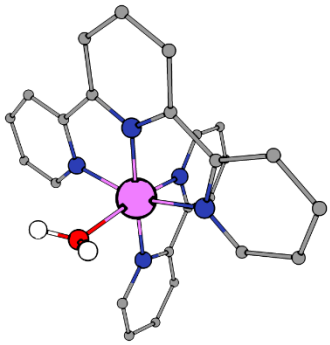

during the electrocatalytic process. Our results provide clear identification of the reaction species present as well as structural information of these complexes without any interference from unreacted catalysts, solvents, counterions, or temperature-related effects.

3.2 Experimental and Theoretical Details

Our homebuilt source is shown in Figure 3.2 and involves a commercial low volume EC flow cell (BASi) that is floated at the ESI voltage (~1 kV), similar to those by Johnson and van Berkel.[18,20] The EC potential applied is referenced to the ESI voltage, and is continuously adjustable between 0-2 V. For the $[Ru(H_2O)]^{2+}$ experiment, a millimolar aqueous solution of $[Ru(H_2O)](ClO_4)_2$ (synthesized according to literature methods[23,31]) with a phosphate buffer at pH 7 was pushed through the EC cell using a syringe pump. Glassy carbon served as the working electrode and the stainless steel block served as the counter electrode and a pseudo-reference electrode. A short electrospray silica tip at the output of the flow cell couples the EC cell to the time-of-flight mass spectrometer where charged species are isolated and identified via their mass-to-charge (m/z) ratio.

To obtain the IR spectra of ruthenium complexes inside the mass spectrometer, tagged $[Ru(L)]^{2+}\cdot(D_2)_n$ complexes were formed inside an ion trap held at 10 K by collisions with buffer gas containing 10% D_2 in helium. The tagged complexes were then mass-selected in the time-of-flight mass spectrometer and irradiated with the output of a tunable IR OPO/OPA laser system (Laservision). Resonant absorption of a single photon induced the evaporation of the weakly bound D_2 tags. Integration of the resulting photofragment signal as a function of laser wavelength yielded the IR spectrum. Due to experimental settings, such as tagging efficiency and mass-gating, the

Figure 3.2 Electrochemical ESI source used to generate $[Ru(H_2O)]^{2+}$ and intermediates. A key for the various components of the cell is given below.

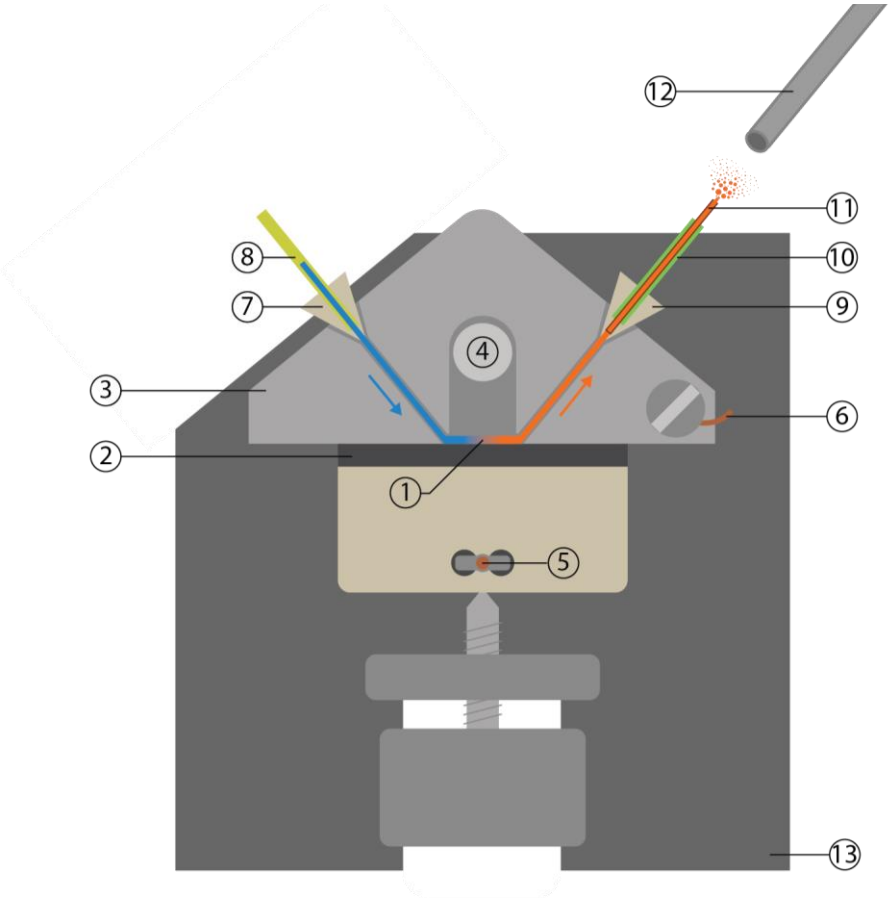

1. Electrochemical reservoir
2. Glassy carbon working electrode
3. Stainless steel housing (counter electrode)
4. Reference electrode reservoir
5. Working electrode lead (to 2 V supply)
6. Counter electrode lead (floated at ESI voltage)
7. Inlet union
8. Tubing from syringe
9. Outlet union
10. ESI capillary sleeve
11. ESI capillary tip
12. MS inlet
13. Cell mounting

doubly tagged $[Ru(H_2O)]^{2+}\cdot(D_2)_2$ and singly tagged$[Ru(OH)]^{2+}\cdot(D_2)$ complexes were probed with IR spectroscopy.

The geometry optimization and vibrational calculation of the $[Ru(H_2O)]^{2+}\cdot(D_2)_2$ and $[Ru(OH)]^{2+}\cdot(D_2)$ complexes are carried out using ORCA[32] at the B3LYP level with the def2-TZVP basis set for all atoms and an ECP treatment for Ru. The RIJCOSX approximation was used in the calculations, with the def2-TZVP/J auxiliary basis set. The vibrational frequency was calculated numerically. The vibrational frequencies were scaled by 0.98 in the 700–1700 cm^{-1} region and 0.96 in the 2800–3800 cm^{-1} region. The experimental spectra are normalized to the most intense peak in the two spectral regions, and the calculated spectra show the calculated IR intensities.

3.3 Results, Analysis, and Discussion

Figure 3.3 shows a plot of current versus working electrode potential for a millimolar aqueous solution of $[Ru(H_2O)](ClO_4)_2$ with phosphate buffer (pH 7) flowed through the electrochemical cell. The increased current readings at 0.8 V and 1.2 V is in general agreement with previous studies.[4, 31] Figure 3.4 shows the mass spectra obtained at four different EC potentials (VEC), applied across the glassy carbon working electrode and the stainless-steel counter electrode. All other experimental parameters were kept constant, that is, any differences observed in the mass spectra are direct results of the applied VEC. At 0 V, the mass spectrum displays a series of peaks between m/z=251.5–256.5, which are readily assigned to the initial $[Ru(H_2O)]^{2+}$ state of the catalyst. The observed relative intensities correspond to the expected natural isotopic abundances shown as red sticks in Figure 3.4A. With VEC increased to +0.8 V, a new feature appears at m/z=251 (highlighted in green), and the relative intensities of the higher

Figure 3.3 Plot of current (I) versus working electrode potential ($E_{Working\ Electrode}$) for a millimolar aqueous solution of $[Ru(H_2O)](ClO_4)_2$ with phosphate buffer (pH 7) flowed through electrochemical cell.

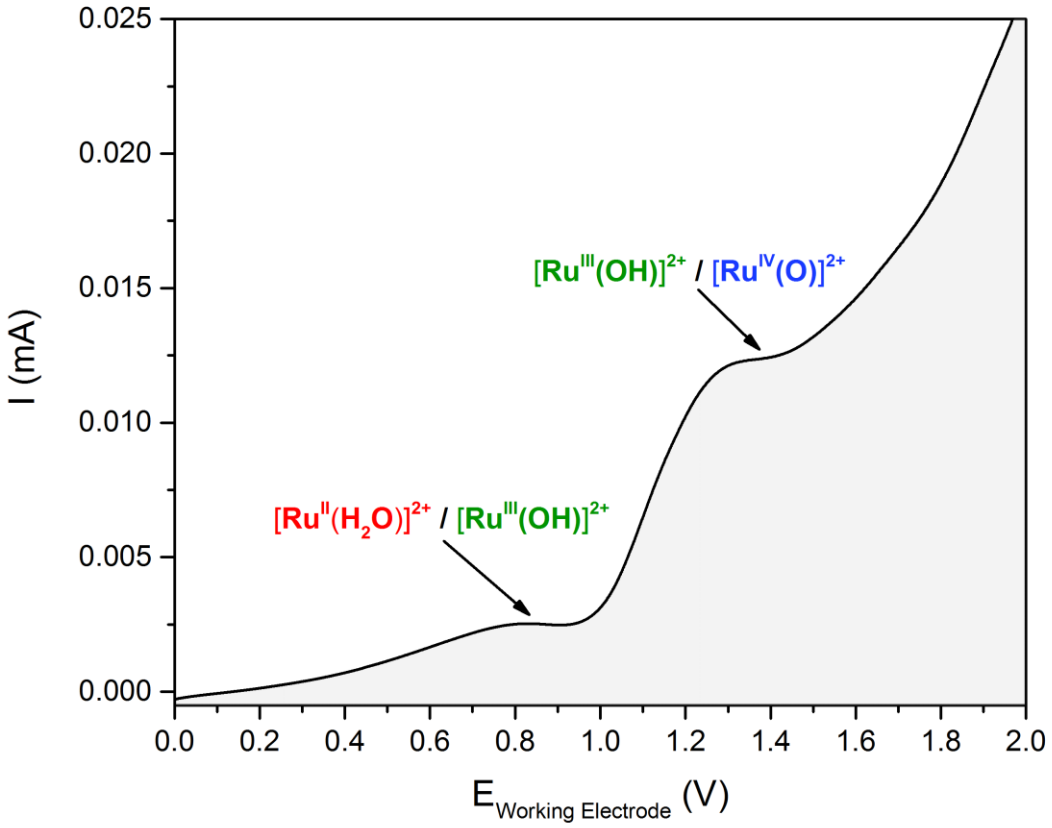

Figure 3.4. Mass spectra acquired at different applied EC potentials (VEC). The stick spectra indicate the deconvoluted relative populations of $[Ru(H_2O)]^{2+}$ (red), $[Ru(OH)]^{2+}$ (green), and $[Ru(O)]^{2+}$ (blue).

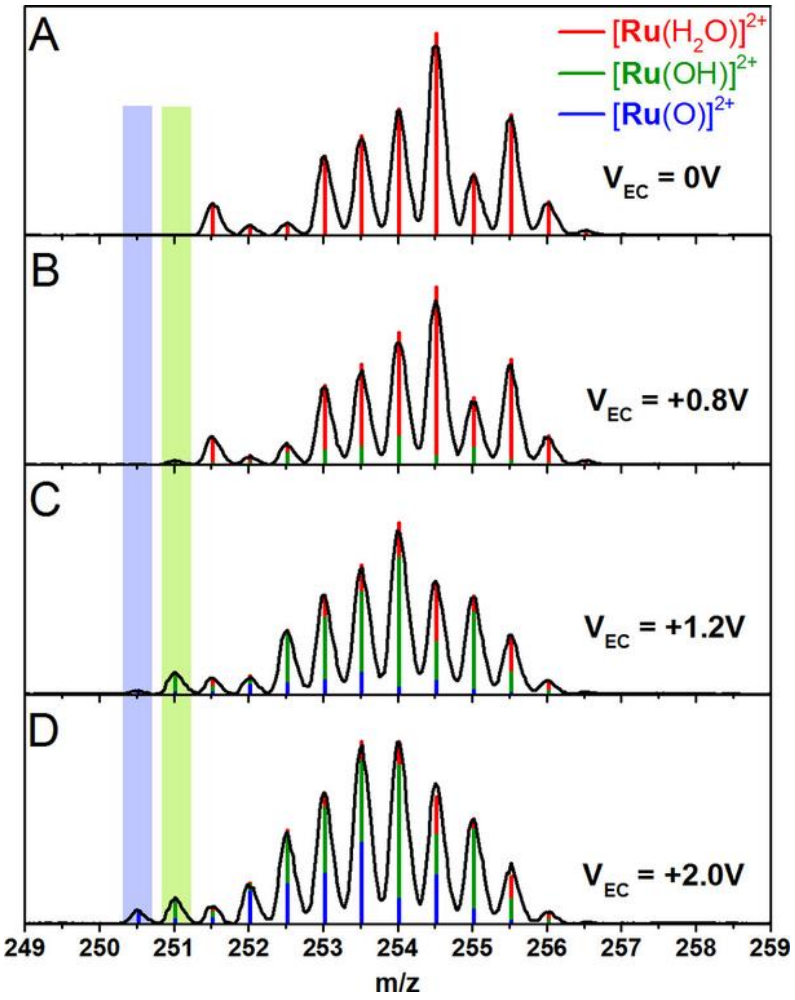

m/z peaks change slightly. This new species is assigned to the $[Ru(OH)]^{2+}$ complex, the formation of which corresponds to the $1e^-/1H^+$ oxidation of $[Ru(H_2O)]^{2+}$.[4] A third species appears with VEC=+1.2 V, as evident from the presence of a peak at m/z= 250.5 (highlighted in blue). It is assigned to the $[Ru(O)]^{2+}$ complex, resulting from the second $1e^-/1H^+$ oxidation step.[4] No new species are observed at VEC above +1.2 V, but the relative intensities of the observed features continue to vary as shown in Figure 3.4D.

The series of m/z features in Figure 3.4A have well-defined isotopic ratios, with the lowest mass at m/z = 251.5 corresponding to the $[Ru(H_2O)]^{2+}$complex containing ^{96}Ru and ^{12}C. The m/z = 251 feature that arises in Figure 3.4B corresponds to $[Ru(OH)]^{2+}$ containing ^{96}Ru and ^{12}C. Based on the fitted Gaussian of this feature and the isotopic abundance ratios from Figure 3.4A, we can estimate the intensities of the higher mass isotope features of $[Ru(OH)]^{2+}$. This is shown by the green stick spectrum in Figure 3.4B. The m/z = 251.5 feature now contains contributions from both $[Ru(H_2O)]^{2+}$ and $[Ru(OH)]^{2+}$. The contribution from $[Ru(OH)]^{2+}$ can be calculated from the m/z = 251 feature, and the rest can be attributed to $[Ru(H_2O)]^{2+}$. The intensity of the m/z = 251.5 feature due solely to $[Ru(H_2O)]^{2+}$ is then used to estimate the intensities of the higher mass isotope features of $[Ru(H_2O)]^{2+}$. This is shown as the red stick spectrum in Figure 3.4B. The sum of these two estimated isotope patterns, shown as the total height of the stick spectrum, corresponds very well with the overall intensity pattern in Figure 3.4B. This process is repeated for Figure 3.4C,D, with the inclusion of $[Ru(O)]^{2+}$ and the m/z = 250.5 feature (blue stick spectrum), as well as for each mass spectrum acquired at 0.2 V VEC steps to generate the data shown in Figure 3.4 and 3.5.

The deconvolution process outlined above allows us to obtain the individual relative intensities of these three complexes despite their overlapping masses. The Gaussian peaks used in the fitting process are used for subsequent analysis. Standard deviation error analysis reported from

the Gaussian peak fits (Origin) are used to estimate errors in the deconvolution process. These are the error bars included in Figure 3.5. Also note that there can be some minor detector saturation for the highest intensity feature(s) in the mass spectrum, which shows up in the Gaussian peak fit (the fitted Gaussian has a higher peak height than the experimental feature).

The individual relative intensities of these three complexes are plotted as a function of the applied EC potential in Figure 3.5. The relative abundance of the $[Ru(H_2O)]^{2+}$ and $[Ru(O)]^{2+}$ complexes can be fitted to sigmoidal curves, shown as solid traces in Figure 3.5. The dashed trace in Figure 3.5 corresponds to the residual of these two complexes (i.e., 1 – $[Ru(H_2O)]^{2+}$ 1 – $[Ru(O)]^{2+}$), and is in excellent agreement with the observed population of $[Ru(OH)]^{2+}$. The relative appearance of the potentials of the $[Ru(OH)]^{2+}$ and $[Ru(O)]^{2+}$ species agree with previous studies.[4,31] Interestingly, we did not detect any other oxidation products at VEC above 1.2 V. Notably, no significant amount of $[Ru(O)]^{3+}$, $[Ru(OOH)]^{2+}$, or $[Ru(O_2)]^{2+}$ was observed. It is possible that these species are too fragile or reactive to survive the ESI process. Another possibility is that oxidation of $[Ru(O)]^{2+}$ is the kinetic bottleneck in the catalytic cycle and the subsequent steps occur very rapidly, preventing these species from building sufficient concentrations.[30] In the case of $[Ru(O)]^{3+}$, it may be thermodynamically inaccessible at our experimental conditions.[33]

Although the reaction complexes have overlapping masses, the $[Ru(OH)]^{2+}$ complex can nonetheless be isolated in the mass spectrometer. To do this, the EC potential was held at +1.0 V. At this potential, the most intense peaks in the mass spectrum have contributions from both $[Ru(H_2O)]^{2+}$ and $[Ru(OH)]^{2+}$. A pure beam of $[Ru(OH)]^{2+}$ was obtained by controlled ion activation in the high pressure region of the ion source, which fragmented the more weakly bound $[Ru(H_2O)]^{2+}$ ions to yield $[Ru]^{2+}$, allowing the $[Ru(OH)]^{2+}$ to be isolated in the mass spectrometer.

Figure 3.5 Relative abundances of the three catalytic species, deconvoluted from mass spectra acquired at 0.2 VEC potential steps. The $[Ru(H_2O)]^{2+}$ (squares) and $[Ru(O)]^{2+}$ (triangles) data are fitted to a sigmoidal function (solid line), and the residual (dashed line) fits the $[Ru(OH)]^{2+}$ (circles) data nicely.

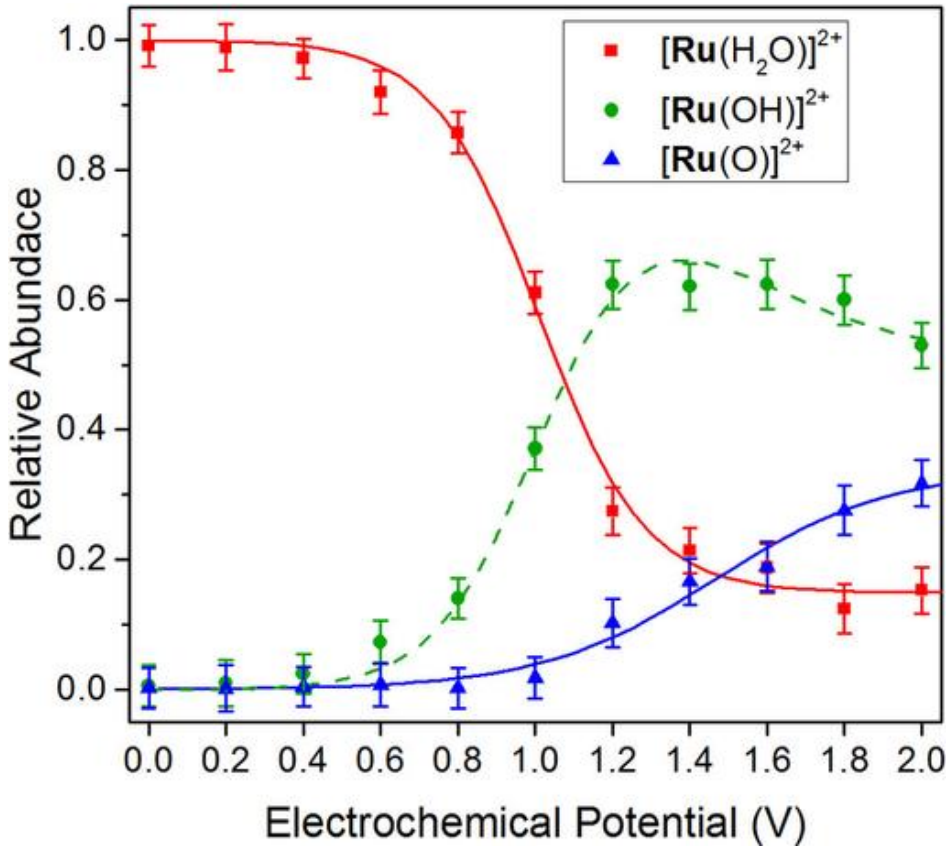

Figure 3.6 (A) At VEC = +0.8 V, both $[Ru(H_2O)]^{2+}$ and $[Ru(OH)]^{2+}$ are formed. (B) By increasing the RF voltages, the $[Ru(H_2O)]^{2+}$ ions are fragmented and are no longer present in this mass range.

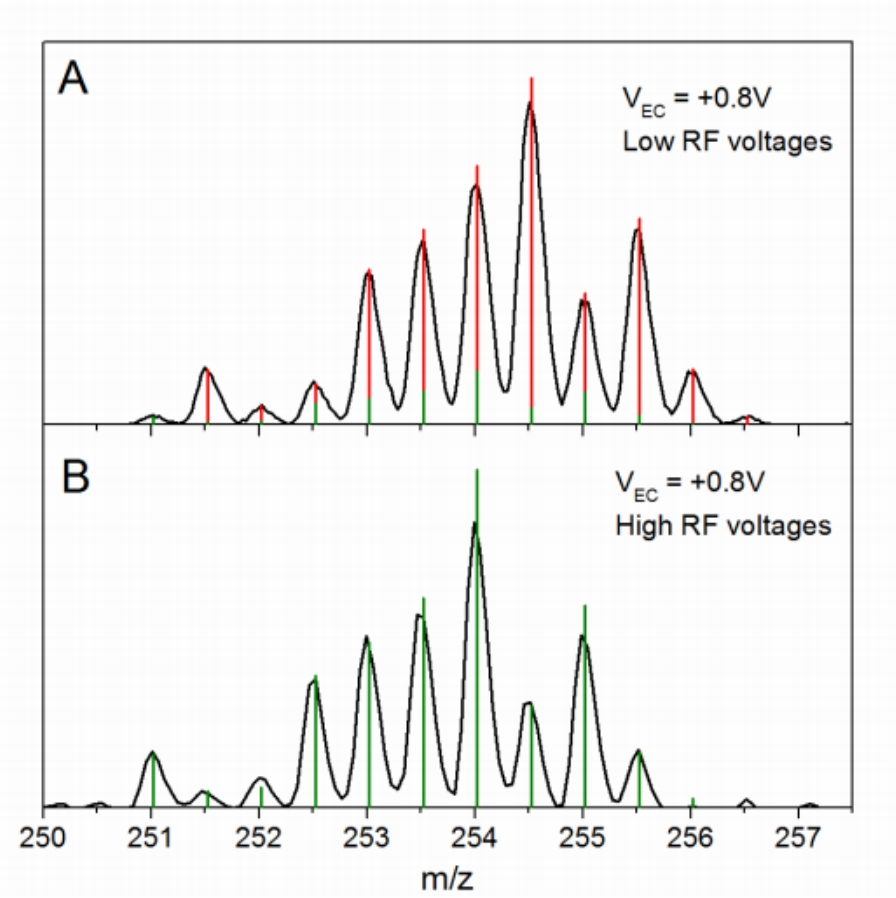

Figure 3.6 shows the mass spectrum with and without controlled ion activation, which shows the loss of the $[Ru(H_2O)]^{2+}$ signal in this mass range. This selective fragmentation can be carried out in part because the binding energies of H_2O and OH to the ruthenium complex are calculated to be quite different. The calculated binding energy of H_2O in $[Ru(H_2O)]^{2+}$ is 1.16 eV, significantly lower than the calculated binding energy of 2.77 eV for OH in $[Ru(OH)]^{2+}$. These values are calculated at wb97xd/def2tzvp/sdd level, for isolated complexes.

The identity of some of the observed catalytic complexes were confirmed by their vibrational spectra by use of using IR predissociation of cold D_2-tagged ions.[11,34] The IR predissociation spectrum of $[Ru(H_2O)]^{2+}(D_2)_2$ acquired at VEC=0 V is shown in Figure 3.7B. The calculated harmonic IR spectrum at the B3LYP/def2-TZVP level of theory using ORCA[32] is shown in Figure 3.7A. The excellent agreement between calculation and experiment provides straightforward assignment for the experimentally observed features. The pair of well-resolved peaks at 3576 and 3654 cm^{-1} are assigned to the symmetric and antisymmetric OH stretches of the water ligand, respectively, and have been discussed previously.[35] The H_2O bending mode is within the broad 1610 cm^{-1} feature, not resolved from the ring deformation modes of the pyridine ligands. The features between 700 cm^{-1} and 1500 cm^{-1} are assigned to the vibrational modes of the terpyridine and bipyridine ligands, with major peaks noted in Figure 3.7A.

Figure 3.7C shows the experimental IR predissociation spectrum of $[Ru(OH)]^{2+}(D_2)$, acquired at VEC=+1.0 V. Complete disappearance of the H_2O ligand symmetric and antisymmetric stretch peaks confirms $[Ru(H_2O)]^{2+}$ does not contribute to this spectrum. Despite the open-shell nature of this complex, the experimental spectrum is in excellent agreement with the calculated spectrum, shown in Figure 3.7D. The calculated result points to two characteristic vibrations of the $[Ru(OH)]^{2+}$ complex, namely the OH stretch at 3564 cm^{-1} and the Ru-OH bend

Figure 3.7 Experimental (B/C) and calculated (A/D) IR spectra of $[Ru(H_2O)]^{2+}(D_2)_2$ and $[Ru(OH)]^{2+}(D_2)$. The calculated spectra are scaled by 0.98 in the 700–1700 cm^{-1} region and 0.96 in the 2800–3800 cm^{-1} region. The experimental spectra are normalized to the most intense peak in the two spectral regions, and the calculated spectra show the calculated IR intensities.

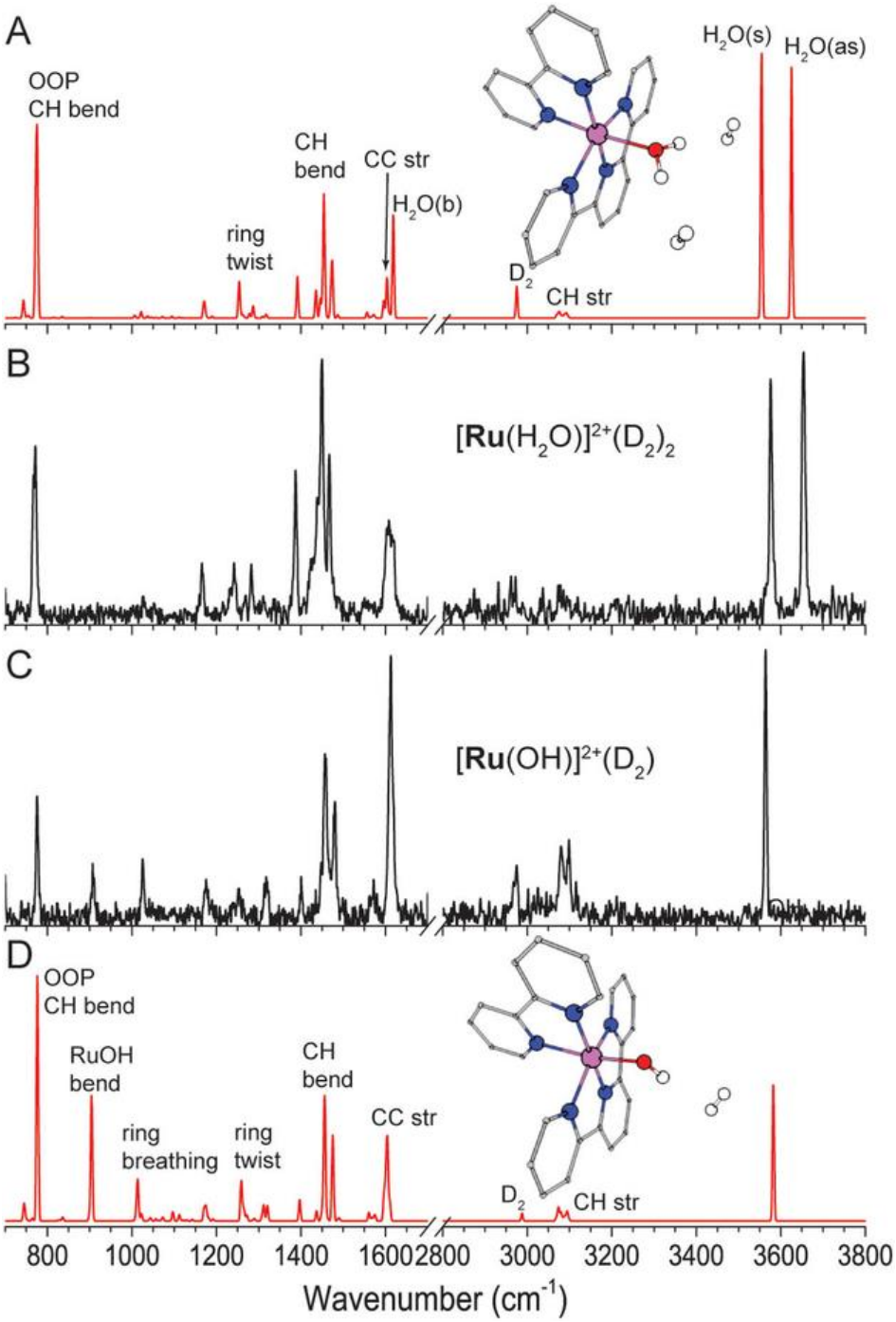

at 908 cm^{-1}. Comparisons of the experimental IR spectra (Figure 3.7B,C) show that the terpyridine and bipyridine vibrational modes remain at similar frequencies despite these two complexes having nominally different Ru oxidation states. The biggest difference is the increased intensity for the pyridine ring breathing modes at 1026 cm^{-1} in the $[Ru(OH)]^{2+}$ spectrum, which is likely due to coupling with the nearby Ru-OH bending mode.

The experimental frequency of the OH ligand contains additional information regarding the Ru-OH interaction. Our previous study on $[MOH]^{+}$ systems showed that the vibrational frequency of the OH stretch can serve as an in situ probe of the M-OH bond polarity owing to a strong vibrational Stark effect.[36–37] Specifically, the OH stretch has a frequency above 3800 cm^{-1} in an ionic system, that is, M^{2+}-OH^{-}, and redshifts as the system goes to a more covalent M^{+}-OH configuration. The experimental OH stretch at 3564 cm^{-1} in $[Ru(OH)]^{2+}$ indicates that the Ru-OH interaction is likely more covalent than ionic. This is supported by natural population analysis[38] (NPA), which yielded a charge of -0.34 for the OH, +0.94 for the Ru center, and a total combined charge of +1.40 for the bipyridine and terpyridine ligands. Additionally, the OH frequency here conforms to the frequency versus charge transfer trend discussed in reference 36. If we compare the NPA charges to those of the $[Ru(H_2O)]^{2+}$ complex, which has a +0.66 charge on Ru, a +0.15 charge on H_2O, and a total charge of +1.17 on the bipyridine and terpyridine, we see that the electron loss upon oxidation is mostly shared between the Ru center and the OH ligand. Furthermore, the minimal change in the bipyridine and terpyridine charge is consistent with their very similar IR frequencies in the spectra of $[Ru(H_2O)]^{2+}$ and $[Ru(OH)]^{2+}$. It is interesting to note that the pyridine modes in the 700–1700 cm^{-1} region remain at similar frequencies for the $[Ru(O_2)]^{2+}$ complex,[39] which is formed after two additional oxidation steps.

Unfortunately, the $[Ru(O)]^{2+}$ complex could not be separated from the more abundant $[Ru(OH)]^{2+}$, and an IR spectrum corresponding to only $[Ru(O)]^{2+}$ could not be acquired to confirm the mass spectral assignment. However, given the changes in the mass spectral features as a function of VEC, as discussed above, the identity of the m/z=250.5 feature is most likely $[Ru(O)]^{2+}$. Synthesis of the $[Ru(H_2O)]^{2+}$ catalyst from isotopically pure ruthenium should allow for such separation and enable the characterization of this species.

3.4 Conclusion

Our results here show that coupling EC-ESI with mass spectrometry and CIVP spectroscopy is a powerful method for *in situ* characterization of homogeneous electrocatalytic reaction intermediates. The control afforded by the EC cell provides a means to study each reaction complex individually, and the concurrent mass spectral and structural analysis leads to unambiguous identification of reaction complexes. Moreover, our instrument is capable of controlled solvation of ionic species with the use of an additional reaction trap,[40] such that solvent-related effects such as structural changes upon hydrogen bonding with water solvents can also be studied.[35] There are some limitations to our current EC-ESI approach. The cell design causes a delay of a few seconds between the EC electrode and ESI, making it difficult to capture short-lived species. A faster flow rate through the cell would shorten the delay, but the amount of reaction solution used is too large for stable ESI conditions. Future EC flow cells will incorporate a microfluidic approach to overcome these limitations.

3.5 References

1. F. Coelho, M.N. Eberlin, *Angew. Chem. Int. Ed.* **2011**, 50, 5261; *Angew. Chem*. **2011**, 123, 5370.

2. J. Roithová, *Chem. Soc. Rev.* **2012**, 41, 547.

3. L. Batiste, P. Chen, *J. Am. Chem. Soc.* **2014**, 136, 9296.

4. D.E. Polyansky, J.T. Muckerman, J. Rochford, R. Zong, R.P. Thummel, E. Fujita, *J. Am. Chem. Soc.* **2011**, 133, 14649.

5. D.J. Wasylenko, C. Ganesamoorthy, M.A. Henderson, B.D. Koivisto, H.D. Osthoff, C.P. Berlinguette, *J. Am. Chem. Soc.* **2010**, 132, 16094.

6. C. Iacobucci, S. Reale, F. De Angelis, *Angew. Chem. Int. Ed.* **2016**, 55, 2980; *Angew. Chem.* **2016**, 128, 3032.

7. K.L. Vikse, Z. Ahmadi, J.S. McIndoe, *Coord. Chem. Rev.* **2014**, 279, 96.

8. D. Schrçder, *Acc. Chem. Res.* **2012**, 45, 1521.

9. N.C. Polfer, *Chem. Soc. Rev.* **2011**, 40, 2211.

10 T.R. Rizzo, J.A. Stearns, O.V. Boyarkin, *Int. Rev. Phys. Chem.* **2009**, 28, 481.

11. A.B. Wolk, C.M. Leavitt, E. Garand, M.A. Johnson, *Acc. Chem. Res.* **2014**, 47, 202.

12. L.S. Wang, C.F. Ding, X.B. Wang, S.E. Barlow, *Rev. Sci. Instrum.* **1999**, 70, 1957.

13. G. Bojesen, P. Hvelplund, T.J.D. Jorgensen, S.B. Nielsen, *J. Chem. Phys.* **2000**, 113, 6608.

14. O.T. Ehrler, J.M. Weber, F. Furche, M.M. Kappes, *Phys. Rev. Lett.* **2003**, 91, 113006.

15. K. Arnold, T.S. Balaban, M.N. Blom, O.T. Ehrler, S. Gilb, O. Hampe, J.E. van Lier, J.M. Weber, M.M. Kappes, *J. Phys. Chem. A* **2003**, 107, 794.

16. J.M. Weber, I.N. Ioffe, K.M. Berndt, D. Loffler, J. Friedrich, O.T. Ehrler, A.S. Danell, J.H. Parks, M.M. Kappes, *J. Am. Chem. Soc.* **2004**, 126, 8585.

17. J.C. Marcum, A. Halevi, J.M. Weber, *Phys. Chem. Chem. Phys.* **2009**, 11, 1740.

18. J.A. Fournier, A.B. Wolk, M.A. Johnson, *Anal. Chem.* **2013**, 85, 7339.

19. C.F. Bçkman, C. Zettersten, P.J.R. Sjçberg, L. Nyholm, *Anal. Chem.* **2004**, 76, 2017.

20. G.J. Van Berkel, K.G. Asano, M.C. Granger, *Anal. Chem.* **2004**, 76, 1493.

21. U. Jurva, P. Bissel, E.M. Isin, K. Igarashi, S. Kuttab, N. Castagnoli, *J. Am. Chem. Soc.* **2005**, 127, 12368.

22. J.J. Concepcion, M.-K. Tsai, J.T. Muckerman, T.J. Meyer, *J. Am. Chem. Soc.* **2010**, 132, 1545.

23. D.J. Wasylenko, C. Ganesamoorthy, B.D. Koivisto, M.A. Henderson, C.P. Berlinguette, *Inorg. Chem.* **2010**, 49, 2202.

24. R. Zong, R.P. Thummel, *J. Am. Chem. Soc.* **2005**, 127, 12802.

25. J.J. Concepcion, J.W. Jurss, M.R. Norris, Z. Chen, J.L. Templeton, T.J. Meyer, *Inorg. Chem.* **2010**, 49, 1277.

26. D.J. Wasylenko, C. Ganesamoorthy, M.A. Henderson, C.P. Berlinguette, *Inorg. Chem.* **2011**, 50, 3662.

27. D.J. Wasylenko, R.D. Palmer, C.P. Berlinguette, *Chem. Commun.* **2013**, 49, 218.

28. L.-P. Wang, Q. Wu, T. Van Voorhis, *Inorg. Chem.* **2010**, 49, 4543.

29. Y. Wang, M.S.G. Ahlquist, *Dalton Trans.* **2014**, 43, 13776.

30. J. Honta, S. Tajima, T. Sato, K. Saito, T. Yui, M. Yagi, *J. Photochem. Photobiol. A* **2015**, 313, 126.

31. K.J. Takeuchi, M.S. Thompson, D.W. Pipes, T.J. Meyer, *Inorg. Chem.* **1984**, 23, 1845.

32. F. Neese, *WIREs Comput. Mol. Sci.* **2012**, 2, 73.

33. Y. Pushkar, D. Moonshiram, V. Purohit, L.F. Yan, I. Alperovich, *J. Am. Chem. Soc.* **2014**, 136, 11938.

34. M.Z. Kamrath, E. Garand, P.A. Jordan, C.M. Leavitt, A.B. Wolk, M.J. Van Stipdonk, S.J. Miller, M.A. Johnson, *J. Am. Chem. Soc.* **2011**, 133, 6440.

35. E.M. Duffy, B.M. Marsh, E. Garand, *J. Phys. Chem. A* **2015**, 119, 6326.

36. B.M. Marsh, J.M. Voss, J. Zhou, E. Garand, *Phys. Chem. Chem. Phys.* **2015**, 17, 23195.

37. B.M. Marsh, J. Zhou, E. Garand, *Phys. Chem. Chem. Phys.* **2015**, 17, 25786.

38. NBO 5.0., E.D. Glendening, J.K. Badenhoop, A.E. Reed, J.E. Carpenter, J.A. Bohmann, C.M. Morales, C.R. Landis, F. Weinhold, Theoretical Chemistry Institute, University of Wisconsin, Madison, WI, USA, 2013.

39. E.M. Duffy, B.M. Marsh, J.M. Voss, E. Garand, *Angew. Chem. Int. Ed.* **2016**, 55, 4079; *Angew. Chem.* **2016**, 128, 4147.

40. B.M. Marsh, J.M. Voss, E. Garand, *J. Chem. Phys.* **2015**, 143, 204201.

CHAPTER 4

IR-IR Conformation Specific Spectroscopy of Na^+(Glucose) Adducts

Published: J.M. Voss, S.J. Kregel, K.C. Fischer, and E. Garand. *Journal of the American Society for Mass Spectrometry*, 29, 42–50 (2018)

Abstract

We report an IR-IR double resonance study of the structural landscape present in the Na^+(glucose) complex. Our experimental approach involves minimal modifications to a typical IR predissociation setup, and can be carried out via ion-dip or isomer-burning methods, providing additional flexibility to suit different experimental needs. In the current study, the single-laser IR predissociation spectrum of Na^+(glucose), which clearly indicates contributions from multiple structures, was experimentally disentangled to reveal the presence of three α-conformers and five β-conformers. Comparisons with calculations show that these eight conformations correspond to the lowest energy gas-phase structures with distinctive Na^+ coordination.

Author Contributions

JMV, SJK, and KCF acquired experimental spectra; JMV, SJK, and EG performed theoretical calculations and data analyses; JMV and EG wrote the manuscript.

4.1 Introduction

Carbohydrates are ubiquitous in biology, and play a vital role in many biological functions, from energy storage to recognition processes. They are rich in structural variation due to the presence of numerous stereocenters as well as linkage diversity in polysaccharides. Mass spectrometry, with its high sensitivity and ability to analyze complex mixtures, has been applied to the characterization of carbohydrates.[1] Uncharged monosaccharides are usually brought into the gas-phase by complexation with a metal ion. Such interactions between carbohydrates and ionic species have also recently been found to play a role in the transformation of biomass into chemical feedstock.[2–4] However, the diversity of metal ion binding sites adds to the overall structural richness. This isomeric complexity poses a distinct challenge for mass spectrometric techniques, requiring additional structural characterization tools. In a very recent study by Masellis et al.,[5] ion mobility separation and cryogenic vibrational predissociation spectroscopy were applied to glycans and the results showed that different isomers of glycans have unique vibrational signatures in the OH stretching region. However, the spectroscopy itself is still hampered by the presence of multiple isomers, which are not separated by ion mobility, leading to increased spectral congestion and difficulties in spectral interpretation. Here, we focus on the relatively simple mass-selected Na^+(glucose) adducts and show that an IR-IR double-resonance scheme can be used to isolate the spectral signatures of individual saccharide conformations and metal ion binding sites.

As shown in Figure 4.1, the pyranose form of D-glucose is characterized by five carbon stereocenters, with C(2) and C(5) being R, C(3), and C(4) being S, and the C(1) stereochemistry defining the α and β anomers. Mutarotation occurs via a ring opening transition state with a barrier of 90–110 kJ/mol in an aqueous environment, and the α:β equilibrium of 36:64 is reached on the order of hours in a room temperature solution.[6–8] Additional structural diversity involves numerous

conformations resulting from rotations of the C(5)–C(6) and C–OH bonds, as well as the boat and chair conformations of the pyranose ring. Extensive density functional theory (DFT) calculations[9–12] have shown that a very rich conformational landscape is expected, especially when coordinated with a metal ion.

Figure 4.1 General structure of α-D-glucose and β-D-glucose, showing conventional carbon and oxygen numbering.

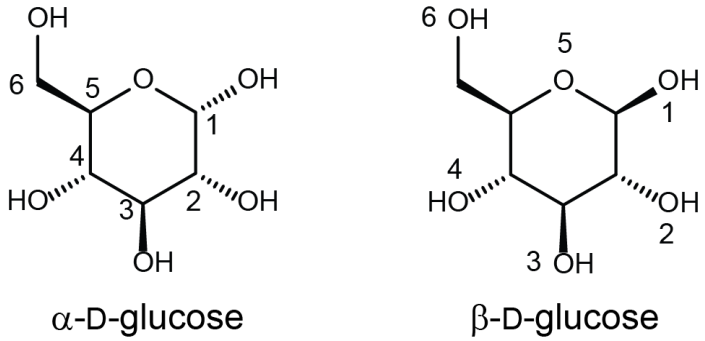

Action spectroscopy has proven to be a powerful tool in providing detailed structural information on mass-selected ions.[13–17] When combined with electrospray ionization (ESI), it is especially well-suited for studying the structures of relatively large complexes found in biological and catalytic processes.[18–25] Furthermore, the application of two-laser resonance schemes can be particularly useful in achieving conformationally specific spectroscopy. The most common two-laser approach uses a UV-UV or UV-IR double resonance scheme, taking advantage of the high sensitivity of a chromophore's electronic absorption to its immediate chemical environment.[18,19,26,27] When the molecule under study does not possess a suitable chromophore, a more general IR-IR double resonance approach, in conjunction with messenger-tagged complexes, can be used.[28–34]

In the current study, we employ an IR-IR double resonance approach to study the rich vibrational spectrum of the D_2-tagged Na^+(glucose) complex. The different conformations of Na^+(glucose) vary in their intramolecular O-H···O hydrogen-bond (H-bond) configuration, making vibrational spectroscopy in the OH stretching region potentially conformationally specific due to the sensitivity of the OH stretch frequency to H-bonding.[35–37] Our results revealed and characterized eight different conformers that significantly contribute to the overall spectrum, and showed that IR spectroscopy can be used to distinguish α/β anomers as well as the interaction motif of the sodium ion.

4.2 Experimental Details

The infrared predissociation spectra of Na^+(glucose)(D_2) were acquired using a home-built instrument, described in detail previously.[38] Briefly, Na^+(glucose) ions were formed by electrospray ionization of ~1 mM aqueous solution of NaCl and α-D-glucose that was allowed to equilibrate for more than 24 h. The Na^+(glucose) complexes were transferred through several differentially-pumped regions via a series of ion guides and biased apertures into a cryogenic 3D quadrupole ion trap held at 10 K by a closed-cycle helium refrigerator. A pulsed solenoid valve introduced a short burst (~1 ms) of buffer gas consisting of 10% D_2 in He into the ion trap to thermalize the trapped ions and form weakly bound D_2 tagged adducts.

The output of a Nd:YAG pumped tunable OPO/OPA laser (Laservision), referred to as "pump laser" hereafter, was focused by a spherical mirror (F.L. = 30 cm) into the ion trap via a 2 mm hole in the middle RF electrode. The pump laser was fired ~90 ms after the introduction of buffer gas and intersected all the trapped ions, allowing for resonant photofragmentation of Na^+(glucose)(D_2) ions. The ~90 ms window provided ample time for removal of the buffer gas

from the trap volume prior to ion–laser interactions, ensuring no additional cooling and formation of D_2-adducts was possible afterwards. A similar 2 mm hole on the opposite side of the ion trap allowed the exit of the pump laser beam. Careful laser alignment to minimize light scattering inside the ion trap was important to avoid nonresonant depletion of D_2-adducts.

Approximately 5 ms after the laser pulse, all trapped ions were extracted from the ion trap into a time-of-flight mass spectrometer, where the remaining Na^+(glucose)(D_2) adducts were isolated with a mass gate and intersected with the output of a second Nd:YAG pumped tunable OPO/OPA laser (Laservision), referred to as "probe laser" hereafter. A two-stage reflectron was used as a secondary mass-selection stage to separate the Na^+(glucose) photofragments produced by the probe laser from the parent Na^+(glucose)(D_2) ions. The intensity of the probe laser photofragment was monitored on an MCP detector and recorded by a digital oscilloscope. A schematic depiction of our IR-IR setup is shown in Figure 4.2E.

Unlike previous IR-IR double resonance experiments,[29, 30] our approach does not require a third mass-selection stage or extensive modification to our one-laser IR photodissociation setup. The main limitation here is the possibility of the pump-laser photofragments overlapping in mass with the target of the probe laser. An obvious example in the present case would be a larger Na^+(glucose)$(D_2)_{n>1}$ cluster that may produce a Na^+(glucose)(D_2) photofragment upon the absorption of a photon inside the ion trap. To avoid this problem, the ion trap buffer gas pressure was optimized for the formation of Na^+(glucose)(D_2) while minimizing larger Na^+(glucose)$(D_2)_{n>1}$ clusters to less than 10%.

Figure 4.2 (A) One-laser IR predissociation spectrum of Na^+(Glucose)(D_2). (B) IR-IR spectrum employing the ion-dip method. (C) IR-IR spectrum employing the isomer-burning method. (D) Spectrum generated by subtracting the spectrum in (C) from the spectrumin (A). (E) An illustration of the IR-IR setup with the spheres representing each type of species. Blue: Na^+(Glucose)(D_2). Yellow: Na^+(Glucose). Red: Na^+(Glucose) photofragment formed by pump-laser. Green: Na^+(Glucose) photofragment formed by probe-laser.

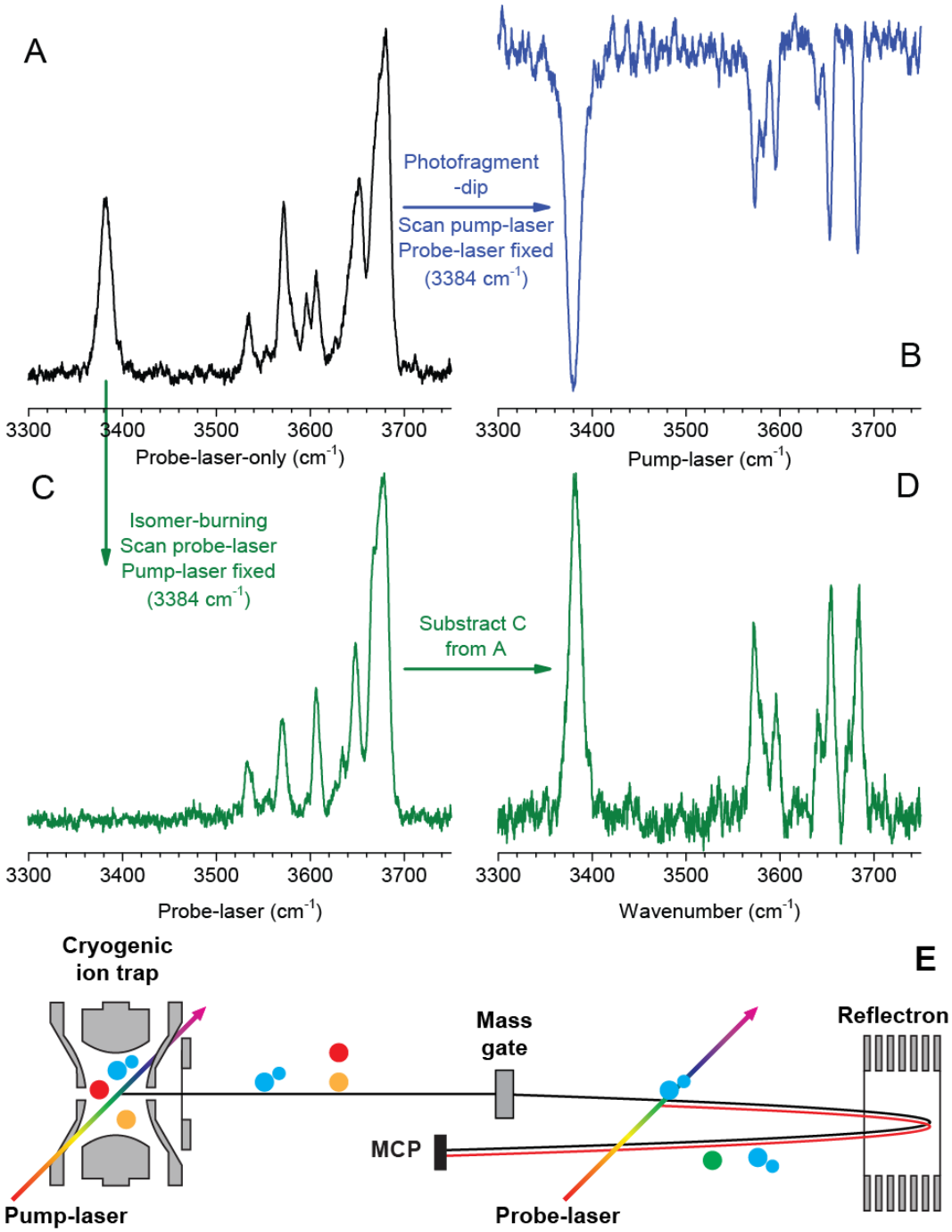

Our IR-IR double resonance scheme provides two means of obtaining structure-specific IR spectra, as shown in Figure 4.2A–D. Note that in all situations, the photofragment from the probe laser is the monitored signal. Figure 4.2A presents a normalized 15-scan averaged IR predissociation spectrum of Na^+(glucose)(D_2), obtained using only the probe laser and monitoring the formation of the Na^+(glucose) photofragment as a function of wavelength. The first IR-IR method uses a pump-probe ion-dip scheme similar to previously reported IR-IR studies.[28–30] In this method, the probe laser is fixed to a specific transition (3384 cm^{-1} in this case) and the wavelength of the pump laser is scanned. When the pump laser is resonant with a transition belonging to the same structure as the probed transition, the depletion of Na^+(glucose)(D_2) in the trap causes a dip in the monitored photofragment signal. The resulting dip spectrum, shown in Figure 4.2B, directly yields the IR transitions of the structure(s) giving rise to the probed transition. The dip spectrum is very sensitive to shot-to-shot fluctuations in the overall ion signal and thus yields poorer signal-to-noise ratio (s/n), as exemplified by Figure 4.2B. This normalized 15-scan averaged IR-IR ion-dip spectrum has a s/n of 26 using the 3420–3510 cm^{-1} region as the baseline. The one-laser spectrum, shown in Figure 4.2A, has a s/n of 74, approximately three times better than the ion-dip spectrum.

The second IR-IR method uses an isomer-burning scheme. In this method, the pump laser is fixed to a specific IR transition (3384 cm^{-1} in this case), removing the structure(s) that has this particular transition from the Na^+(glucose)(D_2) population in the trap. The probe laser is then scanned, utilized in essentially the same manner as the conventional single laser IR predissociation experiment. The resulting 15-scan averaged spectrum is shown in Figure 4.2C. The complete disappearance of the ~3380 cm^{-1} feature confirms that nearly 100% of the Na^+(glucose)(D_2) structures possessing this feature have been depleted. This uniform depletion efficiency is due to

the tight confinement of the translationally cooled ions inside the Paul trap, which provides a very favorable spatial overlap with the focused pump laser beam. The main advantage of the isomer burning method is its "background-free" nature that leads to higher s/n spectra compared to the ion-dip method. For example, the spectrum in Figure 4.2C has a s/n of 70, comparable to the one-laser spectrum shown in Figure 4.2A. However, the resulting spectrum contains all other structures not possessing the ~3380 cm^{-1} vibration, and is not particularly useful in the present case where numerous conformations are present. The subtraction of spectrum 4.2C from 4.2A, shown in Figure 4.2D, reveals the spectrum of the structure(s) that was depleted, i.e., possessing the ~3380 cm^{-1} vibration. Comparison of Figure 4.2B and 4.2D shows that the two methods yield comparable spectra with similar s/n of 26 and 30, respectively. The main drawback of the isomer-burning method is that the subtraction requires a good reference spectrum. This can be difficult to obtain if some experimental fluctuations are present. For the current Na^+(glucose) experiments, where conformational populations are difficult to reproduce exactly day-to-day, we utilized the ion-dip method. Nevertheless, in simpler cases with fewer isomers, or for quick population assessment, the isomer-burning scheme presents some definite advantages.

4.3 Computational Details

Analysis of the experimental spectra was assisted by DFT and MP2 calculations carried out using Gaussian 09.[39] Based on previous computational studies[9,10] and chemical intuition, a series of initial geometries with Na^+ located around glucose were optimized at the cam-B3LYP/3-21+G level. These ~110 geometries resulted in ~60 unique structures, which were further optimized at the cam-B3LYP/6-311+G(d,p) level. The 9 and 10 lowest energy structures for the α and β anomers, respectively, were further optimized using several methods and basis sets. Their

relative energetics are summarized in Table 4.1 These results are generally in agreement with each other and to previous studies.[9, 10] Note that the naming scheme used here relates to the binding site of Na^+. For example, α34a refers to an α anomer with the Na^+ interacting with O(3) and O(4). For each Na^+ binding motif, several conformations involving the rotations of OH groups are possible and are alphabetized in order of their relative energies. Calculations on selected structures showed that the D_2 tag preferentially binds to the charged Na^+ site and causes negligible perturbation to the glucose vibrations (see Figure 4.3). Therefore, we used the calculated spectra of the bare Na^+(glucose) complexes for our analysis. We chose the harmonic frequencies calculated at the cam-B3LYP/def2-TZVP level for comparison with the experimental spectra based on their generally better agreement with a selected subset of conformers. These harmonic frequencies are scaled by 0.953 and the spectra are Gaussian convoluted with the Gaussian area corresponding to the calculated intensity. All vibrations are convoluted with a 7 cm^{-1} width except for OH stretches below 3540 cm^{-1}, which are convoluted with a 15 cm^{-1} width.

4.4 Results

The one-laser IR predissociation spectrum of Na^+(glucose)(D_2) in the 3250–3750 cm^{-1} OH stretching region is shown in the top panel of Figure 4.4. The glucose molecule has five individual OH stretching vibrations, but there are more than 12 fully and partially resolved features present here. This clearly indicates the presence of multiple structures with varying degrees of intramolecular H-bonding. A free OH group, i.e., one that is not donating an H-bond, would have a stretch frequency around 3680 cm^{-1}. For example, methanol has an OH stretch of 3681 cm^{-1}.[40] A donor H-bond interaction redshifts the frequency to an extent that is roughly proportional to the square of the strength of that H-bond interaction.[35–37] Therefore, the redshifted OH stretch is quite

Table 4.1. Relative energies (kJ/mol) of the lowest energy structures found. Each structure is optimized at the specified level and basis set, with corresponding frequency calculation and unscaled ZPE correction. The experimentally observed structures are highlighted in bold italics.

	cam-B3LYP /6311	cam-B3LYP/ def2TZVP	cam-B3LYP /aug-cc pVTZ	ωB97XD/def2TZVP	B3LYP/ def2TZVP	B3LYP-D3/ def2TZVP	MP2/ def2TZVP
α34a	***0.0***	***0.0***	***0.0***	***0.0***	***0.0***	***0.0***	***0.0***
α34b	8.5	8.3	7.9	9.0	8.1	8.7	8.0
α156a	***8.6***	***8.7***	***7.2***	***5.7***	***8.3***	***5.6***	***10.7***
α23a	***8.8***	***8.7***	***8.7***	***7.9***	***8.5***	***9.1***	***8.2***
α156b	8.9	9.0	7.8	6.6	8.4	5.8	10.9
α356a	9.5	12.5	12.7	7.1	14.1	4.5	12.8
α156c	15.4	14.0	12.8	9.4	13.1	9.6	15.1
α356b	19.1	20.8	21.1	14.2	21.3	11.6	21.5
α46a	20.0	19.3	19.5	19.5	17.9	18.6	20.9
β34a	***6.0***	***5.1***	***4.7***	***5.7***	***4.6***	***6.4***	***6.3***
β1356a	***4.4***	***7.0***	***7.5***	***2.6***	***8.4***	***-1.1***	***11.3***
β1356b	9.9	11.1	11.7	6.4	12.5	2.5	15.7
β156a	***12.3***	***12.6***	***11.7***	***8.8***	***12.0***	***9.7***	***16.2***
β23a	***13.7***	***12.8***	***12.6***	***13.2***	***12.2***	***14.3***	***12.8***
β156b	***14.3***	***14.6***	***13.5***	***10.5***	***13.3***	***13.4***	***16.2***
β156c	22.5	21.2	20.3	15.6	19.2	18.7	22.1
β156d	22.6	21.2	20.7	16.0	19.9	17.0	24.0
β46a	25.6	24.2	23.6	25.7	22.0	24.6	27.0
β12a	25.8	25.3	24.8	24.1	24.4	27.1	25.6

Figure 4.3. camB3LYP/def2TZVP calculated results for the perturbation of D_2 tag on the IR spectrum. The D_2 binds to Na^+ in both structures.

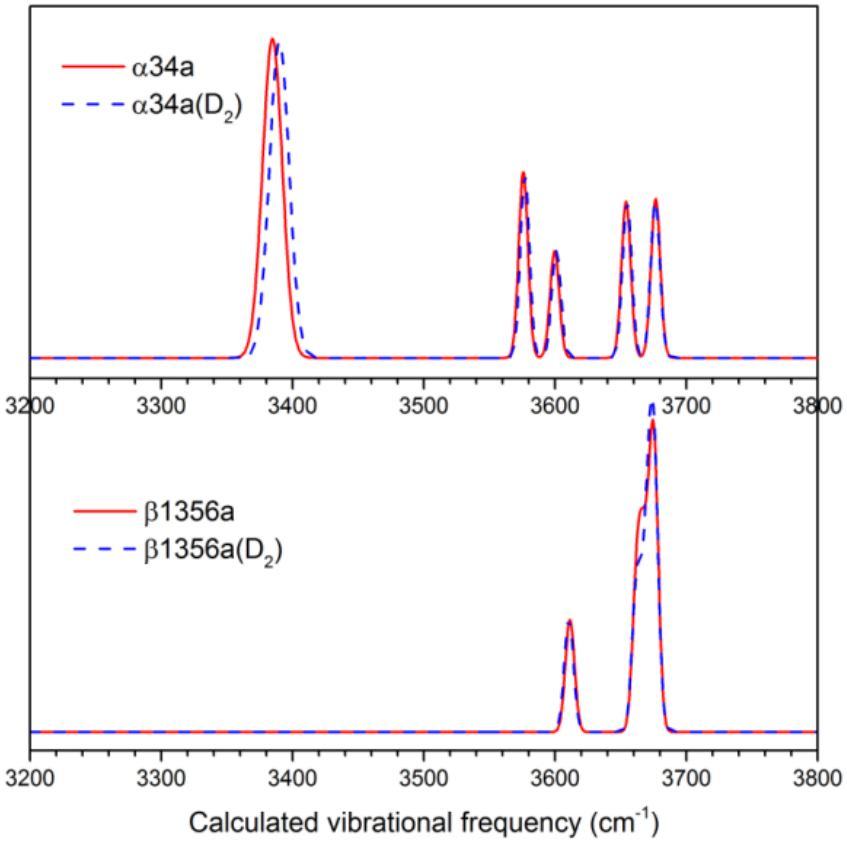

sensitive to the exact nature of the intramolecular H-bonding, and by extension, the overall glucose conformation.

Using the ion-dip method described above, we selectively acquired the IR-IR spectra associated with features at 3384 cm^{-1}, 3534 cm^{-1}, 3555 cm^{-1}, 3565 cm^{-1}, 3572 cm^{-1}, 3585 cm^{-1}, 3596 cm^{-1}, 3606 cm^{-1}, 3625 cm^{-1}, and 3635 cm^{-1}, as shown in Figure 4.4a-j, respectively. Cursory inspection of the calculated spectra indicates that many conformations have vibrations above 3635 cm^{-1}, representing the free or very weakly H-bonded OH groups. The IR-IR spectra, all showing similar features in this region, further support this. Hence, the higher frequency features were not probed.

The 10 IR-IR spectra have distinctive appearances, but many show more than five OH stretch features, implying the presence of more than one structure. For example, the IR-IR spectrum associated with feature A displays seven peaks at 3380 cm^{-1}, 3573 cm^{-1}, 3583 cm^{-1}, 3595 cm^{-1}, 3641 cm^{-1}, 3653 cm^{-1}, and 3683 cm^{-1}, indicating that at least two structures contribute to the intensity at 3380 cm^{-1}. This is supported by comparing the IR-IR spectra associated with features F and G. Both of these spectra contain the 3380 cm^{-1} peak, but the other four major peaks all have different frequencies. Therefore, the five most intense peaks in spectrum f and spectrum g likely represent the signatures of the two structures contributing to spectrum a. Unfortunately, spectrum f and spectrum g each has a series of weaker features due to minor contributions from other structures that have absorption at 3585 or 3596 cm^{-1}. This demonstrates a situation where a single IR-IR spectrum is insufficient to obtain conformer specific information. Note that due to the intrinsic widths (>7 cm^{-1}) associated with the experimental features, the vibrational frequencies of two different structures do not have to be perfectly overlapping for both to contribute to an IR-IR spectrum.

Figure 4.4 (top) One-laser IR predissociation spectrum of Na^+(glucose)(D_2). (a–j) correspond to the IR-IR ion-dip spectrum with the probe laser fixed at the frequency indicated by the dotted lines. a: 3384 cm^{-1}, b: 3534 cm^{-1}, c: 3555 cm^{-1}, d: 3565 cm^{-1}, e: 3572 cm^{-1}, f: 3585 cm^{-1}, g: 3596 cm^{-1}, h: 3606 cm^{-1}, i: 3625 cm^{-1}, j: 3635 cm^{-1}

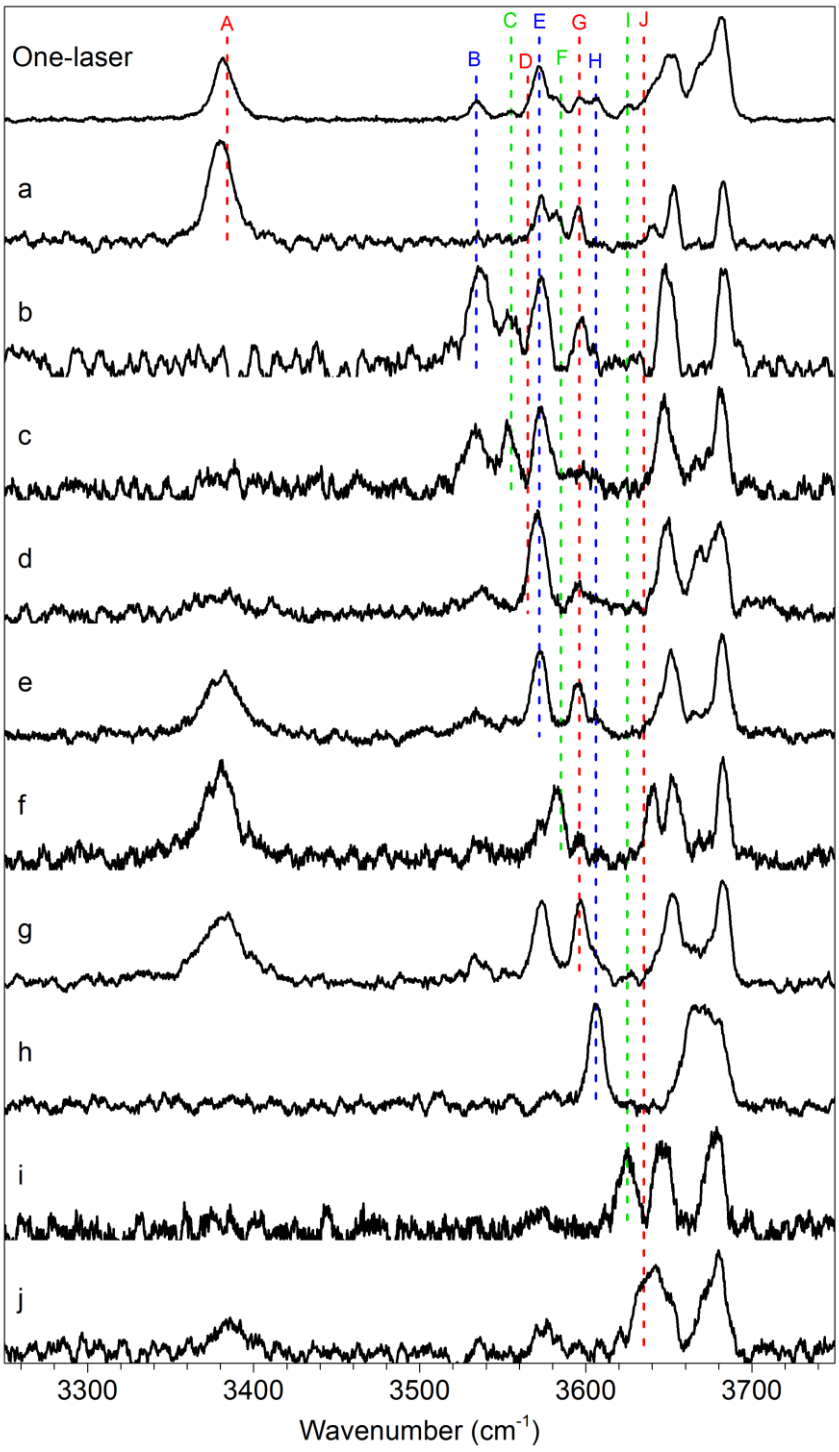

The following section details the processing of the IR-IR spectra to extract conformer specific spectra, the results of which are displayed in Figure 4.5 together with the corresponding calculated spectra. The structures of the assigned conformers are shown in Figure 4.6 and specific peak assignments are summarized in Table 4.2.

We begin with the two simplest IR-IR spectra that can readily be assigned to a single conformation. Spectrum h is assigned to β1356a. This β-conformer has Na^+ binding to O(1), O(3), O(5), and O(6), with the pyranose ring in a boat conformation. It has a single intramolecular H-bond, which leads to O(4)-H having a stretch frequency at 3606 cm^{-1}. All the other OH groups are free and contribute to the broad feature centered at ~3670 cm^{-1}. Similarly, spectrum i can be assigned to the β156b conformer, in which the Na^+ is binding to O(1), O(5), and O(6). The experimental 3625 cm^{-1} feature is assigned to the stretch of O(1)–H, which has a weak H-bond donation to O(2), exhibiting a slight redshift.

Next, we consider subtractions of two IR-IR spectra to yield a conformer-specific spectrum. Feature F in the one-laser spectrum is a partially resolved shoulder on the more intense feature E, and the probe laser frequency for spectrum f is only 13 cm^{-1} away from that for spectrum e. Therefore, a scaled spectrum e (see Figure 4.7) was subtracted from spectrum f to remove the minor features. The resulting spectrum agrees well with the calculated spectrum of conformer β34a. The redshifted 3379 cm^{-1} feature is assigned to the stretch of O(4)–H, which has a relatively strong H-bond with O(6). The strength of this H-bond is likely enhanced by the coordination of Na^+ to O(4), resulting in this ~300 cm^{-1} redshifted stretch. Spectrum c shows similar minor contributions from secondary structures. Again we see the weaker feature C is near the more strongly absorbing feature D. The probe laser frequency for spectrum c is only 10

Figure 4.5 Experimental (black) and calculated (red) spectra corresponding to individual conformations. The calculated geometries and energies are shown in Figure 4.6.

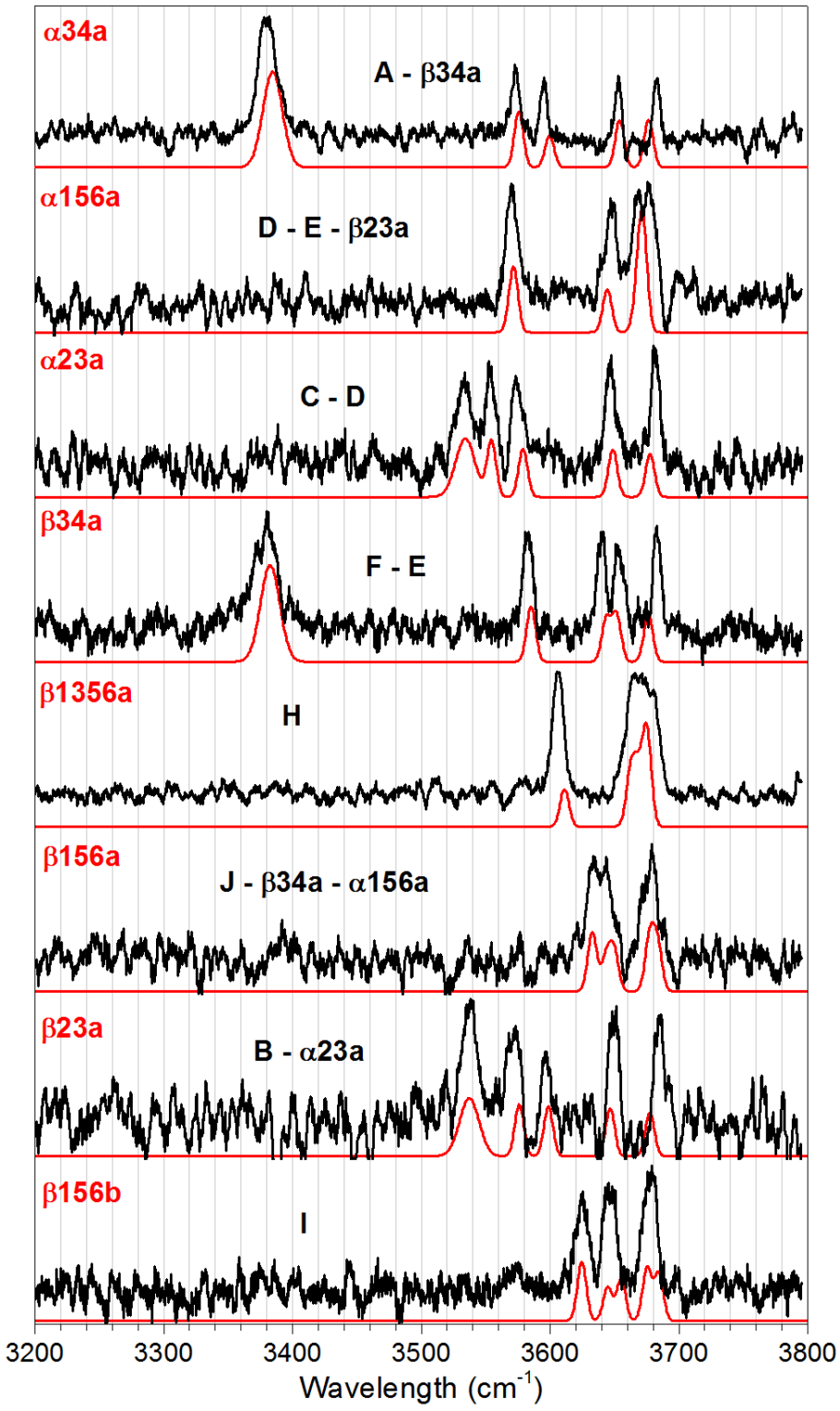

Figure 4.6 Calculated, at cam-B3LYP/def2TZVP with unscaled ZPE correction, structures and relative energies of Na^+(glucose) conformations relating to Figure 4.5. The relative energy of MP2 optimized geometries is included in parentheses. The energy of β34a is 5.1 (6.3) kJ/mol higher than α34a.

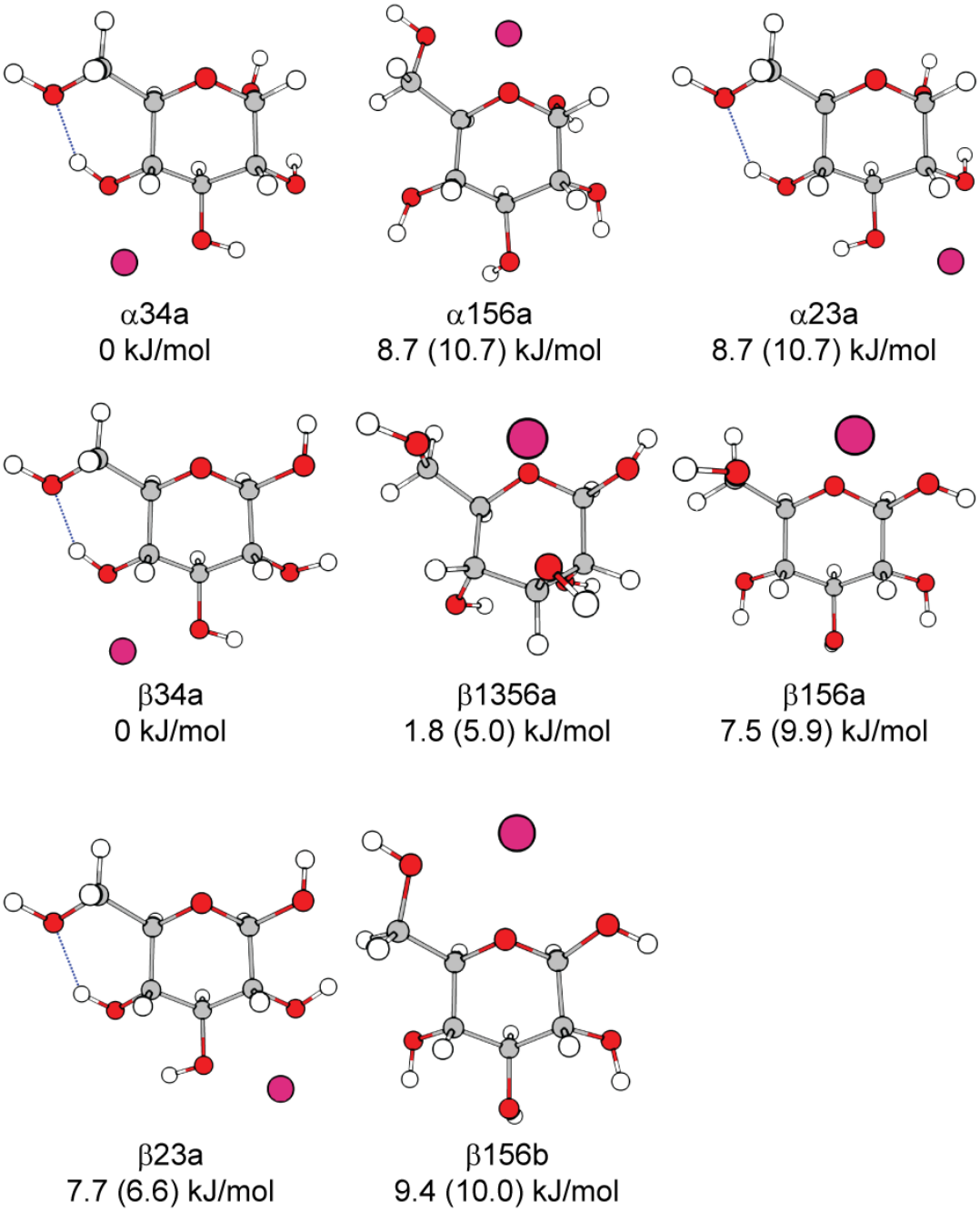

Table 4.2 Assignment of experimental OH stretch features from Figure 4.5. The experimental frequencies are listed in cm^{-1}.

	O(1)H	O(2)H	O(3)H	O(4)H	O(6)H
α34a	3653	3595	3573	3380	3683
α156a	3570	3647	3668/3678	3668/3678	3668/3678
α23a	3647	3554	3575	3533	3682
β34a	3654	3640	3582	3379	3683
β1356a	3662	3681	3671	3606	3681
β156a	3634	3646	3678	3646	3678
β23a	3649	3597	3571	3537	3685
β156b	3625	3646	3677	3646	3677

cm^{-1} from that of spectrum d. Subtraction (Figure 4.8) of a scaled spectrum d from spectrum c yielded a spectrum that is in good agreement with the calculated spectrum of α23a. The experimental 3533 cm^{-1} feature is assigned to the stretch of O(4)-H, H-bonded to O(6). The H-bond here is weaker compared to β34a because Na^+ is not directly interacting with O(4).

Next we utilize the spectra of conformers isolated thus far. As discussed above, at least two structures give rise to feature A, one being conformer β34a, which has already been identified. Subtraction of the β34a spectrum from spectrum a yields an experimental spectrum (Figure 4.9) that agrees very well with the calculated spectrum for α34a. The spectra of α34a and β34a show that both structures indeed have a ~3380 cm^{-1} vibrational mode. Similar subtraction of the α23a spectrum from spectrum b yielded an experimental spectrum (Figure 4.10) that agrees well with the calculated spectrum for β23a. The spectra of α23a and β23a show that both conformers have a vibrational mode near the 3534 cm^{-1} probe frequency.

The remaining structures require a more complex subtraction process. Spectrum d is an IR-IR spectrum with the probe laser fixed on the low frequency side of feature E. Nonetheless, spectrum d is quite distinctive from spectrum e, and exhibits the dominant presence of one conformation. Subtraction of spectrum e from d yields a spectrum with minor contributions that can be traced to β23a, the presence of which is expected due to its vibration at 3571 cm^{-1}. The result obtained by subtracting scaled spectra e and β23a from spectrum d (Figure 4.11) is in good agreement with the calculated spectrum of α156a. Finally, spectrum j was acquired with the probe laser fixed at 3635 cm^{-1}. Both β34a and α156a conformers have some intensity at that frequency and subtraction of scaled spectra of these two conformers from spectrum j (Figure 4.12) results in a spectrum in good agreement with the calculated spectrum of β156a. This

Figure 4.7 (Top) Subtraction of spectrum e from spectrum f to yield (Bottom) spectrum of conformer β34a.

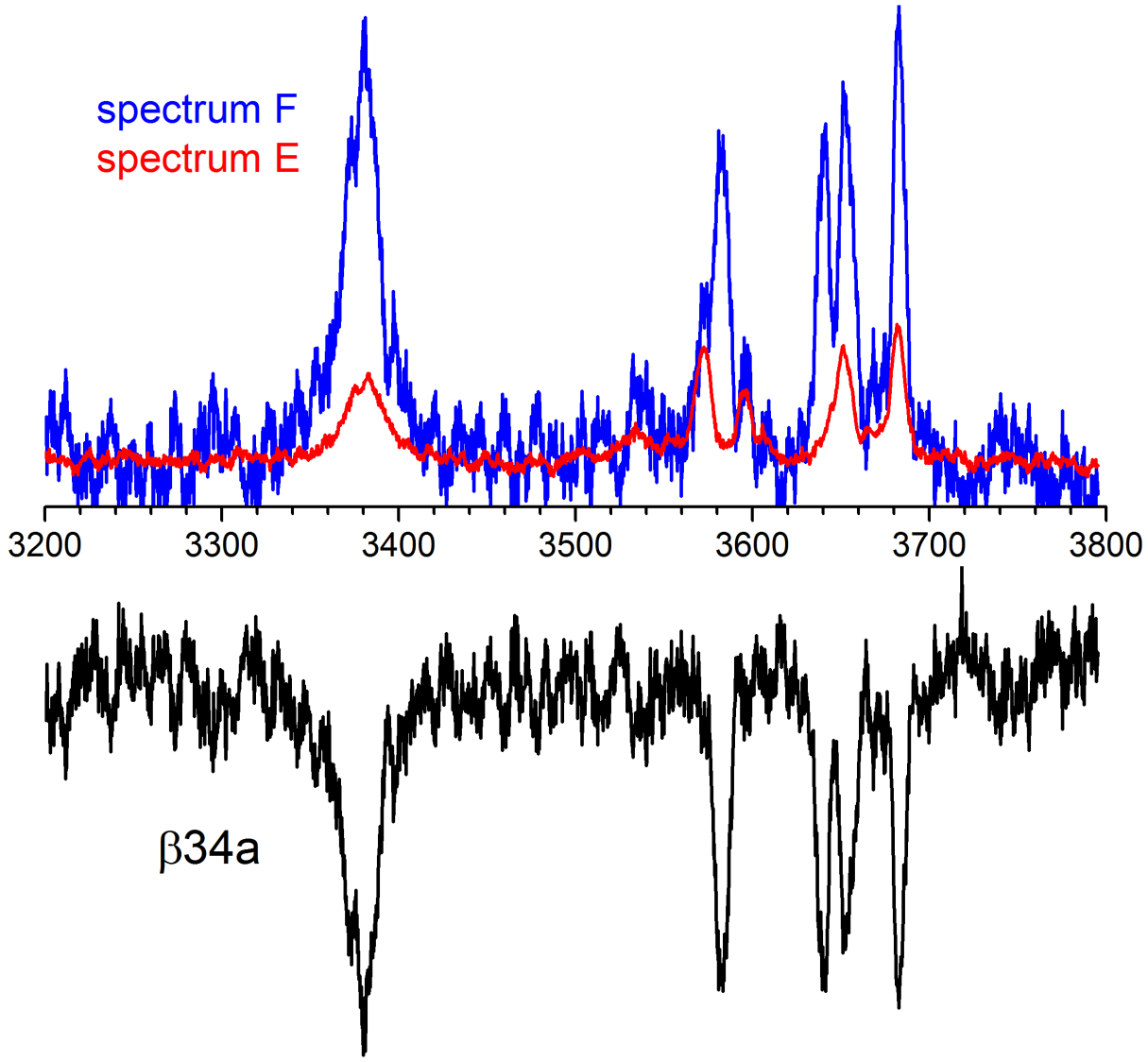

Figure 4.8 (Top) Subtraction of spectrum d from spectrum c to yield (Bottom) spectrum of conformer α23a.

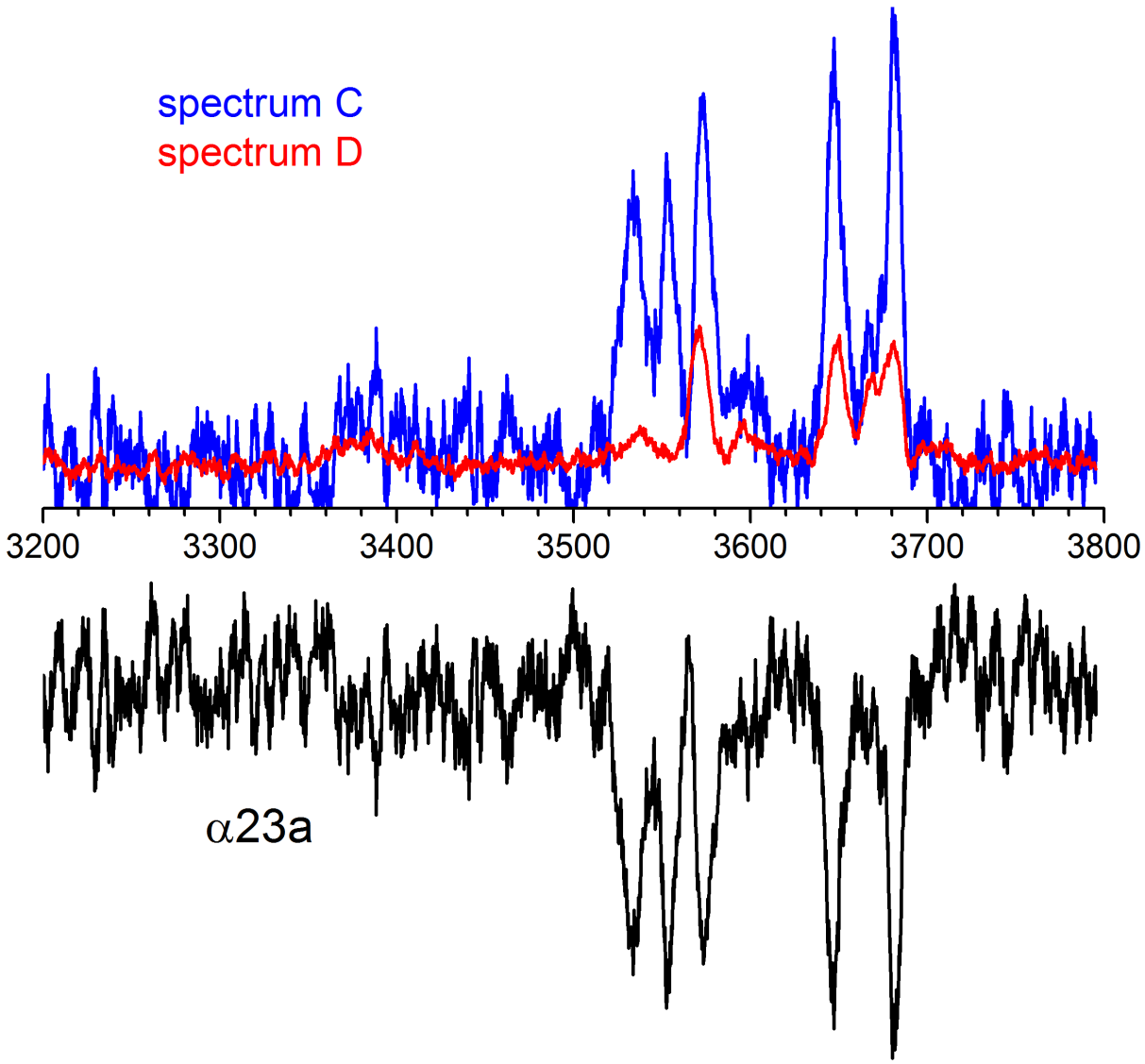

Figure 4.9 (Top) Subtraction of β34a spectrum from spectrum a to yield (Bottom) spectrum of conformer α34a.

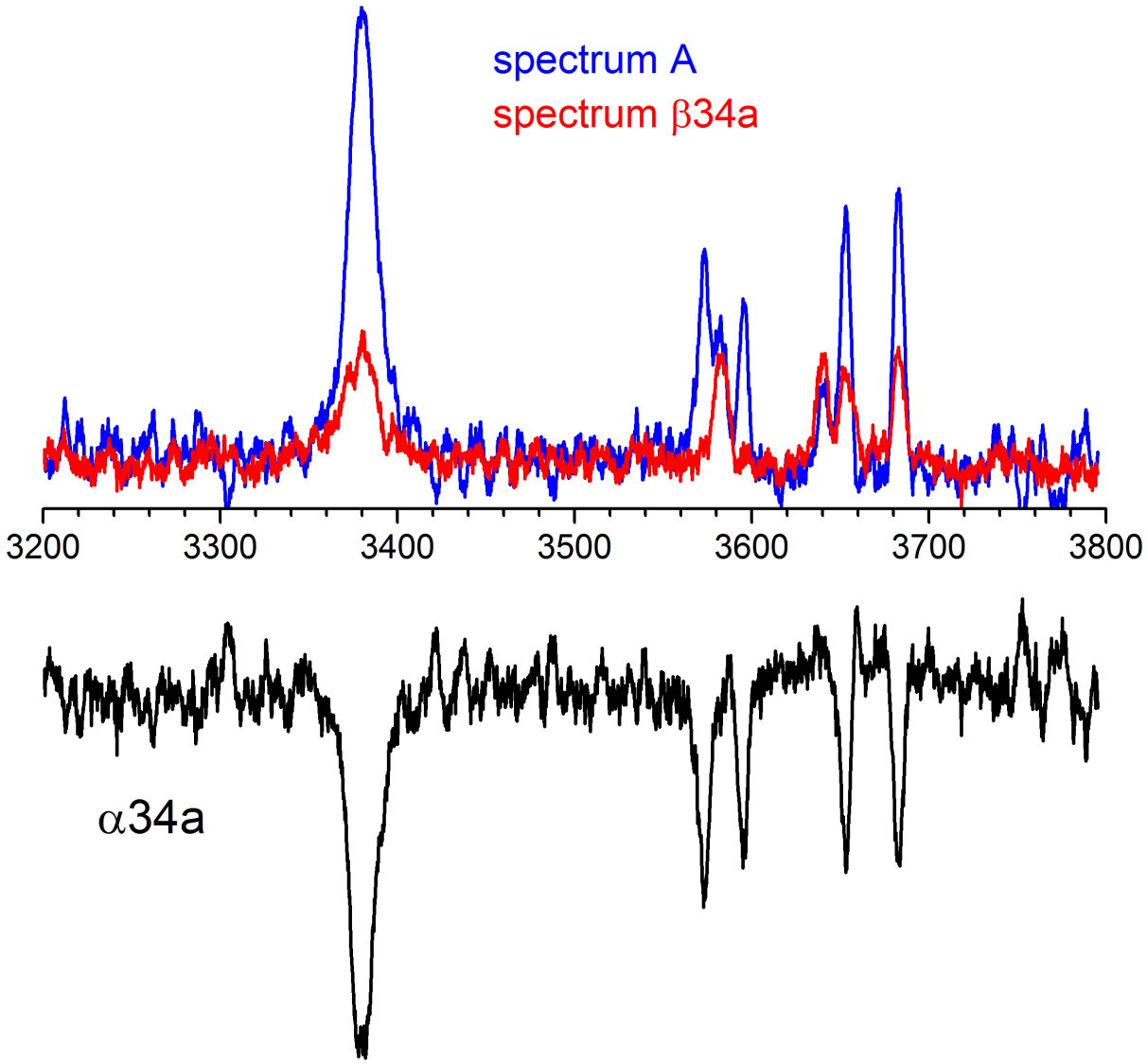

Figure 4.10 (Top) Subtraction of α23a spectrum from spectrum b to yield (Bottom) spectrum of conformer β23a.

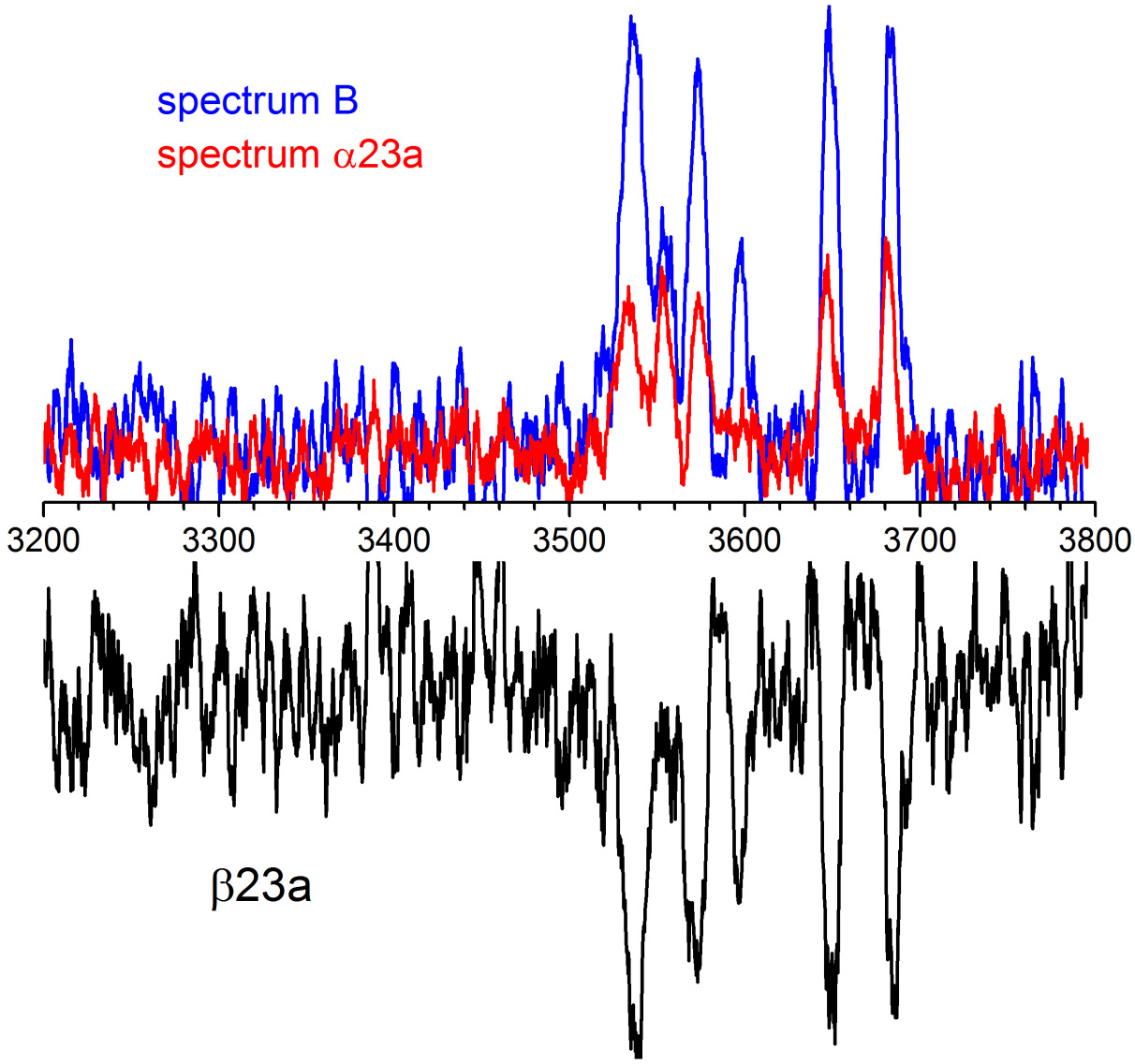

Figure 4.11 (Top) Subtraction of spectra e and β23a from spectrum d to yield (Bottom) spectrum of conformer α156a.

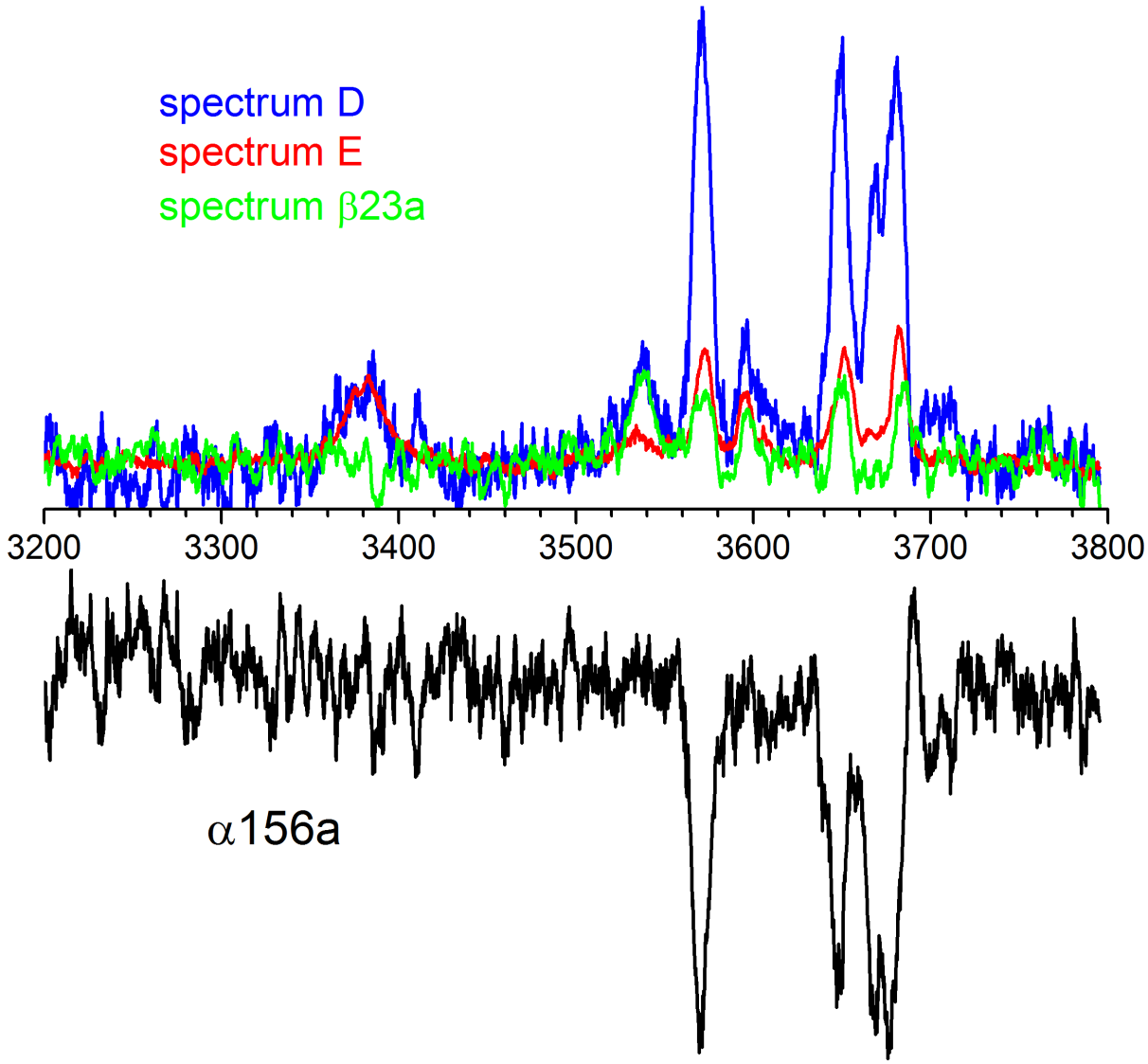

Figure 4.12 (Top) Subtraction of spectra β34a and α156a from spectrum j to yield (Bottom) spectrum of conformer β156a.

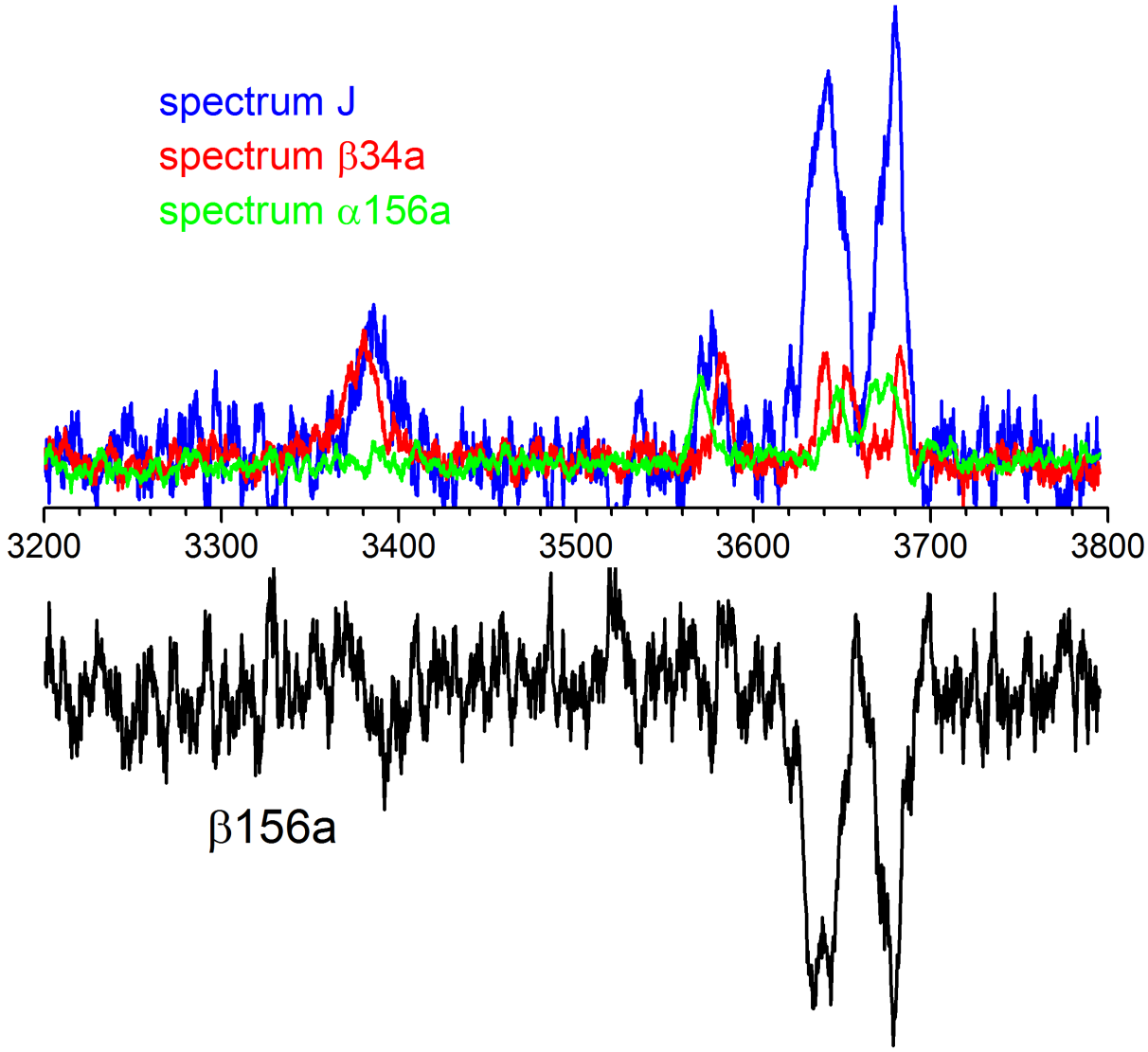

conformer is similar to β156b, differing mainly in the location of Na^+ relative to the pyranose ring.

4.5 Discussion

The analysis outlined above allowed us to identify and isolate the spectral signatures of eight distinct conformations of Na^+(glucose) contributing to the one-laser spectrum. Figure 4.13 shows a fit of the one-laser spectrum using the individual conformer-specific spectra displayed in Figure 4.5. We can see that all experimental features are well accounted for, and no conformer with significant contribution is missing.

The observed three α-anomers and five β-anomers (Figure 4.6) are among the lowest energy structures found in the calculations and are all within ~10 kJ/mol of the lowest energy conformer for each anomer. However, there are some low-energy conformers that are not observed experimentally here. For example, α34b is calculated to be 8.3 kJ/mol above α34a, and has the same Na^+ binding motif, differing mostly in the rotation of the O(2)H group. The barrier for isomerization to α34a involves a rotation of O(2)H that breaks the relatively weak H-bond to O(1). Therefore, α34b is not likely to survive the collisional cooling inside the cryogenic trap. Similarly, β1356b differs from β1356a by the orientation of the O(2)H and O(4)H groups, and is calculated to be 4.1 kJ/mol higher in energy. Again, isomerization, involving rotation of these OH groups, is likely relatively easy and we do not observe any significant contribution from β1356b in the experimental spectrum. In general, the experimentally observed conformers correspond to the lowest energy structure for a distinct anomer-specific Na^+ binding motif. Conversion between these conformers would require breaking at least one Na^+-O interaction (~100 kJ/mol at the cam-B3LYP/def2-tzvp level of theory), which is unlikely. The one exception

Figure 4.13 Fit of the one-laser spectrum using the individual conformer-specific spectra displayed in Figure 4.5.

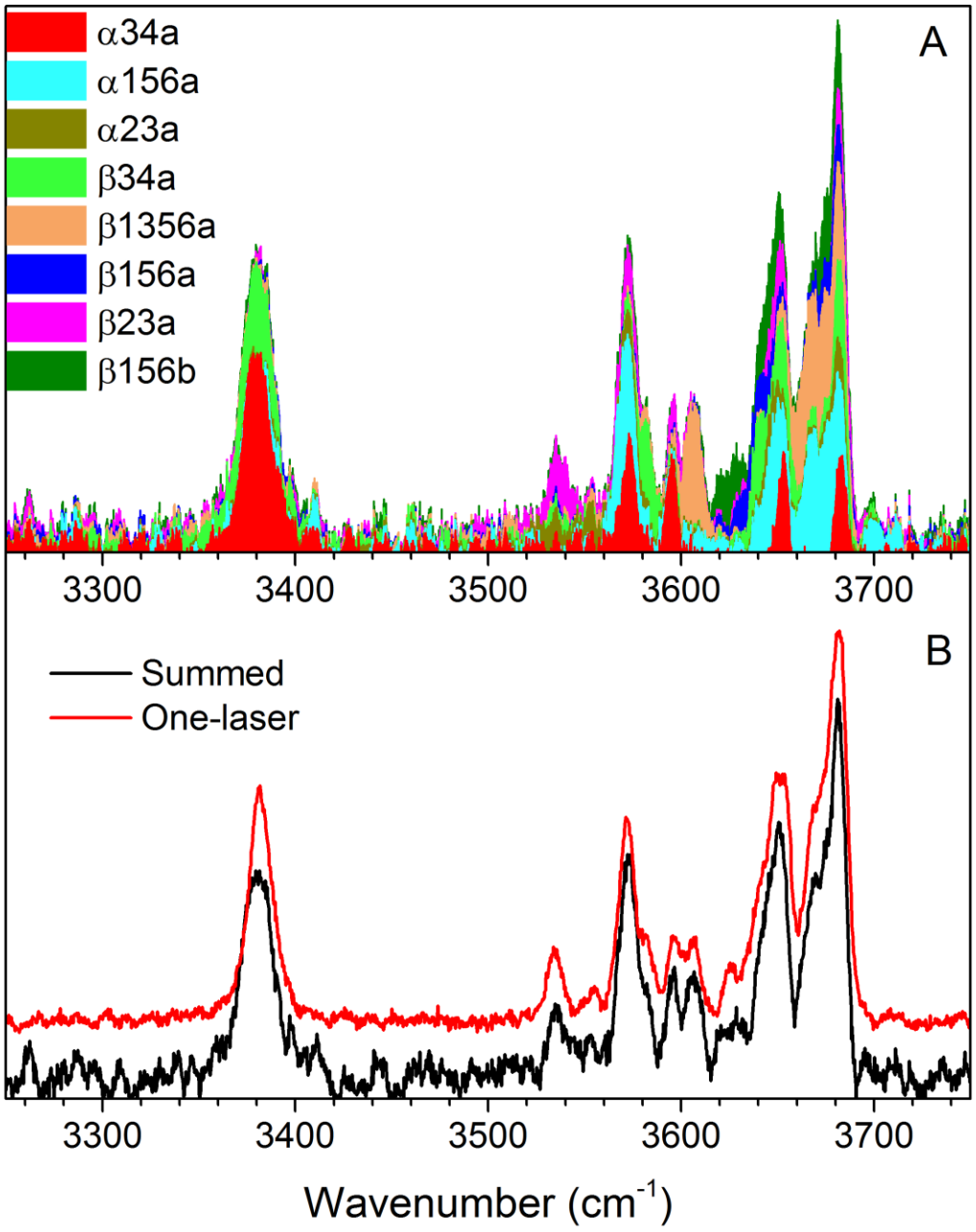

here is β156b, which differs from β156a mainly in the location of Na^+ relative to O(5) and associated rotations of O(6)H and O(1)H, and the barrier between these two conformations would not break any Na^+–O interactions. The presence of β156b can be explained by its energy, which is calculated to be only 2 kJ/mol higher than β156a at cam-B3LYP/def2TZVP and equal in energy at MP2/def2TZVP levels. Therefore, both conformations are expected to be present under the experimental conditions.

Due to the large barrier associated with the α-β mutarotation in the gas phase, we expect the α:β ratio to be close to the solution phase ratio of 36:64. However, the gas phase relative stabilities of these structures likely differ, and the more fragile conformers might be preferentially lost during transport or cooling. Moreover, because the absolute IR absorption cross-section cannot be readily determined experimentally, it is difficult to provide an exact experimental value of the relative population of each structure. One possible approach is to use laser-induced population transfer to determine the relative fractional population[41, 42] but the large number of conformers present in this situation, as well as their overlapping spectral features, make its application extremely complicated. Therefore, we approximate the relative populations in the one-laser IR spectrum in Figure 4.4 using calculated IR intensities. The fit shown in Figure 4.13 provides an estimate of relative contributions from the eight conformer-specific spectra. Individual conformer contributions are obtained by using fitted peak areas and scaling them by their calculated IR intensities. This provides five estimates of population for each conformation, one from each OH stretch, allowing us to obtain an averaged value and associated standard deviation. See Table 4.3 for further details. This analysis gave a relative abundance of α34a (15 ± 3%), α156a (21 ± 5%), α23a (6 ± 1%), β34a (13 ± 2%), β1356a (20 ± 9%), β156a (6 ± 0.3%), β23a (8 ± 2%), and β156b (11 ± 1%). Summing these relative abundance values, the

Table 4.3 Derivation of the relative populations of Na^+(glucose) conformers.

	Exp. Freq.[a]	Exp. Area[b]	Calc. Freq.[a]	Calc. Int.	Norm. Calc. Int.	Global fit[c]	Peak Contrib.[d]	Ave. (stdev)	% pop
α34a	3380	18.12	3386	483.76	4.306	0.379	1.59	**1.35** (0.27)	**0.15** (0.03)
	3573	4.76	3576	131.42	1.170		1.54		
	3595	2.81	3600	75.62	0.673		1.58		
	3653	2.53	3654	110.68	0.985		0.97		
	3683	2.82	3677	112.34	1.000		1.07		
α156a	3570	10.6	3572	154.91	1.379	0.252	1.94	**1.88** (0.43)	**0.21** (0.05)
	3647	9.6	3644	100.3	0.893		2.70		
	3668	17.9	3668	319.58	2.845		1.58		
	3678		3671				1.58		
	3678		3672				1.58		
α23a	3533	11.12	3534	295.3	2.629	0.072	0.30	**0.53** (0.13)	**0.06** (0.01)
	3554	7.61	3555	131.9	1.174		0.47		
	3575	7.98	3579	112.26	0.999		0.58		
	3647	8.87	3649	112	0.997		0.64		
	3682	8.26	3678	101.03	0.899		0.66		
							Total α population		**0.42**
β34h	3379	21.14	3383	487.71	4.341	0.188	0.91	**1.20** (0.15)	**0.13** (0.02)
	3582	7.71	3585	129.94	1.157		1.25		
	3640	6.44	3644	100.73	0.897		1.35		
	3654	6.76	3652	111.23	0.990		1.28		
	3683	6.48	3676	112.74	1.004		1.21		
β1356a	3606	11.73	3611	88.23	0.785	0.223	3.33	**1.79** (0.77)	**0.20** (0.09)
	3662	26.14	3662	463.9	4.129		1.41		
	3671		3668				1.41		
	3681		3674				1.41		
	3681		3676				1.41		
β156a	3634	17.54	3633	313.13	2.787	0.094	0.59	**0.57** (0.03)	**0.06** (0.00)
	3646		3644				0.59		
	3646		3650				0.59		
	3678	12.03	3677	235.69	2.098		0.54		
	3678		3683				0.54		
β23a	3537	16.46	3537	293.71	2.614	0.096	0.60	**0.72** (0.20)	**0.08** (0.02)
	3571	10.08	3576	121.44	1.081		0.89		
	3597	4.78	3599	117.22	1.043		0.44		
	3649	8.15	3647	112.4	1.001		0.78		
	3685	8.39	3677	102.09	0.909		0.88		
β156b	3625	9.23	3625	139.21	1.239	0.143	1.06	**0.96** (0.07)	**0.11** (0.01)
	3646	10.91	3645	176.55	1.572		0.99		
	3646		3655				0.99		
	3677	12.86	3675	235.63	2.097		0.87		
	3677		3684				0.87		
							Total β population		**0.58**

[a] in cm^{-1}

[b] Area of Gaussian peak fit of the IR-IR spectra in Fig. 4.5

[c] Ratios that yielded the best fit to the one-laser spectrum

[d] "Global fit" * "Exp. Area" / "Norm. Calc. Int."

one-laser spectrum in Figure 4.4 has an experimental α:β ratio of 42±9 : 58±13. The solution phase anomeric ratio is within the error bars, which indicates that the transfer to the gas phase may be indifferent to anomeric forms, despite their differences in gas-phase energetics. Note that while the observed conformations are among the lowest energy structures in the gas phase, their observed relative abundances are not reflective of their calculated gas-phase stabilities. Even without α/β isomerization in the gas phase, a Boltzmann distribution based on the calculated Gibb's free energy at 298 K would heavily favor α34a and β34a structures. Moreover, the presence of these eight structures is in general agreement with their relative calculated energies in solution[10] where they have smaller energy differences. This points to the experimental observation, to some degree, of kinetically trapped conformations derived from solution structures, although the preservation of these structures may be somewhat dependent on their gas-phase stabilities.

Lastly, we note that the OH stretch frequencies are indeed quite indicative of the local H-bonding environment. For example, in the present structures, O(6)H is either accepting an H-bond or coordinating with Na^+, with the hydrogen pointing away from the molecule. Correspondingly, the O(6)H stretch frequency is near the free OH stretch frequency in all conformers. In another example, comparing α34a and β34a, as well as α23a and β23a, we can see that the difference lies mainly in the stereocenter at C(1). In both pairs, the α-anomers exhibit a lower frequency for the O(2)H stretch, relating to the shorter O(2)H···O(1) induced by the axial position of the O(1)H group. The difference between α34a and β34a is 0.33 Å (2.258 Å versus 2.584 Å), resulting in a 45 cm^{-1} shift, while the difference between α23a and β23a is 0.22 Å (2.100 Å versus 2.320 Å), resulting in a 43 cm^{-1} shift. The relative shift is larger in the latter pair, likely due to Na^+ interaction with O(2). Figure 4.14 summarizes the consistent redshift

behaviors of the OH stretch, where the experimental frequencies exhibit an exponential dependence[43, 44] on the OH···O distance, relating to the strength of the H-bond. Coordination with Na^+ induces a further redshift, such that the H-bond is stronger at any given OH···O distance, and the asymptotic OH stretch frequency is 3677 cm^{-1} with Na^+ and 3686 cm^{-1} without. This well behaved in-situ probe can be a valuable tool to enable fast structural assignments in other similarly sodiated carbohydrate complexes.

Figure 4.14 Experimental OH stretch frequency as a function of OH···O distance. The fit to the function $y = y_0 - Ae^{-kx}$ is shown; (black trace: $y = 3686 - 8666e^{-2.093x}$; red trace: $y = 3677 - 24822e^{-2.483x}$)

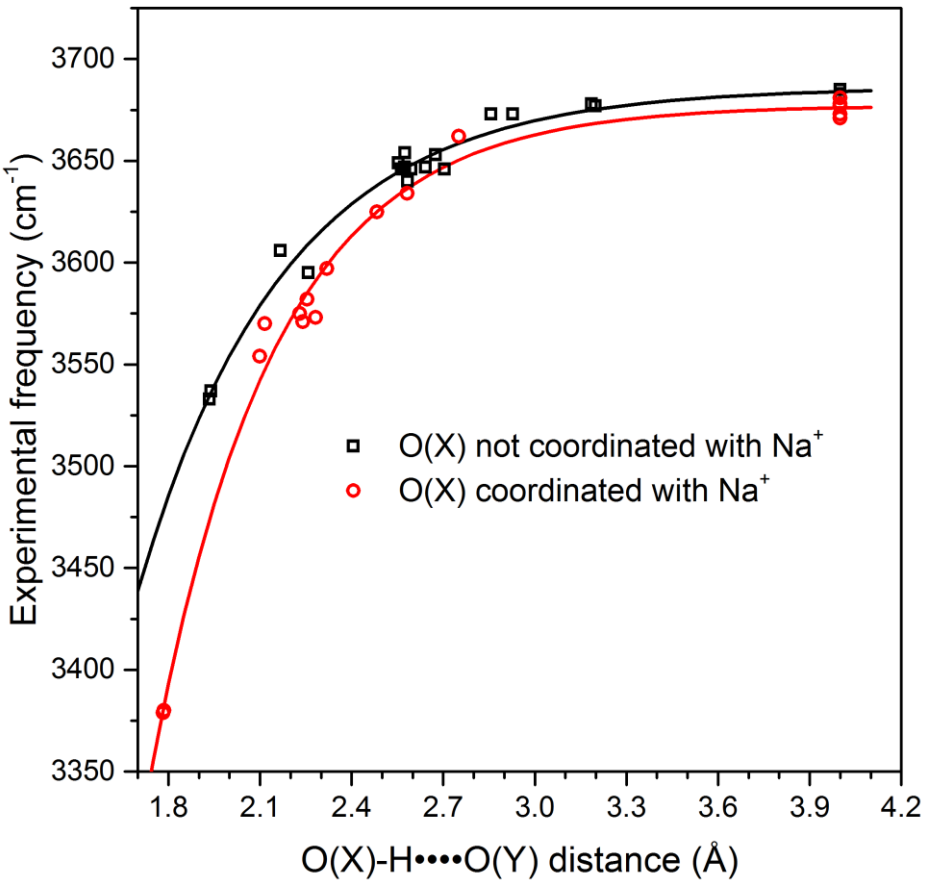

4.6 Conclusion

We have used a two-laser IR-IR double resonance approach to probe structurally complex Na^+(glucose) adducts. The current setup requires minimal modification to a typical cryogenic ion vibrational predissociation spectrometer, and the double resonance experiments can be carried out via either ion-dip or isomer-burning methods. The ion-dip study of the Na^+(glucose) complex revealed the presence of eight conformations in the one-laser IR predissociation spectrum. Calculations reveal that these three α-anomers and five β-anomers are among the lowest energy geometries with distinctive Na^+ binding sites. The difference in the C(1) stereocenter leads to more diversity in β-anomer conformations, but the general structures of these complexes are quite similar between the α- and β-anomers. Furthermore, the overall ratio between the two anomers is similar to the solution phase value, with β-anomers having a higher presence despite their higher gas-phase energies. The results also reveal that collisional cooling removes conformations that are connected by lower barriers, i.e., those involving relatively weak intramolecular H-bonds, while higher barriers allow high-energy structures to be preserved. Comparisons between experimental spectra and calculated geometries show the experimental OH stretch frequencies can directly provide structural information relating to intramolecular H-bonding. Lastly, in applications to larger polysaccharide systems, the increased structural diversity and metal ion binding sites can potentially lead to an increased number of conformations. However, the number of observed kinetically trapped structures is ultimately determined by the size of the barriers connecting them. To obtain conformer-specific information for more complex species, it is likely necessary to extend our approach to include the fingerprint region (600–1500 cm^{-1}). Ultimately, one would want to collect a full 2D correlated IR map and use covariance analysis to tackle systems with large numbers of conformations.

4.7 References

1. M.J. Kailemia, L.R. Ruhaak, C.B. Lebrilla, I.J. Amster, *Anal. Chem.,* **2014,** 86, 196–212

2. E. Combs, B. Cinlar, Y. Pagan-Torres, J.A. Dumesic, B.H. Shanks, *Catal. Commun.*, 2**013,** 30, 1–4

3. P. Gallezot, *Chem. Soc. Rev.*, **2012,** 41, 1538–1558

4. S.D. Zhu, Y.X. Wu, Q.M. Chen, Z.N. Yu, C.W. Wang, S.W. Jin, Y.G. Ding, G. Wu, *Green Chem.*, **2006**, 8, 325–327

5. C. Masellis, N. Khanal, M.Z. Kamrath, D.E. Clemmer, T.R. Rizzo, *J. Am. Soc. Mass Spectrom.*, **2017**. https://doi.org/10.1007/s13361-017-1728-6

6. C.E. Lin, C.J. Yu, C.L. Chen, L.D. Chou, C. Chou, *J. Phys. Chem. A.,* **2010,** 114, 1665–1669

7. B.E. Lewis, N. Choytun, V.L. Schramm, A.J. Bennett, *J. Am. Chem. Soc.,* **2006,** 128, 5049–5058

8. A.M. Silva, E.C. da Silva, C.O. da Silva, *Carbohydr. Res.*, **2006,** 341, 1029–1040

9. A.L. Heaton, P.B. Armentrout, *J. Phys. Chem. A.,* **2008,** 112, 10156–10167

10. H.B. Mayes, J. Tian, M.W. Nolte, B.H. Shanks, G.T. Beckham, S. Gnanakaran, L.J. Broadbelt, *J. Phys. Chem. B.,* **2014,** 118, 1990–2000

11. S.E. Barrows, J.W. Storer, C.J. Cramer, A.D. French, D.G. Truhlar, *J. Comput. Chem.*, **1998,** 19, 1111–1129

12. C.J. Cramer, D.G. Truhlar, A.D. French, *Carbohydr. Res.,* **1997,** 298, 1– 14

13. R.C. Dunbar, *Mass Spectrom. Rev.*, **2004,** 23, 127–158

14. J.M. Lisy, *J. Chem. Phys.*, **2006,** 125, 132302

15. J. Oomens, B.G. Sartakov, G. Meijer, G. Von Helden, *Int. J. Mass Spectrom.,* **2006,** 254, 1–19

16. N.C. Polfer, *Chem. Soc. Rev.,* **2011,** 40, 2211–2221

17. A.B. Wolk, C.M. Leavitt, E. Garand, M.A. Johnson, *Acc. Chem. Res.,* **2014,** 47, 202–210

18. T.S. Zwier, *J. Phys. Chem. A.*, **2006,** 110, 4133–4150

19. T.R. Rizzo, J.A. Stearns, O.V. Boyarkin, *Int. Rev. Phys. Chem.,* **2009,** 28, 481–515

20. K.R. Asmis, D.M. Neumark, *Acc. Chem. Res.,* **2012,** 45, 43–52

21. E. Garand, M.Z. Kamrath, P.A. Jordan, A.B. Wolk, C.M. Leavitt, A.B. McCoy, S.J. Miller, M.A. Johnson, *Science.,* **2012,** 335, 694–698

22. B.J. Knurr, J.M. Weber, *J. Am. Chem. Soc.,* **2012,** 134, 18804–18808

23. E.M. Duffy, B.M. Marsh, E. Garand, *J. Phys. Chem. A.,* **2015,** 119, 6326–6332

24. S. Heiles, R.J. Cooper, M.J. DiTucci, E.R. Williams, *Chem. Sci.,* **2015,** 6, 3420–3429

25. E.M. Duffy, B.M. Marsh, J.M. Voss, E. Garand, *Angew. Chem. Int. Ed.,* **2016,** 55, 4079–4082

26. E.J. Cocinero, P. Carcabal, T.D. Vaden, J.P. Simons, B.G. Davis, *Nature*, **2011,** 469, 76–79

27. W.Y. Sohn, S. Ishiuchi, M. Miyazaki, J. Kang, S. Lee, A. Min, M.Y. Choi, H. Kang, M. Fujii, *Phys. Chem. Chem. Phys.,* **2013,** 15, 957–964

28. B.M. Elliott, R.A. Relph, J.R. Roscioli, J.C. Bopp, G.H. Gardenier, T.L. Guasco, M.A. Johnson, *J. Chem. Phys.,* **2008,** 129, 094303

29. C.M. Leavitt, A.B. Wolk, J.A. Fournier, M.Z. Kamrath, E. Garand, M.J. Van Stipdonk, M.A. Johnson, *J. Phys. Chem. Lett.,* **2012,** 3, 1099–1105

30. N. Heine, M.R. Fagiani, M. Rossi, T. Wende, G. Berden, V. Blum, K.R. Asmis, *J.Am. Chem. Soc.,* **2013,** 135, 8266–8273

31. R.A. Relph, T.L. Guasco, B.M. Elliott, M.Z. Kamrath, A.B. McCoy, R.P. Steele, D.P. Schofield, K.D. Jordan, A.A. Viggiano, E.E. Ferguson, M.A. Johnson, *Science.,* **2010,** 327, 308–312

32. N. Heine, M.R. Fagiani, K.R. Asmis, *J. Phys. Chem. Lett.,* **2015,** 6, 2298–2304

33. N. Heine, K.R. Asmis, *Int. Rev. Phys. Chem.* **2015,** 34, 1–34

34. M.R. Fagiani, H. Knorke, T.K. Esser, N. Heine, C.T. Wolke, S. Gewinner, W. Schollkopf, M.P. Gaigeot, R. Spezia, M.A. Johnson, K.R. Asmis, *Phys. Chem. Chem. Phys.* **2016,** 18, 26743–26754

35. A.V. Iogansen, *Spectrochim. Acta, Part A.,* **1999,** 55, 1585–1612

36. M. Rozenberg, A. Loewenschuss, Y. Marcus, *Phys. Chem. Chem. Phys.*, **2000,** 2, 2699–2702

37. M. Rozenberg, G. Shoham, I. Reva, R. Fausto, *Phys. Chem. Chem. Phys.*, **2005,** 7, 2376–2383

38. B.M. Marsh, J.M. Voss, E. Garand, *J. Chem. Phys.*, **2015,** 143, 204201

39. M.J. Frisch, G.W. Trucks, H.B. Schlegel, G.E. Scuseria, M.A. Robb, J.R. Cheeseman, G. Scalmani, V. Barone, B. Mennucci, G.A. Petersson, H. Nakatsuji, M. Caricato, X. Li, H.P. Hratchian, A.F. Izmaylov, J. Bloino, G. Zheng, J.L. Sonnenberg, M. Hada, M. Ehara, K. Toyota, R. Fukuda, J. Hasegawa, M. Ishida, T. Nakajima, Y. Honda, O. Kitao, H. Nakai, T. Vreven, J.A. Montgomery, J.E. Peralta, F. Ogliaro, M. Bearpark, J.J. Heyd, E. Brothers, K.N. Kudin, V.N. Staroverov, R. Kobayashi, J. Normand, K. Raghavachari, A. Rendell, J.C. Burant, S.S. Iyengar, J. Tomasi, M. Cossi, N. Rega, J.M. Millam, M. Klene, J.E. Knox, J.B. Cross, V. Bakken, C. Adamo, J. Jaramillo, R. Gomperts, R.E. Stratmann, O. Yazyev, A.J. Austin, R. Cammi, C. Pomelli, J.W. Ochterski, R.L. Martin, K. Morokuma, V.G. Zakrzewski, G.A. Voth, P. Salvador, J.J. Dannenberg, S. Dapprich, A.D. Daniels, O. Farkas, J.B. Foresman, J.V. Ortiz, J. Cioslowski, D.J. Fox: Gaussian 09: Wallingforf CT, **2009**

40. T. Shimanouchi, Molecular vibrational frequencies, in: NIST chemistry webBook, NIST standard reference database number 69; Linstrom, P.J., Mallard, W.G., Eds. National Institute of Standards and Technology, Gaithersburg, MD 20899 (**Accessed: 2017**)

41. B.C. Dian, J.R. Clarkson, T.S. Zwier, *Science*, **2004,** 303, 1169–1173

42. C. Seaiby, A.V. Zabuga, A. Svendsen, T.R. Rizzo, *J. Chem. Phys.*, **2016,** 144, 014304

43. E. Libowitzky, *Monatsh. Chem.*, **1999,** 130, 1047–1059

44. W. Mikenda, *J. Mol. Struct.*, **1986,** 147, 1–15

CHAPTER 5

Revealing the Structure of Isolated Peptides: IR-IR Predissociation Spectroscopy of Protonated Triglycine Isomers

Published: J.M. Voss, K.C. Fischer, and E. Garand. *Journal of Molecular Spectroscopy*, 347, 28 – 34 (2018)

Abstract

We report an isomer specific IR-IR double resonance study of the mass-selected protonated triglycine peptide. Comparison of experimental spectra with calculations reveals the presence of two isomers, with protonation occurring at either the terminal amine site or one of the amide oxygen sites. The amine protonated isomer identified in our experiment contains an atypical *cis* amide configuration as well as a more typical *trans* amide. The amide protonated peptide, on the other hand, contains two *trans* amide moieties. Both isomers are found to be the lowest energy structures for their respective protonation site, but it is unclear, from experiments and calculations, which one is the global minimum. The presence of both in our experiments likely points to kinetic trapping of a higher energy structure. Finally, the observed frequencies of the N-H and O-H stretch vibrations are used to estimate the hydrogen-bond strengths present in each isomer, accounting for the relative stabilities of these structures.

Author Contributions

JMV and KCF acquired experimental spectra; JMV performed theoretical calculations and data analyses; JMV and EG wrote the manuscript.

5.1 Introduction

With multiple amide linkages connecting the amine and carboxyl terminals, there are a myriad of intramolecular interactions, such as hydrogen-bonding, present in a peptide. Various combinations of these interactions govern the relative stabilities of different structures, providing the flexibility that allows a peptide to structurally adapt to different environments. Studying these interactions at the molecular level can therefore reveal how three-dimensional structures and functionalities are regulated in larger species in specific environments. For instance, one of the simplest model peptides, protonated triglycine (Gly_3H^+), exhibits some interesting competing stability factors in the gas phase. Observations of protonation at either the amine nitrogen N^1 or amide oxygen O^1 site (see Figure 5.1) have been reported.[1,2] The latter is surprising for this small peptide because the gas phase proton affinity of an amide is ~23 kJ/mol less than that of an amine,[3] indicating that an amine protonated Gly_3H^+ structure should be considerably more stable. The observation of an O^1-protonated isomer therefore points to the presence of stronger intramolecular interactions that make this structure energetically competitive. Numerous isomers are possible even for this small peptide, and inaccuracies associated with calculating non-covalent interactions make it difficult to predict the exact energetic ordering.[4] Therefore, experimentally probing the precise structure of each isomer can provide valuable insights into their relative stabilities and the strengths of the related intramolecular interactions.

Mass spectrometry (MS) is often used to characterize higher order structures in biological systems, especially in combination with other methods such as ion mobility,[5-7] hydrogen/deuterium exchange,[8-10] or chemical cross-linking.[11,12] In such experiments, electrospray ionization (ESI)[13,14] is generally employed to gently transfer the species of interest to the gas phase. Moreover, by combining vibrational spectroscopy with MS, it is possible to probe the structures

and specific non-covalent interactions present in a peptide. Such studies have been carried out via infrared multiple photon dissociation (IRMPD) spectroscopy,[1,15-19] UV-IR double resonance spectroscopy,[20-23] and cryogenic ion vibrational predissociation spectroscopy (CIVS).[24-27] In previous studies[1,2] of the Gly_3H^+ system via IRMPD in the 1050–1900 cm^{-1} region, the results indicated the presence of at least two isomers, one with a bent N^1-protonated structure and another linear structure with protonation occurring between adjacent amide C=O groups.

Here, we present the isomer-specific IR-IR double resonance CIVS spectroscopy of protonated triglycine. The IR-IR approach is an extension of CIVS that allows for isomer selective spectroscopy of any mass-selected ions.[24,28] Moreover, the use of a cryogenic ion trap and weakly-bound D_2 as messenger tags ensure low internal energies in the Gly_3H^+ ions, minimizing spectral broadening and congestion, as well as reducing the number of isomers present. The resulting isomer-specific vibrational spectra in a broad 1000–3800 cm^{-1} spectral window provide unambiguous identification of the structures present. We further characterize the N-H and O-H (hydrogen-bond donor) stretch vibrations to reveal the strength of the intramolecular interactions present in each isomer.

Figure 5.1 An example of a neutral triglycine molecule showing the numbering scheme of N and O groups starting from the amine terminal.

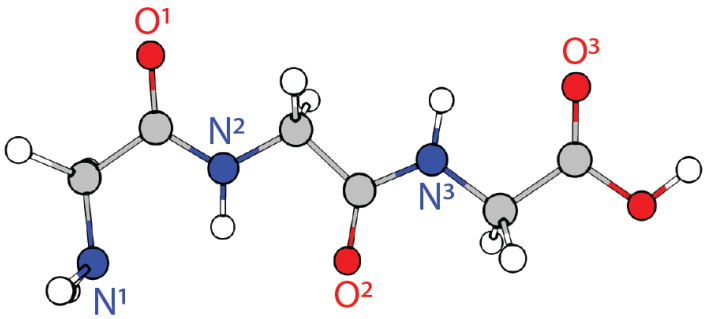

5.2 Experimental Details

The infrared spectra of Gly_3H^+ were obtained using our homebuilt cryogenic ion vibrational spectrometer described in detail previously.[29] Briefly, ESI of a ~1 mM solution of triglycine in methanol with a trace amount of formic acid was used to generate the Gly_3H^+ ions. The ions were transferred through several differentially pumped regions by a series of hexapole ion guides and biased apertures into a 3D quadrupole ion trap held at 10 K by a closed-cycle helium cryocooler. A pulsed solenoid valve introduced a ~1 ms burst of helium buffer gas, seeded with 10% D_2, into the trap volume, which thermalized the trapped ions and formed weakly bound D_2-tagged adducts. To acquire the one-laser IR predissociation spectrum, the $Gly_3H^+(D_2)$ complexes were ejected into the time-of-flight (TOF) mass spectrometer, mass selected via a gated deflector, and intersected with the output of a Nd:YAG pumped tunable OPO/OPA laser. Resonant absorption of a single photon was sufficient to induce the dissociation of the D_2 tag. The Gly_3H^+ photofragments were separated from $Gly_3H^+(D_2)$ in a two-stage reflectron, and photofragment intensity was monitored as a function of photon wavelength to yield the IR spectrum. The intensities in each spectral region, i.e. the 1000–2300 cm^{-1} and 2800–3800 cm^{-1} regions, are normalized to the most intense feature in the respective region.

To acquire isomer-specific IR-IR ion-dip spectra, detailed in Reference 28, the output of another Nd:YAG pumped tunable OPO/OPA laser, i.e. the “pump laser”, intersected the trapped ions at the center of the 10 K 3D ion trap. The pump laser was triggered ~90 ms after the introduction of the buffer gas to ensure no new tagged adducts could form after photofragmentation, and all trapped ions were ejected into the TOF region ~5 ms after the pump laser. In these experiments, the “probe laser”, i.e. the laser intersecting the D_2-tagged ions inside the TOF region, was fixed at a frequency resonant with a specific vibration while the pump laser

was scanned. When the pump laser frequency was resonant with a vibration belonging to the same structure as the probed transition, the depletion of that structure inside the ion trap led to a dip in the probed photofragment signal. This ion-dip as a function of pump laser frequency yielded the isomer specific spectra.

5.3 Computational Details

The ten lowest-energy structures found by Mookherjee et al.[4] via an extensive search, which also included structures found by Wu and McMahon[1] and Li et al.,[30] were re-optimized with various DFT methods and MP2 using several different basis sets. All calculations were carried out using Gaussian 16.[31] For clarity, we will name the structures according to the protonation site and configuration of the amide groups. The O^t and N^t isomers have protonation at the amide ($C{=}O^1$) or amine (N^1) site, respectively, with both amides in *trans* configuration, while the N^c isomers are protonated at N^1 and have one amide in *cis* configuration. Within each series, the structures are alphabetized according to their relative energies. All the DFT calculations resulted in O^tA as the lowest energy isomer, while MP2 predicts N^cA as the lowest in energy. Despite this disagreement, the various levels of theory point to the same six structures as the lowest energy isomers (see Figure 5.2 and Table 5.1). We will focus on these structures as we make spectral assignments.

Based on the general good agreement in the cam-B3LYP/def2TZVPP harmonic spectra (see Figures 5.3 and 5.4) they are used for comparison with experimental IR spectra in the following discussions. Calculations further show that the D_2 tag has only minor perturbations on the Gly_3H^+ vibrational spectrum, as shown in Figures 5.5 and 5.6. For simplicity, the bare Gly_3H^+ harmonic spectra are used in our analyses. To scale the harmonic spectra, we compared the calculated frequencies of the O^tA isomer carboxyl group OH and CO stretches to those found

Figure 5.2 Six lowest energy Gly_3H^+ structures along with cam-B3LYP/def2TZVPP relative energies (in kJ/mol, unscaled ZPE corrected). MP2/def2TZVPP energies (in kJ/mol, unscaled ZPE corrected) are included in parentheses.

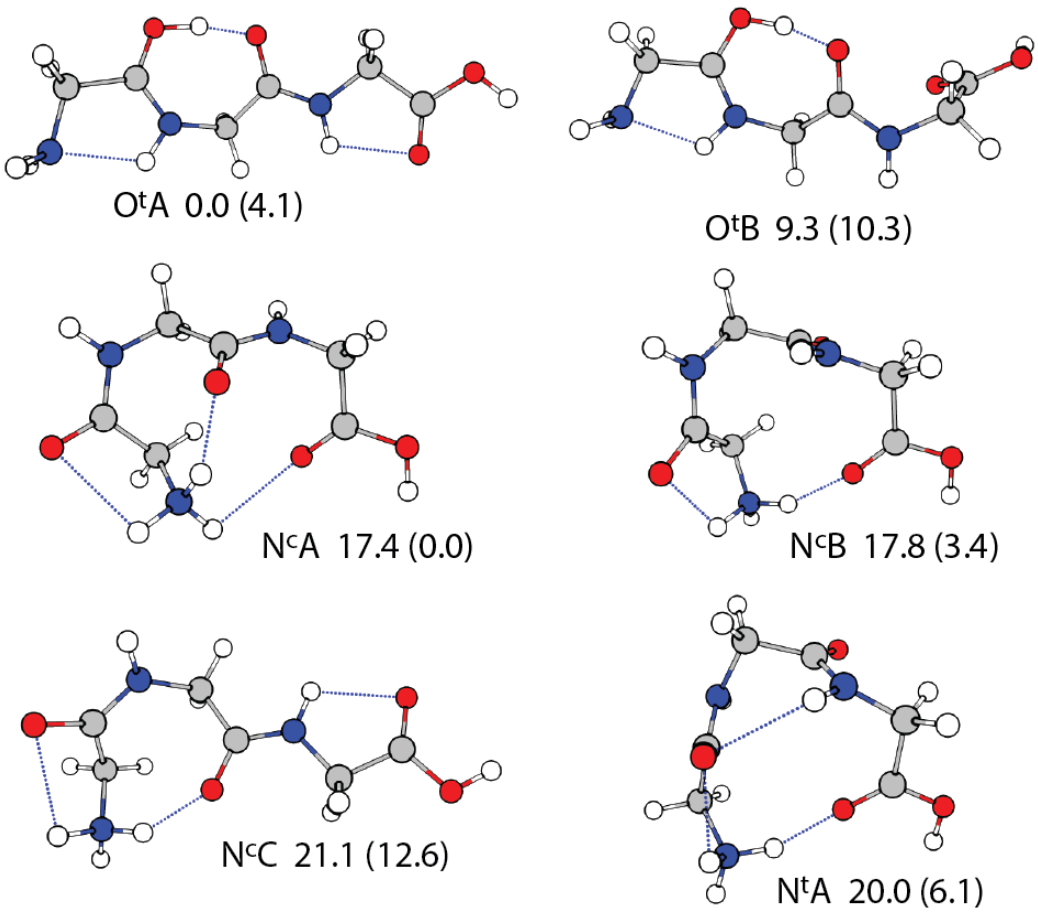

Table 5.1 Relative energies (kJ/mol) of the ten lowest energy Gly_3H^+ structures found. The structures are optimized at the specified levels, and the energies include unscaled ZPE correction.

	Mookherjee structures[a]	**B3LYP /def2TZVPP**	**cam-B3LYP /def2TZVPP**	**wB97XD /def2TZVPP**	**MP2 /6-311+g[b]**	**MP2 /def2TZVPP**	**CCSD /6-31++g[b]**
O^tA	$[O^{1t}]$-ctgttttt	0.0	0.0	0.0	13.6	4.1	10.6
O^tB	$[O^{1t}]$-ctgttgtt	9.3	9.3	7.8	16.4	10.3	13.0
N^cA	$[N^1]$-gcgttgtt	20.2	17.4	3.8	0.0	0.0	0.0
N^cB	$[N^1]$-tcgctgtt	19.6	17.8	3.7	6.4	3.4	7.4
N^cC	$[N^1]$-gcgttttt	19.6	21.1	13.2	15.2	12.6	-
N^cD	$[N^1]$-gcgttgtc	39.0	36.3	21.6	19.7	17.9	-
N^tA	$[N^1]$-ttggtgtt	21.0	20.0	8.5	6.2	6.1	6.0
N^tB	$[N^1]$-ttggtgtc	31.5	30.4	17.8	16.7	15.6	-
N^tC	$[N^1]$-ttgctgtt	33.5	32.7	21.6	20.3	19.1	-
N^tD	$[N^1]$-gtgttttt	28.2	28.6	21.2	20.0	18.8	-

[a] Nomenclatures from Reference 4
[b] Values from Reference 30

Figure 5.3 Comparison of the experimental ion-dip spectrum associated with the 3480 cm^{-1} feature and harmonic spectra of the bare $N^cA\ Gly_3H^+$ structure calculated at different levels of theory. The methods used are given in each panel, with lower and upper frequency range scaling given in parentheses, respectively. To scale the harmonic spectra, we compared the calculated frequencies of the O^tA isomer carboxyl group OH and CO stretches to those found experimentally.

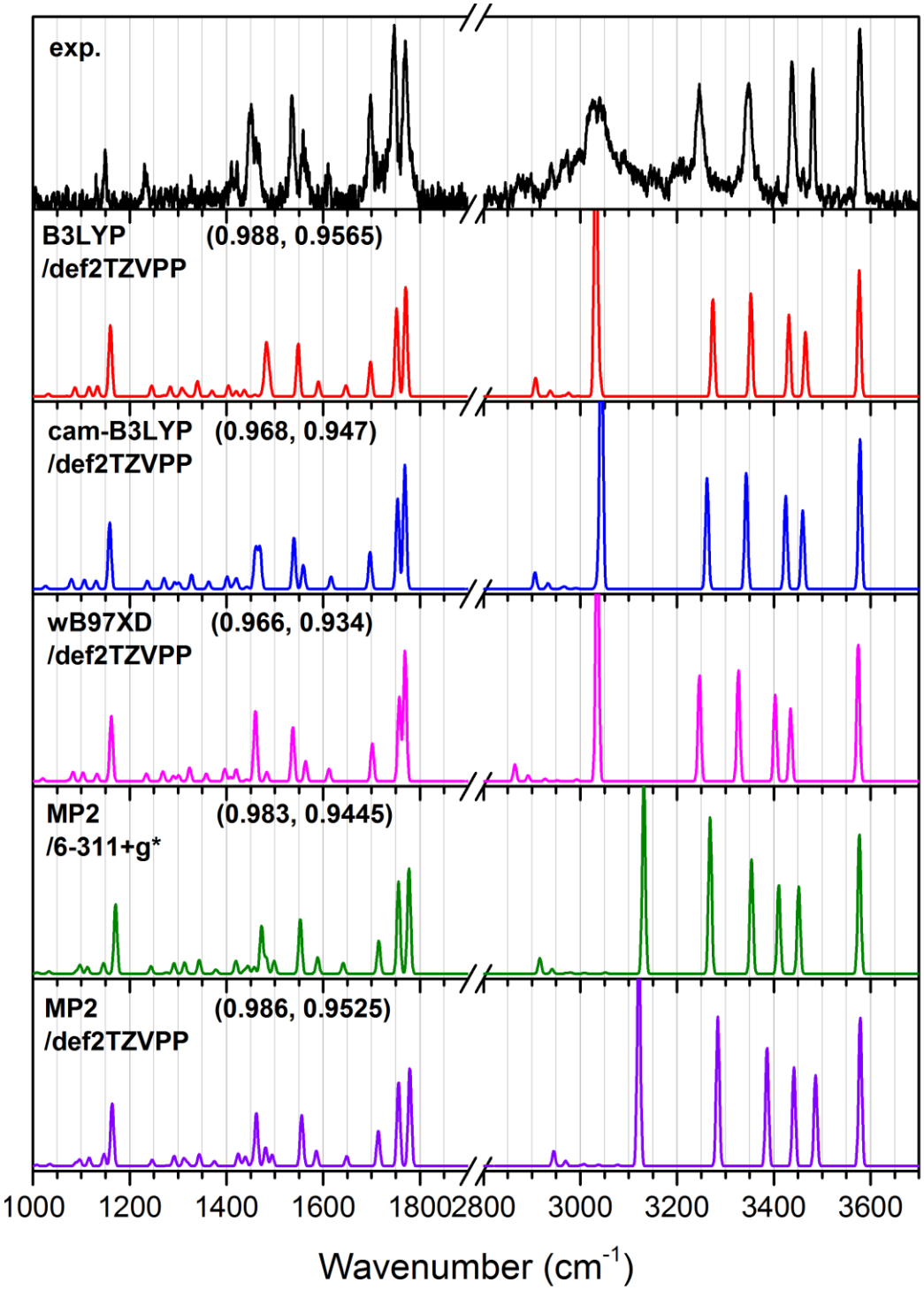

Figure 5.4 Comparison of the experimental ion-dip spectrum associated with the 3200 cm^{-1} feature and harmonic spectra of the bare O^tA Gly_3H^+ structure calculated at different levels of theory. The methods used are given in each panel, with lower and upper frequency range scaling given in parentheses, respectively. To scale the harmonic spectra, we compared the calculated frequencies of the O^tA isomer carboxyl group OH and CO stretches to those found experimentally.

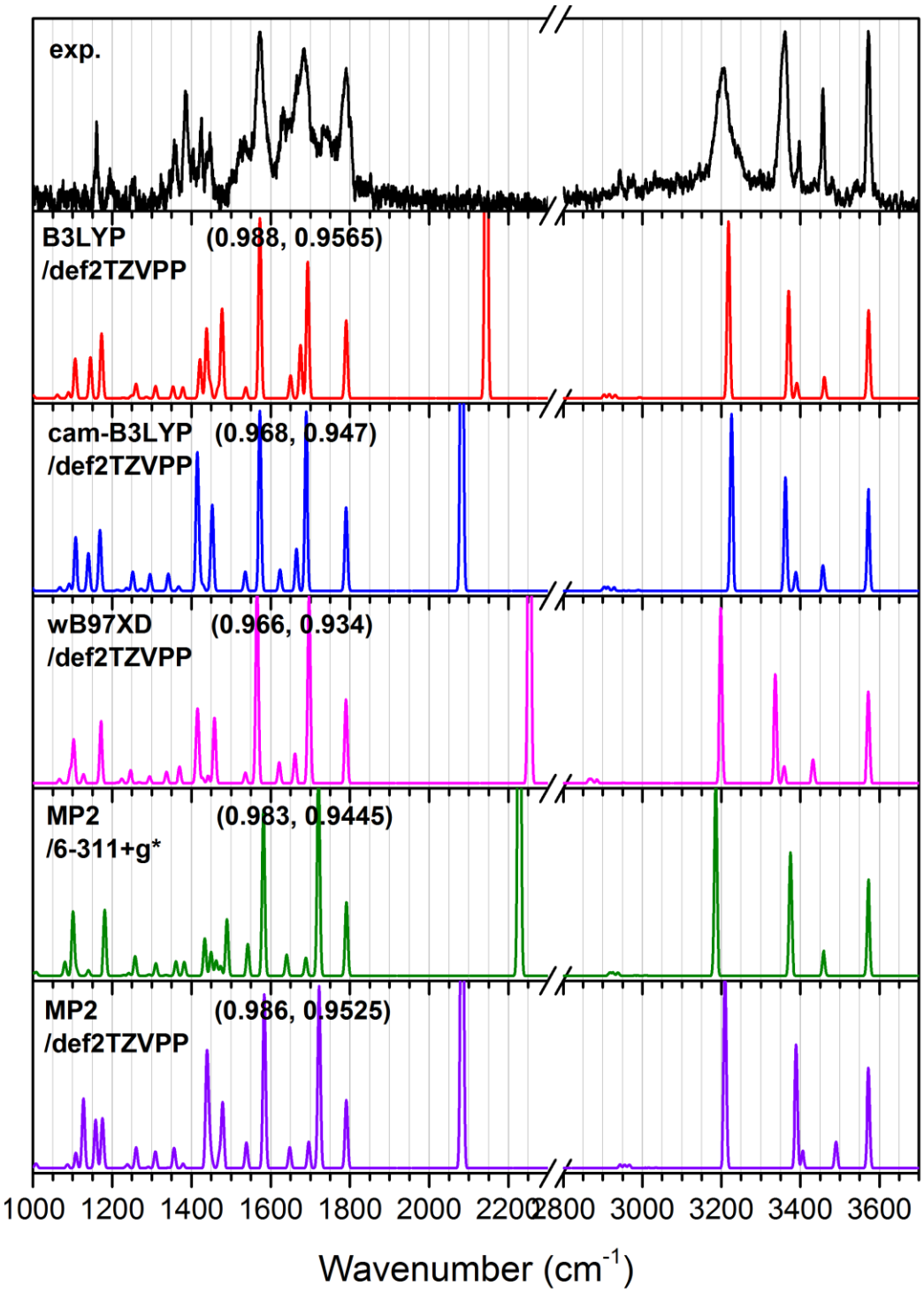

Figure 5.5 Comparison of the experimental ion-dip spectrum associated with the 3480 cm^{-1} feature and harmonic spectra of the bare and D_2-tagged N^cA Gly_3H^+ structures. Harmonic spectra are calculated at the cam-B3LYP/def2TZVPP level of theory and are scaled by 0.947 and 0.968 in the upper and lower frequency regions, respectively.

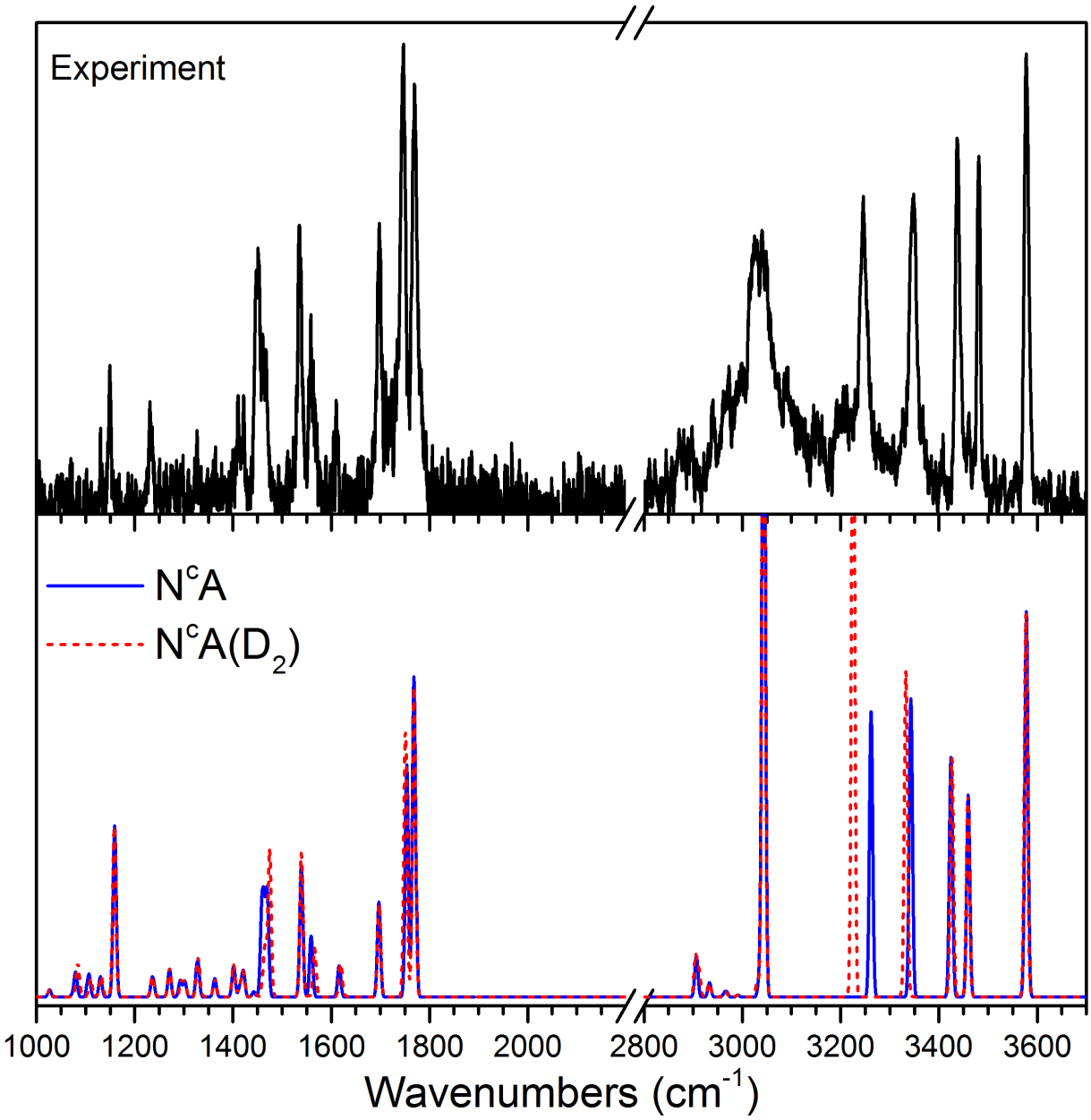

Figure 5.6 Comparison of the experimental ion-dip spectrum associated with the 3200 cm^{-1} feature and harmonic spectra of the bare and D_2-tagged O^tA Gly_3H^+ structures. Harmonic spectra are calculated at the cam-B3LYP/def2TZVPP level of theory and are scaled by 0.947 and 0.968 in the upper and lower frequency regions, respectively.

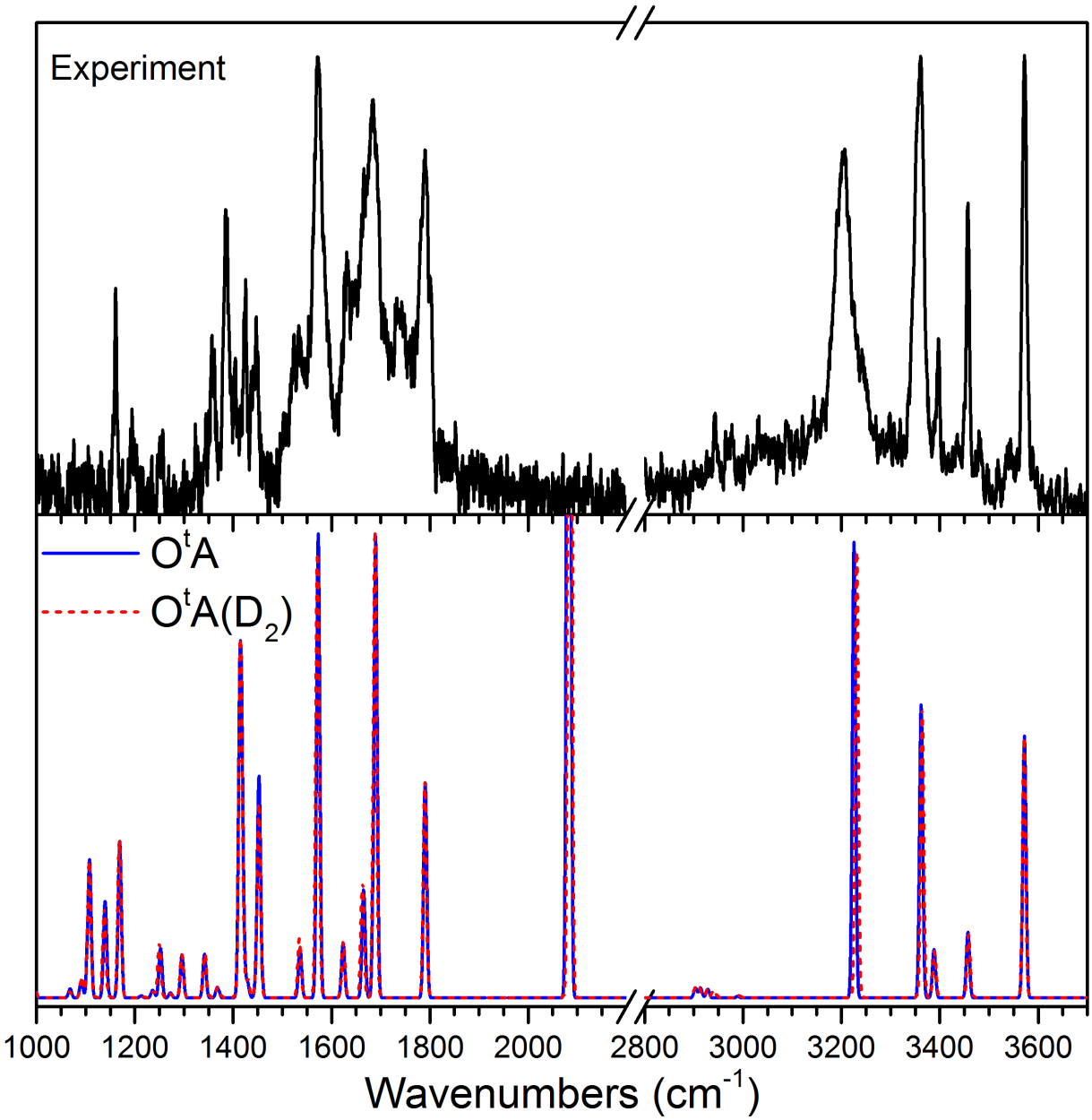

experimentally. For the cam-B3LYP/def2TZVPP harmonic spectra, this yielded a scaling factor of 0.968 in the 1000–2300 cm^{-1} range and 0.947 in the 2800–3800 cm^{-1} range.

5.4 Results

The one-laser IR predissociation spectrum of $Gly_3H^+(D_2)$ is shown in Figure 5.7A. It contains spectral features relating to the O-H and N-H stretches (2800–3600 cm^{-1}), the amide I modes (mostly C=O stretches, 1600–1800 cm^{-1}), and the amide II modes (combination of C=N stretches and N-H bends, 1500–1600 cm^{-1}). Additionally, there is an extremely broad feature that extends from ~1300 cm^{-1} all the way to ~2200 cm^{-1}, and is most noticeable by the sloping baseline in the 1800–2200 cm^{-1} region. In the 3000–3600 cm^{-1} region, a single Gly_3H^+ structure is expected to have up to six distinct features arising from the six O-H and N-H bonds present in the molecule. Figure 5.7A shows nine distinct features in that region. Furthermore, it also shows five overlapping and partially resolved peaks in the 1600–1800 cm^{-1} region, where only three transitions, corresponding to the three C=O moieties, are expected. These observations suggest multiple structures of Gly_3H^+ are contributing to the one-laser spectrum, similar to the IRMPD studies.[1,2]

The two isomer-specific IR-IR spectra, shown in Figure 5.7B and C, were acquired with the probe laser wavelength fixed at 3480 cm^{-1} and 3200 cm^{-1}, respectively. Spectrum B has six N-H and O-H stretch features at 3035 cm^{-1}, 3246 cm^{-1}, 3347 cm^{-1}, 3438 cm^{-1}, 3481 cm^{-1}, and 3578 cm^{-1}. The 3035 cm^{-1} feature is significantly broader than the others, indicating that it is associated with an N-H or O-H that is involved in a strong hydrogen-bond. The amide I region shows three narrow features at 1698 cm^{-1}, 1746 cm^{-1} and 1770 cm^{-1}, consistent with the dominant presence of a single isomer. Spectrum C is quite distinctive from spectrum B. The N-H and O-H

Figure 5.7 (A) One-laser IR predissociation spectrum of $Gly_3H^+(D_2)$. The IRMPD spectrum from Reference 2 is shown in grey. (B) and (C) IR-IR ion-dip spectra with probe laser fixed at 3480 cm^{-1} and 3200 cm^{-1}, respectively, as indicated by dotted lines. The two spectral regions in each spectrum are normalized independently.

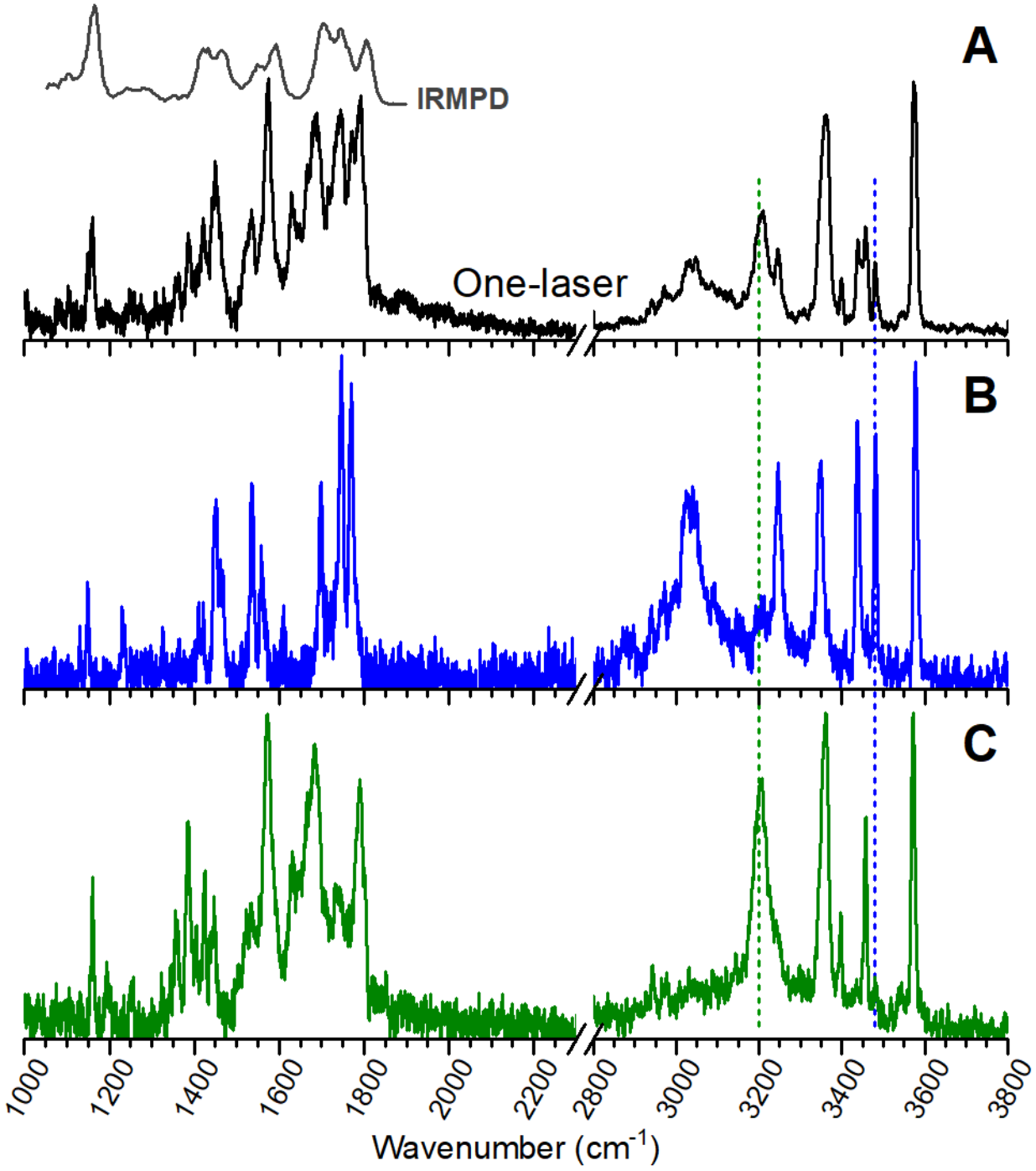

stretch region has five peaks at 3205 cm^{-1}, 3358 cm^{-1}, 3397 cm^{-1}, 3457 cm^{-1}, 3572 cm^{-1}. Again, the lowest frequency feature is broader than the others, although it is 170 cm^{-1} bluer than the similar feature in spectrum B. The C=O stretch region is dominated by two features at 1684 cm^{-1} and 1790 cm^{-1}, which are both surprisingly broad. Additionally, spectrum C contains the very broad feature that was noted earlier in the one-laser spectrum, as it also shows a sloping baseline in the 1800–2200 cm^{-1} region.

5.5 Analysis and Discussion

We begin our analysis with the IR-IR spectrum in Figure 5.7B, shown again in Figure 5.8A. Cursory inspection of the calculated spectra revealed that the broad and intense feature at 3035 cm^{-1} is characteristic of the N-H stretch of the terminal $-NH_3^+$ group, redshifted and broadened due to hydrogen-bond interactions with C=O group(s). This motif eliminates the two O^t structures. The calculated harmonic spectra of the four remaining N^t and N^c isomers are shown in Figure 5.8B–E. In addition to the 3035 cm^{-1} feature, these structures all exhibit a vibration at 3578 cm^{-1} that corresponds to the carboxylic acid O-H stretch.[32] The four remaining peaks between 3200 and 3500 cm^{-1} are due to the other four N-H stretches, and exhibit conformation specific frequencies that allow us to assign the experimental IR-IR spectrum to the N^cA isomer. Its calculated spectrum also has the best agreement with the experimental spectrum in the amide I and amide II regions. While there may be minor contributions to the experimental spectrum from N^cB and N^tA, the dominant features in the IR-IR spectrum can all be assigned to those of the N^cA isomer, and the assignments are listed in Table 5.2.

The folded N^cA structure (see Figure 5.2) has the protonated amine N^1-H donating a hydrogen-bond to the *trans* amide $C=O^2$, leading to the redshifted N^1-H stretch at 3035 cm^{-1}. The

Figure 5.8 (A) Ion-dip spectrum with probe laser fixed at 3480 cm^{-1}. (B–E) Calculated harmonic spectra, see Figure 5.2 and Table 5.1 for structures and relative energies. The harmonic intensities for the two spectral regions are normalized independently.

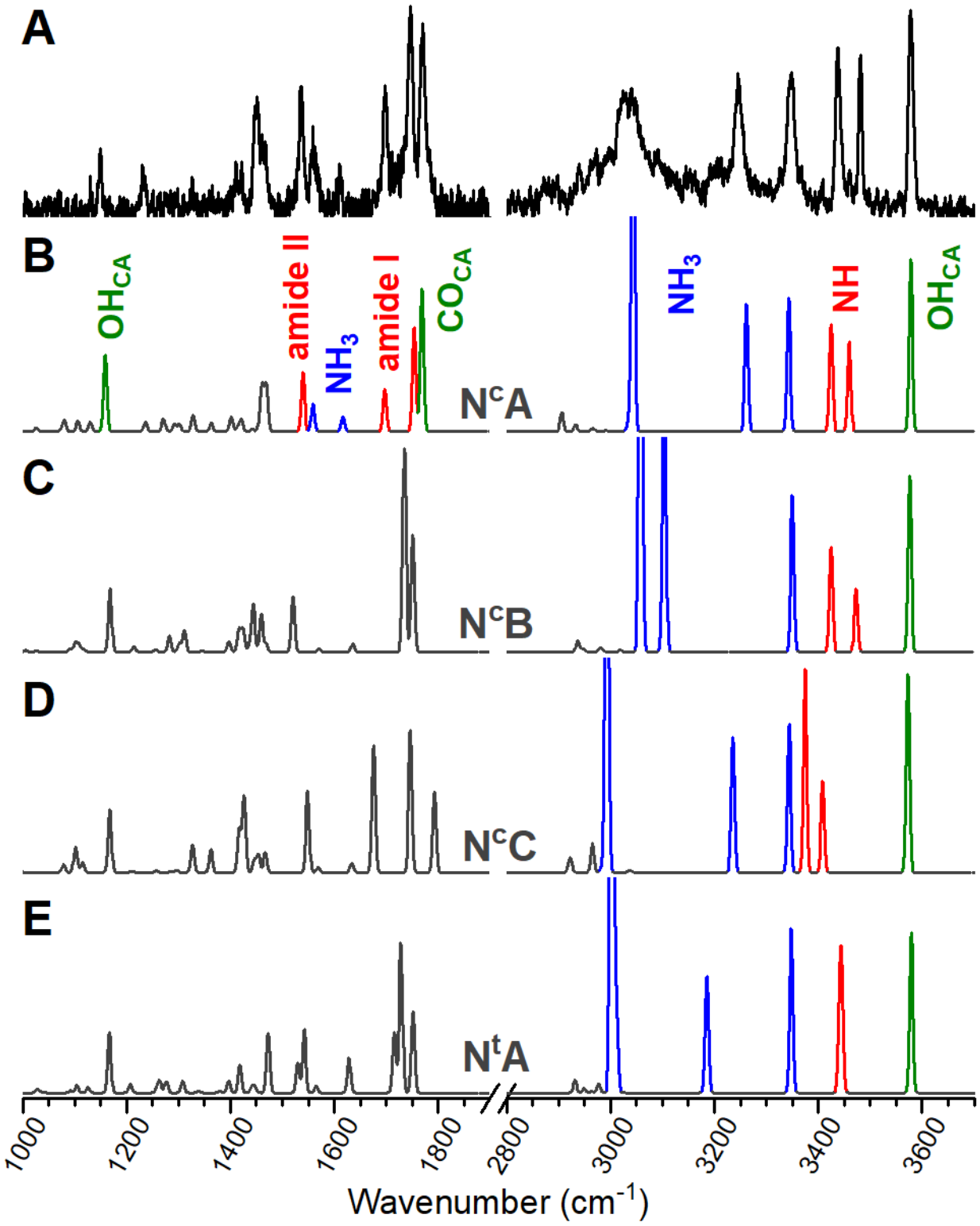

3481 cm^{-1} feature is assigned to the *trans* amide N^3-H stretch, while the 3438 cm^{-1} feature is assigned to the *cis* amide N^2-H stretch. In the C=O stretch region, the 1770 cm^{-1} feature is assigned to the $C=O^3$ stretch, slightly redshifted compared to a free carboxylic acid (e.g., that of acetic acid is at 1788 cm^{-1})[32] due to a weak interaction with $-NH_3^+$. The 1746 cm^{-1} feature is assigned to the *cis* amide $C=O^1$ stretch (i.e., amide I), and the amide I mode of the hydrogen-bond accepting *trans* amide is at 1698 cm^{-1}. The 1610 cm^{-1} and 1560 cm^{-1} features are assigned to the symmetric and asymmetric scissoring modes of the hydrogen-bond donating NH_3^+ group. The feature at 1536 cm^{-1} is assigned to the *trans* amide II mode, while the *cis* amide II mode is more extensively coupled with $-NH_3$ and $-CH_2$ modes in the 1400–1470 cm^{-1} region. Finally, the 1149 cm^{-1} feature is assigned to the C-O-H bending of the carboxyl group. Some of these peak assignments are summarized in Table 5.2.

Table 5.2 Assignment of experimental features of N^cA and O^tA. Experimental frequencies are given in cm^{-1}.

	O^1-H	**O^3-H_{CA}**	**$NH_{2\ asy.}$**	**$NH_{2\ sym.}$**	**N^1-H**	**N^2-H**	**N^3-H**	**$C=O^1$**	**$C=O^2$**	**$C=O^3{}_{CA}$**
N^CA	-	3578	3347	3246	3035	3438	3481	1746	1698	1770
O^tA	1300-2200	3572	3457	3397	-	3205	3358	-	1684	1790

Figure 5.9A shows again the other IR-IR spectrum, acquired with the probe laser fixed at 3200 cm^{-1}. In our calculated spectra of the ten lowest energy structures, the presence of a $-NH_3^+$ group is associated with intense features near ~3000 cm^{-1} (for example, see those in Figure 5.8). The lack of such features near ~3000 cm^{-1} in this spectrum eliminates amine-protonated

structures, hence the calculated harmonic spectra of the two O^t isomers are shown in Figure 5.9B,C for comparison. The spectrum of the lower energy O^tA isomer shows an excellent agreement with the overall experimental spectrum. The O^tB isomer, on the other hand, cannot account for all the experimentally observed features. The rotation of the carboxyl group breaks the hydrogen-bond to N^3-H, blueshifting the calculated N^3-H stretch by ~90 cm^{-1} compared to that in O^tA, overlapping it with the NH_2 asymmetric stretch. However, the presence of the O^tB conformation in our experiment cannot be completely ruled out because all the other vibrations are at very similar frequencies as those in O^tA. The O^tB structure is calculated to be 2.4–9.3 kJ/mol higher in energy than O^tA at all levels of theory listed in Table 5.1, and the calculated barrier for carboxyl rotation is less than 1 kJ/mol (cam-B3LYP/def2TZVPP). This low barrier makes it quite unlikely for significant O^t populations to be in the O^tB conformation after collisional cooling in the 10 K ion trap. Therefore, we assign the major features in the experimental IR-IR spectrum to those of the O^tA isomer.

The features at 3397 cm^{-1} and 3457 cm^{-1} are assigned to the symmetric and asymmetric NH_2 stretches of the terminal amine, which is slightly blueshifted compared to a free amine (e.g. that of the methylamine is 3361 cm^{-1} and 3427 cm^{-1}).[32] This blueshift is likely due to the hydrogen-bond accepting interaction with the nearby N^2-H, whose stretch is observed at 3205 cm^{-1}. The feature at 3358 cm^{-1} is assigned to the N^3-H stretch, which has a weaker interaction with the nearby C=O^3. In the lower frequency region, the feature at 1790 cm^{-1} is assigned to the C=O^3 stretch while the feature at 1684 cm^{-1} is assigned to the amide I modes. The intense feature at 1572 cm^{-1} corresponds to the amide II modes. The notably broad 1300–2200 cm^{-1} feature is assigned to the protonated O^1-H stretch, which is involved in a strong hydrogen-bonding

Figure 5.9 (A) Ion-dip spectrum with probe laser fixed at 3200 cm^{-1}. (B,C) Calculated harmonic spectra, see Figure 5.2 and Table 5.1 for structures and relative energies. The harmonic intensities for the two spectral regions are normalized independently.

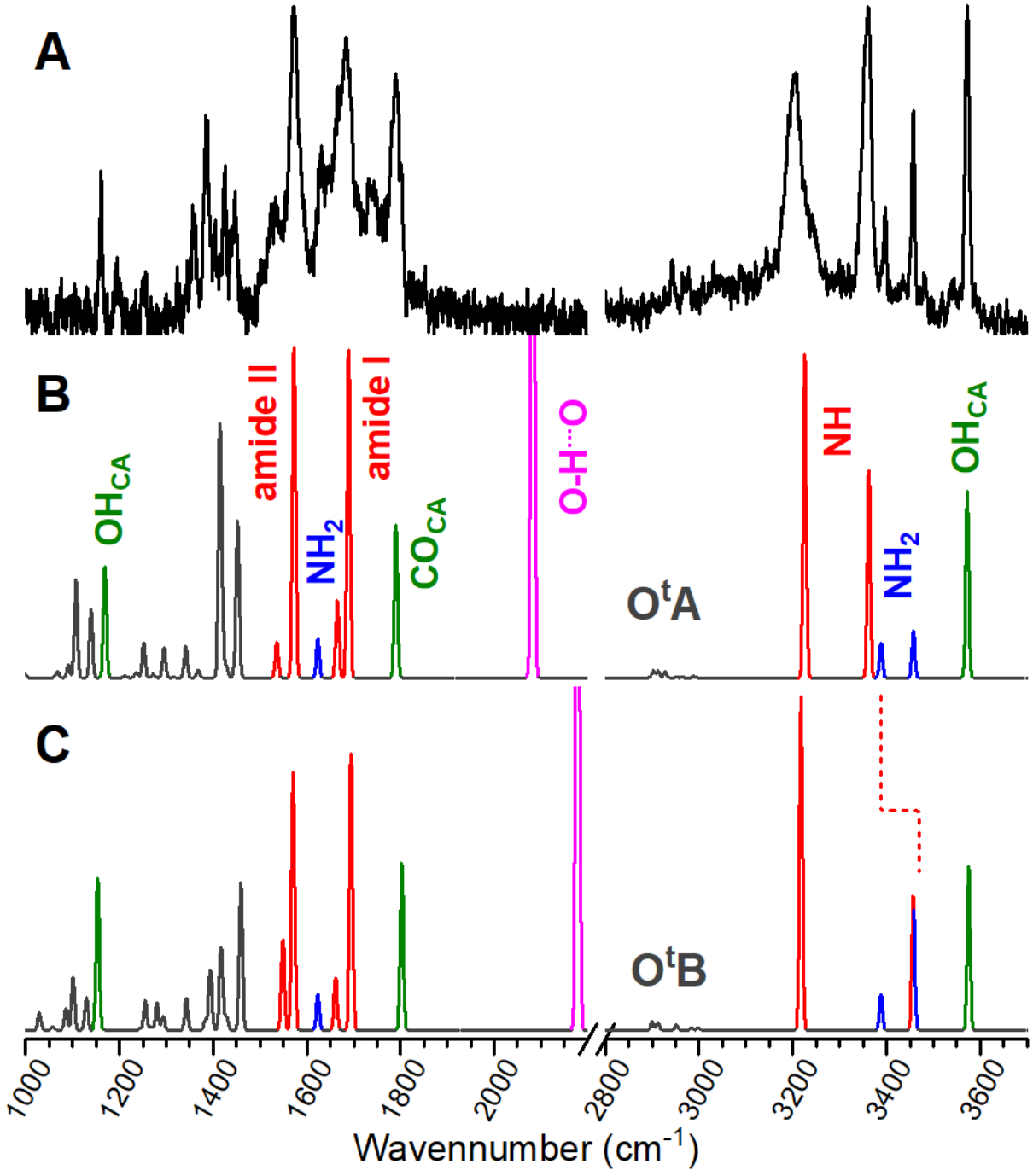

interaction with $C{=}O^2$, where the $H{\cdots}O^2$ distance is only 1.391 Å. This strong interaction leads to the very broad experimental feature associated with significant anharmonicity. This O-H stretch is coupled to numerous vibrational modes, including the amide I and II modes, giving rise to the broader appearance of the vibrational features in this region, especially compared to those in the N^cA spectrum. It is also coupled to the -CH_2 modes in the 1350–1450 cm^{-1} region, giving these features additional intensities. This anharmonic coupling likely accounts for some of the minor experimental features that are not present in the harmonic spectrum.

The IR-IR spectra therefore reveal the dominant presence of two distinct Gly_3H^+ isomers in our experimental conditions, with protonation occurring either at N^1 or O^1. The relative energy of the N^cA and O^tA isomers are difficult to pin down, as the calculated values are highly dependent on the level of theory used. Nonetheless, all the calculations agree that each isomer is the lowest energy structure of their respective protonation site. The interconversion between them would involve breaking at least one strong hydrogen-bond, as well as an amide *cis-trans* isomerization, a combination of which likely gives rise to a significant barrier. For example, Li et al.[30] calculated a free energy barrier of 67 kJ/mol for the proton transfer between the O^1 and N^1 site. It is therefore not too surprising to find both isomers in our experimental spectra, even if the energy difference between them is large enough that a Boltzmann distribution at 10–30 K[23,33] would yield all the population in one structure. Given that one of the structures is likely kinetically trapped, it would be interesting to estimate the relative populations of the two isomers. While this is difficult to determine directly from the one-laser spectrum because the absolute absorption cross-sections of these transitions are not known, we can provide a rough estimate using the relative peak intensities in the experimental IR-IR spectra and the calculated IR intensities. We used only the N-H and O-H stretch features in the 2800–3800 cm^{-1} region for this analysis because the O^tA isomer appears

to have significantly more anharmonicity in the lower frequency region than N^cA, making the harmonic intensities less useful there. See Table 5.3 and Figure 5.10 for details of this analysis, which yielded a relative population of N^cA ($35 \pm 3\%$) and O^tA ($65 \pm 18\%$). As discussed above, these values are not expected to be representative of the 0 K gas-phase relative energies, and therefore cannot conclusively determine which structure is lower in energy. This observed relative population more likely represents the populations of various isomers at 300 K, originating from the ESI conditions where these ions are formed, that then funnel into either of these two minima as the ions are collisionally cooled down.

The presence of two major contributors in the one-laser spectrum and the presence of the O^tA isomer is consistent with the conclusions of Wu and McMahon[1] based on the analysis of their IRPMD spectra in the 1050–1900 cm^{-1} region. However, our IR-IR spectrum points to the presence of the N^cA isomer instead of the N^tA isomer as the other contributor. As noted by Li et al.,[30] this is likely due to the omission of structures containing a *cis* amide group in the computational search by Wu and McMahon.[1] The analysis of only the 1050-1900 cm^{-1} region, as well as the congestion due to the simultaneous presence of multiple isomers, would make differentiating between N^cA and N^tA quite difficult. In our experiments, cryogenic temperatures and single photon predissociation processes result in experimental IR features with narrow FWHM, except for strongly anharmonic features, across the 1000–3800 cm^{-1} range. Furthermore, when an IR-IR scheme is employed, we can easily distinguish the presence of each isomer, making spectral and structural assignments more straightforward and less ambiguous.

The relatively significant stability of the O^tA isomer is quite interesting since it has an atypical protonation site. For reference, the gas phase proton affinity of n-methylacetamide is 888.5 kJ/mol while that of ethylamine is 912.0 kJ/mol.[3] Therefore, other interactions must play an

Table 5.3 Derivation of the relative populations of the two observed isomers using their experimental and calculated (cam-b3lyp/def2TZVPP) vibrational modes.

	Exp Freq.[a]	Exp. Area[b]	Calc Freq.[a]	Calc. Int.	Norm. Calc. Int.	Global Fit	Peak Contrib.[d]	Avg. (std dev)	Rel. Pop
N[c]A	3033	26.32	3043.31	312.39	1.87	0.35	4.93	5.25 (0.48)	0.35 (0.03)
	3246	9.19	3261.90	105.08	0.63		5.12		
	3347	10.71	3342.87	108.92	0.65		5.75		
	3438	8.87	3424.49	87.54	0.52		5.93		
	3481	6.26	3459.61	73.88	0.44		4.96		
	3578	11.53	3577.97	140.86	0.84		4.79		
O[t]A	3204	26.98	3225.51	290.57	1.74	0.65	10.09	9.59 (2.66)	0.65 (0.18)
	3358	20.22	3362.06	187.22	1.12		11.73		
	3397	1.81	3388.16	31.06	0.19		6.33		
	3457	4.80	3457.22	42.04	0.25		12.41		
	3572	11.34	3572.00	167.15	1.00		7.37		

[a] in cm^{-1}
[b] Area of Gaussian peak fit of the IR-IR spectra in Fig 3B and 3C.
[c] Ratios that yielded the best fit to the one-laser spectrum, as show in Figure 5.10
[d] "Global Fit" * "Exp. Area" / "Norm. Calc. Int."

Figure 5.10 Sum of isomer specific IR-IR spectra (red) to reproduce the one-laser spectrum (black).

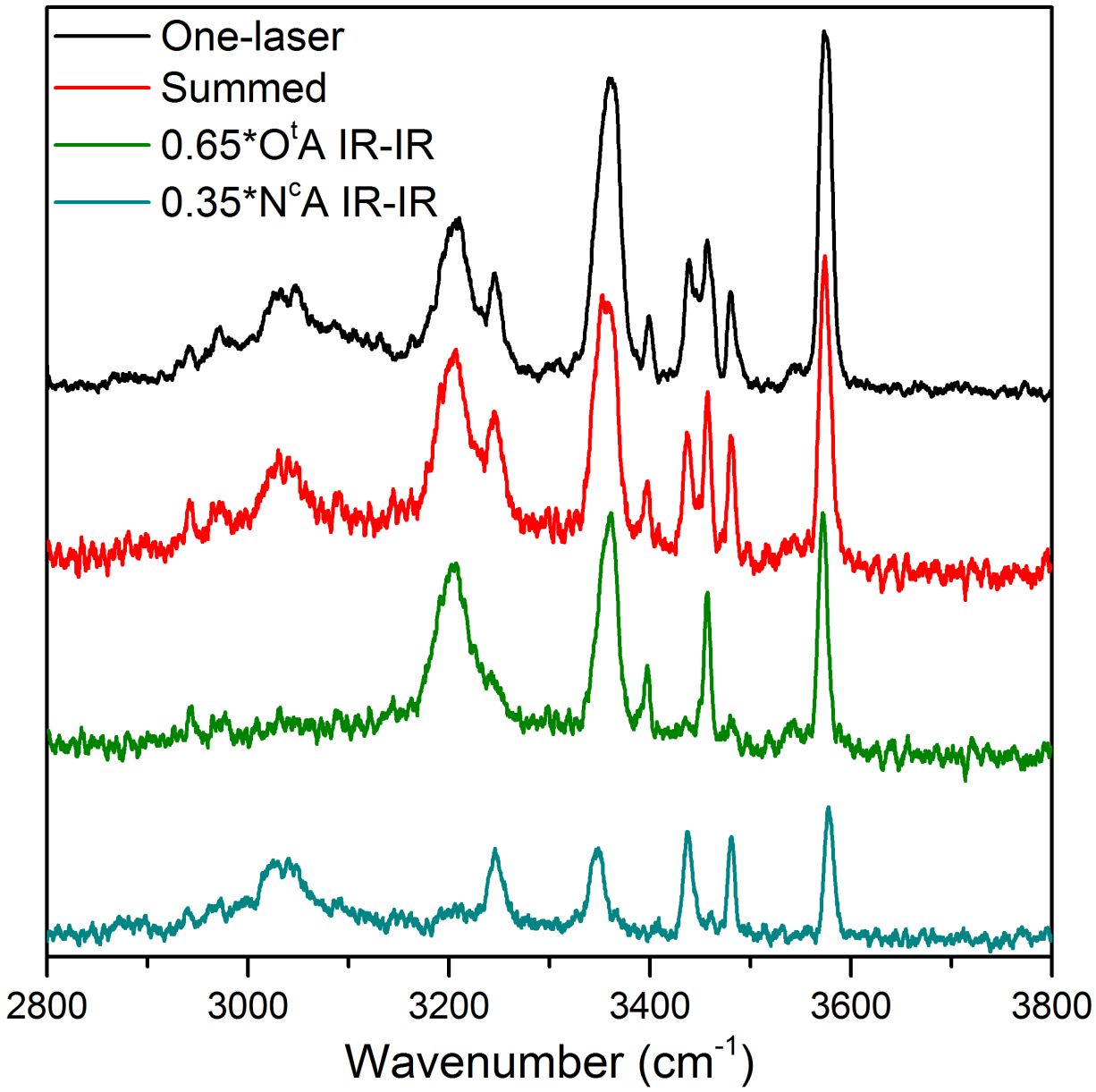

important role in stabilizing the O^tA structure. Decomposing the overall energy into specific interactions is not straightforward, but rough estimates of the hydrogen-bonding strengths can be made using the observed experimental vibrational frequencies. Previous studies have shown that the interaction enthalpy ($-\Delta H$) and the redshift ($\Delta\nu$) of an A-H oscillator stretch frequency upon hydrogen-bonding roughly follows a $-\Delta H = 1.3(\Delta\nu)^{1/2}$ empirical relationship.[34–36] Hence, we can compare our experimental frequencies with literature values[32,37] for non-interacting oscillators to estimate the magnitude of the hydrogen-bond association enthalpies. Another way to estimate these hydrogen-bond interaction enthalpies is to use the calculated hydrogen-bond length (r) which has been shown to follow an empirical $-\Delta H = 0.134r^{-3.05}$ relationship.[35] Table 5.4 shows the calculated hydrogen-bond lengths, experimental redshifts, and the derived hydrogen-bond interaction strengths involving the different hydrogen-bond donor groups in the N^cA and O^tA isomers. As expected, shorter calculated AH···B distances correspond to larger spectral redshifts and stronger interaction strengths. In the N^cA isomer, all three hydrogen-bond donors involve the terminal NH_3^+ group. The strongest hydrogen-bond, at ~24 kJ/mol, is between N^1H and $C{=}O^2$, while the other two are weaker at ~10 kJ/mol. Overall, the protonation at the terminal amine involves an additional ~47 kJ/mol of stabilizing intramolecular interactions. The strengths of these interactions further show how protonation may increase the *cis* amide characteristics in a peptide.[38] On the other hand, the total estimated hydrogen-bond interactions in O^tA is almost twice as large at ~88 kJ/mol, which helps to explain why it is energetically competitive with N^cA despite its nominally lower proton affinity. The bulk of the stabilizing interactions come from the strong ~53 kJ/mol hydrogen-bond that exists between O^1H and the neighboring amide $C{=}O^2$, highlighting the stabilization of the proton by both amides. Furthermore, the excess charge is also distributed via additional hydrogen-bond donating interactions of both amide N-H's. The above

Table 5.4 Calculated hydrogen-bon lengths (cam-B3LYP/def2TZVPP), vibrational frequency shifts, and hydrogen-bond interaction strengths.

		$r_{H\text{-}bond}$ (nm)	ν_{free} (cm^{-1})	$\nu_{exp.}$ (cm^{-1})	$\Delta\nu$ (cm^{-1})	$-\Delta H_r$ (kJ/mol)[e]	$-\Delta H_{\Delta\nu}$ (kJ/mol)[f]
N^cA	$N^1H_{2\ asy.}$	0.2509	3427[a]	3347	80	9	12
	$N^1H_{2sym.}$	0.2427	3361[a]	3246	115	10	14
	N^1H	0.1816	3394[a]	3035	359	24	25
O^tA	N^3H	0.2108	3498[b]	3358	140	16	15
	N^2H	0.2035	3498[b]	3205	293	17	22
	O^1H	0.1391	3583[c]	2080[d]	1503	55	50

[a] Methylamine, values from Reference.[32] The average of *sym* and *asym* mode is used for N^1H.
[b] n-methylacetamide, values from Reference 37.
[c] Acetic acid, values from Reference 32.
[d] The cam-B3LYP/def2TZVPP calculated frequency is used to estimate the frequency of this very broad feature.
[e] $-\Delta H_r = 0.134r^{-3.05}$
[f] $-\Delta H_{\Delta v} = 1.3(\Delta v)^{1/2}$

discussion is of course only looking at one aspect of the overall stabilities without considering other factors such as angle strains and energy differences between *cis* and *trans* amides. Nonetheless, it provides useful insights into the relative stabilities of these two considerably different structures.

5.6 Conclusion

The structures of the protonated triglycine peptide is investigated using an IR-IR double resonance method. Comparisons of the IR-IR isomer-specific spectra and calculations revealed the presence of two Gly_3H^+ isomers in our experiment. The main isomer found is the same amide O^1 protonated structure identified by Wu and McMahon via IRMPD.[1,2] The other isomer exhibits protonation at the N^1 site and contains a *cis* amide group, differing from the structure assigned by Wu and McMahon. Our assignment is consistent with recent computational surveys[4,30] that identified this structure as the lowest energy conformation for the N^1 protonation site. Although calculations show that the two isomers studied here are the lowest energy isomer of their respective protonation site, their relative energies are very sensitive to the computational method used. Moreover, even though we observe higher population of the O^tA isomer in our experimental spectra, the significant barriers that exist between the two structures make it difficult to extract relative energy information from this result alone. Analysis of the N-H and O-H stretch frequencies provides a quantitative look at the hydrogen-bond strengths present in each isomer, accounting for the relative stabilities of these structures.

5.7 References

1. R. Wu, T.B. McMahon, *J. Phys. Chem. B,* **2009,** 113, 8767–8775

2. R. Wu, T.B. McMahon, *J. Am. Chem. Soc.*, **2007,** 129, 11312–11313

3. E.P.L. Hunter, S.G. Lias, *J. Phys. Chem. Ref. Data.*, **1998,** 27, 413–656

4. A. Mookherjee, M.J. Van Stipdonk, P.B. Armentrout, *J. Am. Soc. Mass Spectrom.*, **2017,** 28 739–757

5. B.C. Bohrer, S.I. Merenbloom, S.L. Koeniger, A.E. Hilderbrand, D.E. Clemmer, *Annu. Rev. Anal. Chem.,* **2008,** 1 293–327

6. J.M. Dilger, S.J. Valentine, M.S. Glover, D.E. Clemmer, *J. Am. Soc. Mass Spectrom.*, **2013,** 24 768–779

7. G.R. Hilton, K. Thalassinos, M. Grabenauer, N. Sanghera, S.E. Slade, T. Wyttenbach, P.J. Robinson, T.J.T. Pinheiro, M.T. Bowers, J.H. Scrivens, *J. Am. Soc. Mass Spectrom.*, **2010,** 21, 845–854

8. H.S. Beeston, J.R. Ault, S.D. Pringle, J.M. Brown, A.E. Ashcroft, *Proteomics,* **2015,** 15, 2842–2850

9. H.A. Cox, R.R. Julian, S.-W. Lee, J.L. Beauchamp, *J. Am. Chem. Soc.,* **2004,** 126, 6485–6490

10. R.A. Harrison, J.R. Engen, *Curr. Opin. Struct. Biol.*, **2016,** 41, 187–193

11. J. Rappsilber, *J. Struct. Biol.*, **2011,** 173, 530–540

12 A. Sinz, *Mass Spectrom. Rev.*, **2006,** 25, 663–682

13. J. Fenn, M. Mann, C. Meng, S. Wong, C. Whitehouse, *Science*, **1989,** 246, 64–71

14. J.B. Fenn, M. Mann, C.K. Meng, S.F. Wong, C.M. Whitehouse, *Mass Spectrom. Rev.*, **1990,** 9, 37–70

15 J. Oomens, N. Polfer, D.T. Moore, L. van der Meer, A.G. Marshall, J.R. Eyler, G. Meijer, G. von Helden, *Phys. Chem. Chem. Phys.*, **2005,** 7, 1345–1348

16. J. Oomens, J.D. Steill, *J. Am. Soc. Mass Spectrom.*, **2010,** 21, 698–706

17. D. Scuderi, C.F. Correia, O.P. Balaj, G. Ohanessian, J. Lemaire, P. Maitre, *ChemPhysChem.,* **2009,** 10, 1630–1641

18 N.C. Polfer, *Chem. Soc. Rev.,* **2011,** 40, 2211–2221

19. N.C. Polfer, J. Oomens, *Mass Spectrom. Rev.,* **2009,** 28, 468–494

20. E.G. Buchanan, W.H. James III, S.H. Choi, L. Guo, S.H. Gellman, C.W. Müller, T.S. Zwier, *J. Chem. Phys.,* **2012,** 137, 094301

21. J.C. Dean, E.G. Buchanan, T.S. Zwier, *J. Am. Chem. Soc.,* **2012,** 134, 17186–17201

22. N.S. Nagornova, T.R. Rizzo, O.V. Boyarkin, *Angew. Chem., Int. Ed.,* **2013,** 52, 6002–6005

23. T.R. Rizzo, J.A. Stearns, O.V. Boyarkin, *Int. Rev. Phys. Chem.,* **2009,** 28, 481–515

24. C.M. Leavitt, A.B. Wolk, J.A. Fournier, M.Z. Kamrath, E. Garand, M.J. Van Stipdonk, M.A. Johnson, *J. Phys. Chem. Lett.,* **2012,** 3, 1099–1105

25. C.M. Leavitt, A.B. Wolk, M.Z. Kamrath, E. Garand, M.J. Van Stipdonk, M.A. Johnson, *J. Am. Soc. Mass Spectrom.,* **2011,** 22, 1941–1952

26. B.M. Marsh, E.M. Duffy, M.T. Soukup, J. Zhou, E. Garand, *J. Phys. Chem. A.,* 2014, 118 3906–3912

27. B.M. Marsh, J. Zhou, E. Garand, *Rsc Adv.,* **2015,** 5, 1790–1795

28. J.M. Voss, S.J. Kregel, K.C. Fischer, E. Garand, *J. Am. Soc. Mass Spectrom*, **(2017),** 29,42-50

29. B.M. Marsh, J.M. Voss, E. Garand, *J. Chem. Phys.,* **2015,** 143, 204201

30. H. Li, J. Jiang, Y. Luo, *Phys. Chem. Chem. Phys.,* **2017,** 19, 15030–15038,

31. M.J. Frisch, G.W. Trucks, H.B. Schlegel, G.E. Scuseria, M.A. Robb, J.R. Cheeseman, G. Scalmani, V. Barone, G.A. Petersson, H. Nakatsuji, X. Li, M. Caricato, A.V. Marenich, J. Bloino, B.G. Janesko, R. Gomperts, B. Mennucci, H.P. Hratchian, J.V. Ortiz, A.F. Izmaylov, J.L. Sonnenberg, Williams, F. Ding, F. Lipparini, F. Egidi, J. Goings, B. Peng, A. Petrone, T. Henderson, D. Ranasinghe, , V.G. Zakrzewski, J. Gao, N. Rega, G. Zheng, W. Liang, M. Hada, M. Ehara, K. Toyota, R. Fukuda, J. Hasegawa, M. Ishida, T. Nakajima, Y. Honda, O. Kitao, H. Nakai, T. Vreven, K. Throssell, J.A. Montgomery Jr., J. E. Peralta, F. Ogliaro, M.J. Bearpark, J.J. Heyd, E. N. Brothers, K.N. Kudin, V.N. Staroverov, T.A. Keith, R. Kobayashi, J. Normand, K. Raghavachari, A.P. Rendell, J.C. Burant, S.S. Iyengar, J. Tomasi, M. Cossi, J.M. Millam, M. Klene, C. Adamo, R. Cammi, J.W. Ochterski, R.L. Martin, K. Morokuma, O. Farkas, J.B. Foresman, D.J. Fox, Gaussian 16, **2016.**

32. T. Shimanouchi, Molecular vibrational frequencies, in: NIST chemistry webBook, NIST standard reference database number 69, P.J. Linstrom, W.G. Mallard (Eds.), National Institute of Standards and Technology, Gaithersburg, MD 20899, **Retrieved 2017**

33. A.B. Wolk, C.M. Leavitt, E. Garand, M.A. Johnson, *Acc. Chem. Res.*, 2014, 47, 202–210,

34. A.V. Iogansen, *Spectrochim. Acta A*, **1999,** 55, 1585–1612

35. M. Rozenberg, A. Loewenschuss, Y. Marcus, *Phys. Chem. Chem. Phys.*, **2000,** 2, 2699–2702

36. M. Rozenberg, G. Shoham, I. Reva, R. Fausto, *Phys. Chem. Chem. Phys.*, **2005,** 7, 2376–2383

37. S. Ataka, H. Takeuchi, M. Tasumi, *J. Mol. Struct.*, 1984,113, 147–160

38 C. Grathwohl, K. Wüthrich, *Biopolymers*, **1976,** 15, 2043–2057

CHAPTER 6

Interaction between ionic liquid cation and water: infrared predissociation study of $[bmim]^+ \cdot (H_2O)_n$ clusters

Published: J.M. Voss, B.M. Marsh, J. Zhou, and E. Garand. *Physical Chemistry Chemical Physics***,** 18, 18905 – 18913 (2016)

Abstract

The infrared predissociation spectra of $[bmim]^+ \cdot (H_2O)_n$, n = 1–8, in the 2800–3800 cm^{-1} region are presented and analyzed with the help of electronic structure calculations. The results show that the water molecules solvate $[bmim]^+$ by predominately interacting with the imidazolium C2–H moiety for the small n = 1 and 2 clusters. This is characterized by a redshifted and relatively intense C2–H stretch. For $n \geq 4$ clusters, hydrogen-bond interactions between the water molecules drive the formation of ring isomers which interact on top of the imidazolium ring without any direct interaction with the C2–H. The water arrangement in $[bmim]^+ \cdot (H_2O)_n$ is similar to the low energy isomers of neutral water clusters up to the n = 6 cluster. This is not the case for the n = 8 cluster, which has the imidazolium ring disrupting the otherwise preferred cubic water structure. The evolution of the solvation network around $[bmim]^+$ illustrates the competing $[bmim]^+$–water and water–water interactions.

Author Contributions

JMV and BMM acquired experimental spectra; BMM and JZ performed theoretical calculations; JZ performed data analyses; JZ and EG wrote the manuscript.

6.1 Introduction

The ubiquitous presence of water within ionic liquids, both as an impurity and a co-solvent, makes their interactions with each other topics of active investigations.[1–4] While the anionic half of the ionic liquid often plays a major role in determining the extent of water sorption and hydrophobicity, the cations can also contribute to interactions with water molecules.[5,6] Salts containing imidazolium cations, such as 1-butyl-3-methylimidazolium ($[bmim]^+$) shown in Figure 6.1, are a class of widely used and studied room temperature ionic liquids. Owing to the electron deficiency of the N–C–N moiety, the C2–H group can actively participate in hydrogen-bond like interactions in addition to electrostatic interactions.[7–9] Raman, IR, NMR, and crystallography studies have shown that the C2–H of $[bmim]^+$ is capable of forming hydrogen-bonds with various anions.[10–17] Although the dominant interaction is likely electrostatic,[18] the presence of these hydrogen-bonds can have a significant effect on the properties of these ionic liquids.[19] When water is added to $[bmim]^+[X]^-$ ionic liquids, experimental and theoretical results point to the water molecules individually coordinating with the anions and cations at low concentrations, but forming water clusters and swelling the ionic liquid at higher water concentrations.[20–22] These results highlight the competition between water–water, cation–anion, and water–ionic liquid interactions.

Here, we present the infrared predissociation spectroscopy of mass selected $[bmim]^+\cdot(H_2O)_n$ clusters to provide a molecular level look at the interactions between the imidazolium cation and water molecules. The isolated cluster approach allows us to look at the intermolecular interactions individually, providing a better understanding of the forces responsible for the observed bulk behaviors. Similar gas phase spectroscopic studies of ionic liquid clusters have revealed detailed information on their molecular properties and provided valuable benchmark data for theoretical calculations.[23–29] Additionally, the $[bmim]^+$–water interaction itself is of interest because it is unclear

how strongly the C2–H group can hydrogen-bond with a water molecule and whether that interaction competes with the overall electrostatic interactions.

In this study, we use the OH and CH stretch vibrations, with the aid of electronic structure calculations, to follow the evolution of both the $[bmim]^+$–water interaction and structure of the water network as a function of cluster size. We find that the solvation geometry is driven mostly by water–water hydrogen-bonds as well as a subtle balance between the C2–H–water interaction and $[bmim]^+$–water electrostatic and dispersion interactions. The small clusters consisting of one to three water molecules do exhibit a weak hydrogen-bond like interaction between the C2–H and water, redshifting the frequency and increasing the intensity of the C2–H stretching vibration. However, for larger clusters, hydrogen-bond interactions between the water molecules drive the formation of ring isomers which interact primarily with the delocalized charge over the top of the imidazolium ring, similar to those found in solvated hydrophobic cations.[30]

Figure 6.1 Optimized structure of $[bmim]^+$ calculated at MP2/def2TZVP level. The electrostatic potential of $[bmim]^+$ mapped onto the density surface (iso = 0.02) is shown. Atom labelling is also indicated.

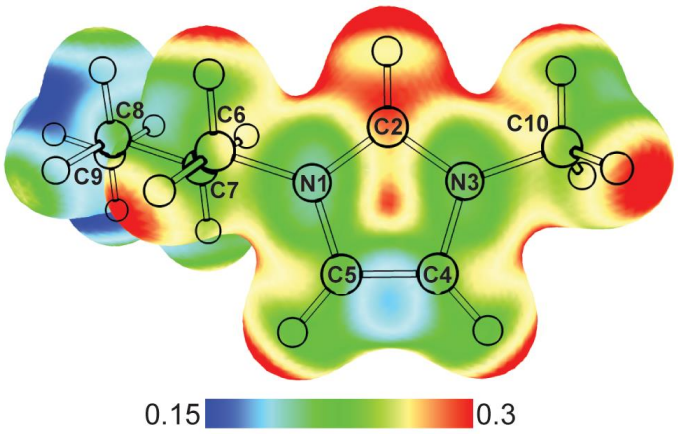

6.2 Experimental and Computational Details

The infrared predissociation spectra of the $[bmim]^+\cdot(H_2O)_n$ complexes were acquired using a homebuilt dual trap cryogenic ion vibrational spectrometer, described in detail previously.[31] Briefly, $[bmim]^+$ ions were generated *via* electrospray ionization of ~1 mM aqueous solution of [bmim][Cl], and were brought into a cryogenic linear octopole ion trap cooled to 80 K by liquid nitrogen. Inside this trap, the $[bmim]^+$ ions were exposed to helium buffer gas seeded with water vapor, resulting in the formation of $[bmim]^+\cdot(H_2O)_n$ clusters.[31] These clusters were then gently transferred into a cryogenic 3D quadrupole ion trap held at 10 K. Collisions with buffer gas consisting of 10% D_2 in He further cooled the ions. The clusters were size-selected inside the mass spectrometer prior to being mass gated and intersected with the output of a Nd:YAG pumped tunable OPO/OPA laser system (Laservision). When the IR photon energy was resonant with a vibrational transition, the absorption of a single photon was sufficient to induce the evaporation of one water molecule. Photofragment ions were then separated from the parent ions by a two-stage reflectron. Infrared predissociation spectra were generated by integrating the intensity of the water loss photofragment peak as a function of laser wavelength. The use of water as messenger tag means that the clusters studied here were likely to have higher internal energies compared to D_2 tagging due to higher binding energies. Unfortunately, the delocalized charge on $[bmim]^+$ made it difficult to form significant amount of D_2 adducts.

To aid the analysis of the experimental spectra, electronic structure calculations were performed using the Gaussian 09 computational package.[32] Geometry optimizations and harmonic frequency calculations were carried out at the MP2/def2TZVP level for n = 1–3 clusters and wB97XD/def2TZVP level for the larger clusters. The def2TZVP[33,34] basis is used for its relatively low computational cost and relatively high accuracy. We have previously used this basis set to reproduce the experimental IR spectra of solvated metal clusters.[35] Comparisons between MP2 and wB97XD results were made for

the n = 3 and 4 clusters to ensure that both methods arrived at similar structures and IR spectra. For the MP2 harmonic frequencies, a scaling factor of 0.957 was applied for comparison to experimental spectra. For the DFT harmonic frequencies, a constant 0.96 scaling factor was applied to the CH stretches while a linear scaling factor[36] of 0.688x + 989 was applied to the OH stretches. Such a linear scaling factor is useful for the larger clusters because their OH stretches span a wider frequency range where a constant scaling factor is no longer sufficient.

6.3 Results and Analysis

An overview of the experimental IR predissociation spectra of $[bmim]^+ \cdot (H_2O)_n$, n = 1–8, in the 2800–3800 cm^{-1} region is shown in Figure 6.2. These spectra are dominated by features in the OH stretch region, and general assignments can be made based on characteristic frequencies. The vibrational features above 3600 cm^{-1} are comparably narrow and correspond to the stretches of free OH groups, *i.e.* those not involved in a donor hydrogen-bond interaction. These features can be separated into two distinct categories. First, peaks appearing around 3640 cm^{-1} and 3730 cm^{-1} can be assigned to the symmetric and antisymmetric OH stretches of water with two free OH groups. Second, peaks appearing near 3700 cm^{-1} can be assigned to the free OH stretch of a water involved in a single donor hydrogen-bond interaction. The vibrational features in the 3200–3600 cm^{-1} region are generally broader, more intense, and gradually redshift with increasing cluster size. These features correspond to the stretches of hydrogen-bond donating OH groups with the interaction strength proportional to the size of the redshift. Note that additional features at 3500–3600 cm^{-1} appear for $n \geq 6$ clusters, indicating a change in the hydrogen-bond network that leads to weaker hydrogen-bonds. Lastly, there is a distinct feature at a fairly constant frequency around 3225 cm^{-1} for the n = 5–8 clusters.

Figure 6.2 Experimental IR predissociation spectra of $[bmim]^+ \cdot (H_2O)_n$, n = 1–8.

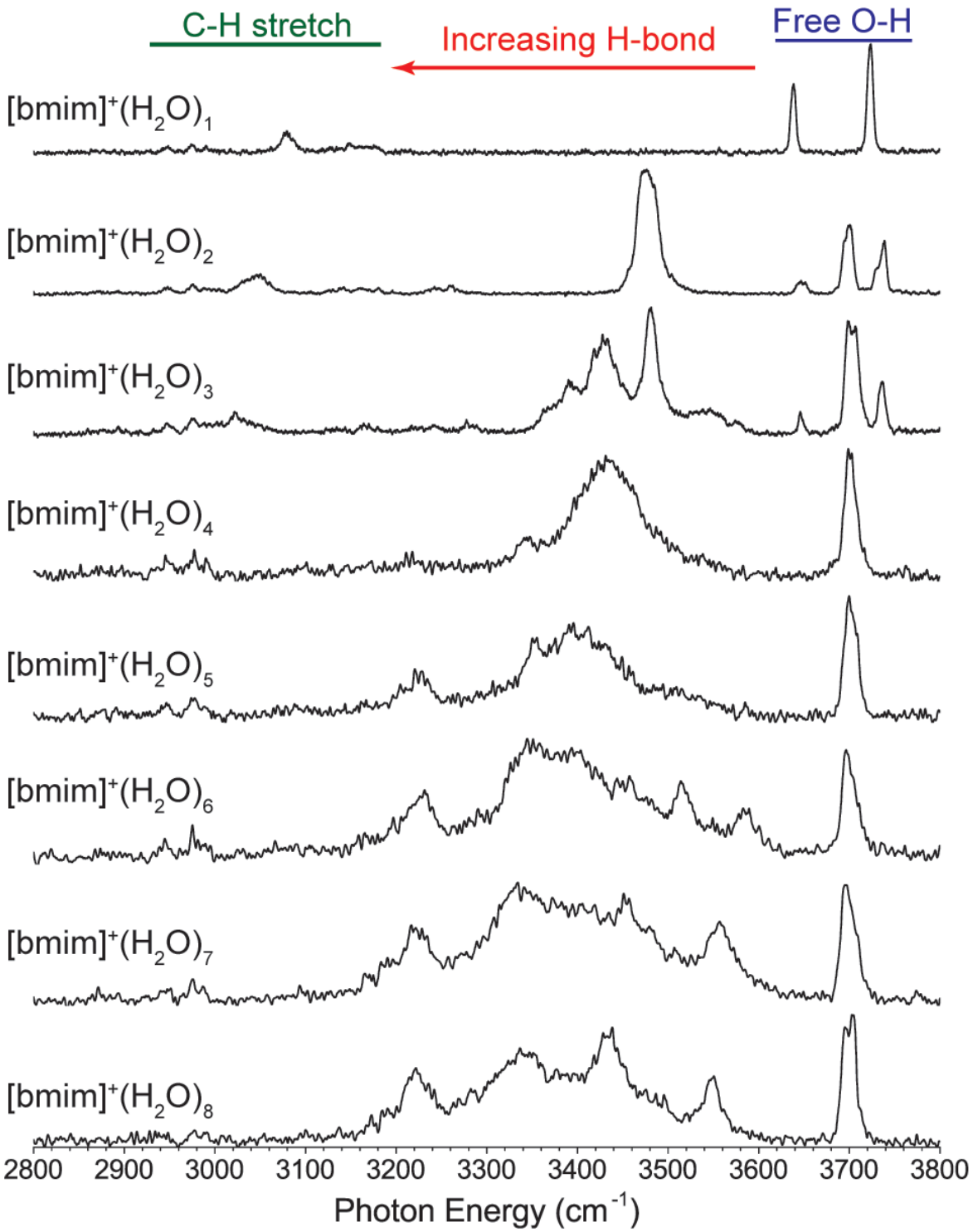

The CH stretches of the $[bmim]^+$ ion, appearing in the 2900–3200 cm^{-1} region, are very weak compared to the OH stretches. These features have been studied in detail for the isolated $[emim]^+$ ion,[24,25] as well as in neat $[bmim]^+[X]^-$ liquid.[14,15] The three imidazolium ring C–H stretches generally appears around 3150 cm^{-1} while the aliphatic C–H stretches of the methyl and butyl groups appear around 2950 cm^{-1}. In the spectrum of the n = 1 cluster, there is a notable broad feature at 3080 cm^{-1}, which gradually redshifts to 3045 cm^{-1} and 3020 cm^{-1} in the spectra of the n = 2 and 3 clusters. Besides this feature, the C–H stretch region shows no solvation-dependent changes.

6.3.1 $[bmim]^+ \cdot (H_2O)_1$

The experimental and calculated IR spectra of $[bmim]^+ \cdot (H_2O)_1$ are shown in Figure 6.3. The peaks at 3638 cm^{-1} and 3723 cm^{-1} are readily assigned to the symmetric and antisymmetric stretches of a water molecule having two free OH groups. These values are slightly redshifted (19 cm^{-1} and 33 cm^{-1} respectively) compared to the OH stretches of an isolated water molecule, but are typical of a water molecule interacting with a positively charged ion.[30,37,38] The positive charge on $[bmim]^+$ is delocalized over the imidazolium ring, as shown in Figure. 6.1, giving rise to several possible interaction sites for the water molecule. The two isoenergetic lowest energy isomers have the water molecule mainly interacting with the imidazolium C2–H, on either the butyl C6–H (Figure. 6.3B) or the methyl C10–H (Figure 6.3C) side. The transition state between these two structures has a linear C2–H···OH_2 geometry and is calculated to lie only 15 cm^{-1} above the minima. Therefore these geometries likely represent a single structure in which the water undergoes large amplitude motion between C6–H and C10–H. The calculated IR spectra of these two isomers are essentially the same and have an intense and redshifted C2–H at 3105 and 3108 cm^{-1}. This calculated frequency agrees well with the experimentally observed broad feature at 3080 cm^{-1}, but the calculated intensity is much larger than the experimental observation.

Figure 6.3 Experimental (A) and MP2/def2TZVP calculated (B–G) IR spectra of $[bmim]^+\cdot(H_2O)_1$. The relative energies of each isomer, including ZPE correction, are listed. The imidazolium C–H stretches and symmetric and antisymmetric H_2O stretches are labelled in (B).

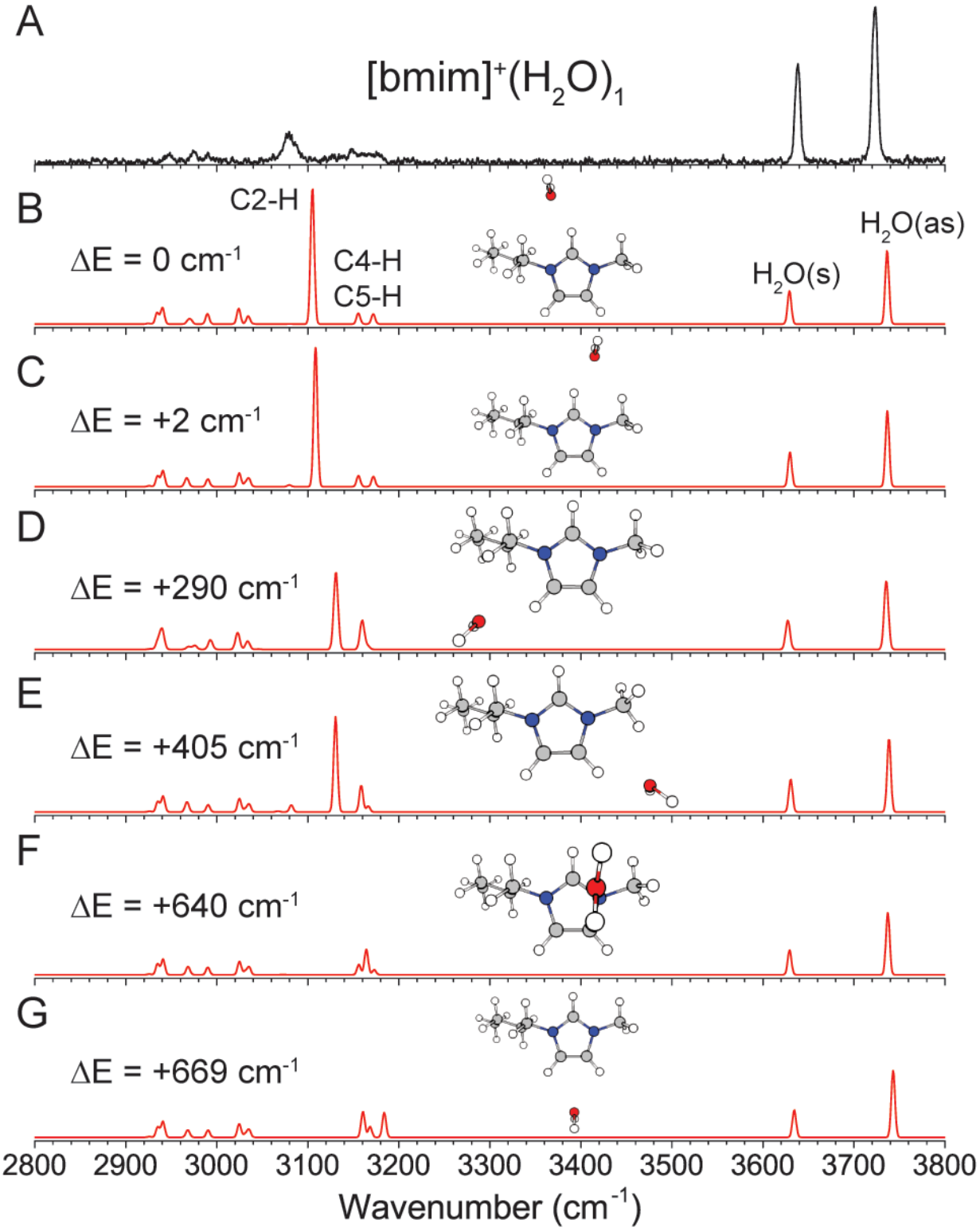

The interaction with the C6–H/C10–H is too weak to induce any noticeable change in their vibrational frequencies. It should be noted that the C2–H stretch is calculated to be further redshifted to 3074 cm^{-1} at the transition state between the two minima. Therefore, the motion of the water from one minima to the other likely explains the broad appearance to the C2–H feature in the experimental spectrum.

Two other isomers in which the water is mainly interacting with C4–H or C5–H are found to lie 290 cm^{-1} and 405 cm^{-1} higher in energy, and are shown in Figure. 6.3D,E. The weaker water interaction leads to a slightly redshifted C4–H/C5–H at 3130 cm^{-1}. Additionally, an isomer in which the water is located on top of the imidazolium ring (Figure. 6.3F) is found to be 637 cm^{-1} higher in energy. This isomer has no redshifted C–H and all the imidazolium C–H stretches appear near 3160 cm^{-1}. Finally, an isomer with the water situated between C4–H and C5–H is found to lie 669 cm^{-1} higher (Figure 6.3G), with minimally perturbed C–H stretches. The presence of small amounts of these higher lying isomers, particularly those shown in Figure 6.3D,E, may contribute to the broad appearance of the spectrum between 3100 cm^{-1} and 3200 cm^{-1}.

6.3.2 $[bmim]^+ \cdot (H_2O)_2$

The experimental and calculated IR spectra of $[bmim]^+ \cdot (H_2O)_2$ are shown in Figure 6.4. Compared to the $n = 1$ spectrum, the addition of the second water molecule gives rise to two new peaks at 3700 cm^{-1} and 3476 cm^{-1}, characteristic of a water having one free OH and donating one hydrogen-bond. Features corresponding to the symmetric and antisymmetric stretch of a water having two free OH are still present but slightly blueshifted to 3647 cm^{-1} and 3735 cm^{-1}. This peak pattern points to a structure in which the two water molecules are hydrogen-bonded to each other. The two isoenergetic lowest energy isomers are found with such a structure, in which the first water is interacting with C2–H on either the C6–H or C10–H side. Both isomers are calculated to have a slightly more redshifted

C2–H stretch than the n = 1 clusters at 3066 and 3069 cm^{-1}, in agreement with the observed feature at 3045 cm^{-1}. This indicates that the water–water hydrogen-bonding leads to a stronger C2–H–water interaction. Again, both isomers show a strong relative intensity for the calculated C2–H stretch that is not reflected in the experimental spectrum. Rotation of the water chain into the imidazolium ring plane leads to low lying isomers (29 cm^{-1} and 129 cm^{-1}) in which the water molecules are also interacting with the alkyl groups. The energies of these isomers point to a very loose and flexible binding motif between the water dimer and $[bmim]^+$, which likely contributes to the observed broadening of the C2–H and OH features.

6.3.3 $[bmim]^+ \cdot (H_2O)_3$

The number of features in the OH stretch region in the experimental IR spectrum of $[bmim]^+ \cdot (H_2O)_3$, shown in Figure 6.5A, suggests that there are more than one distinct isomer present. The lowest energy isomer found has a linear chain of water molecules interacting with C2–H and C6–H (Figure 6.5B), a continuation of the structure of the n = 2 cluster. This isomer gives rise to the observed H_2O symmetric and antisymmetric features at 3646 cm^{-1} and 3736 cm^{-1}, as well as the hydrogen-bonded features around 3390 and 3430 cm^{-1}. The cooperative hydrogen-bonding interaction in the water chain leads to an intense and redshifted C2–H stretch calculated at 3046 cm^{-1}, in agreement with the observed broad feature around 3020 cm^{-1}. Similarly to the n = 2 cluster, the linear water chain is fairly free to rotate, and additional isomers, such as that shown in Figure 6.5D, are energetically accessible. The presence of these isomers also likely contributes to the broad appearance of the C2–H and associated OH stretches.

Figure 6.4 Experimental (A) and MP2/def2TZVP calculated (B–E) IR spectra of $[bmim]^+\cdot(H_2O)_2$. The relative energies of each isomer, including ZPE correction, are listed. The imidazolium C2–H and symmetric and antisymmetric H_2O stretches are labelled in (B).

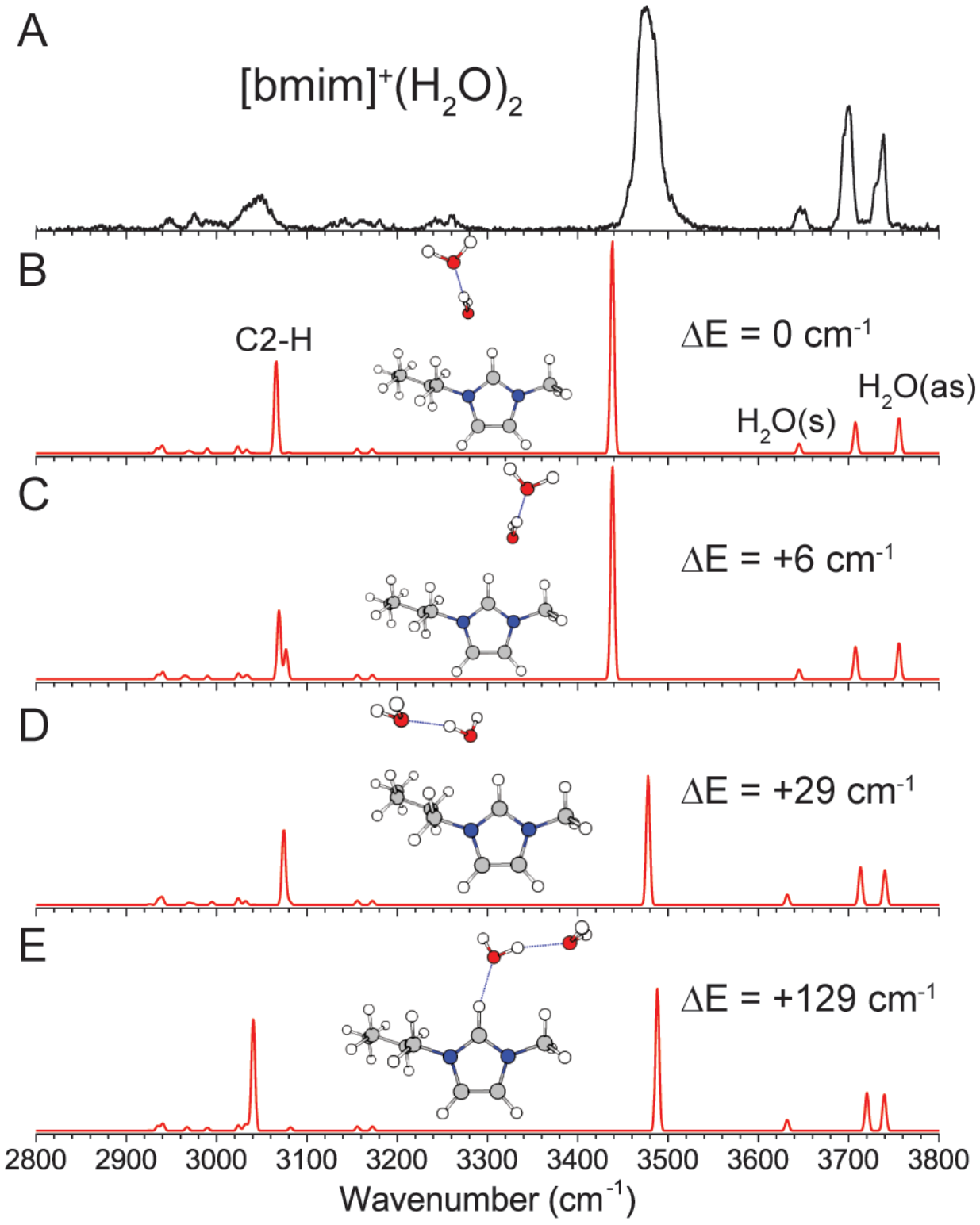

Figure 6.5 Experimental (A) and MP2/def2TZVP calculated (B–D) IR spectra of $[bmim]^+ \cdot (H_2O)_3$. The relative energies of each isomer, including ZPE correction, are listed. The imidazolium C2–H and symmetric and antisymmetric H_2O stretches are labelled in (B).

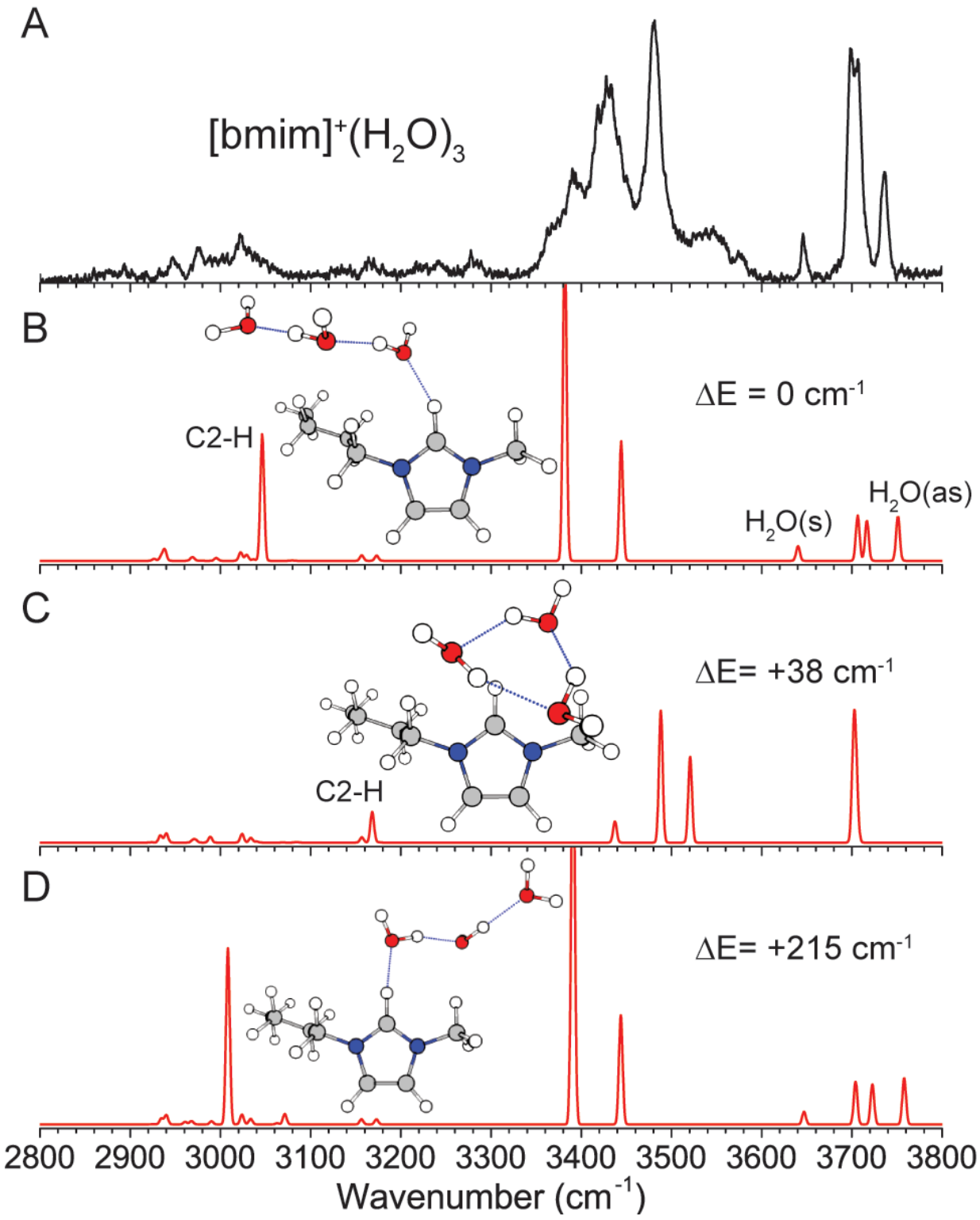

Figure 6.6 Comparison of the n = 3 isomer with the water ring, calculated with various methods with the def2TZVP basis set. The MP2 calculation is the same as that shown in Fig. 6.5C. The calculated IR spectrum is scaled by 0.957 (MP2), 0.941 (wB97XD), and 0.955 (cam-B3LYP and cam-B3LYP/GD3BJ). The DFT optimizations are started from the MP2 optimized geometry. The inclusion of dispersion correction is necessary for reproducing the minimum geometry. Also note that for the DFT calculations, the CH stretches requires a different scaling factor than the OH stretches, especially for wB97XD.

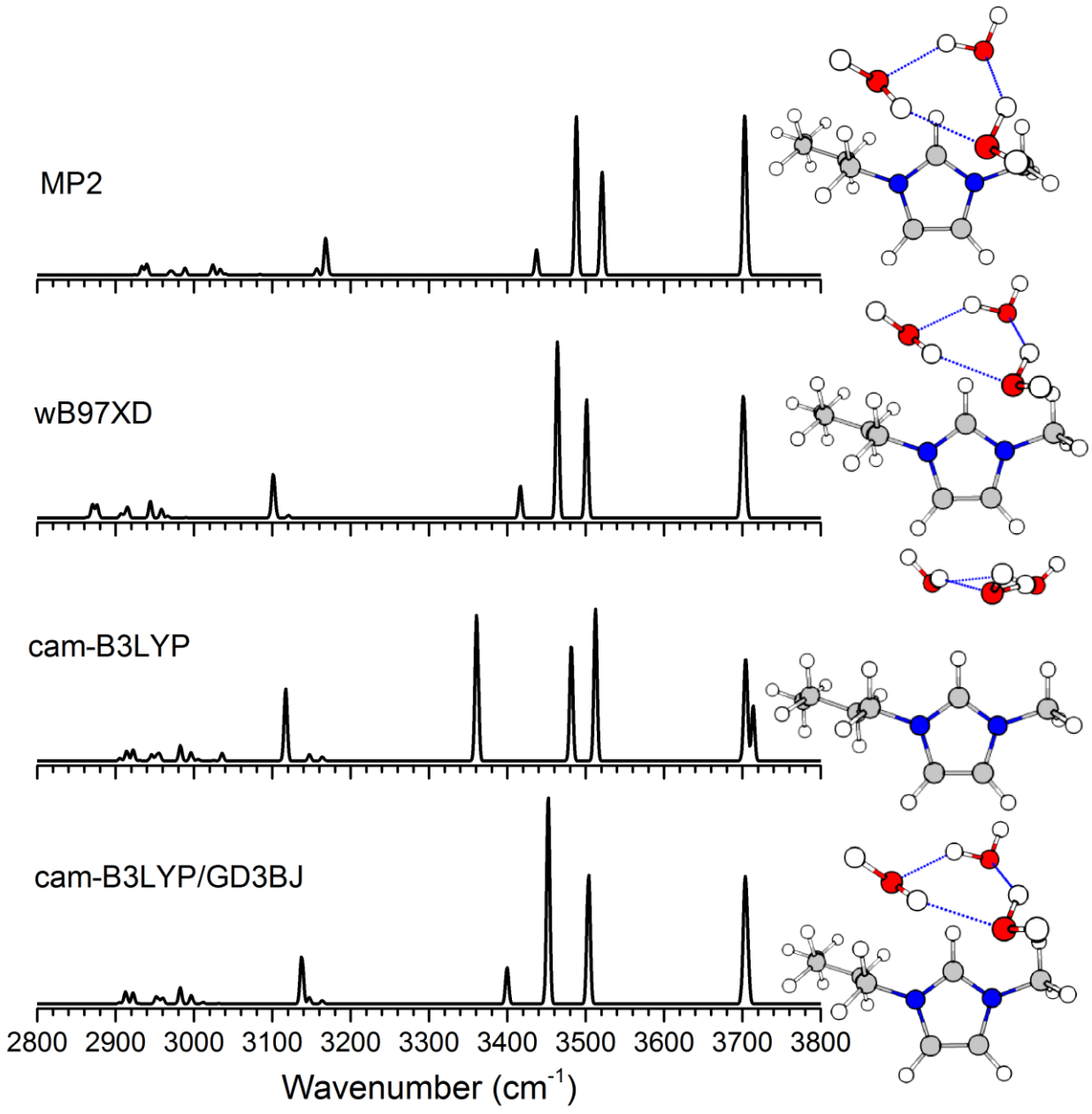

A different isomer, with a three-membered water ring situated on top of the imidazolium ring (Figure 6.5C), is found to be nearly isoenergetic with the lowest energy structure, lying only 38 cm^{-1} higher in energy. The water network in this isomer corresponds to the lowest energy structure of the neutral water cluster,[39–41] where all three water molecules are involved in a similar single-donor–single-acceptor hydrogen-bonding environment, leading to a single peak at 3700 cm^{-1} in the free OH region. Additionally, there is no direct C2–H–water interaction, and all the imidazolium CH have frequencies near 3160 cm^{-1}. This isomer can account for the strong peak at 3700 cm^{-1} as well as the two higher frequency hydrogen-bonded feature at 3480 cm^{-1} and 3540 cm^{-1}. It should be noted that no stable structures were found for a 3-membered water ring interacting more directly with C2–H at the MP2 level of theory, which differs from DFT calculations. The wB97XD functional yielded a similar structure as MP2, but the water ring is tilted more towards the C2–H, resulting in a shorter C2–H···O distance. The cam-B3LYP functional, on the other hand, gives a structure in which the water ring is mostly interacting with the C2–H and is almost perpendicular to the plane of the imidazolium ring. Upon inclusion of the GD3BJ empirical dispersion, the structure is again similar to the MP2 result. These results (Figure 6.6) indicate that the exact location of the water ring involves subtle competition between the two binding sites and requires accurate treatment of long-range interactions. The importance of including dispersion correction in DFT is similar to theoretical treatment of pure ionic liquids.[42,43]

6.3.4 $[bmim]^+\cdot(H_2O)_4$ and $[bmim]^+\cdot(H_2O)_5$

The experimental IR spectra of the $[bmim]^+\cdot(H_2O)_4$ and $[bmim]^+\cdot(H_2O)_5$ clusters, shown in Figure 6.7, are simpler than the smaller clusters. The presence of a single free OH feature at 3700 cm^{-1} indicates that all water molecules are involved in a hydrogen-bond donor interaction. Additionally, a single dominant broad feature centered at 3430 cm^{-1} indicates that all the water molecules are in a

fairly similar hydrogen-bonding environment. These observations are consistent with the 4- and 5-membered ring structures of the isolated neutral water clusters.[39–41] We find that the lowest energy isomer for both clusters has such a water ring located on top of the imidazolium ring. The resulting calculated IR spectra show a good agreement with the experiment for both species. It should be noted that there are multiple isomers with this general structure, *i.e.* the water ring can sit nearer to C2–H or C4–H/C5–H. In particular, MP2 calculations give the isomer shown in Figure 6.7B as the lowest energy isomer for $n = 4$ cluster, while wB97XD calculations show the isomer with the water ring sitting closer to C2–H to be 17 cm^{-1} lower. This points to a very flexible interaction between the water network and the top of the imidazolium ring, similar to the interaction with the C2–H. For the $n = 5$ cluster, we also considered isomers with a more cage like water network involving a 4-membered ring, but the calculated IR spectrum contained additional vibrational features near 3600 cm^{-1}, which is not observed experimentally. The 3220 cm^{-1} feature in the experimental spectrum of the $n = 5$ cluster is not reproduced in the calculation. We attribute this feature to the Fermi resonance between the overtone of the H_2O bend and the most redshifted OH stretch. This coupling, in which the overtone band borrows intensity from the OH stretch, has been described in detail in the case of benzene–water clusters.[36,44] Lastly, the larger and more flexible water ring in the $n = 5$ cluster allows for some C2–H–water interaction, as indicated by a redshifted calculated C2–H stretch. However, with increasing number of water molecules, the OH stretches dominate the experimental spectrum and redshift into the CH spectral region, making C–H stretch assignments difficult.

Figure 6.7 Experimental (A and C) and wB97XD/def2TZVP calculated (B and D) IR spectra of $[bmim]^+\cdot(H_2O)_4$ and $[bmim]^+\cdot(H_2O)_5$.

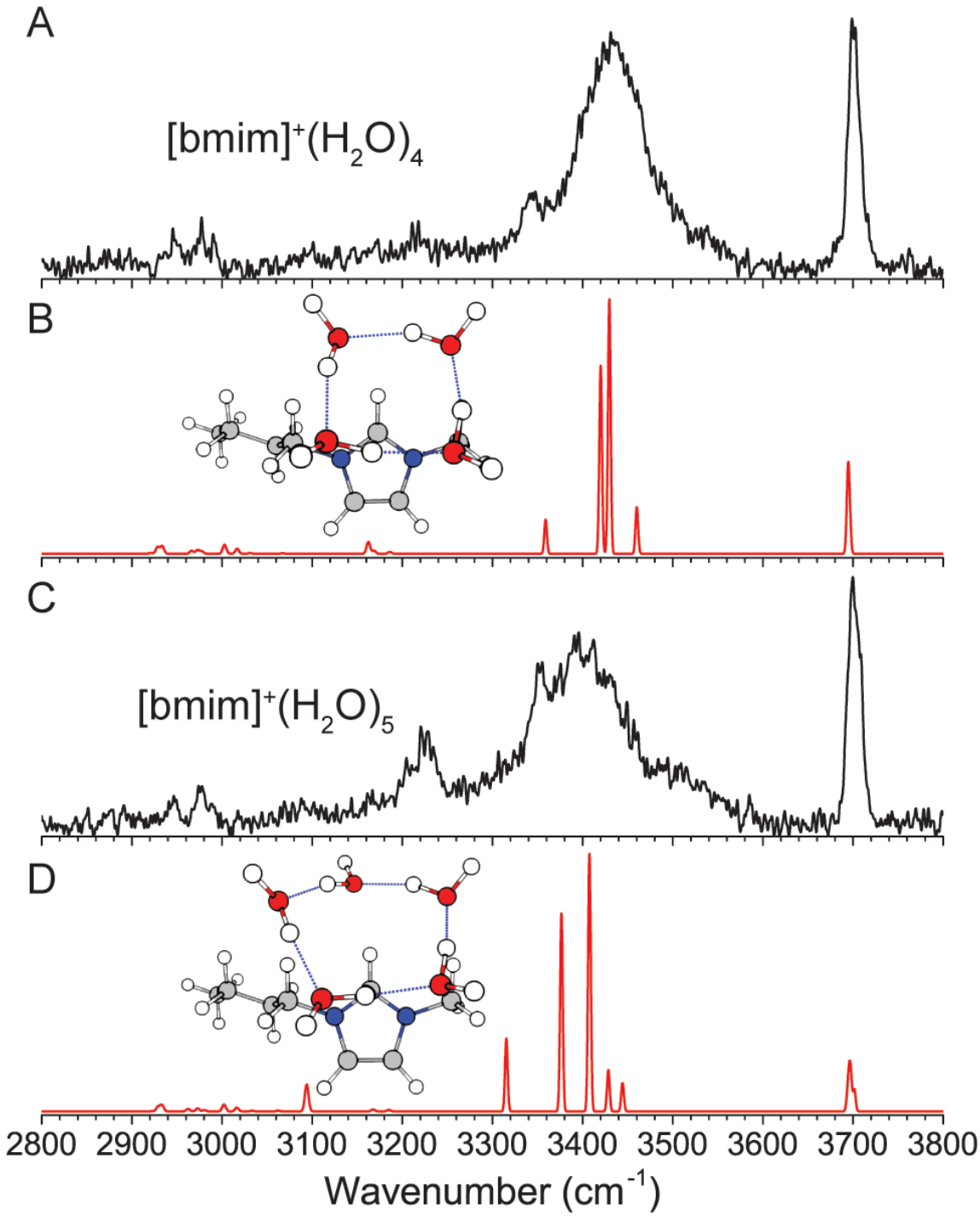

6.3.5 $[bmim]^+ \cdot (H_2O)_6$

The experimental IR spectrum of $[bmim]^+ \cdot (H_2O)_6$, shown in Figure 6.8A, has a broad distribution of peaks in the hydrogen-bonded region, but again only one feature in the free OH region, indicating that all water molecules are hydrogen-bond donors. The corresponding isolated neutral water cluster has five energetically close-lying isomers, namely the "ring", "bag", "book", "cage", and "prism" isomers, which have been the subject of numerous studies.[40,45,46] We considered solvation geometries where these water clusters are interacting with the imidazolium ring in various configurations. The lowest energy isomer found, shown in Figure 6.8B, has the water molecules arranged in the "book" geometry, draped on top and onto the C2–H side of the imidazolium ring. This structure involves a stable water cluster geometry that overlaps with the two strongest binding sites on the imidazolium. The calculated IR spectrum shows that it is sufficient to account for all the observed experimental features if the peak at 3225 cm^{-1} is again assigned to a Fermi resonance involving the H_2O bend overtone. Note that the transition away from a ring structure results in a higher frequency OH stretch, at around 3585 cm^{-1}, corresponding to one of the OH stretch of the water molecule that is a double hydrogen-bond donor. The next isomer, calculated to be 206 cm^{-1} higher in energy, involves a 6-membered water ring (Figure 6.8C), and may also contribute to the experimental spectrum. These two isomers have water network that maximizes direct interaction with the charged imidazolium, in contrast to the more three-dimensional structures such the bag (Figure 6.8D), cage or prism isomers, which all lie higher in energy.

6.3.6 $[bmim]^+\cdot(H_2O)_7$ and $[bmim]^+\cdot(H_2O)_8$

A comprehensive isomer search for the n = 7 and 8 clusters is not feasible here, but the geometries determined so far can be used to extrapolate plausible structures. We know a more open arrangement of the water molecules that can wrap around the imidazolium ring is energetically favorable, and the water molecules favor four-membered and five-membered rings. Additionally, the spectrum for the n = 7 and 8 clusters are very similar to that of the n = 6 cluster, supporting the assignment to similar structures. Therefore, we considered the extension of the n = 6 "book" water network, leading to the 5 + 2 "book" arrangement for the n = 7 cluster and the 4 + 4 "open-u" arrangement for the n = 8 cluster, as shown in Figure 6.9B and D. The calculated IR spectra show similar features as the experimental spectra, suggesting that these isomers are reasonable candidates. The arrangement of the water molecules in the n = 7 cluster is similar to one of the low energy neutral water isomers.[40] However, the n = 8 isomer is different than the corresponding isolated water cluster which distinctly favors a cubic geometry. We do not think such an isomer has a major presence in our experiment because a cubic water arrangement situated on top of the imidazolium ring would result in half of the water molecules not interacting with $[bmim]^+$. Additionally, this type of water clusters would lead to stronger hydrogen-bonds and lower frequency OH stretches,[47] which are not observed in the n = 8 spectrum.

Figure 6.8 Experimental (A) and wB97XD/def2TZVP calculated (B–D) IR spectra of $[bmim]^+\cdot(H_2O)_6$. The relative energies of each isomer, including ZPE correction, are listed.

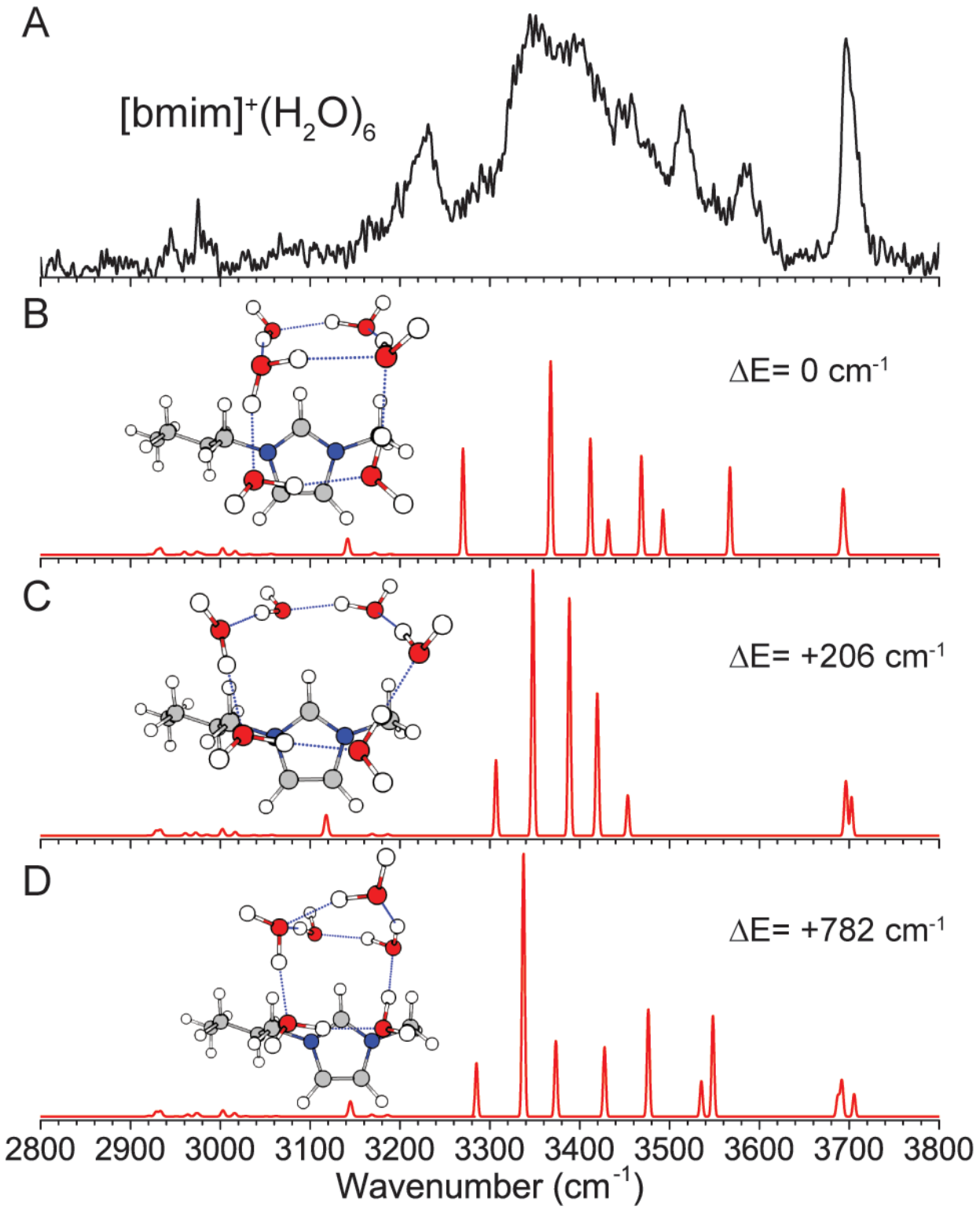

Figure 6.9 Experimental (A and C) and wB97XD/def2TZVP calculated (B and D) IR spectra of $[bmim]^+\cdot(H_2O)_7$ and $[bmim]^+\cdot(H_2O)_8$

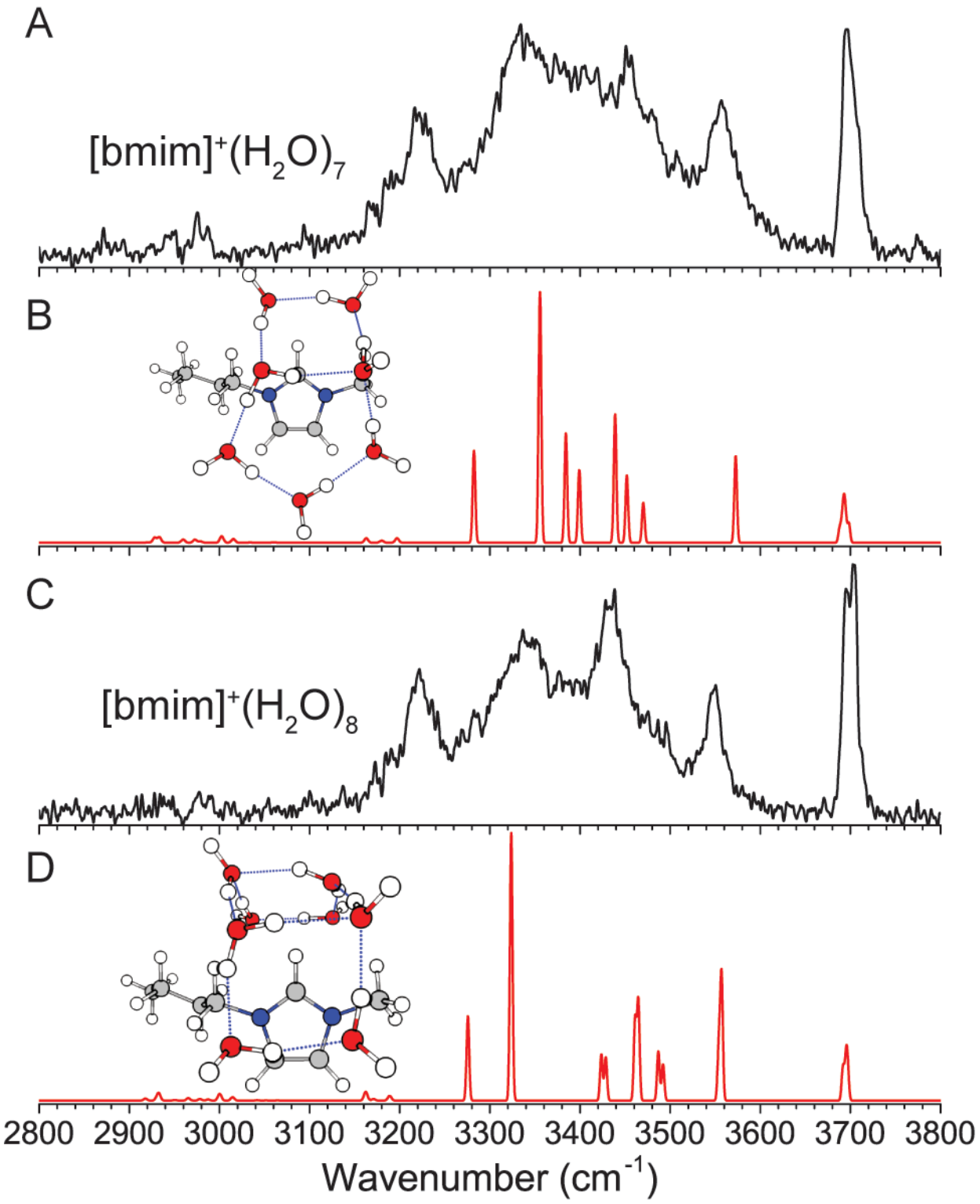

6.4 Discussions

IR predissociation spectroscopy of the isolated $[bmim]^+\cdot(H_2O)_n$ clusters allow us to examine in detail the competing long range interactions present here. The calculated structures show that the water arrangement in $[bmim]^+\cdot(H_2O)_n$ is similar to those found for neutral water clusters for n = 1–5. For the smallest n = 1 and n = 2 clusters, the preferred water binding site is centered on the C2–H group. The n = 3 cluster represents the tipping point in which the water molecules form a ring and the interaction site switches to the top of the imidazolium ring. For clusters with $n \geq 6$, the water network evolves in such a manner that the interaction with the delocalized charge on the imidazolium is maximized. This leads to water arrangements with a more open structure than the isolated water clusters.

The interaction between water and C2–H has been described as a hydrogen-bonding interaction.[7,21] Our experimental spectra and calculation results show that this interaction has some hydrogen-bonding character. Notably, interaction with the first water molecule redshifts the C2–H frequency from 3160 cm^{-1} to 3080 cm^{-1}. The formation of a water chain in n = 2 and 3 clusters further redshifts the C2–H frequency to 3045 $cm^{-1}$and 3020 cm^{-1}, respectively. The calculated structures show that the C2–H bond lengthens slightly from 1.078 Å in the bare $[bmim]^+$ ion to 1.082 Å in n = 1, 1.085 Å in n = 2 and 1.086 Å for the n = 3 water chain isomer. This relatively small bond length change is the only notable change in the geometry of $[bmim]^+$ upon solvation, and points to a weak hydrogen-bonding interaction. A weak hydrogen-bond is also consistent with the lack of directionality observed for the C2–H–water interaction. Hydrogen-bonds usually have a linear X–H···A geometry while the C2–H···O angle is calculated to be about 150° with a very flat double-well potential. However, these weak hydrogen-bond characteristics are not consistent with the substantial 9.8 kcal mol^{-1} binding energy calculated for the water in the n = 1 clusters. Therefore, electrostatic and dispersion interactions with the overall positively charged imidazolium are the main contributions to the overall binding energy.

This is evidenced by the $n = 1$ isomer shown in Figure. 6.3F, in which the water is located on top the imidazolium ring and not interacting with any C–H group. The binding energy for this isomer is only reduced by 1.8 kcal mol^{-1}. Additionally, the binding energy of a water molecule to the hydrophobic tetramethylammonium cation is calculated to be at a similar value of 10.5 kcal mol^{-1}.[30]

A typical mass spectrum showing the distribution of solvated $[bmim]^+$ clusters formed in the cold ion trap was published in ref. 31 and is shown in Figure 6.10. It shows a distinct intensity distribution which indicates that the sixth water should have a comparably lower binding energy while the fourth water should have a distinctively higher binding energy. This is confirmed by the calculated binding energy of each subsequent additional water molecule, listed in Table 6.1. The wB97XD/def2TZVP calculations predict a 9.9 kcal mol^{-1} binding energy for the sixth water molecule. This is noticeably smaller than the 12.5 kcal mol^{-1} binding energy calculated for the fourth water, as well as the consistent 10.4–10.5 kcal mol^{-1} binding energies of the fifth, seventh, and eighth water molecule.

The $[bmim]^+ \cdot (H_2O)_n$ results presented here can be compared to those of a similar solvated cluster, benzene$\cdot(H_2O)_n$, studied by Zwier and coworkers.[44,47,48] For the $n = 1$–6 clusters, we find that the water network adopts very similar structures in both cases and the vibrational spectra in the OH stretch region are remarkably similar. The main difference is that in the benzene$\cdot(H_2O)_n$ clusters, one water always has an OH pointed towards the electron density above the benzene ring, leading to an OH stretch feature at ~3650 cm^{-1} for all clusters. In the case of $[bmim]^+ \cdot (H_2O)_n$, the positive charge on the $[bmim]^+$ forces the water to interact *via* the oxygen end with the OH pointing outward. Interestingly, the IR spectra of the two systems differ significantly for the $n = 8$ cluster. The weak interaction between benzene and water leads to the formation of a cubic water network situated on top of benzene, which gives rise to a group of OH stretches below 3200 cm^{-1} and a group of OH stretches above 3400 cm^{-1}.

Figure 6.10 Mass spectrum of solvated $[bmim]^+$ clusters.

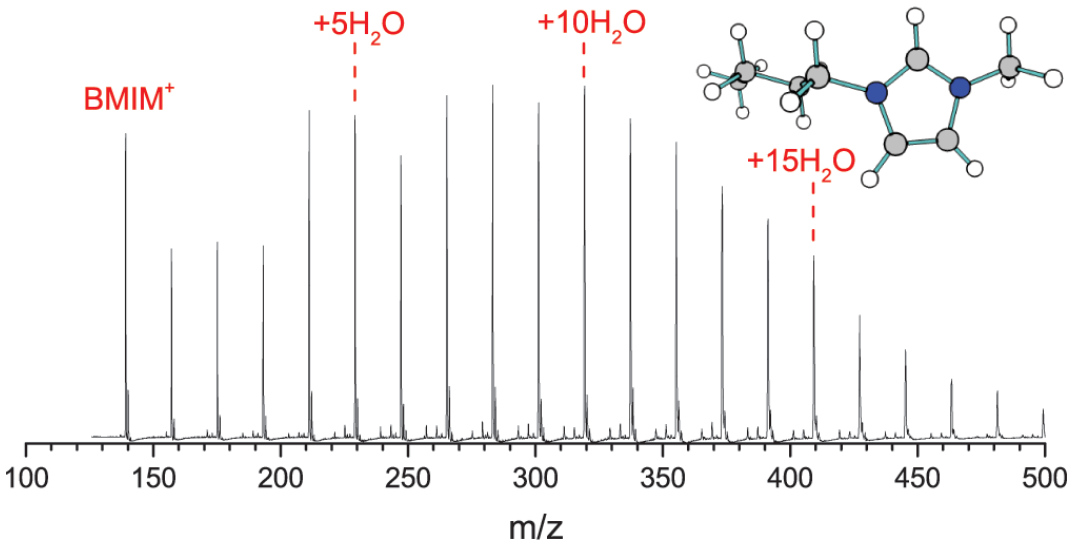

Table 6.1 The calculated binding energy (BE, in kcal mol^{-1}), corresponding to $[bmim]^+\cdot(H_2O)_n$–$[bmim]^+\cdot(H_2O)_{n-1}$–$H_2O$, at the MP2/def2TZVP and wB97XD/def2TZVP levels

$[bmim]^+\cdot(H_2O)_n$		
n	**BE (MP2)**	**BE (wB97XD)**
1	9.76	9.89
2	9.07	9.36
3	9.23	9.67
4	13.14	12.54
5	-	10.43
6	-	9.92
7	-	10.48
8	-	10.42

The $[bmim]^+\cdot(H_2O)_8$ cluster, on the other hand, has a water network wrapped around $[bmim]^+$, giving rise to OH stretches extending the range between 3200 cm^{-1} and 3600 cm^{-1}. This difference highlights the effect of the delocalized charge on the solvation structure. We also note that the IR predissociation spectra of $[bmim]^+\cdot(H_2O)_n$, especially the smaller clusters, are also very similar to those of $[tetramethylammonium]^+(H_2O)_n$, a solvated hydrophobic system.[30]

Finally, it is of interest to compare our results to what is known about the interaction of water in bulk $[bmim]^+[BF_4]^-$ ionic liquid. The cation–anion, cation–water and anion–water interactions have been studied by NMR using nuclear Overhauser enhancement measurements[20] and analyzed by molecular dynamics simulations.[21] The NMR data showed two distinct hydration regimes as the water concentration increased. At low concentrations, the water molecules were found to disrupt the short range network of the neat ionic liquid by interacting mainly with the imidazolium C–H groups, with preferential interaction with the C2–H. Additionally, the H2 NMR shift was found to be linearly correlated with those of the H6 and H10. This is consistent with our results for the $n = 1$ and $n = 2$ clusters, which show that the water interaction is centered on C2–H but is loose and flexible enough to also interact with C6–H and C10–H. At higher water concentrations, the ionic liquid network is perturbed by the insertion of whole water clusters, and the interaction between $[bmim]^+$ and water becomes non-selective with respect to the various C–H groups. This is again consistent with the picture emerging from the work presented here, in which the dominant electrostatic and dispersion interactions and comparably stronger water–water hydrogen-bonds lead to water clusters located on top of the imidazolium ring for the $n \geq 3$ clusters.

6.5 Conclusion

The intermolecular interactions between water molecules and imidazolium cation are revealed by the IR predissociation spectra of $[bmim]^+ \cdot (H_2O)_{1–8}$ in the CH and OH stretch region. The experimental and calculated results show that the imidazolium C2–H can form a weak hydrogen-bond type interaction with a water molecule, but the solvation is energetically dominated by electrostatic and dispersion interactions. For the small n = 1–3 clusters, water molecules solvate the $[bmim]^+$ by predominately interacting with the C2–H moiety, and the linear chain water arrangement strengthens the C2–H–water interaction. For the larger clusters, water–water hydrogen-bonds dominate and drive the formation of water ring isomers, which preferentially interact with the delocalized positive charge by situating on top of the imidazolium ring. The geometry of the water arrangement in $[bmim]^+ \cdot (H_2O)_n$ mirrors the low energy isomers of neutral water clusters for the n = 1–6 cluster sizes, while the larger clusters adopt a more open arrangement that envelops the positively charged imidazolium ring rather than developing a tight water–water network. The observed solvation behavior reported here is in agreement with solution phase studies that showed concentration-dependent solvation effects in ionic liquid–water mixtures.

6.6 References

1. J.P. Hallett, T. Welton, *Chem. Rev.*, **2011,** 111, 3508–3576.

2. L.M. Varela, T. Mendez-Morales, J. Carrete, V. Gomez-Gonzalez, B. Docampo-Alvarez, L.J. Gallego, O. Cabeza, O. Russina, *J. Mol. Liq.*, **2015,** 210, 178–188.

3. H. Weingaertner, *Angew. Chem., Int. Ed.*, **2008,** 47, 654–670.

4. Y. Kohno, H. Ohno, *Chem. Commun.*, **2012,** 48, 7119–7130.

5. Y. Cao, Y. Chen, X. Sun, Z. Zhang, T. Mu, *Phys. Chem. Chem. Phys.*, **2012,** 14, 12252–12262.

6. M.G. Freire, C.M.S.S. Neves, P.J. Carvalho, R.L. Gardas, A.M. Fernandes, I.M. Marrucho, L.M.N.B.F. Santos, J.A.P. Coutinho, *J. Phys. Chem. B*, **2007,** 111, 13082–13089.

7. M. Brehm, H. Weber, A.S. Pensado, A. Stark, B. Kirchner, *Phys. Chem. Chem. Phys.*, **2012,** 14, 5030–5044.

8. R. Hayes, G.G. Warr, R. Atkin, *Chem. Rev.*, **2015,** 115, 6357–6426.

9. K. Fumino, A. Wulf, R. Ludwig, *Phys. Chem. Chem. Phys.*, **2009,** 11, 8790–8794.

10. E.R. Talaty, S. Raja, V.J. Storhaug, A. Dolle, W.R. Carper, *J. Phys. Chem. B*, **2004,** 108, 13177–13184.

11. S. Saha, S. Hayashi, A. Kobayashi, H. Hamaguchi, *Chem. Lett.*, **2003,** 32, 740–741.

12. N.E. Heimer, R.E. Del Sesto, Z.Z. Meng, J.S. Wilkes, W.R. Carper, *J. Mol. Liq.*, **2006,** 124, 84–95.

13. J.H. Antony, D. Mertens, A. Dolle, P. Wasserscheid, W.R. Carper, *ChemPhysChem*, **2003,** 4, 588–594.

14. S. Cha, M. Ao, W. Sung, B. Moon, B. Ahlstrom, P. Johansson, Y. Ouchi, D. Kim, *Phys. Chem. Chem. Phys.*, **2014,** 16, 9591–9601.

15. A. Yokozeki, D.J. Kasprzak, M.B. Shiflett, *Phys. Chem. Chem. Phys.*, **2007,** 9, 5018–5026.

16. E.I. Izgorodina, D.R. MacFarlane, *J. Phys. Chem. B*, **2011,** 115, 14659–14667.

17. Y. Gao, L. Zhang, Y. Wang, H. Li, *J. Phys. Chem. B*, **2010,** 114, 2828–2833.

18. S. Tsuzuki, H. Tokuda, M. Mikami, *Phys. Chem. Chem. Phys.*, **2007,** 9, 4780–4784.

19. K. Fumino, S. Reimann, R. Ludwig, *Phys. Chem. Chem. Phys.*, **2014,** 16, 21903–21929.

20. A. Mele, C.D. Tran, S.H.D. Lacerda, *Angew. Chem., Int. Ed.*, **2003,** 42, 4364–4366.

21. M. Moreno, F. Castiglione, A. Mele, C. Pasqui, G. Raos, *J. Phys. Chem. B*, **2008,** 112, 7826–7836.

22. Q.-G. Zhang, N.-N. Wang, S.-L. Wang, Z.-W. Yu, *J. Phys. Chem. B*, **2011,** 115, 11127–11136.

23. D. Strasser, F. Goulay, M.S. Kelkar, E.J. Maginn, S.R. Leone, *J. Phys. Chem. A*, **2007,** 111, 3191–3195.

24. J.A. Fournier, C.T. Wolke, C.J. Johnson, A.B. McCoy, M.A. Johnson, *J. Chem. Phys.*, **2015,** 142, 064306.

25. C.J. Johnson, J.A. Fournier, C.T. Wolke, M.A. Johnson, *J. Chem. Phys.*, **2013,** 139, 224305.

26. E.I. Obi, C.M. Leavitt, P.L. Raston, C.P. Moradi, S.D. Flynn, G.L. Vaghjiani, J.A. Boatz, S.D. Chambreau, G.E. Douberly, *J. Phys. Chem. A*, **2013,** 117, 9047–9056.

27. R. Cooper, A.M. Zolot, J.A. Boatz, D.P. Sporleder, J.A. Stearns, *J. Phys. Chem. A*, **2013,** 117, 12419–12428.

28. A.J.A. Harvey, A. Sen, N. Yoshikawa, C.E.H. Dessent, *Chem. Phys. Lett.*, **2015,** 634, 216–220.

29. K. Hanke, M. Kaufmann, G. Schwaab, M. Havenith, C.T. Wolke, O. Gorlova, M.A. Johnson, B.P. Kar, W. Sander, E. Sanchez-Garcia, *Phys. Chem. Chem. Phys.*, **2015,** 17, 8518–8529.

30. J.S. Prell, E.R. Williams, *J. Am. Chem. Soc.*, **2009,** 131, 4110–4119.

31. B.M. Marsh, J.M. Voss, E. Garand, *J. Chem. Phys.*, **2015,** 143, 204201.

32. M.J. Frisch, G.W. Trucks, H.B. Schlegel, G.E. Scuseria, M.A. Robb, J.R. Cheeseman, G. Scalmani, V. Barone, B. Mennucci, G.A. Petersson, H. Nakatsuji, M. Caricato, X. Li, H.P. Hratchian, A.F. Izmaylov, J. Bloino, G. Zheng, J.L. Sonnenberg, M. Hada, M. Ehara, K. Toyota, R. Fukuda, J. Hasegawa, M. Ishida, T. Nakajima, Y. Honda, O. Kitao, H. Nakai, T. Vreven, J.A. Montgomery Jr., J.E. Peralta, F. Ogliaro, M. Bearpark, J.J. Heyd, E. Brothers, K. N. Kudin, V.N. Staroverov, R.Kobayashi, J. Normand, K. Raghavachari, A. Rendell, J.C. Burant, S.S. Iyengar, J. Tomasi, M. Cossi, N. Rega, N.J. Millam, M. Klene, J.E. Knox, J.B. Cross, V. Bakken, C. Adamo, J. Jaramillo, R. Gomperts, R.E. Stratmann, O. Yazyev, A.J. Austin, R. Cammi, C. Pomelli, J.W. Ochterski, R.L. Martin, K. Morokuma, V.G. Zakrzewski, G.A. Voth, P. Salvador, J.J. Dannenberg, S. Dapprich, A.D. Daniels, Ö. Farkas, J.B. Foresman, J.V. Ortiz, J. Cioslowski, D.J. Fox, *Gaussian 09*, Gaussian, Inc., Wallingford CT, **2009**

33. F. Weigend, R. Ahlrichs, *Phys. Chem. Chem. Phys.*, **2005,** 7, 3297–3305.

34. F. Weigend, *Phys. Chem. Chem. Phys.*, **2006,** 8, 1057–1065.

35. B.M. Marsh, J.M. Voss, J. Zhou, E. Garand, *Phys. Chem. Chem. Phys.*, **2015,** 17, 23195–23206.

36. D.P. Tabor, R. Kusaka, P.S. Walsh, E.L. Sibert III, T.S. Zwier, *J. Phys. Chem. Lett.*, **2015,** 6, 1989–1995.

37. T.D. Vaden, J.M. Lisy, P.D. Carnegie, E.D. Pillai, M.A. Duncan, *Phys. Chem. Chem. Phys.*, **2006,** 8, 3078–3082.

38. T.D. Vaden, C.J. Weinheimer, J.M. Lisy, *J. Chem. Phys.*, **2004,** 121, 3102–3107.

39. R. Ludwig, *Angew. Chem., Int. Ed.*, **2001,** 40, 1808–1827.

40. B. Temelso, K.A. Archer, G.C. Shields, *J. Phys. Chem. A*, **2011,** 115, 12034–12046.

41. M.F. Vernon, J.M. Lisy, D.J. Krajnovich, A. Tramer, H.S. Kwok, Y.R. Shen and Y.T. Lee, *Faraday Discuss.*, **1982,** 73, 387–397.

42. S. Zahn, D.R. MacFarlane, E.I. Izgorodina, *Phys. Chem. Chem. Phys.*, **2013,** 15, 13664–13675.

43. S. Grimme, W. Hujo, B. Kirchner, *Phys. Chem. Chem. Phys.*, **2012,** 14, 4875–4883.

44. D.P. Tabor, R. Kusaka, P.S. Walsh, T.S. Zwier, E.L. Sibert III, *J. Phys. Chem. A*, **2015,** 119, 9917–9930.

45. J. Kim, K. S. Kim, *J. Chem. Phys.*, **1998,** 109, 5886–5895.

46. D.M. Bates, G.S. Tschumper, *J. Phys. Chem. A*, **2009,** 113, 3555–3559.

47. C.J. Gruenloh, J.R. Carney, C.A. Arrington, T.S. Zwier, S.Y. Fredericks, K.D. Jordan, *Science*, **1997,** 276, 1678–1681.

48. R.N. Pribble, A.W. Garrett, K. Haber, T.S. Zwier, *J. Chem. Phys.*, **1995,** 103, 531–544

CHAPTER 7

Accessing the Vibrational Signatures of Amino Acid Ions Embedded in Water Clusters

Published: J.M. Voss, K.C. Fischer, and E. Garand. *Journal of Physical Chemistry Letters*, 9 (9), 2246–2250 (2018)

Abstract

We present an infrared predissociation (IRPD) study of microsolvated $GlyH^+\cdot(H_2O)_n$ and $GlyH^+\cdot(D_2O)_n$ clusters, formed inside of a cryogenic ion trap via condensation of H_2O or D_2O onto the protonated glycine ions. The resulting IRPD spectra, showing characteristic O−H and O−D stretches, indicate that H/D exchange reactions are quenched when the ion trap is held at 80 K, minimizing the presence of isotopomers. Comparisons of $GlyH^+\cdot(H_2O)_n$ and $GlyH^+\cdot(D_2O)_n$ spectra clearly highlight and distinguish the vibrational signatures of the water solvent molecules from those of the core $GlyH^+$ ion, allowing for quick assessment of solvation structures. Without the aid of calculations, we can already infer solvation motifs and the presence of multiple conformations. The use of a cryogenic ion trap to cluster solvent molecules around ions of interest and control H/D exchange reactions is broadly applicable and should be extendable to studies of more complex peptidic ions in large solvated clusters.

Author Contributions

JMV and KCF acquired experimental spectra; JMV, KCF, and EG performed theoretical calculations; JMV and EG performed data analyses and wrote the manuscript.

7.1 Introduction

Gas-phase action spectroscopy is a powerful tool for revealing the intricate details of noncovalent interactions, where well-resolved vibrational spectra of cold mass-selected clusters can selectively probe the chemical environment around each individual oscillator.[1] Methods such as infrared multiple photon dissociation (IRMPD),[2–5] UV–IR double resonance,[6–8] and infrared predissociation (IRPD) of tagged species[9–12] are well-established approaches to vibrationally characterize mass-selected ions and clusters. We recently demonstrated that a liquid-nitrogen-cooled ion trap is well-suited for clustering solvent molecules around any ion generated via electrospray ionization (ESI).[13] This affords the possibility to study a wide variety of large molecules, e.g., biologically relevant peptides or ligand-coordinated catalysts, in a well-controlled microsolvated environment, providing insights into the microscopic solvation structures and interactions of these species in bulk environments.

However, even at low (<50K) temperatures, inherent spectral congestion makes obtaining precise structural information from the IR spectrum increasingly difficult with increasing cluster sizes. For example, when studying peptides, the frequencies of the characteristic vibrational modes relating to the amide, amine, and carboxyl groups directly overlap with those of the solvent water bending and stretching modes. Hence, in larger solvated clusters, the peptide spectral signatures are difficult to disentangle from those of the solvent. Coupled with the possible presence of multiple solvation isomers and peptide conformations, extensive theoretical efforts are required to digest the rich experimental vibrational spectrum. To partially circumvent this issue, solution-phase IR spectroscopy of peptides is alternatively carried out in D_2O solvent[14,15] because the D–O–D bending modes (~1180 cm^{-1}) do not overlap with the characteristic amide I and II modes. However, peptidic N–H and O–H groups undergo rapid H/D exchange with D_2O in solution, such

that the analyte and solvent vibrations still overlap in the X–H/X–D stretching region. This unfortunately makes studying these N–H and O–H stretches, which are quite informative about the local solvation environment and strengths of hydrogen bonds,[6,16,17] more difficult.

In this Letter, using the simple protonated glycine ($GlyH^+$) amino acid as an example, we demonstrate that the formation of solvated clusters can be achieved with minimal solvent–peptide H/D exchange under the proper conditions in a cryogenic ion trap. Mass spectral and IRPD data show that it is possible to controllably access solvated clusters in which an all-hydrogen $GlyH^+$ is surrounded by D_2O molecules, such that the characteristic ion core vibrations are clearly distinguished from those of the solvent. Furthermore, comparisons of the H_2O- and D_2O-solvated cluster IRPD spectra in the 2600–3800 cm^{-1} region are presented to illustrate the structural information accessible with this approach, allowing for direct assignments of spectral features. The approach outlined here is related to previous H_2O/D_2O cluster isotopologue studies by Johnson and co-workers,[18,19] with increased capabilities that can solvate ESI ions under temperature-controlled conditions, making it more generally applicable and extendable to larger ions such as protonated peptides.

7.2 Experimental

The experiments presented here were performed in a dual cryogenic ion trap spectrometer, which has been described in detail previously.[13] Briefly, a ∼1 mM solution of glycine in methanol with trace formic acid was used to generate the all-hydrogen $GlyH^+$ ions using an ESI source. The ions were transferred into a linear octupole reaction trap, which is mounted to a liquid nitrogen cryostat that can maintain temperatures of 80–300 K. Collisions with helium or nitrogen buffer gas, seeded with either D_2O or H_2O vapor, thermalized the trapped ions and condensed the solvent

molecules onto $GlyH^+$. The products formed inside of the reaction trap were analyzed using a time-of-flight mass spectrometer that is situated after a second ion trap held at 10 K, which further thermalized the ions prior to IRPD.

To acquire the IRPD spectra, the solvated clusters from the reaction trap were further thermalized inside of the 10 K tagging trap via collisions with buffer gas comprised of 10% D_2 in helium. In the process, weakly bound D_2 adducts were formed for clusters with $n < 4$ solvent molecules. These clusters were extracted into the time-of-flight mass spectrometer, mass-selected, and intersected with the output of a Nd:YAG pumped OPO/OPA. Resonant absorption of a single photon resulted in loss of the D_2 tag for the smaller clusters (n = 0–3) and loss of a H_2O or D_2O molecule for the larger ones (n = 4–8). The photofragments were separated from the parent clusters inside of a two-stage reflectron, and the yield was monitored as a function of laser wavelength to produce the IRPD spectra.

7.3 Results and Analysis

Mass analyses of the products formed from the all-hydrogen $GlyH^+$ reacting with D_2O inside of the reaction trap at different temperatures are presented in Figure 7.1. At a trap temperature of 210 K, two dominant peaks at m/z = 76 and 77 are observed, as well as weaker features at m/z = 78, 79, and 80. The m/z = 76 feature corresponds to the all-hydrogen $GlyH^+$, which we will designate as D_0-$GlyH^+$ hereafter. The m/z = 77 feature therefore corresponds to $GlyH^+$ that has undergone one H/D exchange event, increasing its mass by 1 amu, i.e., D_1-$GlyH^+$. The dominance of the D_1-$GlyH^+$ species at >200 K is consistent with previous studies[20] that showed this species as the main product of the room-temperature gas-phase reaction between $GlyH^+$ and D_2O. Small amounts of $GlyH^+$ are observed to undergo multiple sequential H/D

exchanges, leading to the peaks at m/z = 78, 79, and 80. With decreasing trap temperature, the presence of partially deuterated species decreases rapidly, as shown in Figure 7.1B–E. At 170 K, only a small fraction of $GlyH^+$ undergoes H/D exchange. At 80 K, the lowest temperature attainable with a liquid nitrogen cryostat and the typical condition in which the clustering experiments are performed, about 6% of the $GlyH^+$ ions undergo H/D exchange. This estimate accounts for the 2% natural abundance of ^{13}C-containing D_0-$GlyH^+$. The residual D_1 species at 80 K is likely the result of the fact that collisional thermalization and H/D exchange occur simultaneously inside of the reaction trap, allowing a small fraction of ions to react with D_2O before they are completely cooled.

Figure 7.1F presents a typical mass spectrum observed when clustering D_2O onto D_0-$GlyH^+$ within the 80 K reaction trap, with the dominant clusters corresponding to D_0-$GlyH^+\cdot(D_2O)_n$. We note the presence of minor satellite peaks on either side of each D_0-$GlyH^+\cdot(D_2O)_n$ feature. The +1 m/z species are due to clustering of D_2O onto the small fraction of D_1-$GlyH^+$ that is present. The −1 m/z peaks are due to the presence of HDO impurities that lead to the formation of D_0-$GlyH^+\cdot(HDO)(D_2O)_{n-1}$, and the relative percentage of clusters containing at least one HDO expectedly increases with increasing cluster size. Mass selection ensures that neither of these isotopologues contribute to the IRPD spectra. However, possible isotopomers of the D_0-$GlyH^+\cdot(D_2O)_n$ clusters, such as D_1-$GlyH^+\cdot(HDO)(D_2O)_{n-1}$, cannot be separated by mass. These species can form via H/D exchange within the cluster or through condensation of HDO onto the small fraction of D_1-$GlyH^+$ ions. The IRPD spectra presented below will conclusively show that these isotopomers have a negligible contribution.

Figure 7.1 (A−E) Mass spectra of products formed when $GlyH^+$ ions are exposed to D_2O inside of the reaction trap held at various temperatures, as indicated, in the mass region around $GlyH^+$. (F) Broader range mass spectrum with the reaction trap held at 80 K, showing D_2O clustering around the ion. The * indicates a methylated $GlyH^+$ impurity and its D_2O clusters.

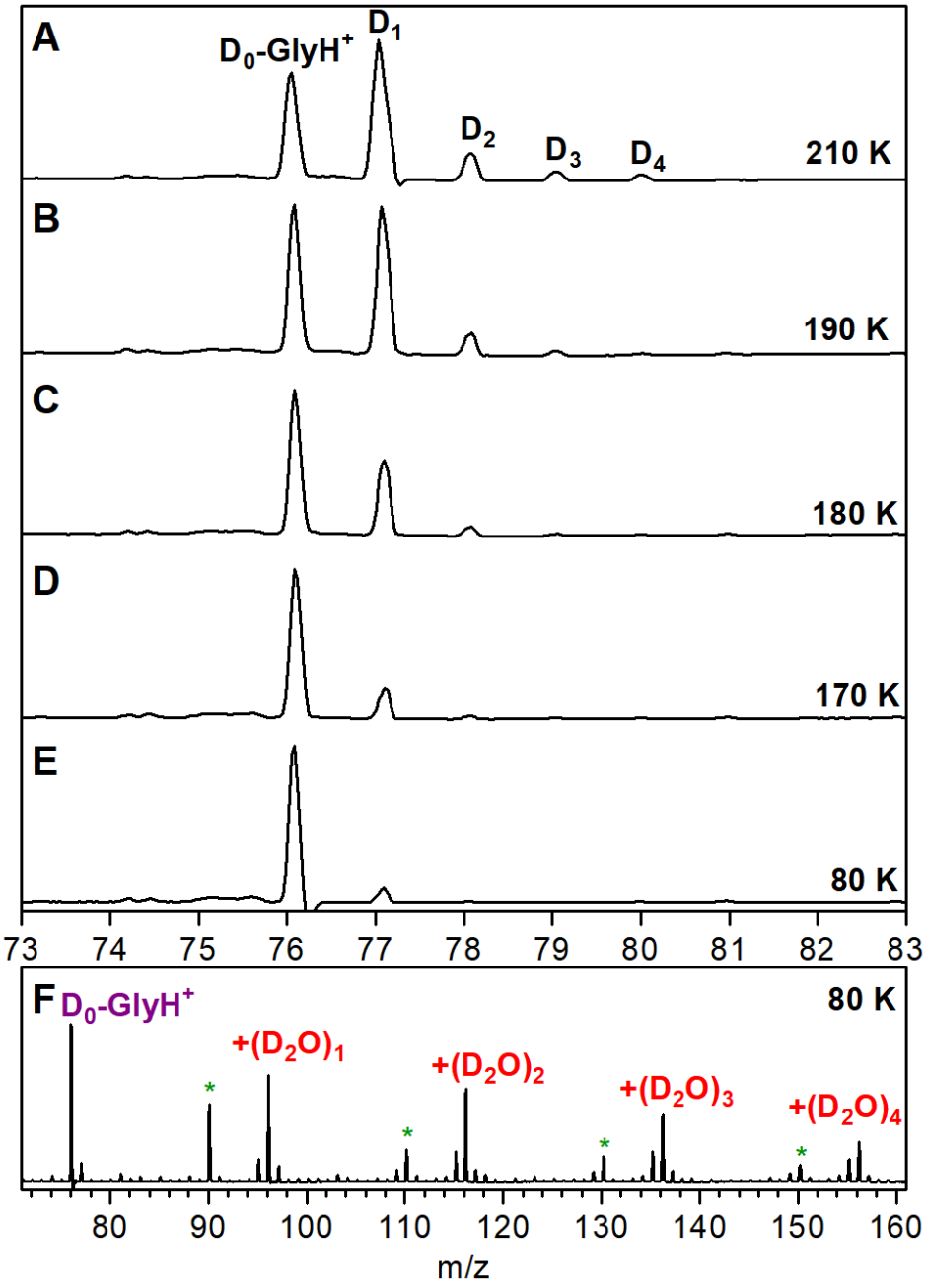

Figure 7.2 compares the IRPD spectrum of the unsolvated D_0-$GlyH^+\cdot(D_2)$ ion with those of the D_0-$GlyH^+\cdot(H_2O)_6$ and D_0-$GlyH^+\cdot(D_2O)_6$ clusters in the 2600–3800 cm^{-1} region. The D_0-$GlyH^+\cdot(D_2)$ spectrum contains four distinct features at 3551, 3351, 3298, and 2966 cm^{-1}, which can readily be assigned to the free carboxyl O–H stretch, the asymmetric and symmetric NH_2 stretches, and the internally hydrogen-bonded (H-bonded) N–H stretch, respectively. In comparison, the D_0-$GlyH^+\cdot(H_2O)_6$ spectrum in Figure 7.2B is more congested, with six distinct features in the 3000–3600 cm^{-1} region, a broad distribution of intensity spanning the 2700–3200 cm^{-1} region, as well as a partially resolved triplet near 3700 cm^{-1}. The features above 3600 cm^{-1} can safely be assigned to the H_2O free O–H stretches as they have higher frequencies than any of the $GlyH^+$ vibrations. On the other hand, the rest of the features can be attributed to either $GlyH^+$ (N–H or O–H groups) or H-bonded O–H stretches of H_2O molecules, and they are not readily assignable based only on the spectrum in Figure 7.2B.

The assignments are much clearer when comparisons are made with the IRPD spectrum of D_0-$GlyH^+\cdot(D_2O)_6$, and we can directly identify all of the observed features as either belonging to the $GlyH^+$ core ion or to the water solvent molecules. The spectra in Figure 2B,C contain the same broad distribution of intensity spanning the 2700–3200 cm^{-1} range as well as the 3060 and 3130 cm^{-1} peaks. These features common to both isotopologues must originate from the D_0-$GlyH^+$ ion and are assigned to H-bonded N–H and O–H stretches of $GlyH^+$. The features at 3341, 3481, 3511, and 3539 cm^{-1} that are present only in the D_0-$GlyH^+\cdot(H_2O)_6$ spectrum are due to H-bonded O–H stretches of H_2O. Similarly, the 3706, 3717, and 3730 cm^{-1} features are due to free O–H stretches of H_2O. Lastly, two features centered at 2750 and 2772 cm^{-1}, present only in the D_0-$GlyH^+\cdot(D_2O)_6$ spectrum, are readily assigned to the free O–D stretches of the D_2O molecules. In principle, the H-bonded O–D stretches of D_2O should be observable below 2600 cm^{-1}. However,

Figure 7.2 IRPD spectra of (A) D_0-$GlyH^+(D_2)$, (B) D_0-$GlyH^+(H_2O)_6$, and (C) D_0-$GlyH^+(D_2O)_6$. The structure of $GlyH^+$ is shown in panel (A). General assignments of observed features are noted and color coded: $GlyH^+$ (purple), H_2O (blue), and D_2O (red).

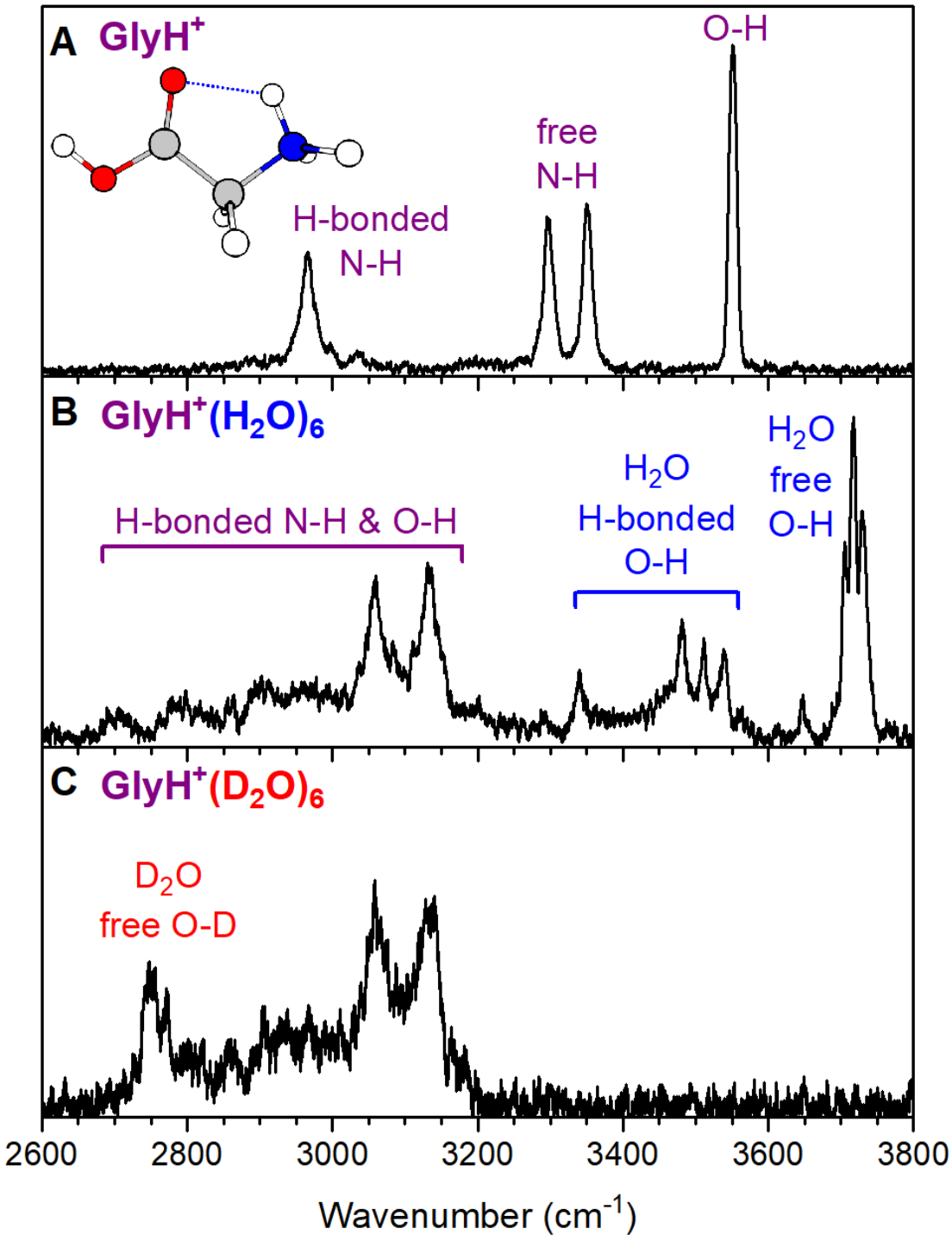

the lower intensity of these features combined with lower laser power in this region make their observation quite challenging. Finally, we note that the absence of features above 3200 cm^{-1} in the D_0-$GlyH^+\cdot(D_2O)_6$ spectrum provides conclusive proof that minimal H/D exchange has occurred within the cluster. Substituting a single hydrogen in D_0-$GlyH^+$ for a deuterium would create an HDO molecule whose O–H stretch would appear near the H_2O modes that are present in the D_0-$GlyH^+\cdot(H_2O)_6$ spectrum. Hence, the dominant species contributing to the observed IRPD spectrum is indeed D_0-$GlyH^+\cdot(D_2O)_6$.

Figure 7.3 shows a series of IRPD spectra corresponding to $GlyH^+$ clusters solvated with n = 0–8 water molecules. Here, the spectra of the isotopologues for each cluster size are plotted on top of each other, with $GlyH^+\cdot(H_2O)_n$ in blue and $GlyH^+\cdot(D_2O)_n$ in red, such that the features that are common to both appear in purple. Displaying the data in this fashion highlights the vibrational signatures corresponding to the H_2O (blue) or D_2O (red) solvent molecules and those of the core $GlyH^+$ ion (purple). Typically, the analysis of such IRPD spectra requires comparison to calculations of many possible isomers, necessitating extensive considerations of energetic accuracies and validity of the harmonic frequencies. Such comparisons would certainly yield deeper insights and will be the subject of a subsequent and more detailed paper. Here, we will focus on highlighting the usefulness of this experimental approach in providing direct structural insights, which also reduces the number of possible solvation structures that need to be explored computationally.

For example, the $GlyH^+$ features in the 3200–3600 cm^{-1} region, i.e., the free N–H and free carboxyl O–H stretches, are present only in the n = 0–3 clusters, promptly disappearing in the n = 4 spectrum. On the other hand, the spectra of n = 1–4 clusters display H_2O O–H stretches in only the free O–H region between 3600 and 3800 cm^{-1}. It is therefore immediately apparent that the

Figure 7.3 IRPD spectra of D_0-$GlyH^+\cdot(H_2O)_n$ (blue) and D_0-$GlyH^+\cdot(D_2O)_n$ (red). The purple area corresponds to features that are common to both isotopologues. Each H_2O spectrum is normalized independently to its most intense feature. Each D_2O spectrum is normalized to its corresponding H_2O spectrum by comparing the overlapped regions. General designations of the spectral regions are noted on top.

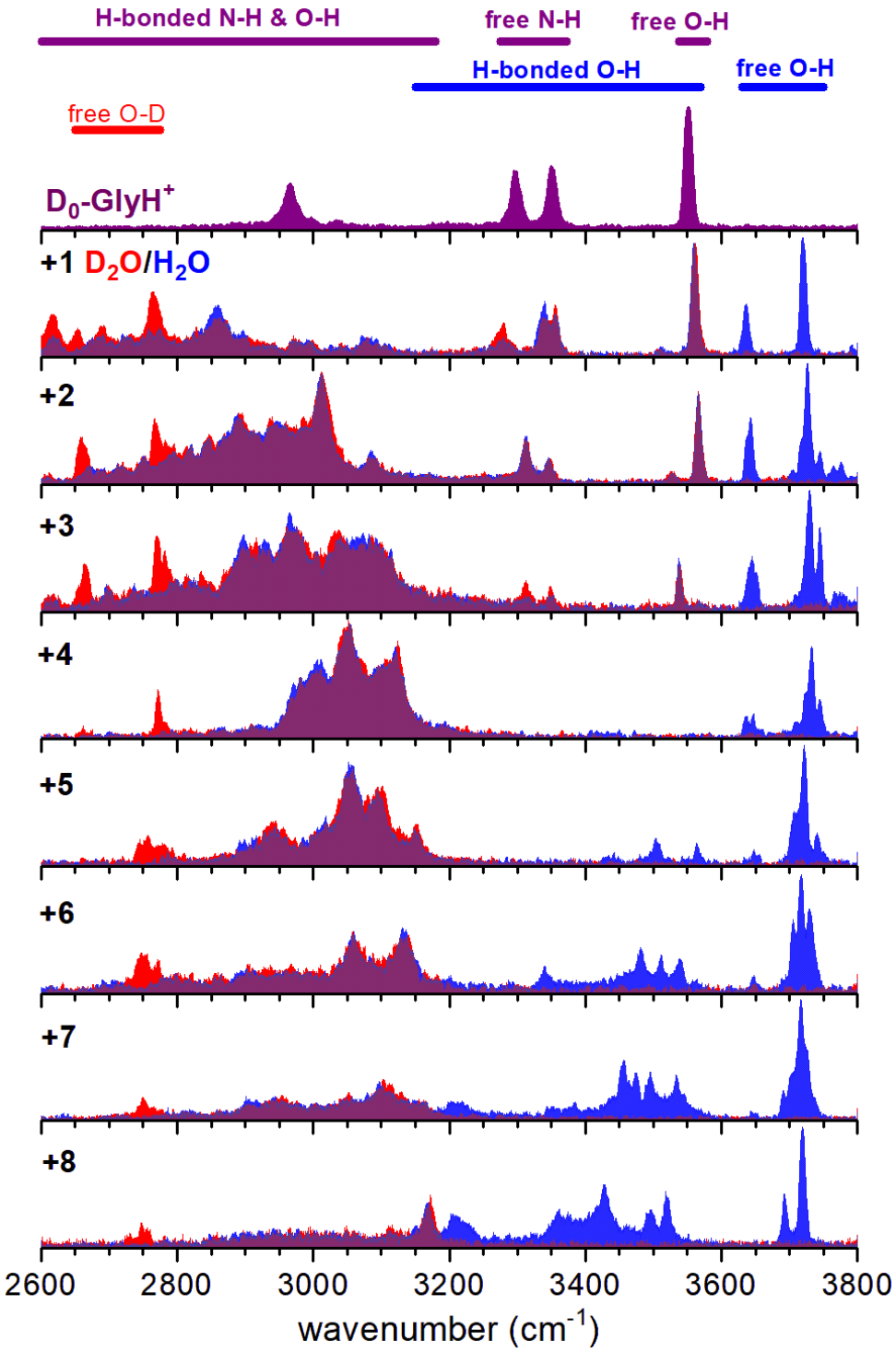

first four water molecules do not act as H-bond donors, quickly eliminating any potential structures with water–water interactions. Moreover, this observation essentially points to a single possible structure for $GlyH^+\cdot(H_2O)_4$ where the four water molecules are in a single H-bond acceptor configuration interacting with the four N–H and O–H groups in the $GlyH^+$ ion. For the n = 0–4 clusters, each addition of a water molecule redshifts one more of the $GlyH^+$ free N–H or O–H stretches to the H-bonded spectral region (2800–3200 cm^{-1}). However, the number of features in the 3200–3600 cm^{-1} region does not decrease gradually with the increasing number of water molecules. This is indicative of the presence of multiple energetically competitive isomers for the n = 1–3 clusters, providing a starting point for computational explorations.

The H-bonded O–H stretches of H_2O appear clearly in the n = 5 spectrum at around 3500 cm^{-1}, evidence that the fifth water molecule H-bonds with another water molecule, starting the formation of the second solvation shell. None of the free N–H and O–H features reappear above n = 4, which indicates that the first solvation shell remains essentially intact in larger clusters. In the 3600–3800 cm^{-1} region, the H_2O symmetric and asymmetric stretches gradually give way to a cluster of features near 3700 cm^{-1}, indicating that each water molecule is donating at least one H-bond in the larger (n = 6–8) clusters.[21] The number of possible structures fulfilling these criteria is still large and will require computational searches for conclusive assignments. However, interesting trends can already be extracted from the rough assignments to either the ion core or the water solvents. For example, the 2800–3200 cm^{-1} region contains the H-bonded $GlyH^+$ N–H and O–H stretches (purple), which are lowest in frequency in the n = 1 spectrum. As solvation increases, these features shift to higher frequencies. On the other hand, the H-bonded O–H stretches of H_2O molecules (blue) in the 3200–3600 cm^{-1} region gradually redshift with increasing solvation from n = 5 to 8. Empirically, the strength of an H-bond interaction involving

an X–H group is proportional to the square root of the frequency shift from the free X–H modes.[22–24] Therefore, the observed trends highlight how the cooperative strengthening of the water–water H-bonded network around $GlyH^+$ has an anticooperative effect on the ion–water interactions. They also suggest that larger clusters are needed to reach the regime that would fully represent the interaction strength present in bulk solvation. In principle, the H_2O/D_2O substitution approach outlined here can allow for such spectroscopic characterization in much larger clusters approaching the bulk limit. Furthermore, the assignment of the ion core features can be further refined by using ^{15}N isotopically labeled glycine to differentiate the N–H and O–H stretches.

Finally, we take a closer look at the IRPD spectra of the $n = 1$ cluster in the $GlyH^+$ free N–H/O–H region, shown in Figure 7.4, which illustrates another layer of information that we can obtain from the experimental data. Because any single D_0-$GlyH^+\cdot(H_2O)_1$ structure can only have a maximum of three distinct features in this region, the observation of four peaks indicates that there are at least two isomers contributing to the experimental spectrum. The H_2O/D_2O substitution indicates that these four features indeed belong to the $GlyH^+$ ion core. However, the D_0-$GlyH^+\cdot(H_2O)_1$ and D_0-$GlyH^+\cdot(D_2O)_1$ spectra do not perfectly overlap, as highlighted in Figure 7.4A by the presence of small residual red and blue regions. This indicates that the relative populations of the isomers are different in the D_0-$GlyH^+\cdot(H_2O)_1$ and D_0-$GlyH^+\cdot(D_2O)_1$ clusters. On the basis of the spectral differences, we can discern which features are common to a single isomer. One isomer contains features at 3277 and 3357 cm^{-1} and the high-frequency part of the 3560 cm^{-1} feature, while another isomer has the 3339 cm^{-1} feature and the lower-frequency part of the 3560 cm^{-1} feature. Because both isomers have the ~3560 cm^{-1} carboxyl free O–H stretch, the water molecule must be solvating the protonated amine in two different configurations. Computations indeed reveal the two conformers, shown in Figure 7.4B,C,

Figure 7.4 (A) Overlapped IRPD spectra of D_0-$GlyH^+ \cdot (H_2O)_1$ (blue) and D_0-$GlyH^+ \cdot (D_2O)_1$ (red). (B,C) Calculated harmonic spectra and structures of D_0-$GlyH^+ \cdot (H_2O)_1$. The calculations were carried out at the B2PLYPD3/def2-TZVPP level and scaled by 0.954.

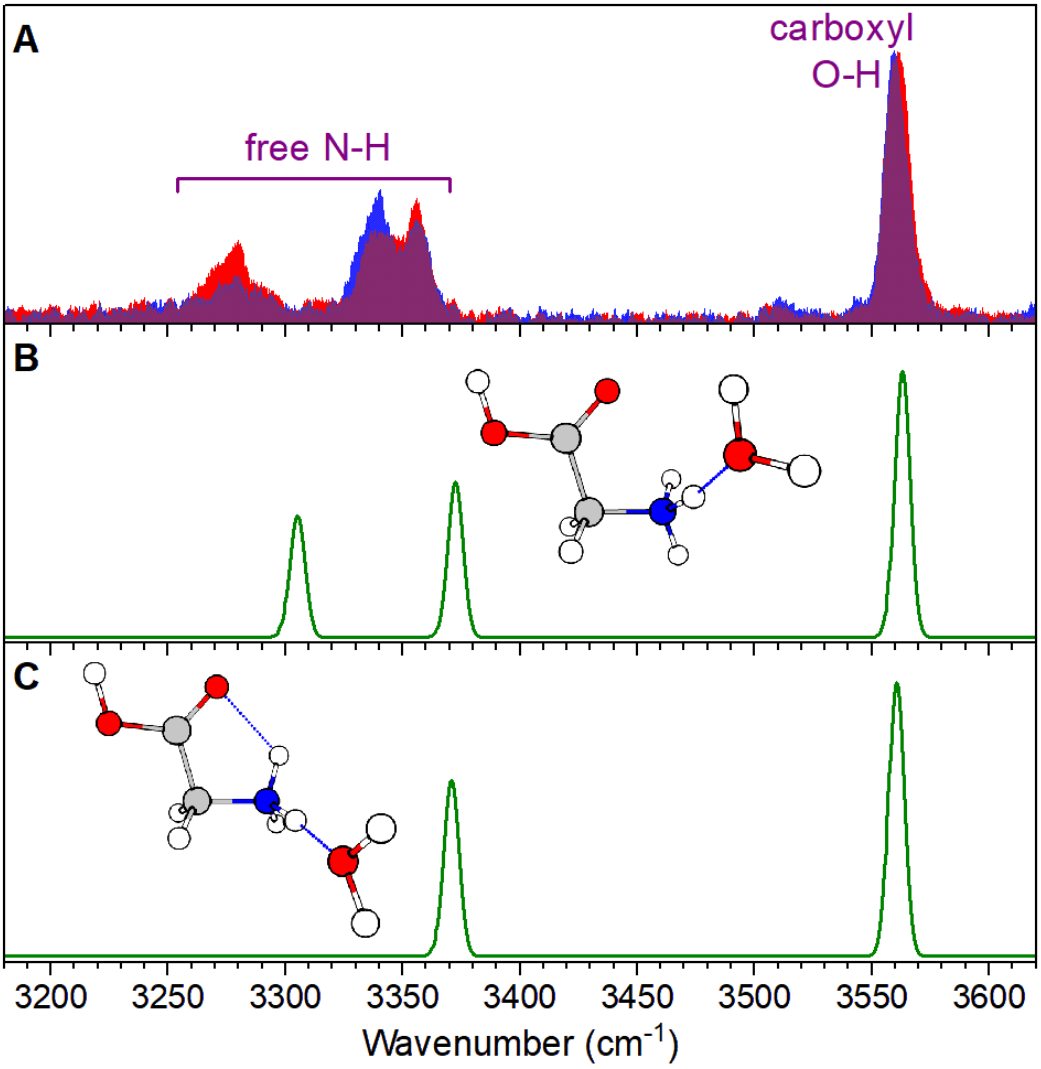

and their calculated harmonic spectra show good agreement with the experiment. The barrier for the internal rotation connecting these two structures is calculated to be very small (~100 cm^{-1}); therefore, these conformers are not likely to be kinetically trapped and we can relate the observed changes in the relative conformer populations to the small difference in zero-point energy change upon isotopic substitution. Specifically, a ΔΔZPE of ~18 cm^{-1}, favoring the conformer shown in Figure 7.4B in the D_0-$GlyH^+\cdot(D_2O)_1$ complex, is obtained using the calculated harmonic frequencies of both structures.

7.4 Conclusion

Overall, using the solvated $GlyH^+$ complexes as an illustrative example, we show that it is possible to minimize ion–water H/D exchange inside of the 80 K reaction trap, allowing for selective formation of clusters containing D_2O solvating an all-hydrogen $GlyH^+$ ion. Such a capability provides a means to selectively shift solvent water vibrations independent of those of the ion core, allowing access to the solvation-sensitive N–H and O–H stretches. Moreover, comparisons of isotopologue spectra can clearly distinguish vibrational signatures of the solvent and solute molecules, allowing for quick assessment of solvation structures and aiding computational searches. It is certainly possible to further explore the amide I and II ranges using this approach as the H_2O and D_2O bend modes should yield similar behaviors. We believe that this approach should facilitate the spectroscopic characterization of more complex peptide ions embedded in large water clusters approaching the bulk solvation limit. Some of the inherent challenges involved with the spectroscopy of large and flexible molecules, such as spectral congestion and the presence of multiple conformations, will not be alleviated by the method outlined here. However, when focusing solely on the structure of the embedded peptide, the

H_2O/D_2O substitution approach will reduce the complexity of the spectral analysis of the ion core itself. Moreover, it can easily be combined with other established tools, such as site-selective $^{13}C/^{15}N$ labeling[25,26] and conformer-selective IR–IR spectroscopy,[16,27,28] to provide additional information necessary for definitive structural characterization. Lastly, we note that improved experimental control over the H/D exchange reactions can potentially be achieved by incorporating an additional cryogenic trap such that the cooling and clustering steps occur in sequence. This should remove the minor presence of isotopomers, which may be necessary for species that have lower barriers for H/D exchange with solvent molecules.

7.5 References

1. R.G Bryant, M.A. Johnson, P.J Rossky, *Acc. Chem. Res.,* **2012,** 45, 1−2.

2. N.C Polfer, *Chem. Soc. Rev.,* **2011,** 40, 2211−2221.

3. N.C., Polfer, J. Oomens, *Mass Spectrom. Rev.,* **2009,** 28, 468−494.

4. J. Oomens, B.G. Sartakov, G. Meijer, G. Von Helden, *Int. J. Mass Spectrom.,* **2006,** 254, 1−19.

5. N. Heine, K.R. Asmis, *Int. Rev. Phys. Chem.,* **2015,** 34, 1−34.

6. N.S. Nagornova, T.R. Rizzo, O.V. Boyarkin, *Science,* **2012,** 336, 320−323.

7. T.R. Rizzo, J.A. Stearns, O.V. Boyarkin, *Int. Rev. Phys. Chem.,* **2009,** 28, 481−515.

8. J.C. Dean, E.G. Buchanan, T.S Zwier, *J. Am. Chem. Soc.,* **2012,** 134, 17186−17201.

9. S. Heiles, R.J. Cooper, M.J. DiTucci, E.R. Williams, *Chem. Sci.,* **2015,** 6, 3420−3429.

10. J.M. Voss, B.M. Marsh, J. Zhou, E. Garand, Phys. *Chem. Chem. Phys.,* **2016,** 18, 18905−18913.

11. A.B. Wolk, C.M. Leavitt, E. Garand, M.A. Johnson, *Acc. Chem. Res.,* **2014,** 47, 202−210.

12. J. Klyne, M. Schmies, M. Miyazaki, M. Fujii, O. Dopfer, *Phys. Chem. Chem. Phys.,* **2018,** 20, 3148−3164.

13. B.M. Marsh, J.M. Voss, E. Garand, *J. Chem. Phys.,* **2015,** 143, 204201.

14. D.M. Byler, H. Susi, *Biopolymers,* **1986,** 25, 469−487.

15. H. Yang, S. Yang, J. Kong, A. Dong, S. Yu, *Nat. Protoc.,* **2015,** 10, 382.

16. C.M. Leavitt, A.B. Wolk, J.A. Fournier, M.Z. Kamrath, E. Garand, M.J. Van Stipdonk, M.A. Johnson, *J. Phys. Chem. Lett.,* **2012,** 3, 1099−1105.

17. J.T. O'Brien, E.R. Williams, *J. Am. Chem. Soc.,* **2012,** 134, 10228−10236.

18. T.L Guasco, B.M. Elliott, M.A. Johnson, J. Ding, K.D. Jordan, *J. Phys. Chem. Lett.,* **2010,** 1, 2396−2401.

19. C.T. Wolke, J.A. Fournier, E. Miliordos, S.M. Kathmann, S.S. Xantheas, M.A. Johnson, *J. Chem. Phys.,* **2016,** 144, 074305.

20. S. Campbell, M.T. Rodgers, E.M. Marzluff, J.L. Beauchamp, *J. Am. Chem. Soc.*, **1995,** 117, 12840−12854.

21. J.-W. Shin, N.I. Hammer, E.G. Diken, M.A. Johnson, R.S. Walters, T.D. Jaeger, M.A. Duncan, R.A. Christie, K.D. Jordan, *Science,* **2004,** 35, 1137−1140.

22. A.V. Iogansen, *Spectrochim. Acta, Part A,* **1999,** 55, 1585−1612.

23. M. Rozenberg, A. Loewenschuss, Y. Marcus, *Phys. Chem. Chem. Phys.*, **2000,** 2, 2699−2702.

24. M. Rozenberg, G. Shoham, I. Reva, R.A. Fausto, *Phys. Chem. Chem. Phys.*, **2005,** 7, 2376−2383.

25. E. Garand, M.Z. Kamrath, P.A. Jordan, A.B. Wolk, C.M. Leavitt, A.B. McCoy, S.J. Miller, M.A. Johnson, *Science,* **2012,** 335, 694−698.

26. J.A. Stearns, C. Seaiby, O.V. Boyarkin, T.R. Rizzo, *Phys. Chem. Chem. Phys.*, **2009,** 11, 125−132.

27. N. Heine, M.R. Fagiani, M. Rossi, T. Wende, G. Berden, V. Blum, K.R. Asmis, *J. Am. Chem. Soc.,* **2013,** 135, 8266−8273.

28. J.M. Voss, S.J. Kregel, K.C. Fischer, E. Garand, *J. Am. Soc. Mass Spectrom.*, **2018,** 29, 42−50.

CHAPTER 8

Future Directions

8.1 Introduction

The experiments presented in Chapters 3-7 showcase the versatility of cryogenic ion vibrational spectroscopy to study catalytic reactions, conformational populations, and solvation effects. These experiments should provide a firm foundation on which to carry out far more sophisticated and informative studies in the future. This Chapter presents preliminary data that demonstrates even more information that can be gathered with carefully crafted CIVS experiments. This data perhaps foreshadows the types of gas-phase experiments that will be routinely achieved in coming years.

8.2 Finding H/D Exchange Reaction Barriers

The previous Chapter outlined an experimental approach for controlling H/D exchange by varying the ion reaction trap temperature. Quenching the H/D reaction completely is obviously useful for disentangling IR spectra of solvated biomolecules, which can be very spectrally congested. However, the trap temperature and the magnitude of reaction can be used to experimentally estimate the activation energy *(E_A)* of the H/D exchange process as well.

Figure 8.1 shows mass spectra of the products formed from glycine betaine (GB^+) reacting with D_2O inside of the reaction trap at different temperatures. At a trap temperature of 209 K (Figure 8.1A), two dominant peaks at *m/z* = 118 and 119 are observed. The *m/z* = 118 feature corresponds to the hydrogen-containing GB^+, which is designated as D_0-GB^+ hereafter. The *m/z* = 119 feature therefore corresponds to GB^+ that has undergone one H/D exchange event inside the

Figure 8.1 (A-C) Temperature dependent mass spectra showing progressive quenching of H/D exchange. (D) Reaction coordinate showing H/D exchange between glycine betaine and D_2O. Deuterium is designated in green.

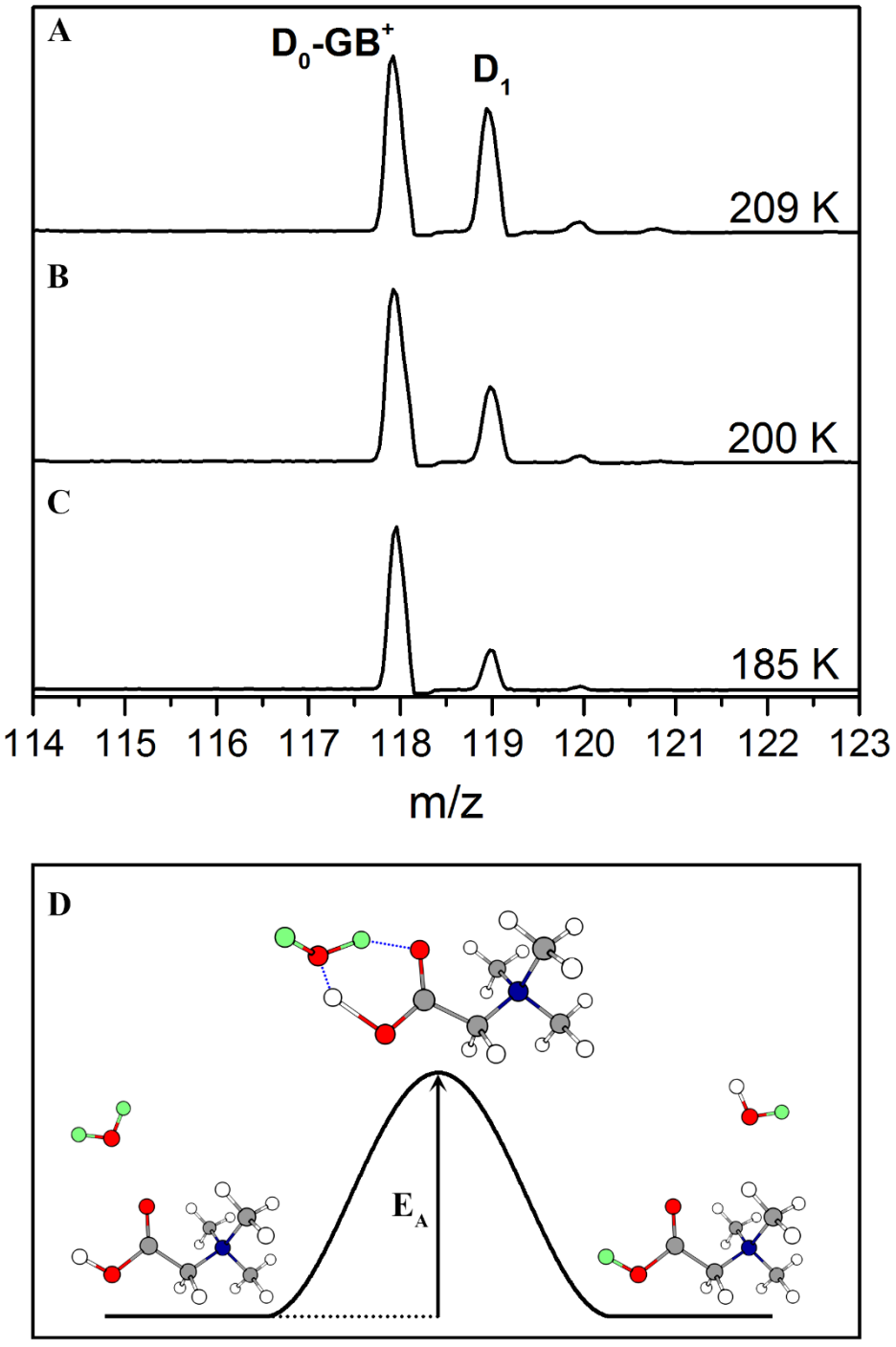

reaction trap, hereafter referred to as D_1-GB^+. It should be noted that because of the methylated amine group, only a single H/D exchange event at the carboxylic acid is expected. With decreasing trap temperature, the presence of D_1-GB^+ decreases as expected (Figure 8.1B,C). Figure 8.1D shows the reaction coordinate for the H/D exchange process between D_2O and GB^+, where deuterium is highlighted in green.

A few simple steps can be taken to experimentally determine the reaction barrier height shown in Figure 8.1D. First, since D_2O is much more abundant than D_0-GB^+, we can assume the reaction is pseudo first-order with respect to D_0-GB^+, i.e., the reaction is overwhelmingly dependent on D_0-GB^+. The reaction is then described by the differential for of the rate law by

$$Rate = \frac{-d[A]}{dt} = k[A] \qquad \text{(eq. 8.2.1)}$$

Upon integration of eq. 8.2.1 we find that

$$\ln[A] - \ln[A]_0 = -kt \qquad \text{(eq. 8.2.2)}$$

Which can be rearranged to give

$$ln\left(\frac{[A]_t}{[A]_0}\right) = -kt \qquad \text{(eq. 8.2.3)}$$

In the present case, $[A]_0$ and $[A]_t$ correspond to the D_0-GB^+ and D_1-GB^+ features at m/z = 118 and 119, respectively. Given our experimental approach, there's an important caveat to note regarding equation eq. 8.2.3: we aren't varying time in order to make our measurements.

Therefore, it's not important how long the reaction takes place, as long as it's constant at each temperature measurement. Thus, we can compare the H/D exchange reaction of D_0-GB^+ at two different temperatures T_1 and T_2 by

$$\frac{ln\left(\frac{[A]_t}{[A]_0}\right)_{T_1} = -k_1 t}{ln\left(\frac{[A]_t}{[A]_0}\right)_{T_2} = -k_2 t} \qquad \text{(eq. 8.2.4)}$$

As outlined above, the time of reaction is the same in both case and therefore cancels to yield

$$\frac{ln\left(\frac{[A]_t}{[A]_0}\right)_{T_1}}{ln\left(\frac{[A]_t}{[A]_0}\right)_{T_2}} = \frac{k_1}{k_2} \qquad \text{(eq. 8.2.5)}$$

The ratio k_1/k_2 is important, as it can be inserted into the integrated Arrhenius Equation.

$$ln\left(\frac{k_1}{k_2}\right) = \frac{E_A}{R}\left(\frac{1}{T_2} - \frac{1}{T_1}\right) \qquad \text{(eq. 8.2.6)}$$

Eq. 8.2.6 shows that the activation energy (E_A) can be found from the slope of an integrated Arrhenius plot, as shown in Figure 8.2. In this manner, the barrier for reaction between D_2O and D_0-GB^+ is determined to be 18.8 ± 0.9 kJ/mol (1570 ± 75 cm^{-1}).

Figure 8.2 Integrated Arrhenius plot for H/D exchange between glycine betaine and D_2O from 188 – 209 K. The slope of the line is used to find the activation energy for the reaction, which is estimated to be 18.8 ± 0.9 kJ/mol (1570 ± 75 cm^{-1}).

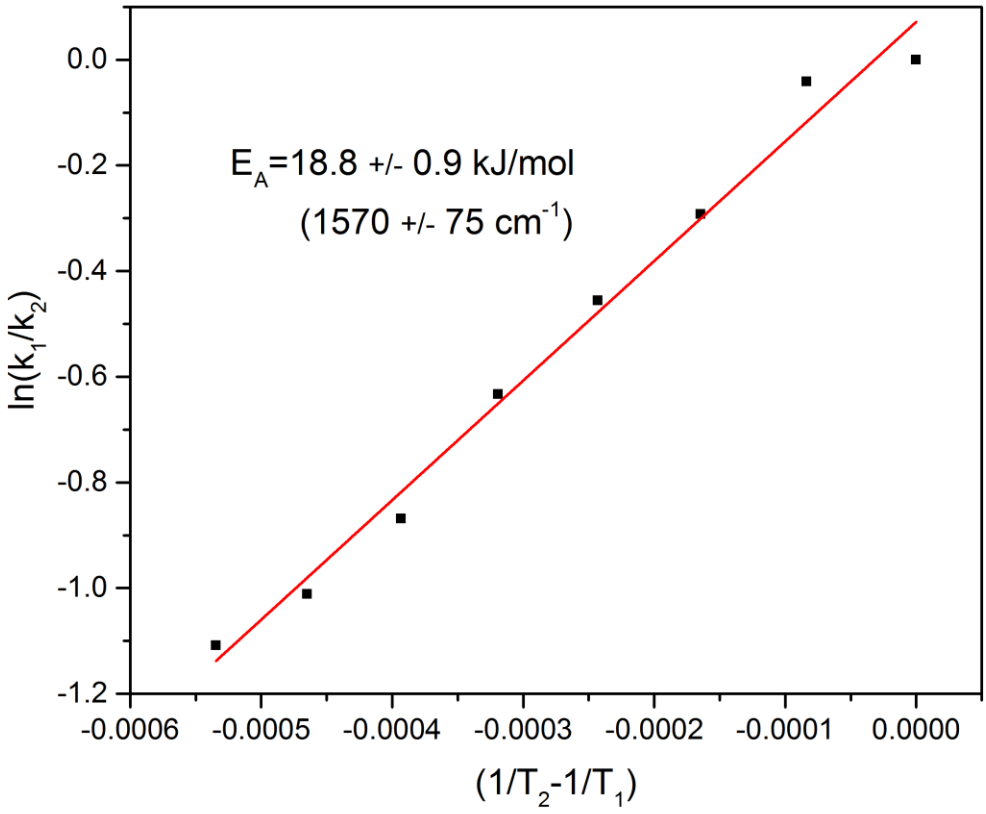

8.3 Pinpointing H/D Reaction Sites

The process outlined in section 8.2 is straightforward for species containing a single exchangeable hydrogen, e.g. glycine betaine. However, the situation becomes much more complicated when there are multiple available H/D exchange sites in a molecular ion. This is exemplified by the mass analyses of products formed from protonated diglycine, Gly_2H^+, and D_2O inside of the reaction trap at different temperatures, as shown in Figure 8.3. Figure 8.3A shows the presence of a large feature at *m/z* = 133 (purple), which corresponds to the all-hydrogen Gly_2H^+, denoted as D_0-Gly_2H^+ hereafter. The small feature present at *m/z* = 134 corresponds to the ^{13}C feature of D_0-Gly_2H^+. Figure 8.3B-F show that as the temperature of the reaction trap is gradually raised, multiple H/D exchange events occur, with *m/z* = 134, 135, 136, 137, and 138 corresponding to D_1-Gly_2H^+ (blue), D_2-Gly_2H^+ (green), D_3-Gly_2H^+ (orange), D_4-Gly_2H^+ (red), and D_5-Gly_2^+ (pink), respectively. Though there are five exchangeable hydrogens, there is surprisingly little intensity at *m/z* = 138, even at temperatures above 200 K. These mass spectra were chosen as they correspond to the temperatures where each isotopologue first appears.

In spite of the overlapping mass features due to ^{13}C, the relative populations of reaction products (D_1-Gly_2H^+, D_2-Gly_2H^+, etc.) can be easily found by the analysis procedure described in Chapter 3.3. Briefly, the analysis involves fitting the experimental features with Gaussian peaks and deducing interferences by natural isotope intensities. The relative populations can then be plotted as a function of temperature, as shown in Figure 8.4A. For comparison, previously published data for Gly_2H^+ reacting with D_2O in a Fourier transform ion cyclotron resonance mass spectrometer[1] is given in Figure 8.4B and shows striking similarity to the temperature-dependent exchange data presented here.

Figure 8.3 Temperature-dependent mass spectra showing gas-phase H/D exchange when Gly_2H^+ and D_2O collide in reaction trap. The selected mass spectra represent the temperatures at which each isotopologue first appears. The highlighted peaks correspond to D_0-Gly_2H^+ (purple), D_1-Gly_2H^+ (blue), D_2-Gly_2H^+ (green), D_3-Gly_2H^+ (orange), D_4-Gly_2H^+ (red), and D_5-Gly_2^+ (pink).

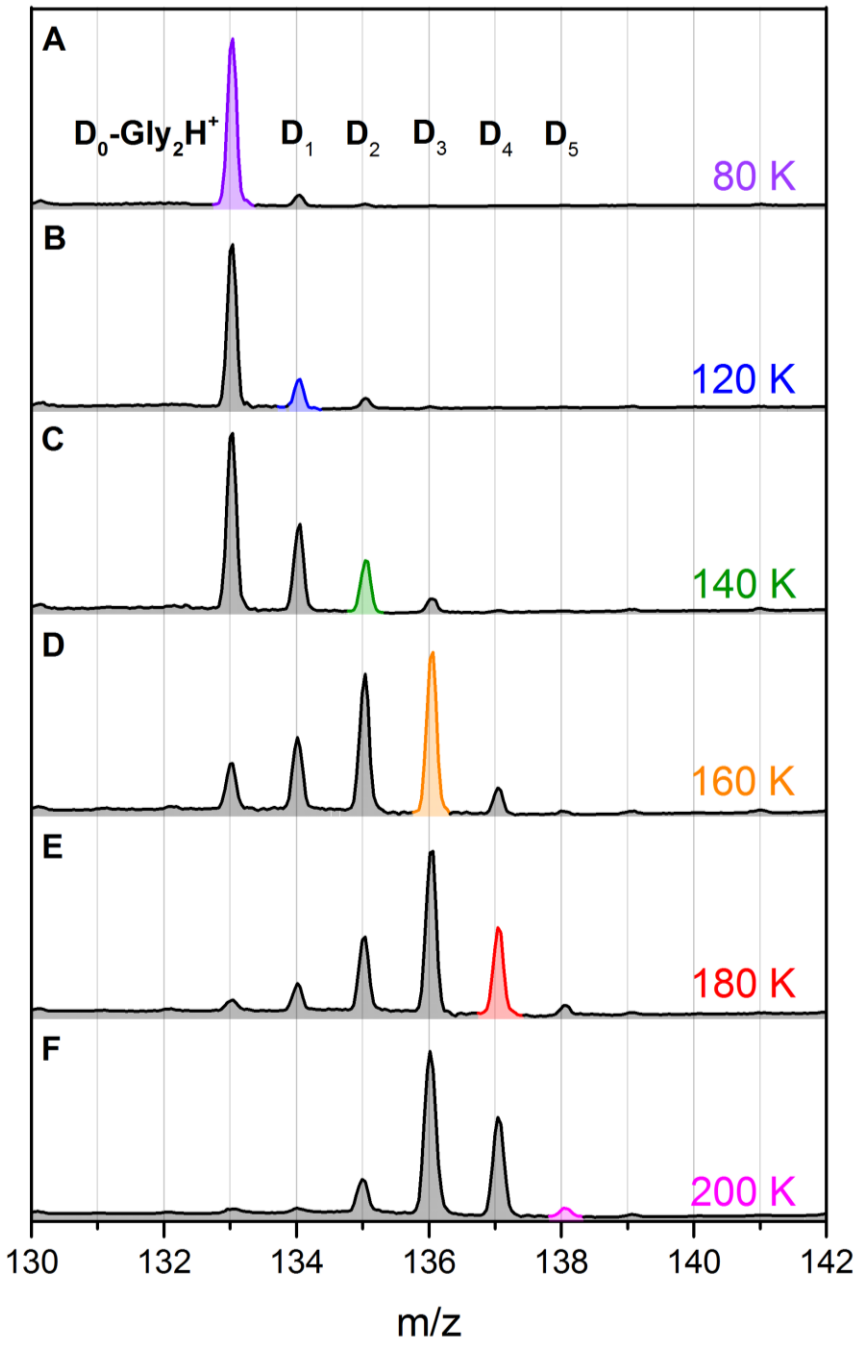

Figure 8.4 (A) Plots showing H/D exchange product relative abundances of Gly_2H^+ with D_2O as a function of reaction trap temperature. (B) Time plots of the H/D exchange products of Gly_2H^+ and D_2O in Fourier transform ion cyclotron mass spectrometer reproduced from Reference 1.

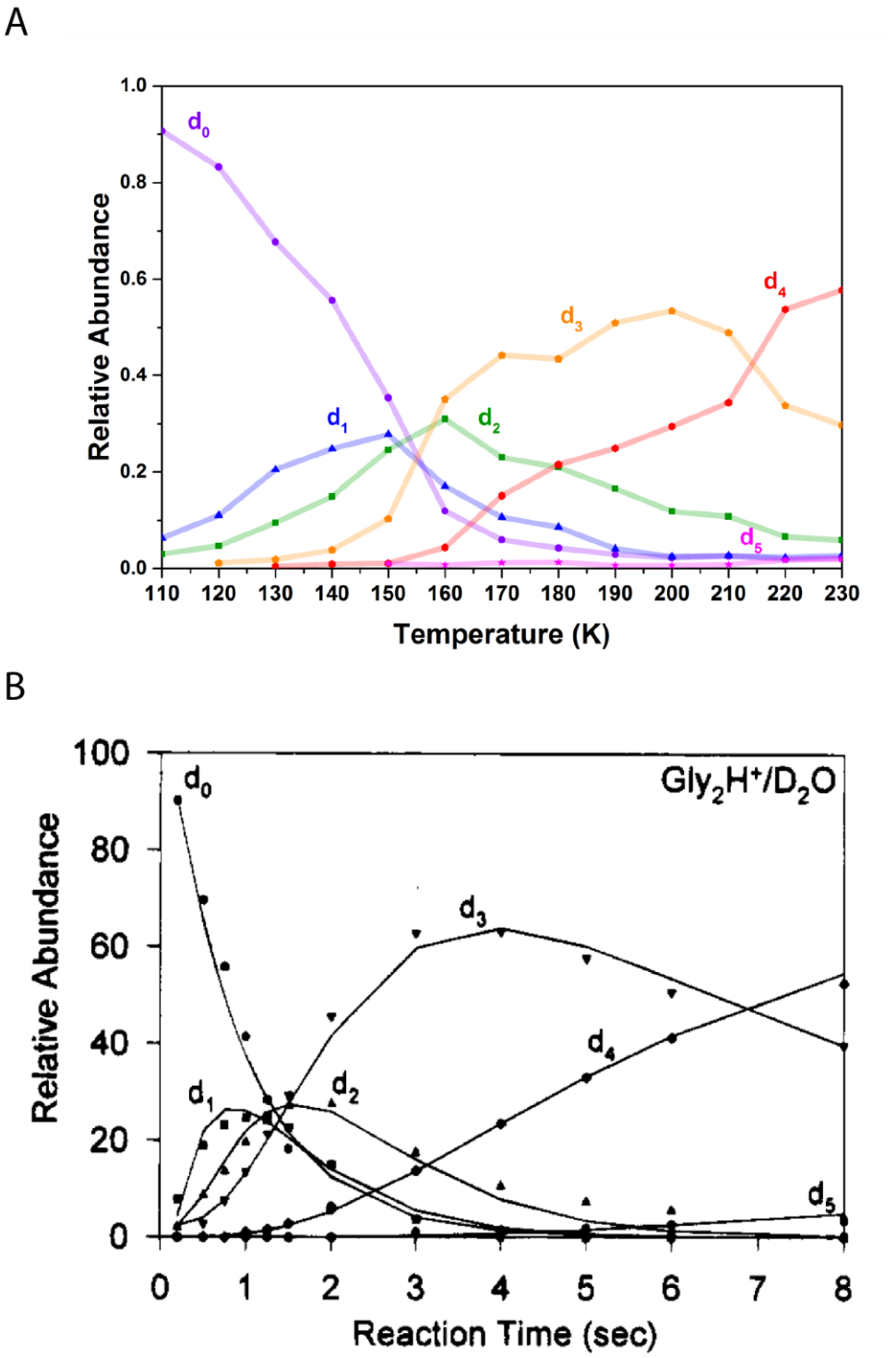

Although the diglycine isotopologue populations at each temperature are readily found, the location of deuteration in each case isn't immediately clear. For example, there are five labile hydrogens capable of incorporating deuterium into Gly_2H^+ during the first exchange event. In order to probe the site of reaction, the infrared predissociation spectra of the different H/D reaction products were acquired, which are shown in Figure 8.5.

Figure 8.5A shows the IRPD spectrum of the D_0-Gly_2H^+ species acquired with the reaction trap held at 80 K (purple spectrum). The 3571 cm^{-1} feature (highlighted in blue) corresponds to the free O-H stretch of the carboxylic acid group. The 3378 cm^{-1} and 3322 cm^{-1} peaks (highlighted in red) are due to asymmetric and symmetric NH_2 stretching of the protonated amine group. Finally, the large feature centered at 3363 cm^{-1} (highlighted in green) corresponds to N-H stretching of the amide group.

Figure 8.5B shows the IRPD spectrum (blue) of the D_1-Gly_2H^+ complex acquired at 120 K. The intensities of the carboxylic acid O-H stretch and the amide N-H stretch remain relatively unchanged in this spectrum. However, the two peaks associated with the asymmetric and symmetric NH_2 stretching of the amine group have decreased significantly, as compared with the D_0-Gly_2H^+ species. The decreased intensity of the 3378 cm^{-1} and 3322 cm^{-1} peaks is the result of deuteration at the NH_3 group, which redshifts these features to the lower part of the spectrum.

Figure 8.5C shows the IRPD spectrum (green) of the D_2-Gly_2H^+ species acquired with the reaction trap held at 140 K. Again, the features related to the carboxylic acid O-H stretch and the amide N-H stretch are unaffected by the second H/D exchange event. Instead, we see that the amine stretching features have decreased even more, and that the 3378 cm^{-1} peak has disappeared entirely. This means that the first two deuteration events occur primarily within the NH_3^+ moiety.

Figure 8.5 IRPD spectra of H/D exchange products of Gly_2H^+ and D_2O at (A) 80 K , (B) 120 K, (C) 140 K, (D) 160 K, and (E) 180 K. The spectral features highlighted by the blue, red, and green rectangles correspond to stretching of the carboxylic acid, amine, and amide groups, respectively. The structure of Gly_2H^+ is also given in top of Figure 8.5A.

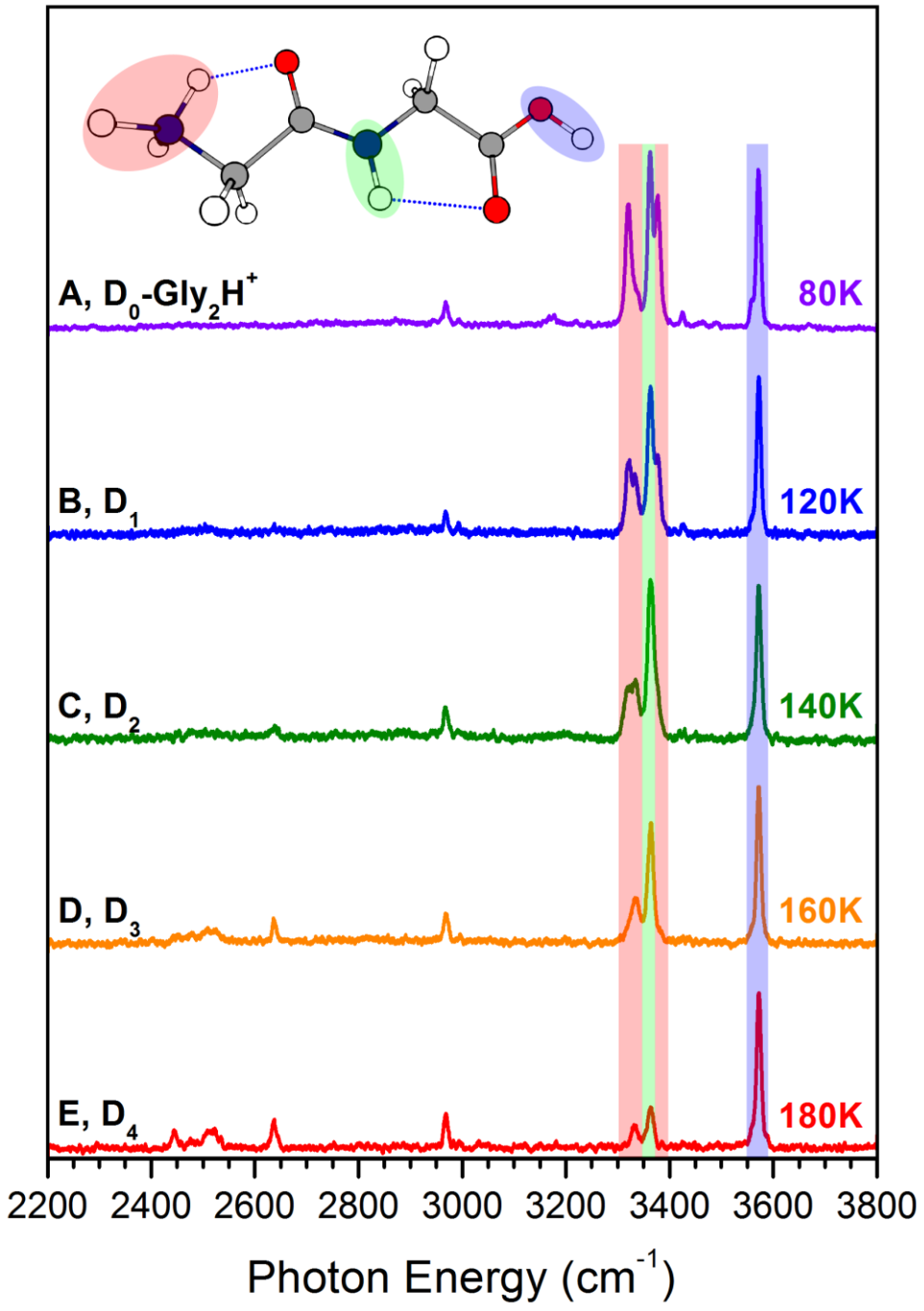

Figure 8.5D shows the spectrum (orange) of the protonated diglycine species which has been deuterated three times at 160 K (D_3-Gly_2H^+) . The carboxylic acid O-H stretch at 3571 cm^{-1} is the most intense feature of the spectrum. While the 3378 cm^{-1} stretching feature is not observed, a free N-H stretch of the amine group is still present at 3334 cm^{-1}. Furthermore, it's apparent that the amide N-H feature in the D_3-Gly_2H^+ species has decreased somewhat in intensity. The deuteration is therefore being shared between the amine and amide groups. Furthermore, it should be noted that the strong H-bonding between the NH_3 group and neighboring amide C=O likely prevents all of the amine hydrogens from being readily exchanged in three sequential reactions.

Figure 8.5E shows the D_4-Gly_2H^+ complex formed in the 180 K reaction trap environment. The vibrational features related to the amine and amide N-H stretching are notably diminished, while the carboxylic acid O-H feature persists. It's clear from this spectrum that the carboxylic group contains the least exchangeable hydrogen.

8.4 H/D Exchange in Solvated Clusters

Finally, it is possible to form and probe solvated clusters that have undergone internal H/D exchange. For example, D_n-Gly_2H^+ products can be minimized at 80 K and Gly_2H^+ can be clustered with D_2O. Figure 8.6A shows the experimental IRPD spectrum of the $Gly_2H^+(+D_2O)_1$ species. Previous work[2] shows the water bridges the amine and carboxyl groups and this structure can be used to help interpret the experimental spectrum in Figure 8.6A. The 3572 cm^{-1}, 3481 cm^{-1}, 3353 cm^{-1}, and 3138 cm^{-1} features correspond to the carboxylic O-H, amide N-H, and asymmetric and symmetric NH_2 stretching of the amine, respectively. Previous experiments demonstrate that the broad feature at ~2730 cm^{-1} is representative of a solvated N-H group resulting from a strong H-

bond interaction with water. The peaks at 3703 cm^{-1} and 3442 cm^{-1} occur in regimes characteristic of a water molecule in an acceptor-donor configuration, and correspond to the free and H-bonded O-H stretching, respectively.

The harmonic spectrum given in Figure 8.6B contains many of the features observed experimentally. For example, it displays peaks at 3572 cm^{-1}, 3461 cm^{-1}, 3356 cm^{-1}, 3210 cm^{-1}, and 2772 cm^{-1} related to the carboxylic O-H, amide N-H, NH_2 stretching of the amine, and the solvated N-H group of the amine, respectively. It also contains features at 2701 cm^{-1} and 2485 cm^{-1}, which are the result free and bound O-D stretching, respectively. The corresponding structure (also given in 8.6B) shows a D_2O molecule solvating the all hydrogen Gly_2H^+, i.e. the D_0-$Gly_2H^+(D_2O)_1$ species. Such a structure represents a population of Gly_2H^+ ions which are thermalized and solvated before H/D exchange can take place.

The calculated spectrum in Figure 8.6C contains all of the same spectral features related to the free stretches of the peptide from Figure 8.6B. This spectrum, however, displays a few distinct differences from spectrum 6.8B. First, there is no strongly redshifted N-H stretch in the lower spectral region. Second, there is an intense feature present at 3437 cm^{-1}. The structure given in 6.8C shows that these peaks are the result of a cluster where H/D exchange has taken place between the D_2O and Gly_2H^+, i.e. a D_1-$Gly_2H^+(HDO)_1$ complex. Here, the deuterium has migrated to the amine portion of the peptide, thus leading to a strongly solvated N-D group, which is redshifted below the spectral window presented here. The hydrogen from the amine group creates a HDO molecule, with the O-H group donating a H-bond to the COOH group of the peptide. This H-bonding peak of the water agrees very well with the experimentally observed 3443 cm^{-1} feature.

Figure 8.6 (A) Experimental IRPD spectrum of $Gly_2H^+(+D_2O)_1 \cdot D_2$. Harmonic spectra corresponding to (B) D_0-$Gly_2H^+(D_2O)_1$, (C) D_1-$Gly_2H^+(HDO)_1$ with a free O-D group, and (D) D_1-$Gly_2H^+(HDO)_1$ with a donor O-D group. The spectral features relating to O-D and O-H water groups are colored in green and blue, respectively. Furthermore, deuterium is highlighted in green in each structure.

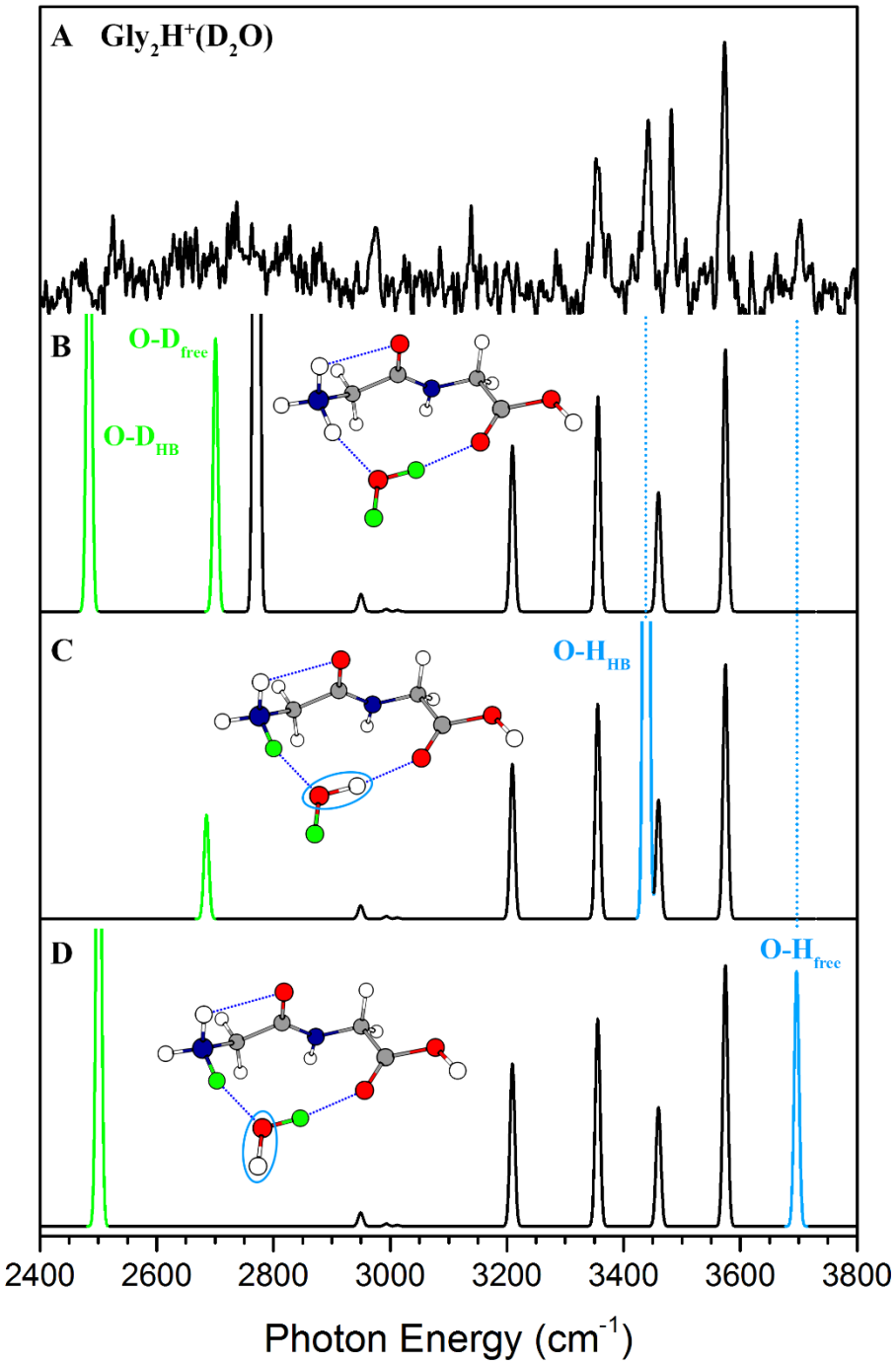

Figure 8.6D shows a calculated spectrum corresponding to another D_1-$Gly_2H^+(HDO)_1$ structure. Like the previous structure, it displays all of the peaks related to the free groups of the peptide and like the species in 8.6C, it does not have the ~2730 cm^{-1} feature of the solvated N-H amine group. However, it has an intense peak at 3697 cm^{-1}, close to that of the experimental peak at 3703 cm^{-1}. The D_1-$Gly_2H^+(HDO)_1$ structure in 8.6D shows that these motifs are well-produced with a solvated N-D group and the exchanged O-H group positioned away from the peptide.

These experiments are certainly not exhaustive and this system should be investigated with a double resonance IR-IR approach in order to disentangle and confirm the presence of these reaction products. Nonetheless, the formation of non-exchanged and exchanged solvated clusters, in addition to the previous experiments outlined in this chapter, open up the possibility to map out reaction pathways in new and exciting ways.

8.5 References

1. S. Campbell, M.T. Rodgers, E.M. Marzluff, J.L. Beauchamp, *J. Am. Chem. Soc.*, **1995**, 117, 12840 – 12854

2. B.M. Marsh, J.M. Voss, E. Garand, *J. Chem. Phys.*, **2015**, 143, 204201